TUBE EROSION IN FLUIDIZED BEDS

by

Jingxu (Jesse) Zhu

B. Eng., Tsinghua University, 1982

A THESIS SUBMITTED IN PARTIAL FULFILLMENT OF
THE REQUIREMENTS FOR THE DEGREE OF
DOCTOR OF PHILOSOPHY
in
THE FACULTY OF GRADUATE STUDIES
Department of Chemical Engineering

We accept this thesis as conforming
to the required standard

THE UNIVERSITY OF BRITISH COLUMBIA

May 1988

©Jingxu Zhu, 1988

In presenting this thsis in partial fulfilment of the requirements for an advanced degree at the University of British columbia, I agree that the Library shall make it freely available for reference and study. I further agree that permission for extensive copying of this thesis for scholarly purposes may be granted by the head of my department or by his or her representatives. It is understood that copying or publication of this thesis for finnancial gain shall not be allowed without my written permission.

Department of *Chemical Engineering*

The University of British Columbia
1956 Main Mall
Vancouver, Canada
V6T 1Y3

Data *May,* 1988

ABSTRACT

Heat transfer tubes suffer erosion when immersed in fluidized beds. This has caused problems, especially in fluidized bed combustors. The mechanism of erosion for horizontal tubes in fluidized beds is not well understood. The purpose of this study was to investigate the erosion mechanism in fluidized beds and to investigate the influence of operating parameters and the mechanical properties of the particles and tube materials.

Horizontal tube erosion tests were carried out in a room temperature three-dimensional fluidized bed with a cross-section of 216 mm by 203 mm and height of 1.52 m. Sample rings of ten different materials were mounted on a solid bar and were weighed before and after each test to determine the erosion rate. The parameters tested were particle size (0.30 to 1.51 mm), particle sphericity (0.84 to 1.0), particle density, particle hardness, superficial air velocity (0.88 to 2.52 m/s), tube diameter (15 mm to 32 mm), tube configuration and material mechanical properties.

Two additional types of experiments were also conducted to help understand the mechanism of erosion. In one particles were dropped freely in an empty column to impact on test specimens at different velocities determined by the dropping distance, in order to investigate erosion due to solid particle impact under known conditions. In the other the particle movement was filmed in the vicinity of a horizontal tube in a two-dimensional fluidized bed in order to investigate the particle flow pattern around a tube. A small number of tests were also conducted at high temperatures.

The erosion of a horizontal tube in fluidized beds was found to be caused mainly by the impact of solid particles on the lower surface. Erosion was found to be strongly dependent on the particle impact velocity, which is closely related to the void (bubble or slug) rise

velocity. The void rise velocity, in turn, is determined by the mean void size which depends on the superficial air velocity, column size and other fluidizing conditions. Particle diameter also has a strong influence on erosion. The target material Young's modulus appears to be the major mechanical property which is closely related to the erosion rate caused by solid impact erosion. Of the materials tested, all non-ferrous metals suffer much more erosion than ferrous metals. Localized high particle velocities due to jets and at bends or near feed points can be extremely harmful.

The mechanism of erosion caused by low velocity ($< 6m/s$) solid particle impacts appears to be different than that caused by high velocity ($> 30m/s$) impacts reported in the literature, although there are some similarities in trends. The erosion at low impact velocities appears to be mainly due to a surface fatigue process, which, instead of plastically deforming a small amount of target material for every impact, deforms the target materials in the elastic range and causes them to crack on or underneath the surface leading to removal of materials.

TABLE OF CONTENTS

ABSTRACT ii

TABLE OF CONTENTS iv

LIST OF TABLES ix

LIST OF FIGURES xii

ACKNOWLEDGEMENTS xix

CHAPTER 1 GENERAL INTRODUCTION 1

1.1 Literature Review 4

1.2 Objectives of This Study 7

CHAPTER 2 BACKGROUND KNOWLEDGE 10

2.1 Hydrodynamic Behaviour of Gas Solid Fluidized Beds 10

2.1.1 Single Bubble Rise in Fluidized Beds 10

2.1.2 Free Bubbling Beds 12

2.1.3 Slug Flow 18

2.2 Flow Patterns in the Vicinity of Immersed Tubes 19

2.3 Solid Impact Erosion 22

2.4 Mechanical Properties of Metals 30

2.4.1 Stress and Strain 30

2.4.2 Modulus of Elasticity – Young's Modulus 32

2.4.3 Tensile Properties – Yield and Tensile Strength 34

2.4.4 Ductility 34

2.4.5 Hardness 37

2.4.6 Other Mechanical Properties 42

CHAPTER 3 EXPERIMENTAL EQUIPMENT AND CONDITIONS 43

3.1 Experimental Conditions 43

3.2 The Three-Dimensional Low Temperature Fluidization Column 47

3.3 Solid Particles 53

3.4 Tube Materials 57

3.5 Two-Dimensional Fluidization Column 61

3.6 High Speed Photography 65

3.7 Particle Dropping Equipment 67

3.8 Combustor for High Temperature Erosion Tests 71

CHAPTER 4 TECHNIQUES OF MEASURING EROSION RATE 75

4.1 Overview of Methods Considered 75

4.2 Weighing Method and Accuracy of Data 80

4.3 Mounting of the Specimens 81

4.4 Incubation Period 87

4.5 Statistical Considerations 87

CHAPTER 5 RESULTS AND DISCUSSION: CONTROLLED DROPPING EXPERIMENTS 94

5.1 Effect of Particle Velocity 94

5.2 Effect of Particle Mass Flow Rate 98

5.3 Effect of Impingement Angle 102

5.4 Effect of Particle Size 106

5.5 Effect of Particle Shape and Hardness 110

5.6 Effect of Mechanical Properties of Specimen Materials 117

5.7 Conclusions 121

CHAPTER 6 RESULTS AND DISCUSSION: TWO-DIMENSIONAL EXPERIMENTS 127

6.1 Single Bubble Injection 129

6.2 Coalescing Bubbles 137

6.3 Free Bubbling with Single Tube 147

6.4 Free Bubbling with Tube Bundle 157

6.5 Viewing from Inside the Tube 159

6.6 Conclusions 166

CHAPTER 7 RESULTS AND DISCUSSION: THREE-DIMENSIONAL ROOM TEMPERATURE EXPERIMENTS 168

7.1 Effect of Fluidizing Conditions 168

7.1.1 Gas Superficial Velocity 168

7.1.2 Particle Size 176

7.1.3 Other Particle Properties 176

7.2 Effect of Tube Diameter 184

7.3 Effect of Tube Location and Configuration 188

7.3.1 Circumferential Distribution of Erosion 188

7.3.2 Axial Distribution of Erosion 191

7.3.3 Tube near Distributor, Inclined Tube and Tube close to Bed Surface 193

7.3.4 Tube within Tube Bundle 196

7.3.5 Square Tube 201

7.4 Effect of Distributor Geometry 202

7.5 Effect of Mechanical and Thermal Properties of the Tube Materials 204

7.5.1 Hardness 204

7.5.2 Young's Modulus 207

7.5.3 Other Mechanical Properties 213

7.5.4 Thermal Properties 214

7.6 Incubation of Fresh Materials 214

7.7 Conclusions 219

CHAPTER 8 RESULTS AND DISCUSSION: ELEVATED TEMPERATURE EXPERIMENTS 221

8.1 Non-Ferrous Metals 223

8.2 Ferrous Metals 225

8.3 Erosion/Corrosion 232

8.4 Conclusions 234

CHAPTER 9 EROSION MECHANISM AND PREDICTION 235

9.1 Mechanisms of Erosion 235

9.2 Model for Low Velocity Particle Impacts 246

9.3 Tentative Model for Horizontal Tubes in Fluidized Bed 249

9.4 General Discussion 266

CHAPTER 10 CONCLUSIONS AND RECOMMENDATIONS **269**

10.1 General Conclusions 269

10.2 Recommendations 270

NOMENCLATURE **271**

REFERENCES **275**

APPENDICES **286**

LIST OF TABLES

Table 1.1 Summary of some previous work reported in the literature 8

Table 2.1 Ratio of hardness to yield strength for cold worked metals (from Tabor 1956) 41

Table 3.1 Range of variables for three-dimensional room temperature fluidized bed experiments 44

Table 3.2 Range of variables for particle dropping solid impact erosion tests 48

Table 3.3 Particle properties 55

Table 3.4 Particle size distribution determined by sieving 56

Table 3.5 Compositions and working conditions of the materials tested 58

Table 3.6 Mechanical properties of the materials used in the tests 59

Table 3.7 Thermal properties of the materials used in the tests 60

Table 4.1 Deviation of experimental results from the low temperature three-dimensional fluidized bed tests 90

Table 4.2 Erosion rate of a 100 hour run from the cold model three-dimensional fluidized bed column 93

Table 5.1 Operating conditions for dropping tests 95

Table 5.2 Influence of particle impact velocity on erosion of brass specimen by 1.0 *mm* silica sand particles 96

Table 5.3 Influence of particle mass flow rate on erosion of brass specimen by 1.0 *mm* silica sand particles 100

Table 5.4 Influence of particle impingement angle on erosion of brass specimen by 1.0 *mm* silica sand particles 104

Table 5.5 Influence of particle diameter on erosion of brass specimen by silica sand particles 108

Table 5.6 Influence of particle properties on erosion of brass specimen 111

Table 5.7 Influence of particle sphericity on erosion of brass specimen by 1.0 mm particles 112

Table 5.8 Influence of particle hardness on erosion of brass specimen by 1.0 mm particles 116

Table 5.9 Influence of target material Young's modulus and hardness on erosion in the dropping experiments 120

Table 5.10 Operating conditions and results of all dropping tests with yellow brass ($Y_m = 97.0GPa$) as the target material 125

Table 5.11 k_6 values for different materials in equation 5.10 126

Table 6.1 Results of film analysis for single bubble injection experiment 134

Table 6.2 Results of film analysis for bubble coalescence experiment 141

Table 6.3 Results of film analysis for free bubbling with $u = 1.87\ m/s$ 151

Table 6.4 Results of film analysis for free bubbling with $u = 1.19\ m/s$ 154

Table 6.5 Results of film analysis for free bubbling with $u = 1.87\ m/s$ with a five tube bundle 158

Table 6.6 Results of film analysis for free bubbling at $u = 1.19$ and $1.87\ m/s$ for view from inside tube 164

Table 6.7 Summary of results for film analysis of all experiments 167

Table 7.1 Operating conditions for tests in the low temperature three-dimensional bed 169

Table 7.2 Calculated void mean diameters and rise velocities 172

Table 7.3 Constants from least square curve fitting of equation 7.1 175

Table 7.4 Constants from least square curve fitting of equation 7.3 178

Table 7.5 Constants from least square curve fitting of equation 7.4 182

Table 7.6 Erosion rates of brass at different positions along the tube 192

Table 7.7 Erosion rates ($\mu m/100h$) of different materials located at different positions along the tube 195

Table 7.8 Comparison of erosion rate between beds of 320 *mm* and 180 *mm* static bed depth 197

Table 7.9 Comparison of erosion rate between tube in bundle and single tube 199

Table 7.10 Material hardness measured at different times during the overall test period 205

Table 7.11 Hardness and heat treatment of rings 208

Table 8.1 Temperature and other operating conditions for erosion tests in the combustor 222

Table 8.2 Erosion rates of non-ferrous metals at different temperatures 224

Table 8.3 Hardness of non-ferrous metals before and after high temperature erosion tests 226

Table 8.4 Hardness of ferrous metals before and after high temperature erosion tests 230

Table 9.1 Exponents in equation 9.9 for different materials obtained from multi-regression analysis 251

Table 9.2 C values for different materials in equation 9.10 with silica sand as the particulate material 252

Table 9.3 Operating conditions and results of all tests with silica sand in the cold model three-dimensional fluidized bed 253

Table 9.4 Comparison of the results from Woodford and Wood (1983) with predictions from equation 9.10 265

LIST OF FIGURES

Figure 1.1 Section through badly eroded tube (from Bao & Ruan 1982) 3

Figure 1.2 Sections through an eroded heat transfer tube taken 125 mm apart after 4000 hours of operation (from Kobro 1984) 5

Figure 2.1 X-ray photograph of three-dimensional bubble in a fluidized bed (from Clift et al. 1978) 11

Figure 2.2 Bubble spatial-distribution across the bed for different height H (copper powder fluidized in a 0.2 m diameter bed, $u = 0.084 m/s$), (from Werther & Molerus 1973) 16

Figure 2.3 Location of the circumference zones of the tube used in the description of particle contact surface (from Peeler & Whitehead 1982) 21

Figure 2.4 Erosion rate vs. angle of impingement for materials with a ductile (Curve 1) and brittle (curve 2) erosion behaviour (from Hogmark et al. 1983) 23

Figure 2.5 Incremental erosion of 1075 steel to steady state rate (from Levy 1982) 25

Figure 2.6 Variation of erosion resistance (defined as the reciprocal of the volume erosion) with indentation hardness for pure metals and alloys. The data were obtained with gas-borne silicon carbide particles (from Finnie et al. 1967) 29

Figure 2.7 Correlation of volume erosion at impingement velocities of 76 and 137 m/s with mechanical energy density for tensile failure (from Rickerby 1983) 31

Figure 2.8 Types of direct stress (from Hearn 1985) 33

Figure 2.9 Typical tensile test curve for mild steel (from Hearn 1985) 35

Figure 2.10 Permanent deformation or "set" after straining beyond yield point (from Hearn 1985) 36

Figure 2.11 The Vickers pyramidal indenter (from McClintock & Argon 1966) 39

Figure 2.12 The Knoop hardness indenter (from McClintock & Argon 1966) 40

Figure 3.1 Multi-axis design of room temperature three-dimensional bed experiments 45

Figure 3.2 General set-up of the three-dimensional room temperature column 49

Figure 3.3 Buffering bottles for the manometer used to measure air flow rate 50

Figure 3.4 Primary features of the three-dimensional fluidization column and its auxiliaries 51

Figure 3.5 Vertical section through the three-dimensional fluidization column 52

Figure 3.6 Side plate of the three-dimensional fluidization column for tube array assembly 54

Figure 3.7 General set-up of the two-dimensional fluidization column 62

Figure 3.8 Tube assembly for the two-dimensional fluidization column 63

Figure 3.9 Tube configuration in the two-dimensional fluidization column 64

Figure 3.10 Tube with tetrahedral mirror set-up 66

Figure 3.11 General set-up of the dropping apparatus 68

Figure 3.12 Upper section of the dropping apparatus 69

Figure 3.13 The combustor for high temperature erosion tests 72

Figure 3.14 Supporting bar for the high temperature erosion test in the combustor 74

Figure 4.1 Erosion rate along the tube circumference of a plexiglass tube with paint coating (from preliminary experiment performed in the two-dimensional column) 76

Figure 4.2 Schemetic of Talysurf 4 78

Figure 4.3 Typical surface texture profile recorded by Talysurf 79

Figure 4.4 Supporting bar for room temperature three-dimensional fluidization column 82

Figure 4.5 Specimen rings 83

Figure 4.6 Supporting bar and ring assembly for room temperature erosion tests in the three-dimensional fluidization column 85

Figure 4.7 Coupling holders for local (segmental) erosion test at room temperature in the three-dimensional fluidization column 86

Figure 4.8 Erosion rate of different materials for 1.0 mm silica sand at superficial velocity of 1.87 m/s, for approximately 20 hours 88

Figure 4.9 Erosion rate of different materials for 1.0 mm silica sand at superficial velocity of 1.87 m/s, for approximately 60 hours 89

Figure 5.1 Erosion rate vs. particle impact velocity, for 1.0 mm silica sand ($\Phi_s = 0.91$) with particle mass flow rate of 5.7 kg/m^2s at 90° impingement angle 97

Figure 5.2 Erosion rate vs. particle mass flow rate, for 1.0 mm silica sand ($\Phi_s = 0.91$) with impact velocity of 5.0 m/s at 90° impingement angle 101

Figure 5.3 Impingement angle for dropping experiments 103

Figure 5.4 Erosion rate vs. particle impingement angle, for 1.0 mm silica sand ($\Phi_s = 0.91$) with particle mass flow rate of 5.7 kg/m^2s and impact velocity of 5.0 m/s 105

Figure 5.5 Particle size distribution of 1.0 mm silica sand 107

Figure 5.6 Erosion rate vs. particle diameter, for silica sand ($\Phi_s = 0.86$) with particle mass flow rate of 5.7 kg/m^2s and particle impact velocity of 5.0 m/s at 90° impingement angle 109

Figure 5.7 Erosion rate vs. particle sphericity, for particle mass flow rate of 5.7 kg/m^2s and particle impact velocity of 5.0 m/s at 90° impingement angle 113

Figure 5.8 Erosion rate vs. particle hardness, for particle mass flow rate of 5.7 kg/m^2s and particle impact velocity of 5.0 m/s at 90° impingement angle 115

Figure 5.9 Erosion rate vs. material hardness, for 1.0 mm silica sand with particle mass flow rate of 5.7 kg/m^2s and particle impact velocity of 5.0 m/s at 90° impingement angle 118

Figure 5.10 Erosion rate vs. material Young's modulus, for 1.0 mm silica sand with particle mass flow rate of 5.7 kg/m^2s and particle impact velocity of 5.0 m/s at 90° impingement angle 119

Figure 5.11 Erosion rate vs. material Young's modulus (Data from Figure 2.6, Finnie 1967) 122

Figure 5.12 Experimental erosion rate vs. calculated erosion rate for all dropping tests with yellow brass as the target material 124

Figure 6.1 Photographs of sequence of a single bubble passing horizontal tube in two-dimensional column 130

Figure 6.2 Particle trajectory for single bubble injection experiment at minimum fluidization with 1.0 mm silica sand 133

Figure 6.3 Particle velocity vs. time for single bubble injection experiment at minimum fluidization with 1.0 mm silica sand (Filming speed is 200 $frames/s$.) 136

Figure 6.4 Impingement angle vs. angular position on tube for single bubble injection experiment at minimum fluidization with 1.0 mm silica sand 138

Figure 6.5 Particle velocity distribution for single bubble injection experiment 139

Figure 6.6 Photographs of sequence of two bubbles coalescing just beneath a horizontal tube in two-dimensional column 142

Figure 6.7 Particle velocity vs. time for bubble coalescing experiment at minimum fluidization with 1.0 mm silica sand (Filming speed is 200 $frames/s$.) 145

Figure 6.8 Particle velocity distribution for bubble coalescing experiment 146

Figure 6.9 Particle velocity vs. time for free bubbling at $u = 1.87\ m/s$ with 1.0 mm silica sand (Filming speed is 200 $frames/s$.) 148

Figure 6.10 Particle classifications for free bubbling experiments 150

Figure 6.11 Impingement angle vs. angular position on tube for free bubbling experiment at 1.87 m/s air superficial velocity and with 1.0 mm silica sand 153

Figure 6.12 Particle velocity distribution for free bubbling with $u = 1.87\ m/s$ 155

Figure 6.13 Particle velocity distribution for free bubbling with $u = 1.19\ m/s$ 156

Figure 6.14 Impingement angle vs. angular position on tube for free bubbling experiment at 1.87 m/s air superficial velocity and with 1.0 mm silica sand and tube bundle of five 160

Figure 6.15 Particle velocity distribution for free bubbling with $u = 1.87\ m/s$ with tube bundle 161

Figure 6.16 Impact particle classifications for viewing from inside the tube 163

Figure 6.17 Distortion of distance due to mirror projection 165

Figure 7.1 Erosion rate vs. superficial air velocity 170

Figure 7.2 Erosion rate vs. void (slug) rise velocity 173

Figure 7.3 Erosion rate vs. particle diameter 177

Figure 7.4 Photographs of 1.0 mm silica sand taken before and after erosion test in the three-dimensional cold model fluidized bed 179

Figure 7.5 Erosion rate vs. particle sphericity 180

Figure 7.6 Erosion rate of different materials with silica sand and silicon carbide particles 183

Figure 7.7 Erosion rate vs. different materials with silica sand and silicon carbide particles (corrected for particle density) 185

Figure 7.8 Erosion rate vs. tube diameter 186

Figure 7.9 Circumferential erosion rate distribution 189

Figure 7.10 Eroded depth as a function of angle around the tube 190

Figure 7.11 Erosion rate at different locations and for different orientations 194

Figure 7.12 Circumferential erosion rate distribution for tube inside tube bundle 200

Figure 7.13 Effect of distributor on erosion rate 203

Figure 7.14 Erosion rate vs. material hardness for different materials 206

Figure 7.15 Erosion rate vs. material hardness for ferrous metal materials 209

Figure 7.16 Erosion rate vs. material hardness for non-ferrous metals before and after heat treatment 210

Figure 7.17 Erosion rate vs. tube elasticity for silica sand particles 211

Figure 7.18 Erosion rate vs. tube elasticity for silicon carbide particles 212

Figure 7.19 Yield strength of different tube materials 215

Figure 7.20 Volume loss vs. operating duration for non-ferrous metals 217

Figure 7.21 Volume loss vs. operating duration for ferrous metals 218

Figure 8.1 Erosion rate vs. bed temperature for 1.0 mm silica sand particles with 32 mm tube at $u - u_{mf} = 1.31\ m/s$ 227

Figure 8.2 Erosion rate vs. tube surface temperature for 1.0 mm silica sand particles with 32 mm tube tube at $u - u_{mf} = 1.31\ m/s$ 228

Figure 9.1 Surface of (a) Brass and (b) Al7075-T6 after erosion 236

Figure 9.2 Surface of brass specimens before and after erosion for 1.0 mm silica sand with mass flow rate of 5.7 kg/m^2s at impact velocity of 1.8 m/s for normal incidence 238

Figure 9.3 Surface of a brass specimen after erosion for 1 min. for 1.0 mm silica sand with mass flow rate of 5.7 kg/m^2s at impact velocity of 1.8 m/s for normal incidence 241

Figure 9.4 Surface of brass and CS1050 rings after erosion in the room temperature three-dimensional fluidized bed 242

Figure 9.5 Surfaces of different angular positions on a SS304 ring after 100 *h* erosion in the room temperature three-dimensional fluidized bed 243

Figure 9.6 Calculated erosion rate vs. experimental erosion rate for erosion tests with silica sand and brass as tube material in the three-dimensional cold model fluidized bed 260

Figure 9.7 Calculated erosion rate vs. experimental erosion rate for erosion tests with silica sand and copper as tube material in the three-dimensional cold model fluidized bed 261

Figure 9.8 Calculated erosion rate vs. experimental erosion rate for erosion tests with silica sand and Al2011 as tube material in the three-dimensional cold model fluidized bed 262

Figure 9.9 Calculated erosion rate vs. experimental erosion rate for erosion tests with silica sand and SS304 as tube material in the three-dimensional cold model fluidized bed 263

Figure 9.10 Calculated erosion rate vs. experimental erosion rate for erosion tests with silica sand and CS1050 as tube material in the three-dimensional cold model fluidized bed 264

ACKNOWLEDGEMENTS

The author like to thank his two supervisors, Dr. J. R. Grace and Dr. C. J. Lim for their consistent guidance and support for this work. My special thanks are also due to Dr. J. A. Lund, Department of Metals and Materials Engineering of UBC, for his continuous advice and patience in answering my endless questions. I am also grateful to Peter Williams, Rachel Yang, and Andrea Townsen for their help in carrying out some of the dropping and two-dimensional tests. My appreciation is also due to the CFBC group here in UBC, without whom the high temperature tests would not have been possible.

My special thanks are also due to my wife Mei, for her constant support and help in typing part of the thesis.

CHAPTER ONE: GENERAL INTRODUCTION

In many fluidized bed systems, heat transfer is of great concern due to the exothermic or endothermic nature of the reactions. Immersed tubes are usually employed for heat transfer purposes. In most applications, horizontal tube bundles are used, although vertical tubes are also quite common.

Fluidized bed reactors have many advantages over conventional reactors, so that they have been receiving more and more attention in the process industries, especially for energy conversion systems. One of the main features of fluidized bed reactors is the rapid turnover of the gas-solid mixture, which provides very good heat and mass transfer. However, because of the motion of the solid particles, components such as heat transfer tubes may suffer severe erosion. Failure of these tubes may result in shutting down the whole system. The failure can occur through corrosion, erosion, erosion-corrosion or buffetting forces associated with bubble and solid movement in the fluidized bed. In most cases, corrosion is not a major problem (Jansson 1985), but erosion has been reported to be the major cause of tube failure (Stringer & Minchener 1984).

Papers in which erosion has been cited as a problem include Smith (1977) , Vaux & Newby (1978), Krause et al. (1979), Wright (1979), Zhang (1980), Jansson (1982), Bao & Ruan (1982), Zhang (1982), Grace et al. (1983), Swift et al. (1984), Kobro (1984), Stringer & Minchener (1984), Andersson (1985), Byam et al. (1985), Jansson (1985), Leckner et al. (1985a), Minchener et al. (1985), Stringer et al. (1985), Stringer & Wright (1986), Levy (1987), Natesan et al. (1987), Monenco (1987) and Stringer (1987). One case in China (Bao & Ruan 1982) showed that if relatively coarse coal particles are used in a fluidized bed combustor, carbon steel tubes with a thickness of 3 *mm* may wear out after only

4000 hours of operation. Figure 1.1 illustrates the severe erosion of a carbon steel tube with thickness of 6.25 mm after 8682 hours of operation. There are also reports of very significant erosion attack on tubes in fluidized bed combustors in the U.S.A. (Gamble 1980) and in China (Zhang 1980). Tube erosion has also been noted in circulating fluidized beds and in pressurized fluidized beds. Krause (1979) reported erosion rates of 10 – 22 $\mu m/100h$ (0.89 – 2.2 $mm/year$) in a fast fluidized bed depending on tube materials. The International Energy Agency (IEA) pressurized fluidized bed combustor at Grimethorpe had a metal wastage rate of 200 $\mu m/100h$ (18 $mm/year$) (Smith et al. 1982, Swift et al. 1984). The 10,000 h AFBC material test carried out in Point Tupper, Nova Scotia has shown that erosion is the major cause of tube failure (Anthony 1988).

In most cases, a corrosive atmosphere and high temperature accompany the motion of the particles in the bed and complicate the problem. The combined effects of erosion and corrosion endanger in-bed heat transfer tubes. Tube life plays a key role in determining the reliability and economics of the reactors. Stringer and Minchener (1984) and Jansson (1985), in reviewing work in this area, have pointed out that tube erosion constitutes a serious problem for fluidized bed combustors. However, less research has been conducted on erosion than on corrosion. Even criteria to minimize the incidence of in-bed tube erosion are not widely accepted nor well understood.

Erosion of tubes in fluidized beds is believed to be caused by the movements of solid particles. These particle movements are closely related to the operating conditions of the bed and the gas and solid properties. There are many papers reporting the combined results of erosion and corrosion of horizontal tubes, but they are of limited value due to the combination factors including deposition on the tube surface.

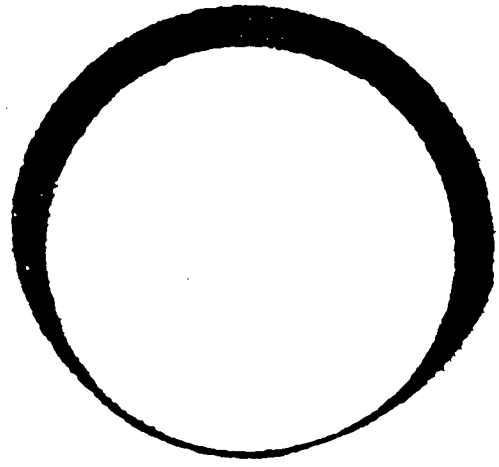

Figure 1.1 Section through badly eroded tube (from Bao & Ruan 1982)

1.1 Literature Review

Little work has been done on the mechanism of tube erosion in fluidized beds.

Krause et al. (1979) investigated corrosion-erosion on boiler tube metals in a multisolids fluidized bed coal combustor. The equipment consisted of an entrained bed superimposed on a dense bed of high specific gravity material into which the coal and limestone were fed. The heat exchange tube was first exposed to the entrained bed having a superficial velocity up to 9.1 – 12.2 m/s, while the tube metal temperature was in the vicinity of 260 C. When the tube was vertical, the erosion rate was very small. On the other hand, when the tube was horizontal, the erosion rate was quite high, reaching 10 – 26 $\mu m/100h$ (890 – 2200 $\mu m/year$). The erosion rate of a horizontal tube in the dense bed was even greater, more than 29 $\mu m/100h$ (2500 $\mu m/year$). Krause et al. (1979) also observed that erosion occurred mostly over a range of impingement angles from 0° to 40° from the bottom of the tube. They concluded that: "The life of heat exchange tube to be incorporated in the multisolids fluidized bed combustor will depend primarily upon erosion".

Kobro (1984) found that the erosion of horizontal tubes in a 16 MW bubbling bed combustor is very unpredictable and non-uniform even along the length of one tube. Figure 1.2 shows two sections taken only 125 mm apart through an eroded tube which had an initial wall thickness of 4.2 mm, after 4000 hours of operation. Uneven erosion caused premature failure of the tube at 4000 hours. Kobro also observed greater erosion on the lower surface of a tube than on the upper surface.

Zhang (1980), in a review of fluidized bed boilers in China, reported relatively high erosion rates for carbon steel bed components: the bed wall erosion rate was only about 8.0 $\mu m/100h$ (700 $\mu m/year$), whereas the in-bed tube erosion rate was nearly 130 $\mu m/100h$ (11,400 $\mu m/year$). Jin (1984) noted that small knobs may be welded along the surface of

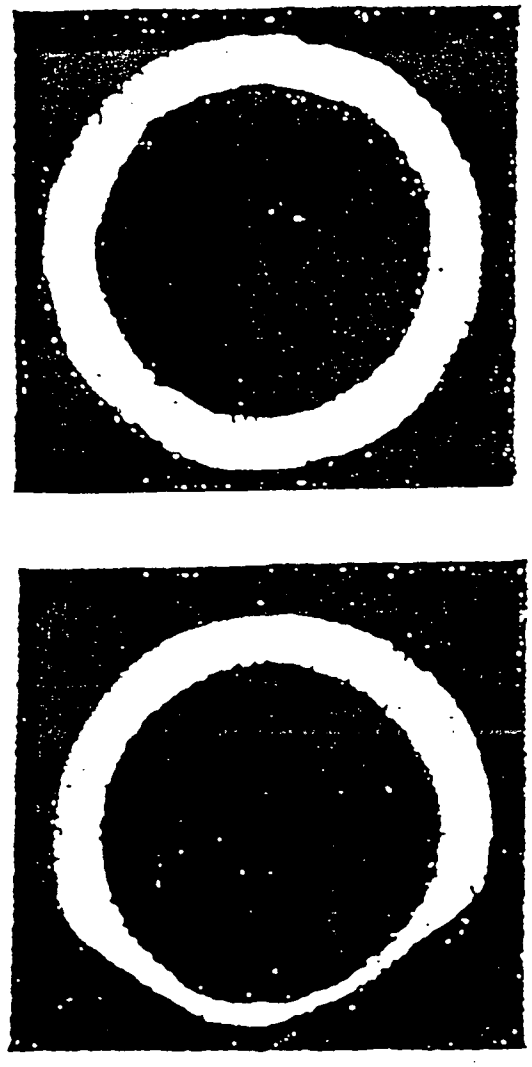

Figure 1.2 Sections through an eroded heat transfer tube taken 125 mm apart after 4000 hours of operation (from Kobro 1984)

heat transfer tubes, with a diameter of roughly 1/8 of the tube diameter. The knobs not only prevent erosion by changing the gas-solid flow pattern around the tube but also increase the heat transfer flux by adding contact surface area. The same finding was reported by the General Electric Company (Bonds 1983).

The only detailed published study of in-bed horizontal tube erosion was conducted by Wood & Woodford (1980, 1983). They employed a 0.2 m by 0.2 m facility operated with air at room temperature to minimize the influence of corrosion. Five elemental metals and five alloys were used as tube materials. Superficial velocities ranged from 1 to 4.8 m/s, while the mean particle size was varied from 0.1 to 1.9 mm . Conclusions were as follows:

(1) Over the lower half of a tube, the erosion rate was high and relatively uniform. However, minimal erosion occurred over the upper surface so that the tube-averaged erosion rates underestimate the extent of local damage.

(2) Particle hardness had little or no effect.

(3) Erosion increased somewhat with increasing superficial velocity.

(4) Particle size had a strong influence, larger particles producing more erosion than smaller particles.

(5) The erosion damage of ductile metals exposed to a fluidized bed resembled that caused by liquid droplet erosion, which produces fatigue damage.

The Wood and Woodford work was restricted to one hydrodynamic regime, (the turbulent regime, with the same overall voidage in all tests), and only three kinds of particles were used, one being limestone, for which results were not very reliable due to considerable attrition.

Parkinson et al. (1985) conducted erosion tests with PVC tube banks in a 0.3 m by 0.3 m cold model pressurized fluidized bed. They found that tube wastage was independent of

particle size, contrary to Wood and Woodford's finding, but proportional to gas superficial velocity for $u/u_t < 0.55$, which corresponded to the boundary between the mixed and turbulent fluidization regimes. At higher velocities (turbulent regime), there was a decrease in tube erosion. They also found that maximum erosion occurred at 35° measured from the tube bottom and that tubes close to bed walls suffered less erosion than tubes in the central region.

While a number of workers have reported erosion as a problem in Fluidized Bed Combustion (FBC), Circulating Fluidized Bed Combustion (CFBC), and Pressurized Fluidized Bed Combustion (PFBC) units, others (Preuit & Wilson 1980) found that erosion was not a problem in their facilities. For those tests which did encounter erosion, the erosion rates were not consistent with each other. This reveals the complexity of tube erosion in fluidized beds and suggests that erosion is not intrinsic to the process, but arises from operational parameters which have yet to be fully identified. Table 1.1 lists some of the test results.

1.2 Objectives of This Study

The principal objectives of this project were to investigate most of the factors which influence tube erosion, to obtain fundamental knowledge of the mechanism of tube erosion in fluidized beds and to correlate the erosion rate with operating parameters.

Most of the experiments were carried out in a cold model three-dimensional fluidized bed. The major parameters varied were particle properties, tube material properties, tube sizes, tube configuration and gas superficial velocity. Ranges of these parameters are listed in Table 3.1.

To help establish a correlation between erosion and those parameters, some auxiliary experiments were also conducted:

Table 1.1: Summary of some previous work reported in the literature

Source	Facility	Superficial gas velocity (m/s)	Particle diameter (mm)	Tube Surface temperature (C)	Tube diameter (mm)	Tube material	Metal wastage rate* (μm/h)
Bao & Ruan (1982)	463 X 324 mm FBC	-	-	550	-	Carbon steel	0.75P
Kobro (1984)	4m dia. FBC	2.2	-	-	42	-	1.15P
Krause (1979)	152 mm dia. FBC	-	-	260	-	Alloys	0.13-0.51A
Krause (1979)	152 mm dia. CFBC	9.1-12.2	-	-		Alloys	0.101-0.255A
Stringer et al. (1985)	FBC	-	-	-	-	-	0.09-0.42P
Swift et al. (1984)	2m x 2m PFBC	-	-	-	-	-	2.0-2.5P
Woodford & Wood (1983)	0.2 X 0.2 m Model FB	1.0-4.8	0.1-1.9	20	15, 25, 32	5 Metals 5 Alloys	0.005-0.500A
Zhang (1980)	FBC	-	-	-	-	Carbon steel	1.3 P
Zhang (1982)	FBC	-	- (Average of a few hot operations)	-	-	-	0.49P

FB : Fluidized bed
FBC : Fluidized bed combustor
CFBC : Circulating fluidized bed combustor
PFBC : Pressurized fluidized bed combustor
- : Data not available

* P -- Peak wastage rate
A -- Average wastage rate

(1) High speed films were taken with a two-dimensional fluidized bed to trace the solid particle motion around horizontal tubes under different operating conditions.

(2) Particles of different properties were dropped onto small specimens of different materials to test the erosion rate under "controlled conditions".

(3) A fluidized bed combustor was used to conduct a small number of erosion tests at elevated temperatures to investigate the temperature effect.

CHAPTER TWO: BACKGROUND KNOWLEDGE

Understanding the erosion of tubes in fluidized beds involves knowledge of the hydrodynamics of the fluidized bed, the mechanism of material surface erosion caused by impacting solid particles and the mechanical properties of the eroding and eroded materials.

2.1 Hydrodynamic behaviour of Gas Solid Fluidized Beds

Conventional gas fluidized beds operate mainly in the bubbling or slug flow regime. With an increase in gas flow rate beyond that required for minimum fluidization, (minimum bubbling for group A particles), gas voids form at or near the gas distributor and grow in size, mostly by coalescence, as they rise. These gas voids are often called bubbles because of the analogies between them and large bubbles in real liquids. If the bubbles grow large enough compared to the column cross-section, they become slugs. It is the bubbles or slugs which are responsible for most of the features that differentiate a packed or moving bed from a fluidized bed. The particle movement which is responsible for rapid heat transfer, most solid mixing and most tube erosion is also caused by bubble or slug movement. In this section we review the basic ideas and predictive equations for bubbling and slugging needed in Chapter 7. For a more complete review of these regimes see Grace (1982), Clift and Grace (1985) and Kunii and Levenspiel (1969).

2.1.1 Single Bubble Rise in Fluidized Beds

Single bubbles rising in fluidized beds are commonly represented as spherically-capped voids with concave indentations at their bases (Davidson & Harrison 1963), although the true shape is often closer to an ellipsoidal cap (Figure 2.1, Clift et al. 1978). The velocity of a rising isolated bubble in a fluidized bed has been investigated by a number of workers.

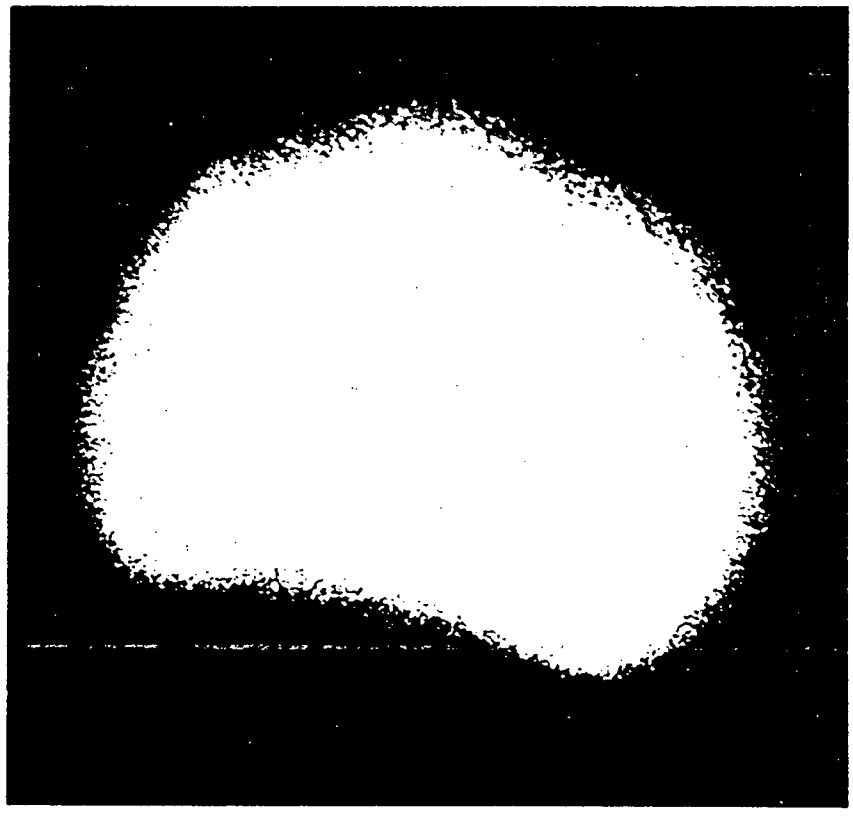

Figure 2.1 X–ray photograph of three–dimensional bubble in a fluidized bed (from Clift et al. 1978)

Davidson et al. (1959) found experimentally that the rise velocity of a single bubble in a fluidized bed is related to the bubble diameter in a similar manner to that for gas bubbles in a true liquid, i.e.

$$u_{b,\infty} = \frac{2}{3}(gr')^{1/2} \tag{2.1}$$

where r is the radius of curvature of the leading edge of the bubble. With some assumptions and simplifications, the expression for fluidized beds is often written (Clift & Grace 1985):

$$u_{b,\infty} = k''(gD_e)^{1/2} \tag{2.2}$$

where D_e is the diameter of sphere having the same volume as the bubble: k'' has a value of 0.71 for spherical-cap bubbles in a true low viscosity liquid, while the experimental value for bubbles in fluidized beds was found to vary between 0.5 and 0.85 (Kunii & Levenspiel 1969, Clift & Grace 1985, Rowe & Partridge 1965). The equation $u_{b,\infty} = 0.71(gD_e)^{1/2}$ is often assumed to apply quite generally to all bubbles in fluidized beds and will be used here.

The pattern of the solids motion with respect to the rising bubble is analogous to potential flow past a sphere (Reuter 1966). Particles continuously stream around the sides of the bubble. Behind the bubble there is a wake region in which particles are carried upward at the bubble velocity (Rowe 1971). The wake fraction, defined as the wake volume per unit bubble volume, is about 0.1 – 0.4 depending on solid properties. Small and rounded particles give larger wakes than coarse or angular particles.

2.1.2 Freely Bubbling Beds

In a bubbling fluidized bed there are regions of very low solids density defined as bubble phase and regions of higher solid density called emulsion or particulate phase. As a first approximation, all gas in excess of that needed to just fluidize the bed passes through the

bed as bubbles, while the emulsion phase remains at minimum fluidizing conditions with a voidage of ϵ_{mf} and interstitial velocity u_{mf}/ϵ_{mf}.

Many studies have been conducted in ordinary bubbling beds to find the rate of bubble growth and coalescence, and the bubble size and frequency. The average bubble size is found to increase rapidly with height and with an increase in gas flow rate, mainly as a result of coalescence. A number of correlations have been proposed to estimate the mean bubble size at a certain level, the best known being those of Geldart (1970–71), Mori and Wen (1975), Rowe (1976), Darton et al. (1977), Werther (1978), Bar-Cohen et al. (1981) and Horio et al. (1987). In all of these correlations, the average bubble diameter is a function of the gas flow rate and the height above the gas distributor. In some, the effect of bed scale, characteristics of the gas distributor and the powder properties are also considered.

The correlation of Darton et al. (1977) is a semi-empirical correlation based on lateral bubble coalescence. The proposed equation is:

$$D_e = 0.54(u - u_{mf})^{0.4}(x + 4A_D^{1/2})^{0.8}/g^{0.2} \tag{2.3}$$

where A_D is the area of distributor plate per orifice and x is the height above the distributor. The above equation agrees well with most literature data, providing that neither a maximum stable bubble size nor slugging is achieved. Bar-Cohen et al. (1981) modified the constants in the semi-empirical correlation of Darton et al. to offer better agreement with the data of recent workers. The modified equation is:

$$D_e = 0.45(u - u_{mf})^{0.4}(x + 4.63A_D^{1/2})^{0.8}/g^{0.2} \tag{2.4}$$

The correlation of Mori and Wen (1975) includes an estimate for the mean bubble size, $D_{e,0}$, formed at the distributor:

$$D_{e,0} = 1.38g^{-0.2}\{A_D(u - u_{mf})\}^{0.4} \qquad \textit{for perforated plates} \tag{2.5}$$

$$D_{e,0} = 0.376(u - u_{mf})^2 \qquad \textit{for porous plates} \tag{2.6}$$

It also includes an estimate for the maximum bubble size, $D_{e,\infty}$, attainable by coalescence,

$$D_{e,\infty} = 1.49\{D^2(u - u_{mf})\}^{0.4} \tag{2.7}$$

where D is the bed mean diameter. Then the bubble size is estimated by:

$$D_e = D_{e,\infty} - (D_{e,\infty} - D_{e,0})exp(-0.3x/D) \tag{2.8}$$

Several functions have been proposed to describe the size distribution of bubbles. These functions include the normal distribution (Park et al. 1969), gamma distribution (Rowe & Yacono 1975) and log-normal distribution (Werther 1974). However, the distribution of bubble size is different at each level, and there is no simple method for predicting the bubble size distribution, especially in the presence of tubes.

A concept of maximum stable bubble diameter was first postulated by Harrison et al. (1961). Subsequent observations have shown that splitting occurs from the roof of the bubble in gas fluidized systems as a result of Taylor instability (Clift & Grace 1985, Jackson 1985). Predictions of maximum bubble diameter depend strongly on the effective viscosity of the dense phase and the form of initial disturbances, both of which are very difficult to determine. An approximate relationship suggested by Geldart for estimating this maximum stable bubble diameter is (Grace 1982):

$$D_{e,m} = 2.0(u_T^2/g) \tag{2.9}$$

where u_T is the terminal settling velocity of spherical particles of diameter $2.7d_p$ in the given gas, d_p being the surface-to-volume (Sauter) mean particle diameter.

The frequency of bubbles passing a given level in a gas fluidized bed has been determined in a number of studies. Kunii and Levenspiel (1969), in summarizing experimental evidence,

suggested that the frequency of bubbles passing a point 10 – 15 *cm* or higher above the distributor is approximately the same no matter what the gas flow rate is. Consequently, the primary effect of gas flow rate is to change the size of bubbles passing a point, not the frequency. Geldart (1970) indicated that the point bubble frequency is relatively insensitive to increases in gas flow rate, in agreement with the finding noted above, while the bubble frequency decreased steadily with increasing bed height. The mean bubble frequency at any level can be estimated (Grace 1982) from:

$$f_b = \frac{G_b/A}{(\pi/6)D_e^3} \tag{2.10}$$

where D_e is the average bubble size at that level and G_b/A is the gas flow carried as bubbles. According to the two-phase theory of fluidization G_b/A equals $(u - u_{mf})$. The frequency of gas bubbles has been found also to increase and their dimensions to decrease as the particle size decreases (Horio et al. 1987).

Spatial distributions of bubbles in fluidized beds have been investigated by a number of workers including Grace and Harrison (1968) and Werther (1973). Both investigations showed a characteristic bubble flow profile development (Figure 2.2). Near the gas distributor more bubbles were found near the bed wall than at the bed center. The zone of increased bubble occurrence moves towards the vessel center-line with increasing height above the distributor. The merging of the annular zone represents the start of the transition to the slugging regime. This development arises naturally from bubble coalescence, even for a uniform spatial distribution of bubbles at the gas distributor.

The absolute rise velocity of bubbles at a particular height in freely bubbling beds, u_b, can be estimated (Davidson & Harrison 1963) from

$$u_b = u_{b,\infty} + u - u_{mf} \tag{2.11}$$

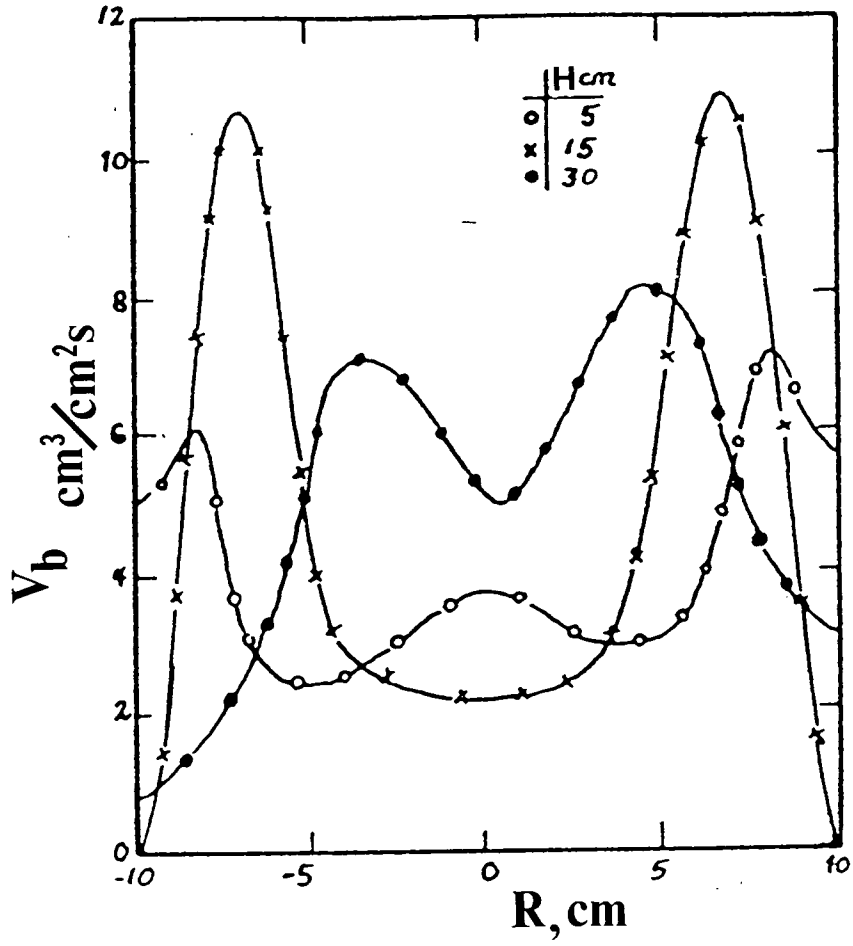

Figure 2.2 Bubble spatial–distribution across the bed for different heights H (copper powder fluidized in a 0.2 m diameter bed, u = 0.084 m/s), (from Werther 1973)

or

$$u_b = 0.71(gD_e)^{1/2} + u - u_{mf} \tag{2.12}$$

where $u_{b,\infty}$ is the velocity of the bubble in isolation, estimated from equation 2.2. A more accurate equation was given by Weimer and Clough (1983):

$$u_b = 0.71\{gD_e(1-\epsilon_b)\}^{1/2} + C_0 G_b/A \tag{2.13}$$

where G_b is the visible bubble flow rate, A is the cross-sectional area of the bed and C_0 is a coefficient depending on the distribution of bubbles across the bed (Clift & Grace 1985). This equation may be compared with equation 2.9. The value of u_b is reduced by a factor $(1-\epsilon_b)^{0.5}$, which is normally close to unity. Since $C_0 > 1$ and $G_b/A < (u - u_{mf})$ (Clift & Grace 1985), the value of $C_0 G_b/A$ is frequently close to $(u - u_{mf})$. Hence equation 2.12 often provides a reasonable approximation for u_b.

The above two equations both imply that the mean bubble velocity increases with distance from the distributor and with the gas velocity. Particle movement and solid circulation in gas fluidized beds are caused primarily by the motion and disturbance of gas bubbles passing through the bed. Rising bubbles cause transport of solids by two mechanisms, firstly by carrying solids in their wakes and pushing solids in their caps, secondly by drawing up the solids in a drift profile behind the bubble. Outside the bubble paths, solids move downward in the bed to replace the particles brought to the surface. The nonuniform spatial distribution of the rising bubbles tends to enhance particle movement and to establish solid circulation patterns depending on the bed depth.

The previous discussion applies when the vessel dimensions greatly exceed the bubble size. If the size of the rising bubble approaches the bed diameter, the bubble tends to elongate, the rise velocity is retarded by the containing wall, and the wake is smaller.

When the ratio $D_e/D < 0.125$, the bubble rise velocity is considered not affected by the wall (Clift & Grace 1985). For $0.125 \leq D_e/D < 0.6$, the retardation may be estimated (Wallis 1969) by:

$$u_b = 1.13 u_{b,\infty} exp\{-D_e/D\} + u - u_{mf} \tag{2.14}$$

When D_e is about $D/2$ or larger, the slug flow regime been achieved.

2.1.3 Slug Flow

For the bed to achieve the slugging regime, the superficial gas velocity must exceed a minimum slugging velocity (Stewart & Davidson 1967):

$$u_{ms} = u_{mf} + 0.07(gD)^{1/2} \tag{2.15}$$

and must be below the value at which turbulent or fast fluidization occurs. The bed also must be sufficiently deep for coalescing bubbles to attain the size of slugs. Baeyens and Geldart (1974) concluded that equation 2.15 is only applicable if $H_{mf} > 1.3D^{0.175}$. Otherwise, the minimum slugging condition is given by:

$$u_{ms} = u_{mf} + 0.07(gD)^{1/2} + 0.16(1.3D^{0.175} - H_{mf})^2 \tag{2.16}$$

The rise velocity of a single slug is in analogy with the slug in liquid (Hovmand & Davidson 1971):

$$u_{s,\infty} = 0.35(gD)^{1/2} \tag{2.17}$$

The rise velocity of a slug in a freely slugging bed is then approximated by:

$$u_s = u_{s,\infty} + u - u_{mf} \tag{2.18}$$

When large particles ($> 600\mu m$) are used and the bed height is less than about 1.5 times the column diameter or width, as in our experiments, a true slug regime cannot be reached,

even if equation 2.15 or 2.16 is satisfied (Staub & Canada 1978). Instead, an apparent slug or developing slug regime, termed by Canada et al. (1978), is achieved. In the apparent slug flow regime, the bubbles coalesce into large-diameter voids which produce large bed oscillations and cyclic heaving of the bed surface (Canada et al. 1978, Cranfield & Geldart 1974). It differs from the usual definition of slug flow in that the bed heights do not permit a train of several slugs to form in series and in that the bubble diameters are not the full bed diameter (Canada et al. 1978). This flow regime is sometimes also termed as "rapidly growing bubble regime" (Ĉatipović et al. 1978).

2.2 Flow Patterns in the Vicinity of Immersed Tubes

Several studies have been conducted on flow patterns around immersed tubes (Glass & Harrison 1964, Harrison & Grace 1971, Rowe & Everett 1972, Ginoux et al. 1973, Hager & Thompson 1973, Rooney & Harrison 1976, Hager & Schrag 1976, Cherrington et al. 1977, Loew et al. 1979, Fakhimi & Harrison 1980, Peeler & Whitehead 1982, Sitnai & Whitehead 1985). It is generally believed that there are three regions in the vicinity of horizontal tubes in two dimensional beds at low superficial velocities: a thin film of air on the upstream surface, an almost stagnant defluidized region at the downstream surface and a region near the 3 o' clock and 9 o' clock positions where the tube sides are contacted intermittently by particles and voids in a fluidized state (Glass & Harrison 1964, Cherrington et al. 1977). In three-dimensional beds at high velocities, the defluidized cap and upstream gas film are neither as large nor as permanent as those observed in two dimensional beds (Rooney & Harrison 1976).

Peeler and Whitehead (1982) describe the solid motion around tubes associated with bubbles based on experiments in a square three-dimensional column of 1.2 m by 1.2 m

cross-section. The surface of the tube is divided into four equal sectors (Figure 2.3). Before a bubble reaches the tube, the tube is surrounded by closely packed particles with a voidage of approximately ϵ_{mf} moving slowly upwards in zones 3 and 2; zone 1 and 4 also experience a slow upward movement, although at the front and rear stagnation points the particles appear to be stationary, except for gentle vibrations. The approach of a bubble is indicated by a sudden increase in particle velocity. In zones 3 and 4, particle velocity increases rapidly, with particles streaking across the tube surface accompanied by a lowering of the emulsion density in zones 2, 3, 4, while in zone 1, the voidage remains substantially unchanged and the surface is covered by a "cap of defluidized particles". These particles are not stationary but tend to slide slowly downwards across zone 1 to either side of the tube until they reach zone 2 where they are swept off, together with particles passing zones 2 and 3. The emulsion density in zone 1 does not fall off as quickly as in the other zones, but remains at an intermediate value. As the bubble arrives at the tube front, the emulsion density is further reduced in zone 3 and zone 4 until finally zone 4 has been swept free of particles. In zone 2, however, the emulsion density rises as particles from zone 1 slide down along the tube surface. In zone 1, the cap is gradually depleted until the tube is left bare. This process ends abruptly with the departure of the bubble. Particles are then swept across zones 3 and 4, leaving the tube surrounded by dense phase again until the approach of the next bubble. As the superficial velocity increases, the above process become more chaotic. At still higher velocities, the bubbles almost permanently envelop the tube (Rowe & Everett 1972).

From the above description, the solid movement is seen to be more vigorous in zones 3 and 4 than in zones 2 and 1. This trend is commonly mirrored by the distribution of erosion around horizontal tubes (Woodford & Wood 1983, Parkinson et al. 1985).

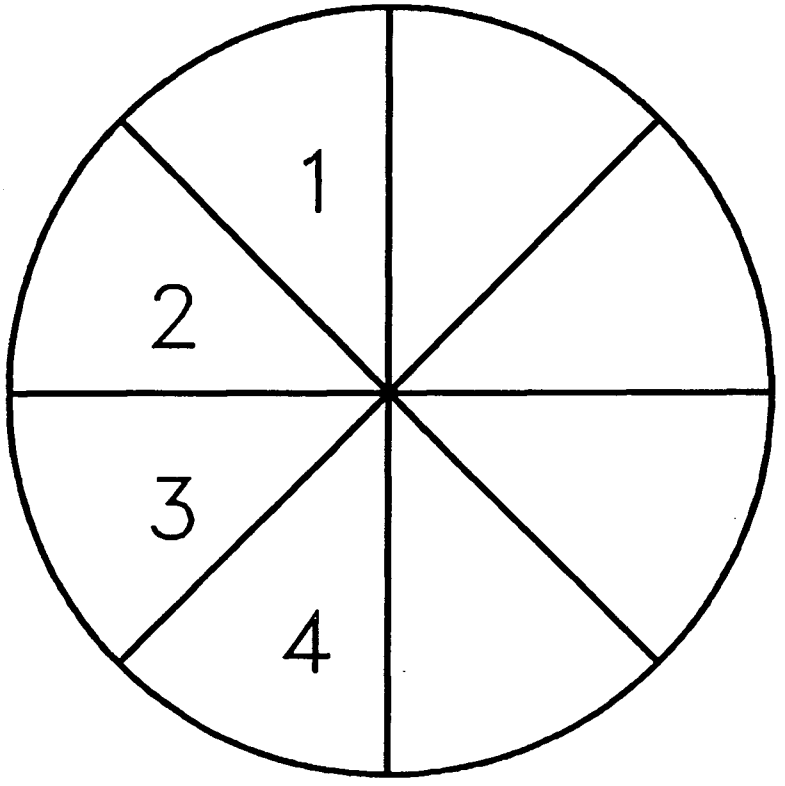

Figure 2.3 Location of the circumference zones of the tube used in the description of particle contact surface (from Peeler & Whitehead 1982)

2.3 Solid Impact Erosion

The mechanism of solid impact erosion has been studied in detail by a number of researchers (eg. Finnie 1958 and 1960, Finnie et al. 1967, Finnie 1972, Ives et al. 1976, Finnie & McFadden 1978, Ruff 1979, Finnie 1979, Finnie et al. 1979, Hutchings 1979a and 1979b, Tilly 1979, Ruff & Wiederhorn 1979, Hutchings 1980, Bellman & Levy 1981, Hutchings 1981, Levy 1982, Cousens & Hutchings 1983, Levy 1983, Rao & Buckley 1983, Sundararajan 1983, Sundararajan & Shewmon 1983, Hutchings 1987). This work is commonly associated with erosion of aircraft and turbines at very high particle impact velocities (100 - 300 m/s). Tests are usually conducted by causing particles to impinge individually or continuously on a target plate. The erosion mechanisms for ductile and brittle target materials are completely different. Impacts on ductile materials result in the deformation of extruded and forged platelets that reach a stage of fracture only when they exceed a local critical strain and are in the final stage of being removed from the surface. In the case of brittle materials, crack formation occurs early in the erosion process, and it is the formation of a network of fine cracks that makes it possible for impacting erodent particles to remove small chips of the brittle materials. The difference in the way ductile and brittle materials erode accounts for the fact that ductile materials have an erosion peak at a shallow impingement angle, whereas brittle materials erode most at 90° (normal incidence, see Figure 2.4). The tube materials of interest in fluidized bed applications are all ductile materials. The focus of attention in this thesis will therefore be ductile materials. Ductility is considered in Section 2.4.4 below.

Erosive wear involves the eroding surface, the particles causing the erosion, and the fluid flow conditions which bring the particles into contact with the surface. Factors which may influence erosion include:

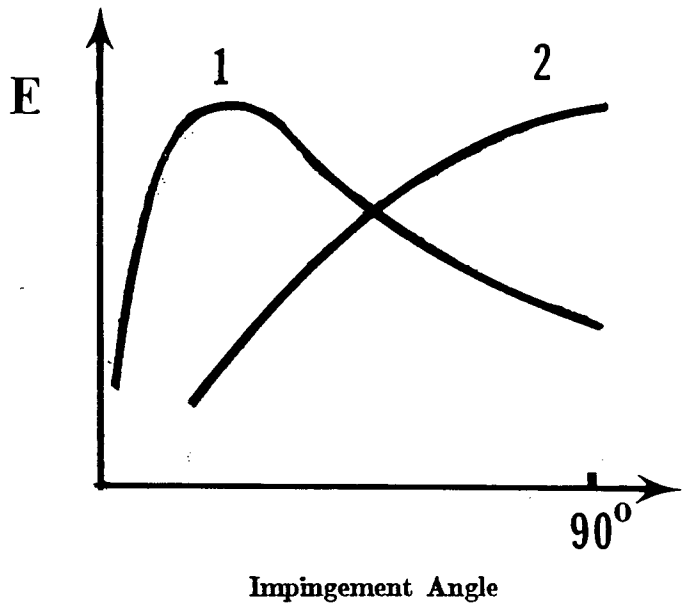

Figure 2.4 Erosion rate vs. angle of impingement for materials with a ductile (Curve 1) and brittle (curve 2) erosion behaviour (from Hogmark et al.1983)

Flow and environmental conditions	Angle of impingement Particle velocity Particle rotation Temperature Number of particles striking Corrosive environment
Particle properties	Size Shape Density Hardness Strength or friability
Surface properties	Shape Hardness Other mechanical and material properties

The first mechanism of erosion of ductile materials, micromachining, was proposed by Finnie (1958). The eroding particles were assumed to cut swaths of metal away as their tips translate along the eroding surface. A model was devised based on this mechanism to predict erosion rates. This model pervaded the literature for more than twenty years until Bellman & Levy (1981), based on a series of careful experiments on a microscopic level, suggested a combined forging-extrusion mechanism, more often called the platelet mechanism of erosion (Bellman & Levy 1981, Levy 1982). The following sequence was said to occur during the erosion process:

In the beginning platelets are formed without loss of material. Then adiabatic shear heating of the immediate surface region begins to occur. Beneath the immediate surface region, the mass of target material forms a work-hardened zone because the kinetic energy of the impacting particles is sufficient to result in considerably greater force being exerted on the metal than required to generate platelets at the surface.

When the surface has been completely converted to platelets and craters and the work hardened zone has reached its stable hardness and thickness, steady state erosion begins (Figure 2.5). Steady state erosion is highest in Figure 2.5 because "the sub-surface cold

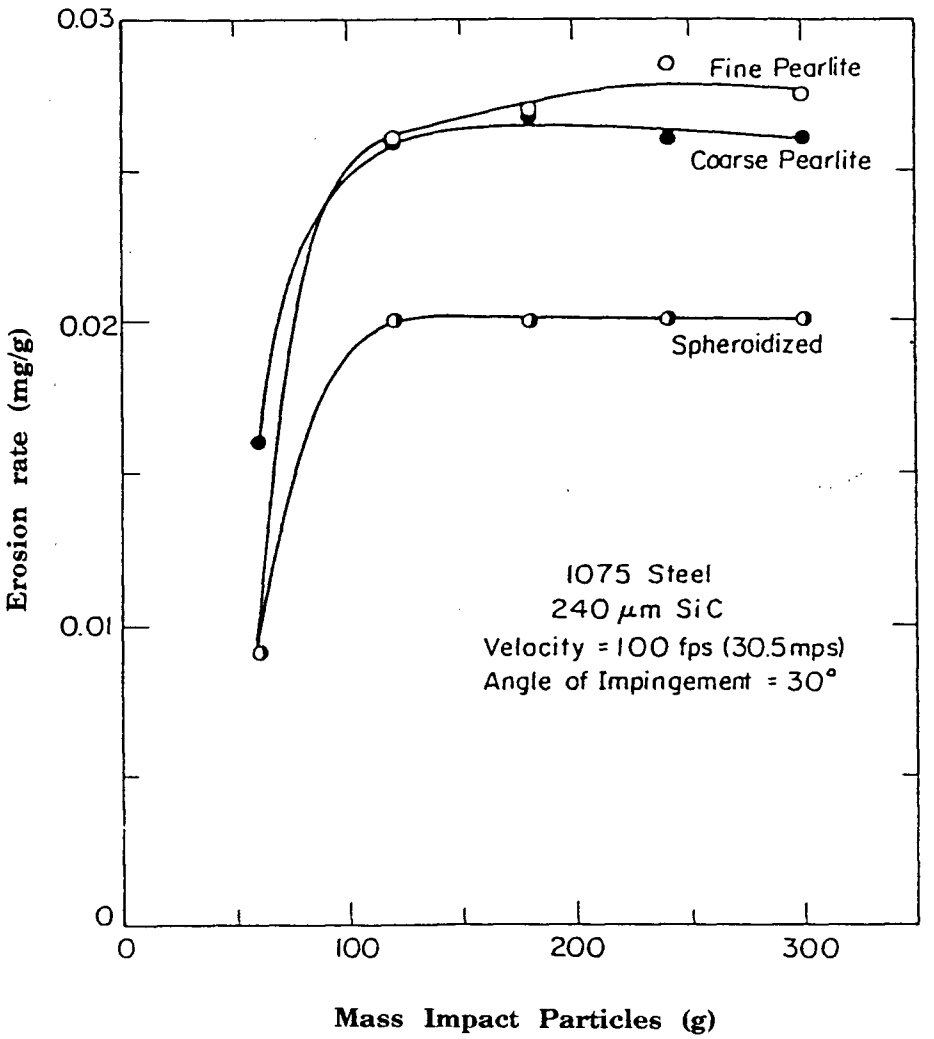

Figure 2.5 Incremental erosion of 1075 steel to steady state rate (from Levy 1982)

worked zone acts as an anvil to increase the efficiency of the impacting particles or hammer to extrude-forge platelets in the now fully heated and most deformable surface region". When the anvil is fully in place and the platelets are fully formed and heated, the material removal rate will reach a maximum. These conditions move down through the metal as erosive loss proceeds.

For ductile materials, the influence of the parameters is as follows:

1. Particle incident angle: Maximum erosion occurs at an angle of about 20° from the target surface while minimum erosion is observed for normal impacts. This phenomenon was first reported by Finnie (1958, 1960) and has been confirmed by many other workers (e.g. Bellman & Levy 1981, Levy 1982, Hutchings 1987). The difference between maximum and minimum erosion rates due to angle are 2 to 3.5 times (Finnie 1979). The equation

$$E = A_1 cos^2\theta + A_2 \tag{2.19}$$

has been given by Tilly (1979) to correlate erosion rate with impingement angle, where A_1 and A_2 are constants.

2. Particle impact velocity, V_p: The influence of impact velocity is generally expressed (Tilly 1979) as:

$$E = const \times V_p^{m_1} \tag{2.20}$$

where m_1 depends on both target and particle properties as well as solid impact angle. Typically m_1 is in the range 2.0 to 3.0 (Finnie 1979); Hutchings (1987) suggested m_1 from 2.0 to 4.0 while Schmitt (1980) reported it to be 2.3 or greater, and Tilly (1979) gave a value of 2.0 to 2.5 for ductile materials. A threshold velocity may exist below which no erosion occurs (Finnie 1979, Tilly 1979).

3. Duration of exposure: Erosion of soft materials involves an incubation phase, but com-

mon engineering materials, including steels, do not have a discernible incubation phase and the process stabalizes very quickly (Tilly 1979).

4. Particle hardness, H_p: The effect of hardness is usually expressed (Tilly 1979) as:

$$E = const * H_p^{m_4} \tag{2.21}$$

where m_4 depends on particle size and on the target material and H_p is the diamond pyramid hardness (Vickers hardness). Tilly (1979) suggested $m_4 = 2.3$ for a particle size of 125 – 150 μm and a normal impact velocity of 130 m/s. It is not necessary for the particles to be harder than the target material to cause erosion.

5. Particle shape: It is generally observed that particles having sharp corners are more erosive than rounded particles. However, the relationship between erosion and sphericity is not very clear (Hutchings 1987). Cousens and Hutchings (1983) even found that when steel was eroded by spherical particles, the maximum erosion occurred for normal impact angle, as for brittle materials, unlike angular particles impacting on ductile materials.

6. Particle size: For particle size larger than a certain value, erosion is independent of size (Finnie 1979, Hutchings 1987). When particle size is smaller than this value, erosion decreases as particle size decreases, but the functional relationships given by different investigators are quite different.

7. Material hardness: The effect of target material hardness on erosion rate has been a puzzling problem. Intuition suggests that erosion rate should decrease as the hardness of the target material is increased. However, poor correlation has been found between erosion resistance and hardness (Hutchings 1987). The original surface hardness appears to have little effect on the erosion process since, under repeated impacts, the work hardening and deforming process alters the condition of the surface being eroded

(Schmitt 1979). Figure 2.6 due to Finnie et al. (1987) shows erosion resistance plotted against hardness for a range of pure metals and three steels. The erosion resistance generally increases with hardness for pure metals, but the resistance changes little with the hardness change due to heat treatments of alloys. Clearly hardness is not the only property which influences the erosion rate.

8. Other material mechanical and thermal properties: Beginning in the late 1970's, researchers started to check other mechanical properties such as ductility, strain hardening, malleability and thermal properties, and also to reassess the 'older' properties like hardness and strength. Levy (1982) demonstrated that higher ductility results in greater erosion resistance.

Hutchings (1980) used a dimensionless Beat & Metz number,

$$B = \rho_s V_p^2 / Y_m \tag{2.22}$$

to classify erosion. Here ρ_s is the density of the impact particle and Y_m is the yield strength of the target material, while V_p is the impact velocity. For $B < 10^{-3}$ the behavior of the target is purely elastic, while for $B > 10^3$ the impact velocity is greater than the speed of sound in the material and hypervelocity phenomena are observed. In high impact velocity erosive wear, B lies between those values, typically with a value close to 1, and the impacts of grit particles cause plastic flow around the impact site (Hutchings 1979b).

Rickerby (1983) reviewed the influence of thermal properties on erosion rates. Based on the accumulated evidence, he suggested that mechanical rather than thermal properties should be more important because: (1) the mechanical work expended in a tensile test is typically a small fraction of the melting energy; (2) the erosion behavior of alloys typically differs markedly from that of the parent metals. He then proposed a

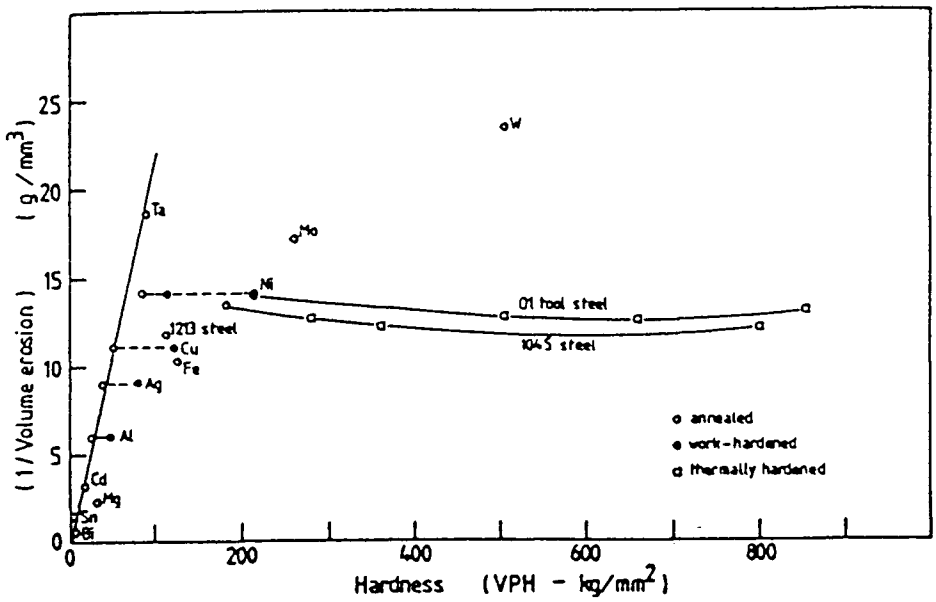

Figure 2.6 Variation of erosion resistance (defined as the reciprocal of the volume erosion) with indentation hardness for pure metals and alloys. The data were obtained with gas–borne silicon carbide particles (from Finnie et al. 1967)

mechanical energy density,

$$W = 1/2(\sigma_y + \sigma_u)\epsilon_f \tag{2.23}$$

to correlate the erosion rate, where σ_y is the yield stress, σ_u is the ultimate tensile stress and ϵ_f is the strain at failure. Figure 2.7 shows a clear trend when erosion rate is plotted against W.

Despite this work, the influence of material properties on erosion rate is far from clear. Erosion behavior can vary widely for materials of the same nominal composition from different sources (Hutchings 1987).

The above dependencies and equations, sometimes called the conventional solid impact erosion mechanism, are almost all based on experiments conducted with incident particle velocities higher than 30 m/s, a value which is up to an order of magnitude higher than velocities commonly encountered in fluidized beds. Nevertheless, they may help to explain some of the experimental results reviewed in Section 1.2. However, not all fluidization experimental results are consistent with the above mechanism. For example Woodford and Wood (1983) indicated that both particle hardness and velocity had little effect on the erosion rate. These findings are not consistent with the conventional high speed solid impact erosion mechanism. The mechanism of low velocity (< 10 m/s) multiple solid impact erosion may differ from that of high velocity impact erosion. This will be examined in the present investigation.

2.4 Mechanical Properties of Metals

2.4.1 Stress and Strain

In any engineering structure, individual components are subjected to external forces arising from the service conditions or environment in which the component works. If the

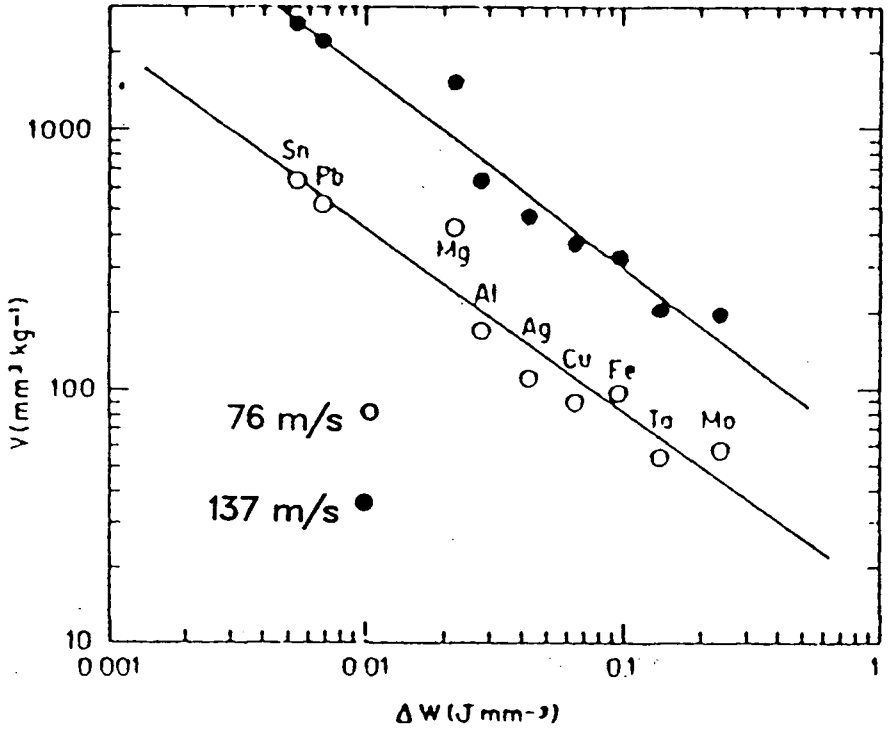

Figure 2.7 Correlation of volume erosion at impingement velocities of 76 m/s and 137 m/s with mechanical energy density for tensile failure (from Rickerby 1983)

component is in equilibrium, the resultant of external forces must be zero. Nevertheless, the forces place a load on the component which tends to deform that component and which must be counteracted by internal stress set up within the material.

Consider a cylindrical bar subjected to normal tension or compression along its axis as shown in Figure 2.8. If the force is uniformly applied across the cross-section, then the bar is said to be subjected to a uniform direct or normal stress defined as:

$$Stress(\sigma) = \frac{Load}{Area} = \frac{P}{A_b} \tag{2.24}$$

where P is the tension force and A_b is the cross-sectional area of the bar. Under this stress, the bar with original length L will change in length by an amount ΔL. The strain produced is then defined as:

$$Strain(\epsilon) = \frac{Change\ in\ length}{Original\ length} = \frac{\Delta L}{L} \tag{2.25}$$

2.4.2 Modulus of Elasticity – Young's Modulus

A material is said to be elastic if it returns to its original dimensions after a load is removed. A particular form of elasticity which applies to a large range of engineering materials produces deformations proportional to the load producing them within certain load limits. In other words, for elastic materials or engineering materials in their elastic range, stress is proportional to strain, and

$$E_y = \frac{Stress}{Strain} = \frac{\sigma}{\epsilon} \tag{2.26}$$

is a constant termed the modulus of elasticity or Young's modulus. Note that

$$E_y = \frac{\sigma}{\epsilon} = \frac{PL}{A_b \Delta L} \tag{2.27}$$

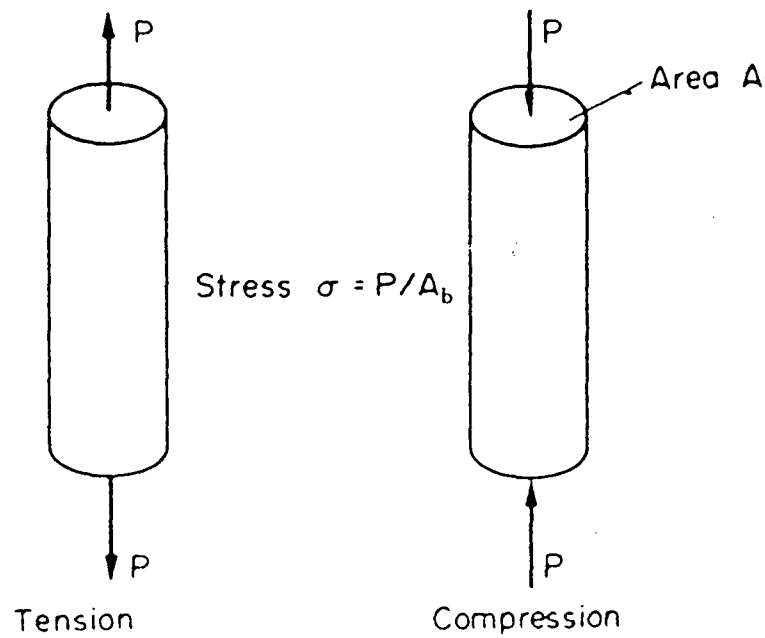

Figure 2.8 Types of direct stress (from Hearn 1985)

2.4.3 Tensile Test – Yield and Tensile Strength

In order to compare the strength of various materials, it is necessary to carry out some standard test to establish their relative properties. The standard tensile test is one such test. In this case a circular bar of uniform cross-section is subjected to a gradually increasing tensile load until failure occurs. Figure 2.9 shows a graph of load against extension or stress against strain for a typical mild steel. Point A is called the limit of proportionality, below which stress is proportional to strain. Point B is called the elastic limit, above which deformations cannot be completely recovered. Instead there will be some permanent deformation or permanent set when the load is removed. Points C and D are called the upper and lower yield points respectively. Beyond these points the strain increases rapidly without very much increase in stress. Since the upper yield point is not as stable as the lower yield point, point D is taken as the yield point, and the corresponding stress, therefore, is called the yield strength. The maximum or ultimate tensile stress, the normal stress at failure, is the stress at point E, also known as the tensile strength.

Between D and E in Figure 2.9, the material is said to be in the elastic-plastic state. If the load is removed at any point S between D and E (Figure 2.10), the strain will not return to the original point, O, but will end up at T after travelling parallel to OC. If the material is loaded again, the yield point will be somewhere close to S, so that the new yield strength will be greater than the original yield strength. This phenomena is called strain hardening or work hardening.

2.4.4 Ductility

Ductility is the ability to be drawn out plastically, i.e. the capacity of a material to allow plastic extension before fracture. A quantitative value of the ductility is obtained by

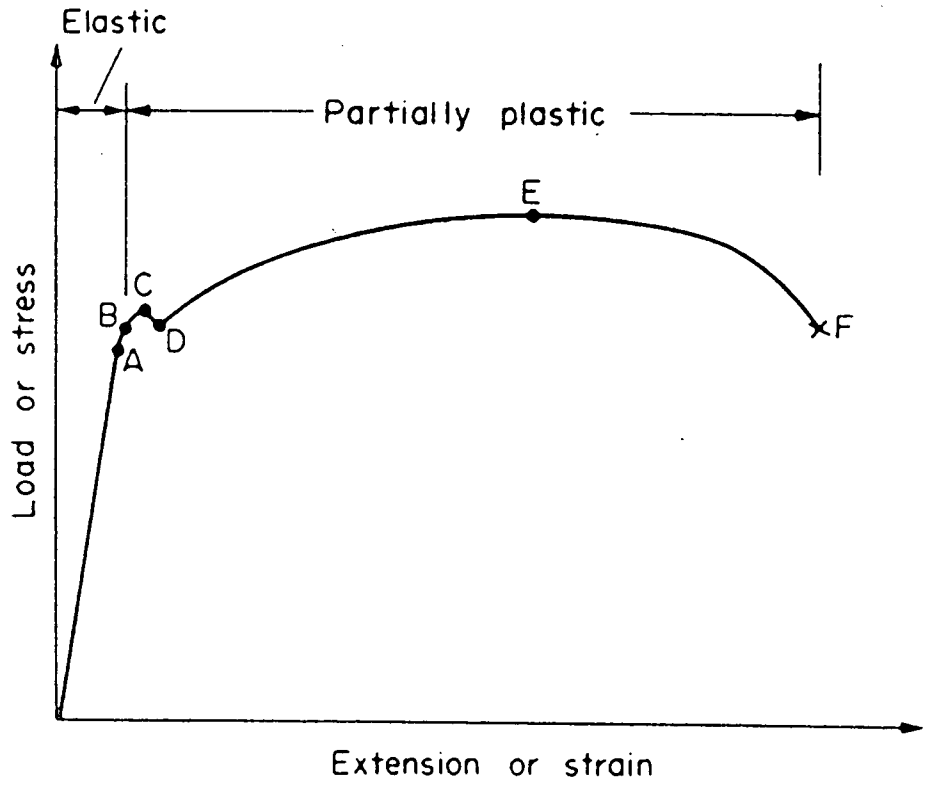

Figure 2.9 Typical tensile test curve for mild steel (from Hearn 1985)

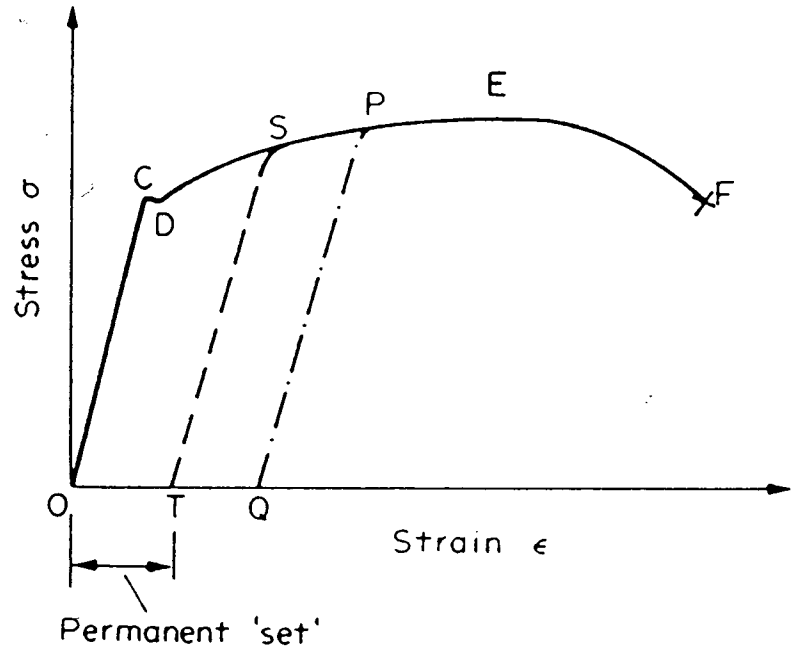

Figure 2.10 Permanent deformation or "set" after straining beyond the yield point (from Hearn 1985)

measuring elongation or the reduction of area:

$$Elongation = \frac{increased\ length\ to\ fracture}{original\ length} \tag{2.28}$$

$$Reduction\ of\ area = \frac{reduction\ in\ cross-sectional\ area}{original\ area} \tag{2.29}$$

The latter value, being independent of any selected gauge length, is generally taken to be the more useful measure of ductility for reference purposes.

Materials with high ductility are termed ductile materials, while materials with low ductility are termed brittle materials. There is no clear boundary between ductile and brittle materials, although materials such as glass and ceramic are considered brittle and most metals and alloys are considered ductile.

2.4.5 Hardness

Hardness is a term associated with resistance to plastic deformation. For testers of materials, hardness is also a value representing the resistance to indentation or tensile strength. There are many methods to measure and present the hardness quantitatively. The most common are Mohs hardness, Brinell hardness, Rockwell hardness, Vickers hardness and Knoop hardness.

Mohs hardness is a scratch type hardness, the measurement of which is a coarse one. The other hardnesses are all based on an indentation test in which a certain load is applied to the materials through a spherical or pyramid indenter and then the depth or the size of the indentation is measured. The earliest such method, giving Brinell hardness, involves a ball indenter and measurement of the diameter of the indentation. The method has the disadvantages of being not constant and requiring a large load ($> 500kg/mm^2$) which has the danger of damaging the specimen. A improved test of this type is the Vickers hardness test in which a relatively low load is applied through a pyramid indenter. The diagonal of

the indentation is then measured (Figure 2.11). The Vickers hardness number then can be calculated as:

$$H_v = \frac{P}{A_c} = \frac{1.854P}{d_1^2} \tag{2.30}$$

where P is the load (kg), A_c is the contact area and d_1 is the diagonal of the indentation. An alternative is the Knoop hardness which has an indenter with an impression diagonal in one direction that is 7.11 times as long as that in the other direction to give a long dimension to measure for a minimum indentation (Figure 2.12). The Knoop hardness is desirable for a thin specimen or brittle materials since it gives shallow indentations.

The Rockwell hardness test is a time-saving method, which, instead of measuring the size of the indentation as in the Brinell, Vickers and Knoop hardness tests, measures the penetration depth by a dial gauge and reads out the Rockwell hardness directly. However, the Rockwell test usually produces a much bigger indentation than the Vickers and Knoop tests so that it is not suitable for thin or brittle materials and for testing the hardness without destroying the surface.

Hardness testing is actually a process of material deformation which has to overcome the yield strength. Thus there must be a certain relation between hardness and yield strength. For pyramid indenters, the relationship according to theory is as follows (Tabor 1956):

$$H_v = P/A_c = 3\,Y_m \tag{2.31}$$

Experimental results (Tabor 1956) show that for fully cold-worked non-strainhardening materials, the relation between pressure of the Vickers indenter and the yield strength is (Table 2.1):

$$H_v = 3.2P \tag{2.32}$$

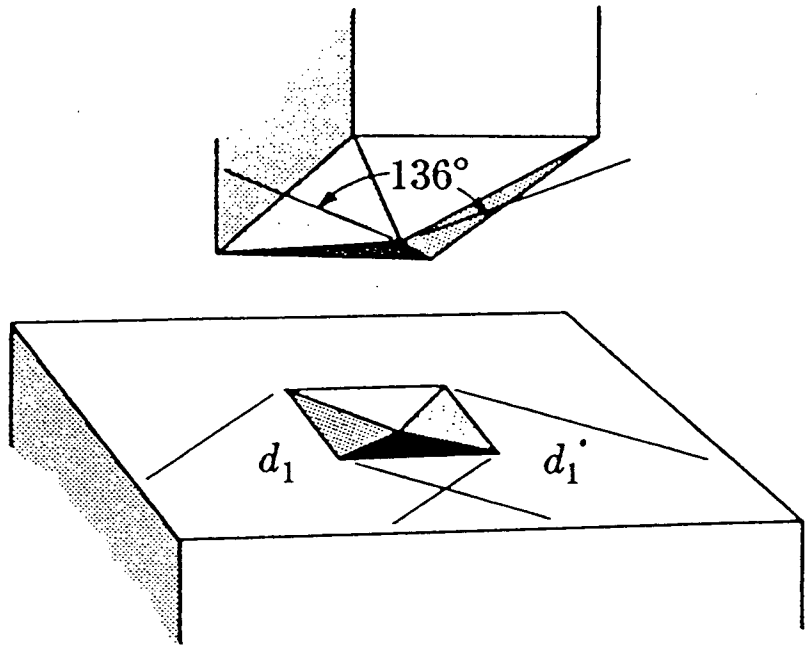

Figure 2.11 The Vickers pyramidal indenter (from McClintock & Argon 1966)

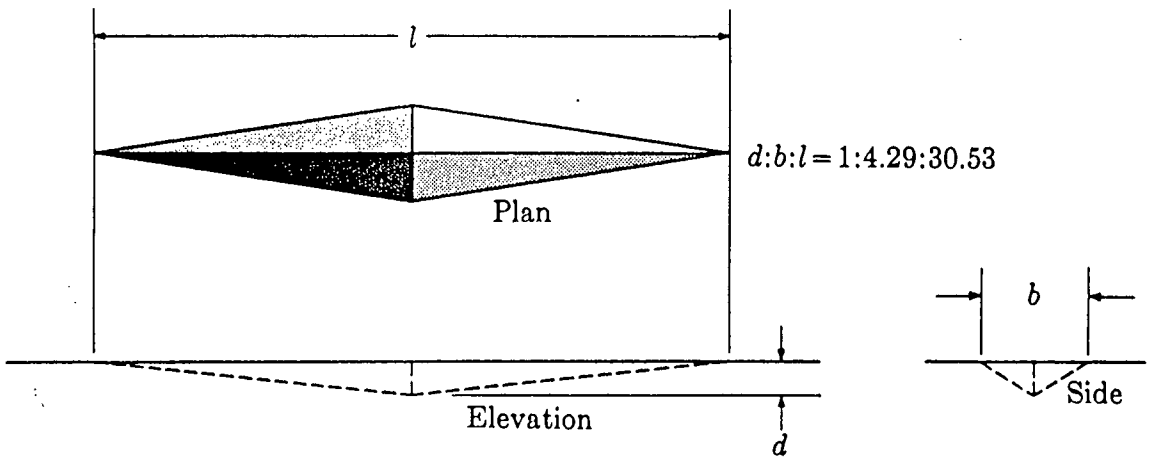

Figure 2.12 The Knoop hardness indenter (from McClintock & Argon 1966)

Table 2.1: Ratio of hardness to yield strength for cold worked metals (from Tabor 1956)

Metal	Y_m kg/mm^2	H_m kg/mm^2	H_m/Y_m
Tellurium-lead	2.1	6.7	3.2
Aluminum	12.3	39.5	3.2
Copper	27	88	3.3
Mild steel	70	227	3.2

for a variety of materials of widely different hardness. The following equation gives the relationship between the indenter hardness and the yield strength (Tabor 1956):

$$3.2P = 3\,Y_m \tag{2.33}$$

Substitution of equation 2.33 into equation 2.32 yields:

$$H_v = 3\,Y_m \tag{2.34}$$

This result is identical with the theoretical equation 2.31.

More details about material mechanical properties are provided by Hearns (1985) and McClintock and Argon (1966).

2.4.6 Other Mechanical Properties

There are other mechanical properties such as strain rate sensitivity, toughness and fatigue properties of materials which may influence erosion rates. These properties are not reviewed here due to the difficulties in determining their quantitative values in the erosion process which take place at or very close to the material surface. Detailed information regarding these properties may be found in the *Metal Handbook* (ASM 1983).

CHAPTER THREE: EXPERIMENTAL EQUIPMENT AND CONDITIONS

3.1 Experimental Conditions

The primary objective of this study was to measure the tube erosion rate in a fluidized bed under different conditions and then to establish a model to account for the erosion rate. To do so, four different pieces of equipment were set up to carry out four sets of experiments.

The first set of experiments was carried out in a three-dimensional fluidization column at room temperature to measure the tube erosion rate under different operating conditions. (Techniques of measuring and procedures for mounting of specimens are discussed in Chapter 4). The independent variables were:

Particle size
Particle properties (hardness, sphericity, density)
Gas superficial velocity
Static bed height
Tube material properties
Tube size
Tube location and configuration
Air distributor

The ranges of these variables are listed in Table 3.1.

The parameters were varied under a 'multi-axes' design, in which a typical set of conditions is chosen as the base case and taken as the origin, then several axes representing different parameters are drawn through the origin to form a coordinate system. From the origin, only one parameter was changed each time along one axis and then returned to the original point before another parameter was tested. The coordinate system and 32 points corresponding to 41 experiments are shown in Figure 3.1. All of these experiments were conducted at room temperature with negligible chemical reaction in order to minimize oxidation and corrosion so that erosion could be studied in isolation.

Table 3.1: Range of variables for three-dimensional room temperature fluidized bed experiments

Variable	Values
Gas superficial velocity (m/s)	0.88, 1.38, 1.86, 1.88, 1.98, 2.03, 2.15, 2.22, 2.52
Particle diameter (mm)	0.30, 0.67, 0.89, 1.00, 1.04, 1.08, 1.10, 1.30, 1.51
Particle sphericity	0.84, 0.86, 0.89, 0.91, 1.0
Particle hardness (kg/mm^2)	350, 590
Angle of impingement (degrees measured from tube bottom)	0 - 180° in 15° steps
Tube outside diameter(mm)	15, 20, 25 and 32
Tube materials	Brass (C36000), Copper (14500), Al2011-T3, SS316, SS304, CS1020, CS1045, Al, Iron, Atlas Keewatin Tool Steel
Tube configuration	Single tube and an array of five tubes (two upstream and two downstream with the test tube in the center)
Tube height and and orientation	Normal tube position 308 mm above the distributor, Tube center placed 32 mm above the distributor and Tube at normal position but inclined at 15 degrees to the horizontal Tube close to bed surface

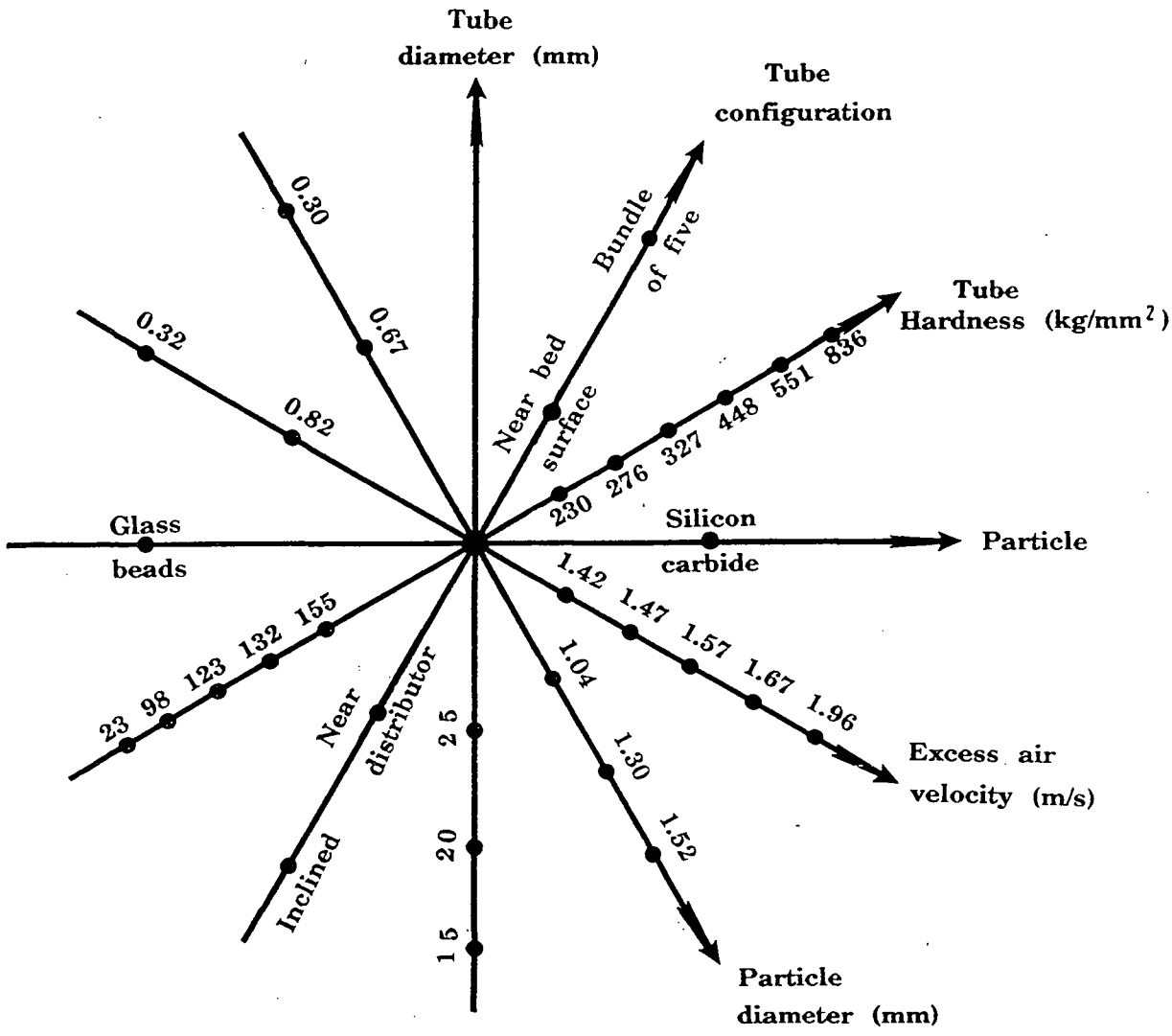

Center point:
32 mm single tube, 308 mm above the distributor, Tube hardness 98 -- 276 kg/mm², 1.0 mm silica sand and excess air velocity of 1.31 m/s

Figure 3.1 Multi-axes design of room temperature three-dimensional bed experiments

The second set of experiments was conducted in a two-dimensional fluidized bed in order to be able to trace the bubble and particle movement around a horizontal tube. The purpose was to help establish the relationship between particle impingement velocity and gas superficial velocity, and between particle impingement velocity and erosion rate. A high speed camera was used to film particle motion through the transparent wall and also from inside the tube using a pyramid mirror mounted in the interior of the tube. The films were then developed and projected at a slower speed or frame by frame to track the paths of single particles. Silica sand with a mean size of 1.0 *mm* was used for all filming, and two superficial velocities were tested, one being the same as in the origin of the first set of experiments. A bundle of five tubes was also installed for one test to compare the particle motion around the central tube with that around a single tube. A separate experiment was carried out with the bed held at minimum fluidization and with additional air injected into the bed under the tube to form isolated bubbles and bubbles coalescing just beneath the tube to correlate the particle impingement velocity with the velocity of single and coalescing bubbles.

The third set of experiments was conducted in a specially designed "dropping device", which allows particles to drop freely from different heights and impact on a test specimen in order to study erosion under "controlled conditions", where every parameter is known, unlike the conditions in a real fluidized bed. The particle impact velocities were determined by filming with a strobelight, and the particle mass flow rates were measured by collecting the particles dropped on the specimen over a given time interval. The erosion rates were calculated from the weight loss during erosion as described in Section 4.2. The parameters were varied using the same "multi-axes" design as described above. The independent variables were:

Particle size
Particle impingement velocity
Particle mass flow rate
Particle impingement angle
Particle properties (hardness, sphericity, density)
Specimen material properties

The ranges over which these properties were varied are listed in Table 3.2.

The fourth set of experiments was carried out in a circulating fluidized bed combustor pilot scale facility, which was operated as a conventional fluidized bed for these tests. The conditions were very similar to those for the base condition for the room temperature three-dimensional bed experiments described earlier in this section, except that a slightly different particle size was used. In addition, the bed temperature was varied from room temperature (20 C) to 780 C to test the influence of temperature.

3.2 Three-dimensional Low Temperature Fluidization Column

Figure 3.2 shows the general set-up of the low temperature fluidization apparatus previously used by Hosny (1982). Air is compressed by a SUTORBILT blower, Model 7HV, which has a maximum capacity of 8 m^3/min at a gauge pressure of 69 kPa and can provide a maximum superficial velocity of 3.0 m/s in the fluidization column. The air flow rate was monitored by an orifice flowmeter and controlled by the combination of the inlet and by-pass valves. As shown in Figure 3.3, two buffering bottles with capillaries inside were connected between each leg of the manometer and the corresponding side of the orifice in order to damp fluctuations and provide a steadier and more accurate reading.

The three-dimensional fluidization column itself was rectangular with a cross-section of 203 mm x 216 mm and a height of 1.5 m. Figure 3.4 shows the column and its cyclone, while Figure 3.5 shows a vertical section through the column with a single tube in the bed. The tube to be tested was centered 308 mm above the gas distributor and supported by

Table 3.2: Range of variables for particle dropping solid impact erosion tests

Variable	Values
Particle impact velocity (m/s)	2.2, 3.3, 4.1, 5.0
Particle diameter (mm)	0.89, 0.93, 1.0, 1.08, 1.30, 1.51
Particle sphericity	0.84, 0.86, 0.89, 1.0
Particle hardness (kg/mm^2)	40, 350, 590
Angle of impingement	22.5°, 45°, 67.5° and 90°
Target materials	Brass(C36000), Al2011-3T, Copper(C14500), SS316, CS1050, PVC, Plexiglass and Oak

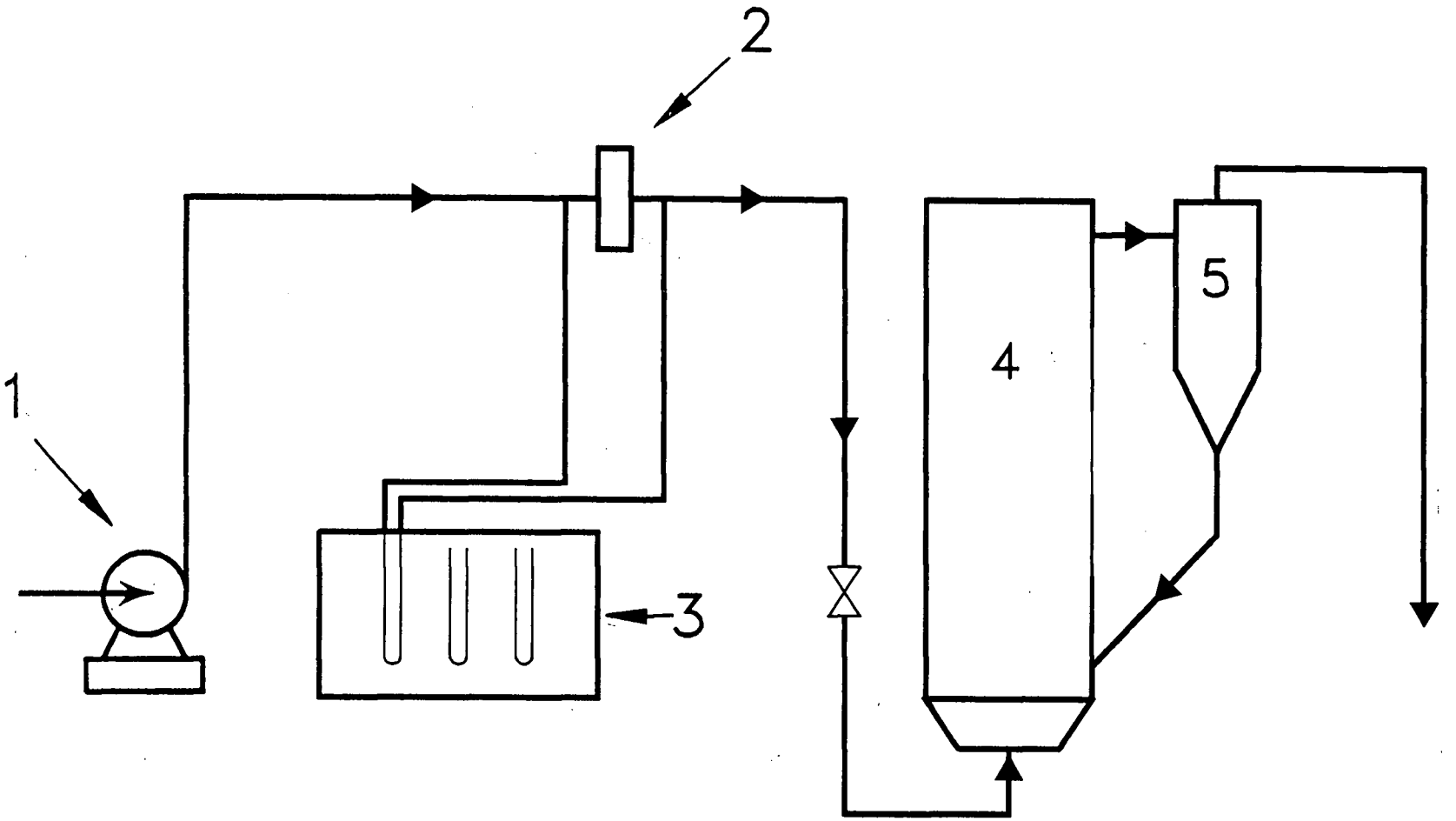

Figure 3.2 General set–up of the three–dimensional room temperature column

(1) air blower, (2) flow measurement orifice, (3) manometer, (4) fluidization column, (5) cyclone.

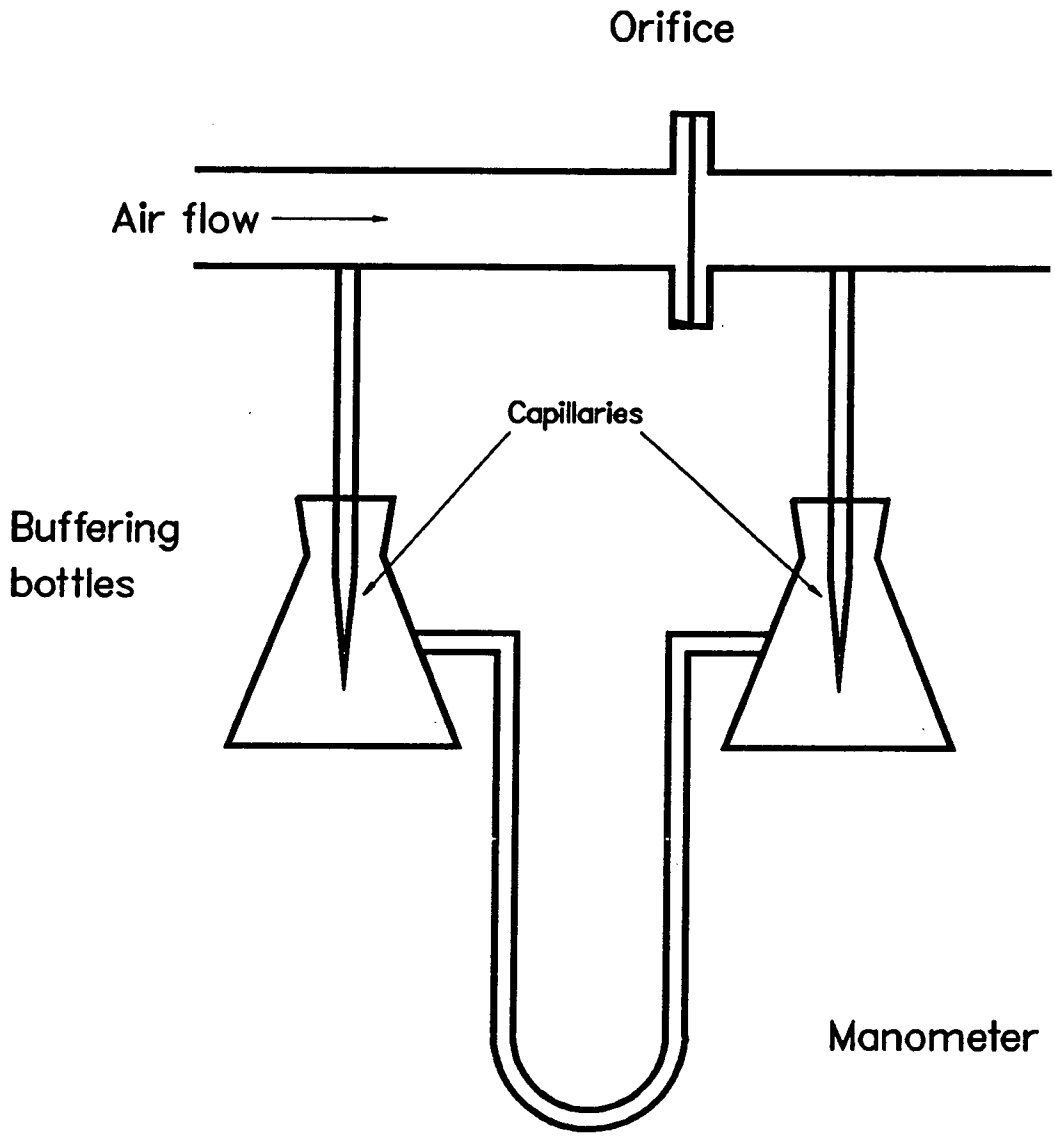

Figure 3.3 Buffering bottles for the manometer used to measure air flow rate

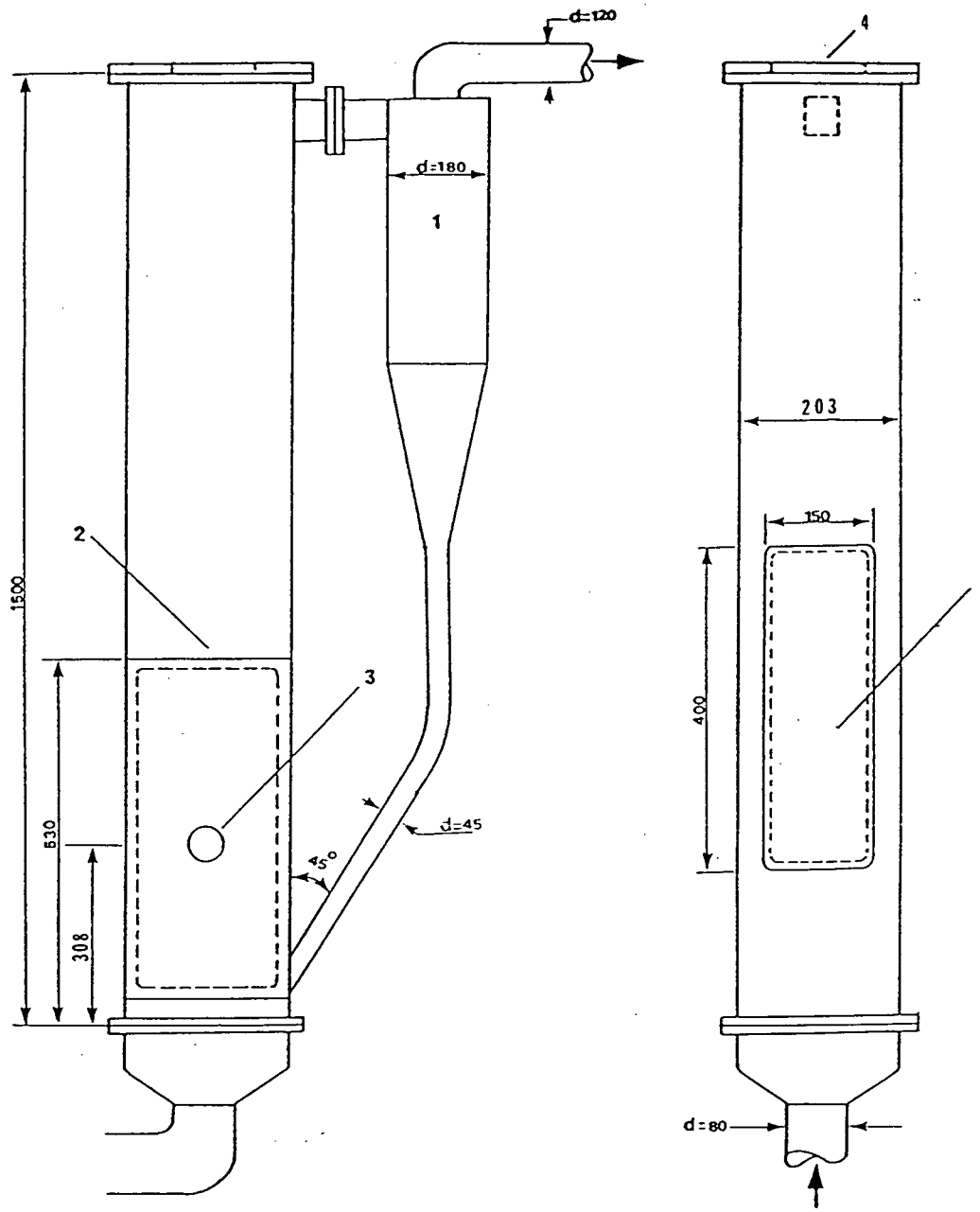

Figure 3.4 Primary features of the three-dimensional fluidization column and its auxiliaries (dimensions are in mm.)

(1) cyclone, (2) tube panel, (3) test tube position, (4) top glass window, (5) right-side glass window

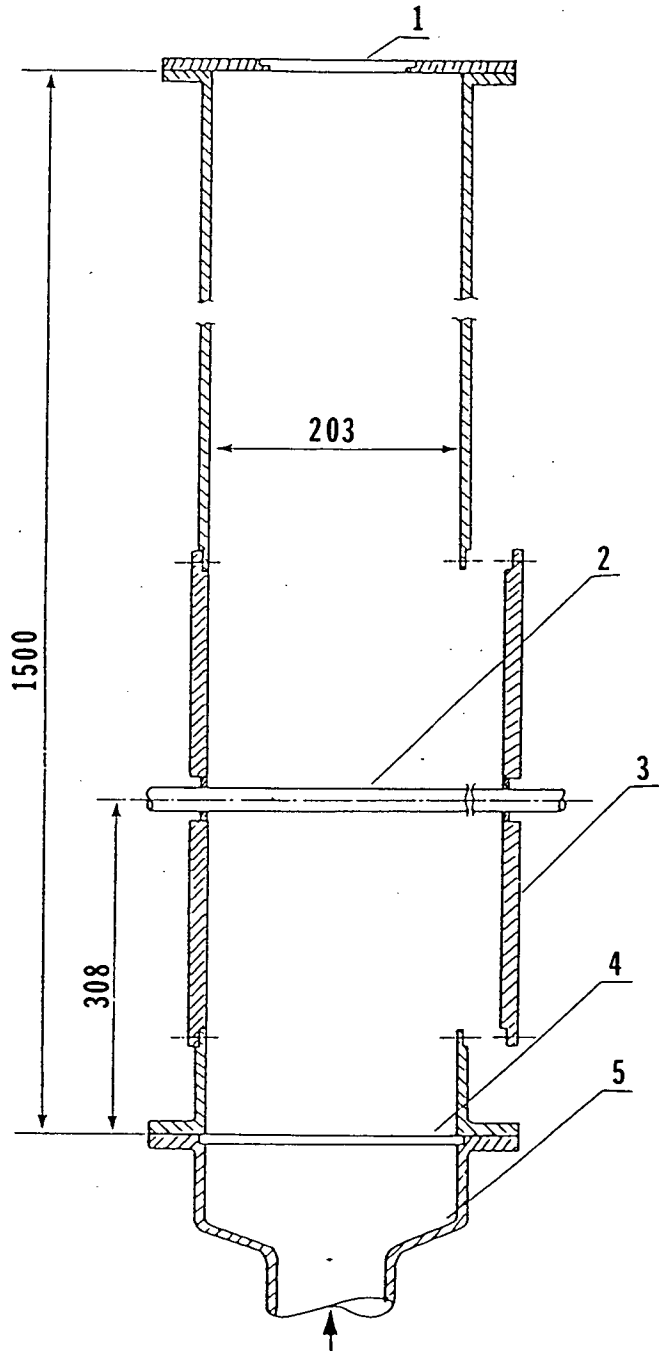

Figure 3.5 Vertical section through the three-dimensional fluidization column (all dimensions are in mm.)

(1) top glass window, (2) test tube position, (3) tube panel, (4)) gas distributor, (5) plenum

a pair of collars, one at each side of the column. There were four more collars on each side of the column so that four more tubes could be added to center the test tube in an array of five identical tubes. In this case, the five tubes were arranged in a triangular pitch configuration, with the tube centers 64 *mm* apart as shown in Figure 3.6.

The column was constructed entirely from mild steel with a thickness of 5 *mm* to achieve wall rigidity and resistance to wear. The air distributor was a multi-orifice plate, 5 *mm* thick with 182 orifices of diameter 3 *mm* and a spacing of 15 *mm*. The plate was covered by a steel fine wire screen to prevent solid particles from dropping through the holes. There were three glass windows, two square windows (125 *mm* x 400 *mm*) on the opposite sides of the column and one round window at the top of the column, allowing viewing and filming of the bed behaviour. Seven pressure taps could be used to measure pressure drops across different height intervals above the distributor. A port of diameter 20 *mm* was also drilled just above the distributor to allow the solid particles to be discharged.

The erosion rates were calculated from the weight loss of small specimen rings mounted on a supporting bar. Details about the installation of the specimen rings are provided in Section 4.3.

3.3 Solid Particles

Nine different types of particles (six grades of silica sand, silicon carbide, glass beads and limestone) were used in the three-dimensional fluidized bed testing. Table 3.3 lists the properties of these particles. Table 3.4 tabulates size distributions of these particles. The mean particle diameters were obtained from

$$d_p = \frac{1}{\Sigma(x_i/d_{p_i})} \tag{3.1}$$

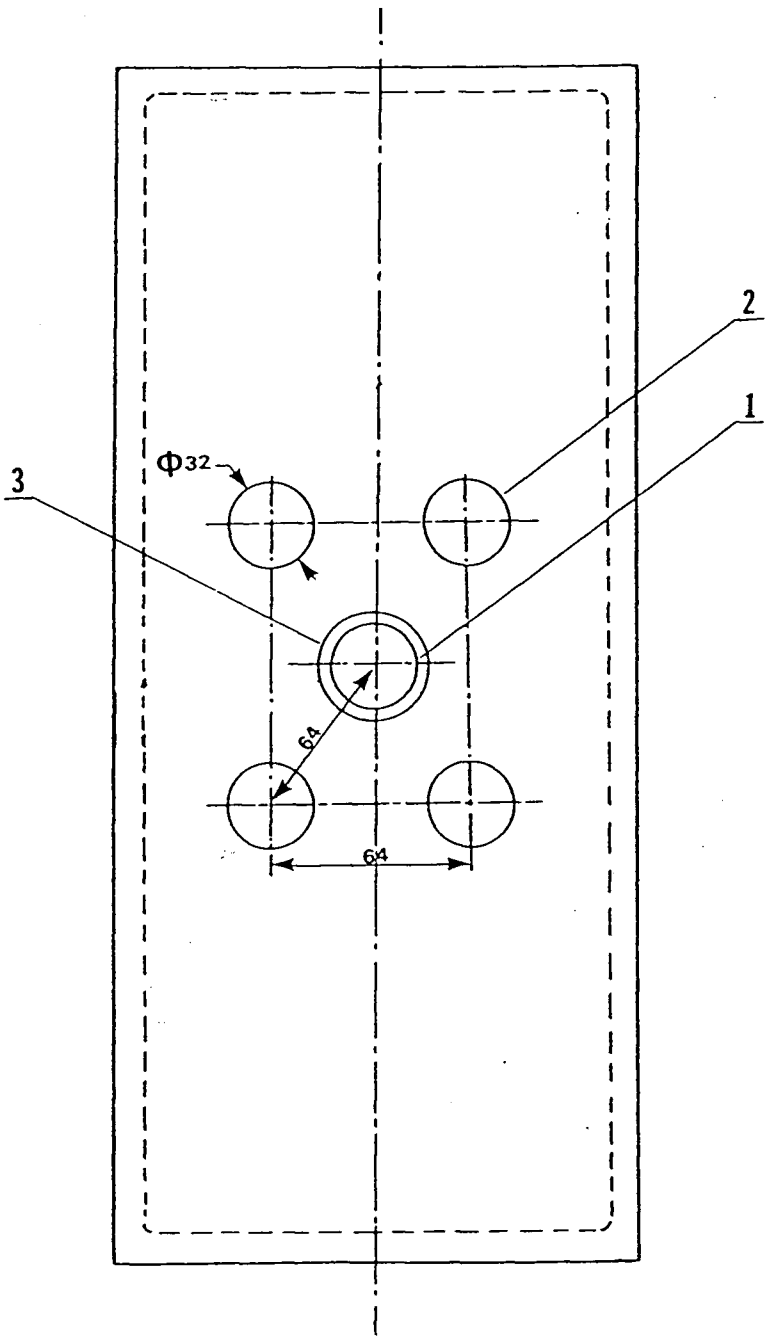

Figure 3.6 Side plate of the three-dimensional fluidization column for tube array assembly (all dimensions are in mm.)

(1) test tube, (2) other tubes, (3) hole in the bed wall

Table 3.3: Particle properties

Particles	Mean diameter (mm)	Density (kg/m^3)	Sphericity	Minimum fluidization velocity (m/s)	Terminal velocity (m/s)	Hardness (kg/mm^2)
Silica sand #1	1.51	2530	0.86	0.74	9.3	350
Silica sand #2	1.30	2610	0.86	0.64	8.7	350
Silica sand #3	1.04	2580	0.86	0.57	7.8	350
Silica sand #4	1.00	2580	0.84-0.91	0.56	7.6	350
Silica sand #5	0.67	2620	0.86	0.40	6.2	350
Silica sand #6	0.30	2600	0.86	0.25	4.1	350
Silica carbide	1.08	3000	0.86	0.70	8.5	590
Glass beads	0.89	2500	1.0	0.48	6.9	340
Limestone	0.93	2690	0.85	0.50	7.5	40

Table 3.4 Particle size distributions determined by sieving
(All sizes are in mm.)

Screen Size	-2.800 +2.000	-2.000 +1.400	-1.400 +1.180	-1.180 +1.000	-1.000 +0.850	-0.850 +0.710	-0.710 +0.500	-0.500 +0.355	-0.355 +0.250	-0.250 +0.180	-0.180 +0.0	
Screen mean diameter	2.366	1.673	1.285	1.086	0.922	0.777	0.596	0.421	0.298	0.212	0.090	
	Weight fraction											Average Size
Silica sand #1	0.083	0.682	0.109	0.054	0.043	0.029	0.0	0.0	0.0	0.0	0.0	1.51
Silica sand #2	0.003	0.271	0.496	0.155	0.047	0.017	0.011	0.0	0.0	0.0	0.0	1.30
Silica sand #3	0.0	0.003	0.250	0.427	0.239	0.053	0.028	0.0	0.0	0.0	0.0	1.04
Silica sand #4	0.0	0.004	0.165	0.399	0.325	0.094	0.012	0.0	0.0	0.0	0.0	1.00
Silica sand #5	0.0	0.0	0.001	0.002	0.152	0.432	0.328	0.067	0.018	0.0	0.0	0.67
Silica sand #6	0.0	0.0	0.0	0.0	0.067	0.0	0.007	0.396	0.217	0.313	0.0	0.30
Silicon carbide	0.001	0.023	0.341	0.450	0.109	0.039	0.038	0.0	0.0	0.0	0.0	1.08
Glass beads	0.0	0.0	0.0	0.027	0.749	0.218	0.006	0.0	0.0	0.0	0.0	0.89
Limestone	0.002	0.144	0.155	0.170	0.191	0.161	0.176	0.0	0.0	0.0	0.0	0.93

where x_i is the weight fraction collected between sieves of mean aperture d_{p_i}. The hardness values were measured using a micro-hardness tester (TUKON Model MO) in the Department of Metals and Materials Engineering at UBC. The minimum fluidization velocities, u_{mf}, were determined from the results of the standard pressure drop versus superficial velocity plot method. The particle density, ρ_s, was determined experimentally by water displacement techniques while the terminal velocity, u_t, was determined by calculation (Zhang 1980). For the particle sphericity, Φ_s, since it was very difficult to measure, the circularity was taken as an appoximation. The circularity is defined by Clift et al. (1978) as the square root of the ratio of the projected area of a particle to the area of the smallest circle circumscribing this projected area. The circularity was determined from pictures of particles in this experiment.

3.4 Tube Materials

Ten tube materials were studied in the three-dimensional fluidized bed tests. They were brass (C36000), copper (C14500), aluminium alloy 2011-T3, pure aluminium, pure iron, stainless steel AISI types 304 and 316, carbon steels 1020 and 1050, and Atlas Keewatin steels heat treated to four different hardnesses. PVC, plexiglass and oak were also used in the dropping tests. The compositions of all of these materials are listed in Table 3.5 and their properties are listed in Tables 3.6 and 3.7. These properties are based on data from handbooks (ASM 1983), from suppliers and from measurements taken at UBC. The tensile properties (Young's modulus, yield strength, tensile strength, elongation and reduction of area) were measured with a tensile tester (INSTRON Model TTC). The hardnesses were determined using both a Vickers hardness tester (VICKERS Model HTM) and a Rockwell hardness tester (ROCKWELL Model 3JR). The densities were determined by dividing the

Table 3.5: Compositions and working conditions of the materials tested

Materials	Short names used in thesis	Composition (%) *	Working conditions before erosion tests**
Free-machining Brass or Yellow Brass (C36000)	Brass, Yellow brass	Cu 61.5 Zn 35.5 Pb 3.0	Cold drawn
Free-machining Copper (C14500)	Copper, Pure copper	Cu 99.4 Te 0.6 P<0.007	Cold drawn
Aluminium Alloy 2011	Al 2011, Al Alloy	Cu 5.0-6.0 Si 0.5-1.2 Fe 0.7 Zn 0.3 Bi 0.2-0.6 Pb 0.2-0.6	Cold drawn
Stainless Steel AISI type 304	SS304	Cr 18-20 Ni 8-11 Mn 2.0 Si 1.0 P 0.04 S 0.04 C < 0.08	Cold drawn and annealed
Stainless Steel AISI type 316	SS316	Cr 16-18 Ni 10-14 Mn 2.0 Si 1.0 P 0.04 S 0.04 C < 0.1 Mo 1.75-2.50	Cold drawn and annealed
Carbon Steel AISI grade 1020	CS1020	C 0.15-0.20 Mn 0.60-0.90 P < 0.040 S < 0.050	Cold drawn
Carbon Steel AISI grade 1050	CS1050	C 0.48-0.55 Mn 0.60-0.90 P < 0.040 S < 0.050	Cold drawn
Pure Aluminum	Pure Al	Al > 99.99	Annealed
Armco Iron	Pure Iron	Fe > 99.9	Annealed
Atlas Keewatin tool steel	Keewatin Steel	C 0.90, Mn 1.20, Si 0.30, Cr 0.50, W 0.50, V 0.20	Oil quenched from 800 C in saltpot, tempered at 600 C, 480 C, 310 C or 105 C for one hour

* From the supplier --- Wilkinson Company Limited's catalogue -- reference No. 12, 1973

** The working condition may change due to the process of machining when the rings were made on the lathe

Table 3.6: Mechanical properties of the materials used in the tests

Materials		Elastic Modulus GPa	Strength Yield MPa	Strength Tensile MPa	Elongation Percent	Reduction of Area Percent	Hardness Vickers kg/mm^2	Hardness Others ***	Density kg/m^3
SS316	(Measured Value)	189	547	648	59%	77%	327		
	(Handbook Data)*	190	760					HRC 35-45	
	(Manufacturer's Data)**	190	276	621	50%	65%		HRB-85	7840
SS304	(Measured Value)						276		
	(Handbook Data)								
	(Manufacturer's Data)	190	262	586	50%	65%		HRB-80	7840
CS1020	(Measured Value)	180	508	646	24%	50%	230	HRA-53	
	(Handbook Data)	210	538	607		35%		HB-177	
	(Manufacturer's Data)		327	441	15%	40%		HB-126	7840
CS1050	(Measured Value)	203	627	692	21%	62%	230	HRA-52	
	(Handbook Data)	210	586	655		30%		HB-179	
	(Manufacturer's Data)		531	628	12%	35%		HB-179	7840
Brass	(Measured Value)	63.2	327	402	21%	59%	155	HRA-41	8410
(C36000)	(Handbook Data)	97	310	400	25%	50%		HRB-78	8500
	(Manufacturer's Data)		297	414	25-53%				8490
Copper	(Measured Value)	115	346	348	21%	70%	98.0	HRA-30	8990
(C14500)	(Handbook Data)	115	305	330	20%	48%		HRB-48	8940
	(Manufacturer's Data)		310	324	10-40%				8910
Al2011-T3	(Measured Value)	67.0	353	420	21%	48%	132	HRA-40	2880
	(Handbook Data)	70.0	296	379	15%			HB-95	2820
	(Manufacturer's Data)	71.0	296	379	15%			HB-95	2820
Pure Al	(Measured Value)	60.1	29.6	43.6	64%	96%	23.0	HRA-24	2670
	(Handbook Data)	62	20	40	50-70%				2700
	(Manufacturer's Data)								
Armco	(Measured Value)		162	327	38%	70%	123	HRA-30	7780
Iron	(Handbook Data)	208							
	(Manufacturer's Data)								
Keewatin	(Measured Value)	200	1132	1166	11%	30%	327	HRC-33	7790
Toolsteel	(Handbook Data)	210							
(1)	(Manufacturer's Data)								7780
Keewatin	(Measured Value)	202	1524	1580	7%	10%	448	HRC-44	7790
Toolsteel	(Handbook Data)	210							
(2)	(Manufacturer's Data)								7780
Keewatin	(Measured Value)	212					551	HRC-50	7790
Toolsteel	(Handbook Data)	210							
(3)	(Manufacturer's Data)								7780
Keewatin	(Measured Value)	204					836	HRC-63	7790
Toolsteel	(Handbook Data)	210							
(4)	(Manufacturer's Data)								7780
P.V.C.	(Measured Value)						14.6		1380
Plexiglass	(Measured Value)						26.6		1140
OAK Wood	(Measured Value)						6.9		690

* The handbook data is from 'Metal Handbook', 9th edition edited by American Society of Metal, 1983
** The supplier's data is from Wilkinson Company Limited's catalogue -- reference No. 12, 1973
*** HRA, B, C -- Rockwell hardness A, B, C scale, HB -- Brinell hardness number

Table 3.7: Thermal properties of the materials used in the tests*

Material	Thermal Conductivity (W/m^2K)	Heat Capacity ($J/kg\ K$)	Thermal Diffusivity ($m^2/s \times 10^5$)	Coefficient of Thermal Expansion ($\mu m/m\ K$)
SS316	17.8	502	0.45	16.2
SS304	17.8	502	0.45	17.8
CS1020	47.0	480	1.25	12.8
CS1050	45.6	486	1.19	13.1
Brass	115	380	3.56	20.5
Copper	355	415	9.56	17.8
Al2011-T3	152	864	6.24	25.0
Pure Al	231	900	9.50	25.5
Ameco Iron	75	494	1.95	12.8

* The data is from 'Metal Handbook', ninth edition edited by American Society of Metal, 1983

measured mass of a specimen by its volume calculated from dimension measurements. There are some differences between data from different sources, due to material non-uniformity, original working conditions, the machining process and/or experimental error. Where different manufacturers quote different values for the properties, our own measured data are used whenever available since the material properties tend to vary with working conditions. However, the Young's modulus data from a handbook (ASM) were used because Young's modulus is independent of heat treatment.

The tensile tester and the two hardness testers were all in the Department of Metals and Materials Engineering at UBC.

3.5 Two-dimensional Fluidization Column

The two-dimensional fluidized bed was contained in a plexiglass column, 10 mm thick, 510 mm wide and 2.4 m tall supported by a structural steel frame. This column has circular holes on one face for installation of up to five tubes as shown in Figure 3.7. Each of the tubes was a short section with one end closed, but with a small hole in the end piece which is used to attach the tube to the holder. The short section of tube was mounted by a screw onto a holder which fitted into the holes in the column wall and held the tube rigid during the experiments (see Figure 3.8). The arrangement of the tubes in the two-dimensional column was identical to that in the three-dimensional column described above, with the axis of the center tube 308 mm above the distributor and the other four tube centers 64 mm away in an equilateral triangular pitch configuration as shown in Figure 3.9.

Air was supplied for fluidization from the UBC Chemical Engineering building's central pressurised air supply which has a maximum gauge pressure of 55 kPa and sufficient capacity to give a maximum superficial velocity of 3 m/s. The air flow rate was measured by three

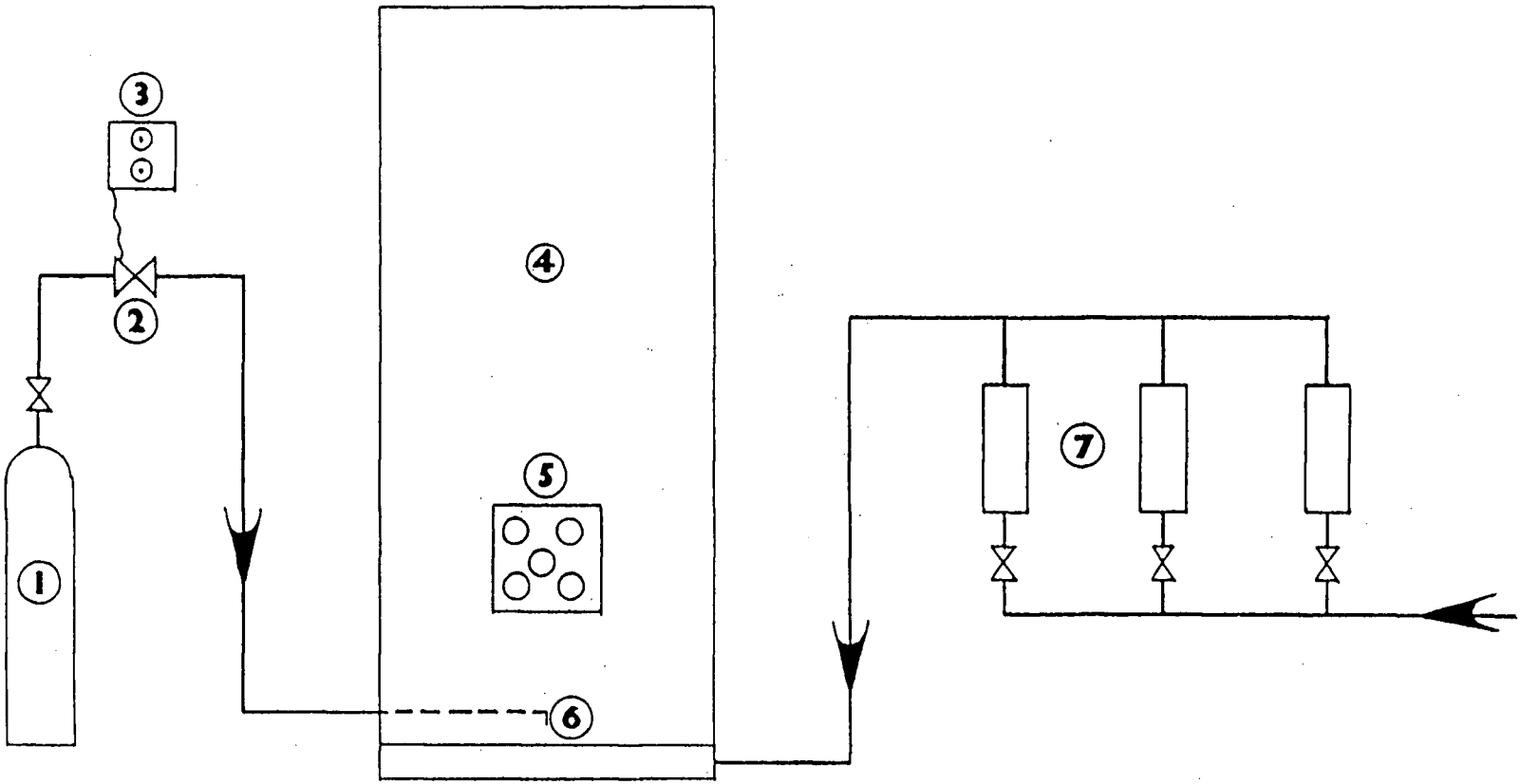

Figure 3.7 General set-up of the two-dimensional fluidization column

(1) medical air cylinder, (2) solenoid valve, (3) solenoid valve controller, (4) the fluidization column, (5) tube array, (6) bubble injection point, (7) rotameters

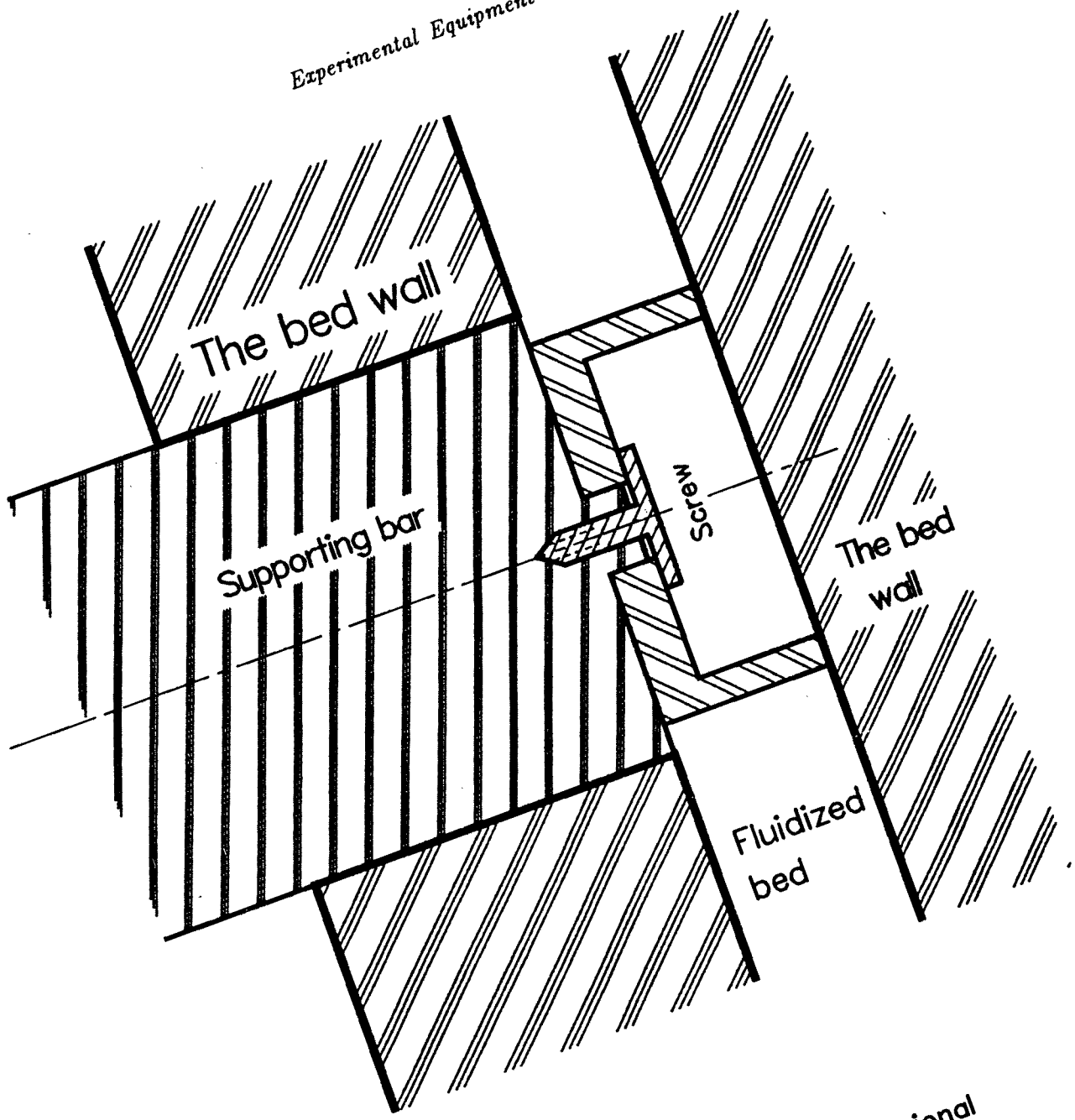

Figure 3.8 Tube assembly for the two-dimensional fluidization column

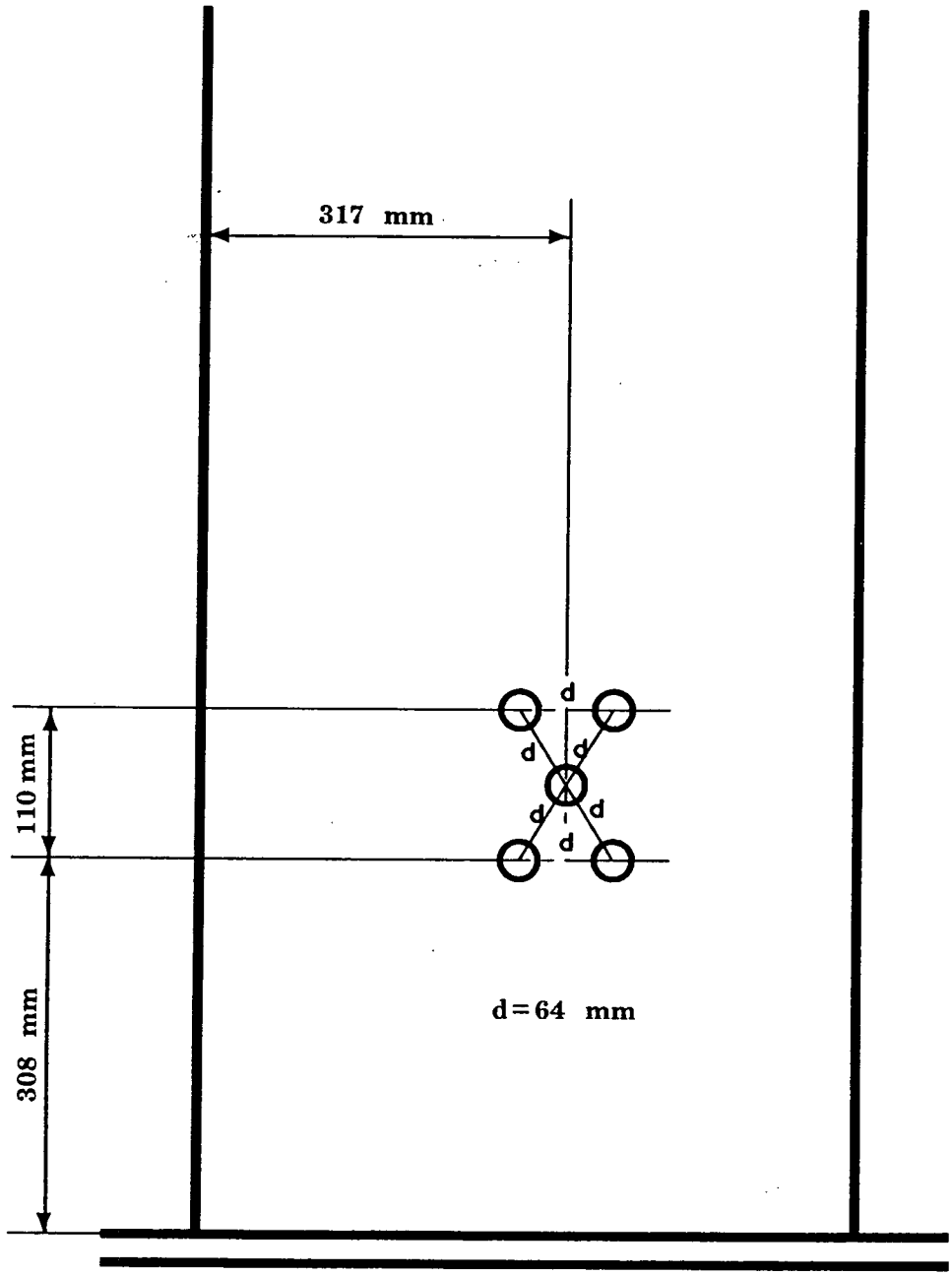

Figure 3.9 Tube configuration in the two-dimensional fluidization column

rotameters of different sizes, connected in parallel, in order to give accurate readings. The air distributor was a multi-orifice plate, with 112 holes of 1.2 *mm* diameter in one line, 5 *mm* apart. The 5 *mm* thick distributor and the windbox were constructed from aluminium alloy to sustain the pressure. Three pressure taps were used to measure pressure drops across different height intervals above the distributor. Solids could be discharged through two 20 *mm* diameter holes at opposite corners of the column, just above the distributor.

For single and multi-bubble injection with the air flow rate through the distributor held at minimum fluidization, a bubble injector with a 3 *mm* diameter injection hole was located 10 *mm* above the distributor. Air for bubble injection was supplied by a pressurized medical air cylinder, delivering air at pressures up to 1500 kPa. In order to control bubble size and the time intervals between bubbles, a solenoid valve with a 4.8 *mm* orifice was used. The opening of the solenoid valve was controlled by two relay timers: the first allowed the solenoid valve to be open for up to 6 seconds, while the second permitted the valve to be closed for up to 10 seconds.

3.6 High Speed Photography

To film the motion of solid particles around a horizontal tube in the two-dimensional column, two cameras were used: Hycam Cinematograph models K20S4E and K2001. The former was employed in most cases, as it had a wider range of operating conditions (100 – 11000 $frames/s$) and was simpler to operate. For the final experiments both cameras were used in order to obtain simultaneous footage inside and outside a single horizontal tube placed in the bed. To make cine photography from inside the tube possible, a special tube was made with a tetrahedral glass mirror set inside the tube as shown in Figure 3.10.

The lenses used throughout the experiments were an Asahi Pentax 1:3.5/135 *mm* and

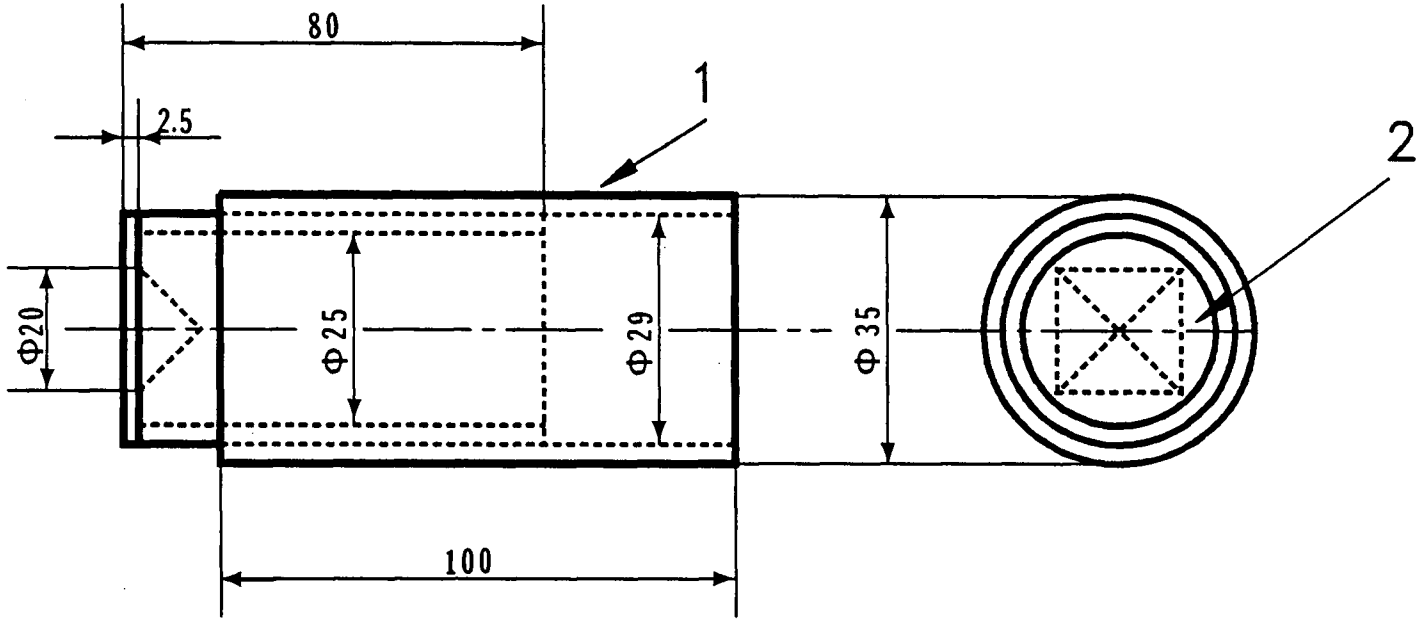

Figure 3.10 Tube with tetrahedral mirror set–up
(all dimensions are in mm.)

(1) tube sleeve, (2) tetrahedral mirror set–up

a Sun-Dionar 1:1.8/15-60 *mm* zoom. Lighting was supplied by a rack of 4 x 500 watt floodlights, a single hand-held 500 watt light and a circular array of 4 x 300 watt projector lamps. The choice of film was found to be critical to obtain high quality, analyzable films. After some experimentation Kodak 7222 double-negative film was chosen for its fine picture grain and its availability.

3.7 Particle Dropping Equipment

Figure 3.11 shows the equipment used for the particle dropping experiments. It consists of a storage and particle releasing section, a plexiglass protected free-fall column, a mounting region for the specimen mounting and a lower particle collecting section.

In the upper section, particles were initially stored in a funnel. Particles moved down by gravity to the level control section (Figure 3.12) where the particle level was kept constant. Particles then flowed down through a small tube onto a tray which was set up just beneath the end of the small tube. Particles piled up on the tray were blown off by air periodically and a small funnel was installed just below to recenter particles before they dropped freely. The air flow was controlled by the same solenoid valve and relay timers as for the two-dimensional photography described above. Building compressed air was used as the air supply. The particle mass flow rate could be changed by changing the tray level, the solid level in the level-control section, the air pressure and the opening-closing time of the solenoid valve. The opening of the lower funnel could also be adjusted to damp the particle flow fluctuations due to the air pulsations to give a continuous mass flow rate.

The intermediate part of the apparatus consisted of plexiglass tube sections, connected together to protect the free dropping particles from any air currents. The sections were square tubes, all having an inside cross-section of 89 *mm* by 89 *mm*, but with different

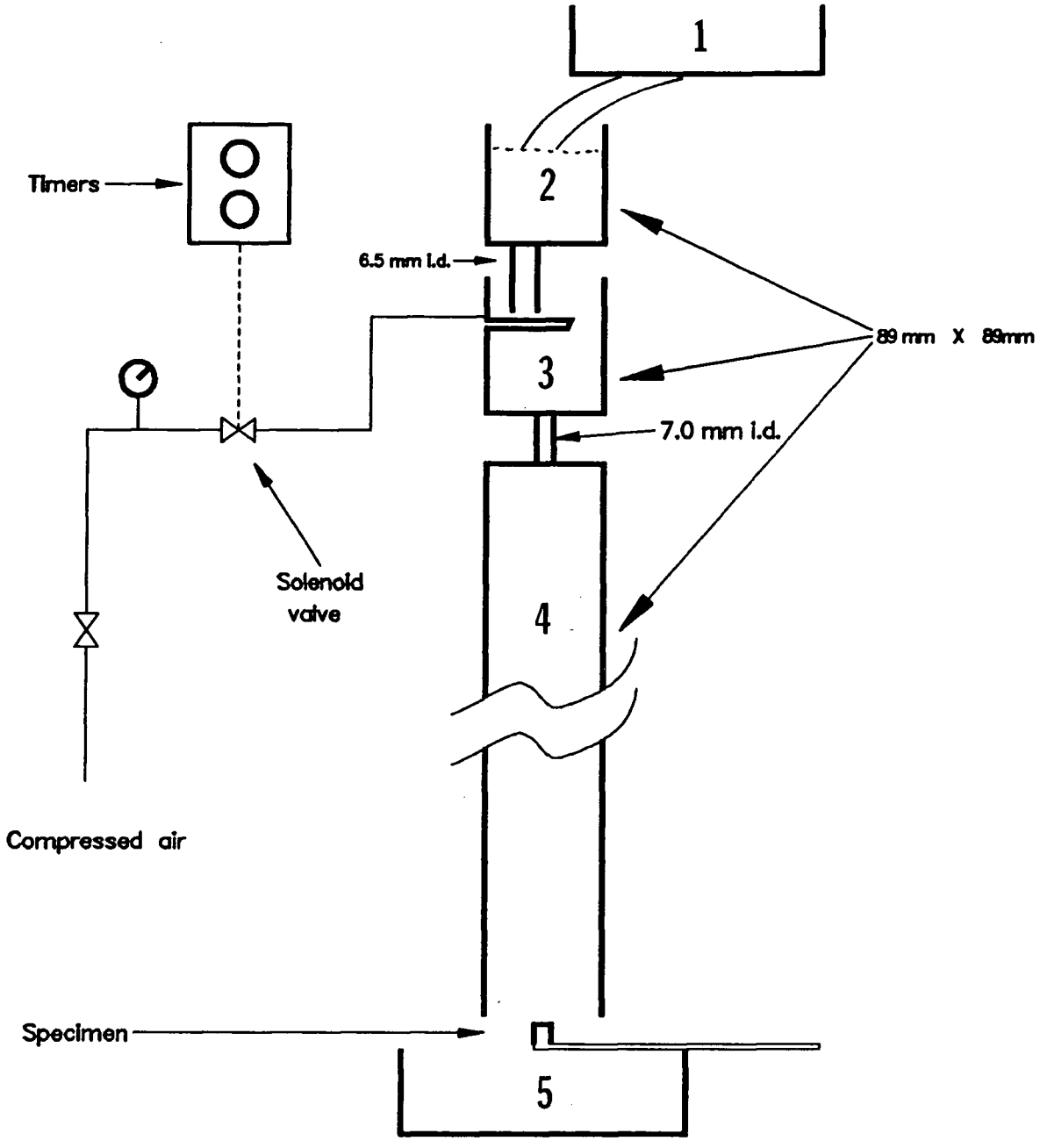

Figure 3.11 General set–up of the dropping apparatus

(1) Storage funnel, (2) Particle level control section
(3) Particle release section, (4) Dropping section
(5) Particle collecting bucket

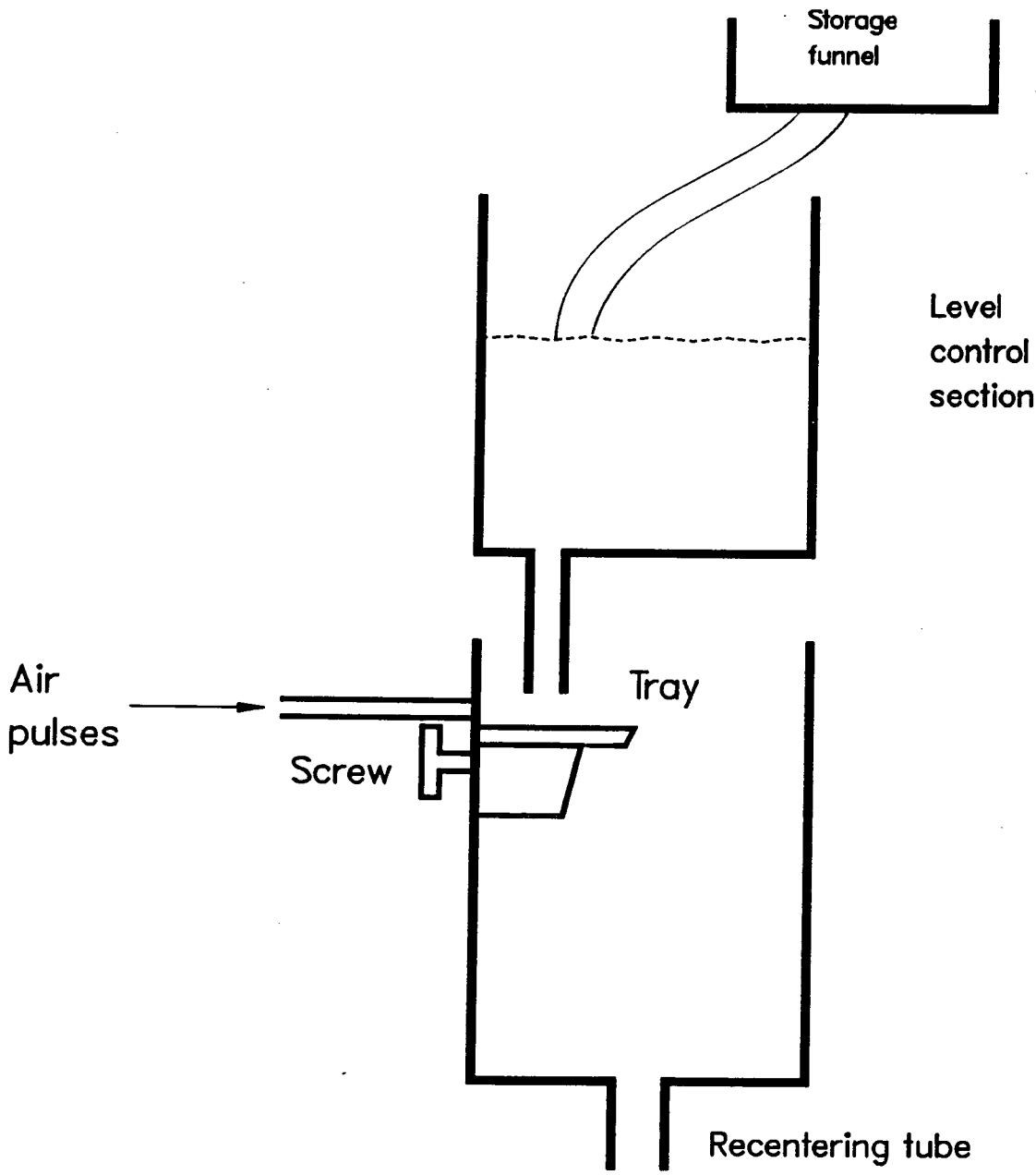

Figure 3.12 Upper section of the dropping apparatus

lengths. Five sections were available with lengths of 0.2 m, 0.3 m, 0.5 m and two of 1.0 m. Any of the sections could be removed or added to change the total dropping distance, thereby varying the particle impingement velocity.

The third and lowest part of the equipment included a support designed to hold the test specimens firmly in position. The specimens were in T shape with a thickness of 6 mm. The top surface of the T had a surface area of 7.0 mm by 14.5 mm, and was facing upward. The bottom leg of the T was clamped in the holder. The holder of the T piece could also be tilted to change the particle impingement angle. A bucket was placed under the holder to collect and recycle particles which had struck and been deflected by the specimen. When the T was tilted, the area with an upward-facing component (other than the top) was covered with masking tape and then uncovered before weighing so that the erosion measurements refer only to the top of the T.

In the experiments, the tray level and the time relays were first set. Then the particles were loaded into the storage funnel. The particles would flow down automatically to fill the level control section and onto the tray, where the particles stopped. The specimens were mounted on the holder at the bottom section and the bucket was placed underneath the holder. The timer power was then turned on, and the solenoid valve began to function. Each pulse of air when the solenoid opened caused the particles to be blown away from the tray. These particles then passed through the recentering funnel and dropped freely. The specimen was eroded for about 10 – 20 minutes and then was weighed to give the "initial" weight. The specimen was weighed again after certain time intervals to determine the erosion rate.

The impact velocity of particles was determined by photographing the dropping particle with a camera and a strobelight. The strobelight was set to flash for each 1/60 s interval

and the camera shutter speed was set at 1/15 s. Both the strobelight and the camera were placed at the same level. Particles were dropped at a higher position so that the distance between the plane of camera and strobelight and the position of particle releasing is the same as the dropping distance in the corresponding dropping distance in the tests. The distance between two consecutive images of the particles on the photos was then measured to determine the particle velocity.

3.8 Combustor for High Temperature Erosion Tests

High temperature experiments were carried out in the bottom section of a circulating fluidized bed combustor equipped with a riser column, a return standpipe and L-valve, two cyclones and a natural gas burner to heat up the combustor during start-up. Details on the pilot plant have been reported by Grace et al. (1987). The general set-up is shown in Figure 3.13. Only the bottom part of the riser column was used for our purpose. The combustor was operated as a conventional fluidized bed combustor at a superficial velocity of about 1.83 m/s. The high temperature was maintained by the natural gas burner, which could operate at 900 C and keep the bed temperature as high as 780 C. Air was supplied by the UBC Pulp and Paper Center building compressor and the air flow rate was monitored by a standard rotameter. Air was passed through the burner before entering the combustor. No coal or any other solid or liquid fuel was burned in the bed during the erosion tests in order to minimize the concentration of sulpher oxides and the influence of chemical reaction.

The refractory-lined riser column had a inside cross-section of 152 mm by 152 mm. The air distributor contained three tuyeres, each with six orifices inclined slightly downwards to the horizontal. Two ports at the center of two opposite walls, 400 mm above the distributor, were used to support a test tube through a pair of holders. The tube had an outside diameter

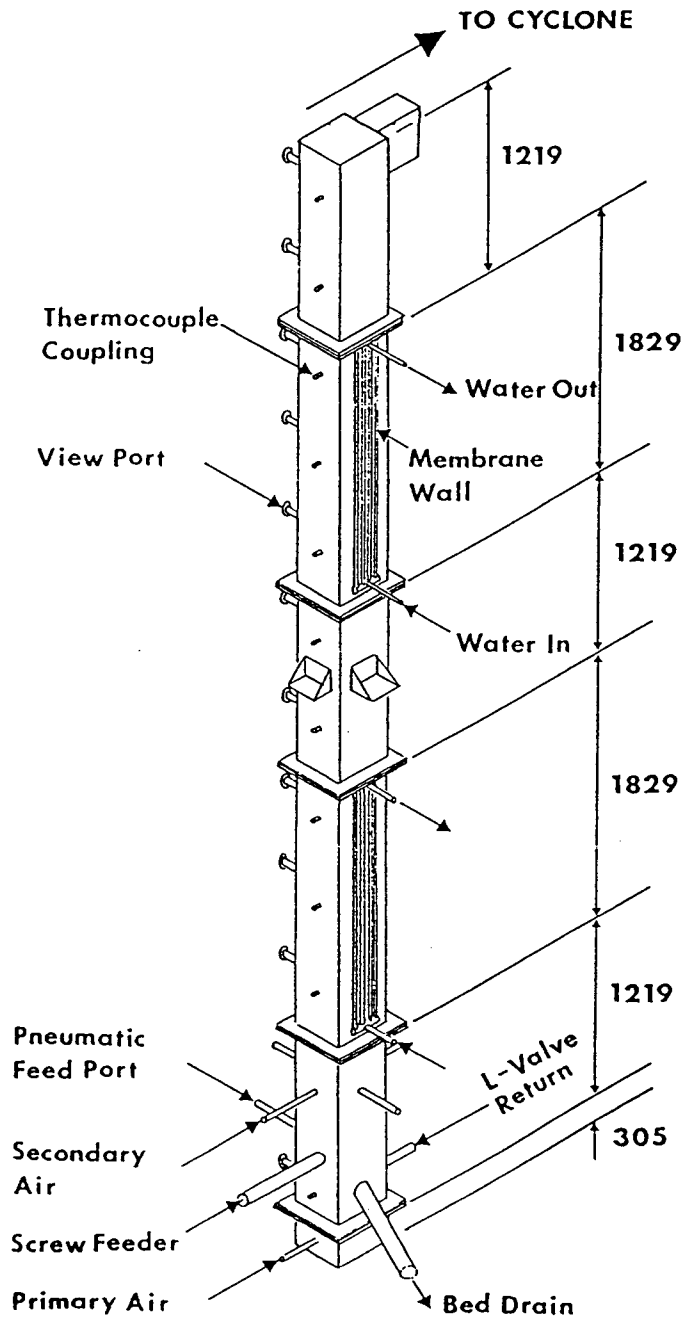

Figure 3.13 The combustor for high temperature erosion tests (all dimensions are in mm.)

(1) test tube, (2) other tubes, (3) hole in the bed wall

of 32.0 *mm* for half of its length and 28.6 *mm* for the other half (Figure 3.14). Rings of 28.6 *mm* i.d. and 32.0 *mm* o.d. were installed to make a smooth tube surface and allow erosion rates to be determined. The inside diameter was 12.7 *mm*. The arrangement of the supporting bar was similar to that in the cold model three-dimensional bed (see Section 4.3). Water or air could be passed through the tube to serve as the coolant. Thermocouples were installed in the burner chamber and in the dense bed to monitor the burner and bed temperature. Two more thermocouples were immersed inside the two ends of the tube to determine the cooling fluid inlet and outlet temperature. Another very thin thermocouple was installed just beneath the outer surface at the right side of the tube being eroded to monitor its surface temperature.

In each experiment, the bed was heated up by the burner to the desired temperature. Then the test tube was installed with the air and burner briefly turned off. Steady conditions were then re-established as quickly as possible with the tube in place and held for the requisite number of hours. The preheated fluidization air was then turned off and the tube was removed from the column as quickly as possible (within 5 minutes).

Erosion rates were calculated from the weight loss of the small rings mounted on the supporting tube, just as in the three-dimensional low temperature fluidized bed experiments. Details on the installation of the specimen rings are described in Section 4.3.

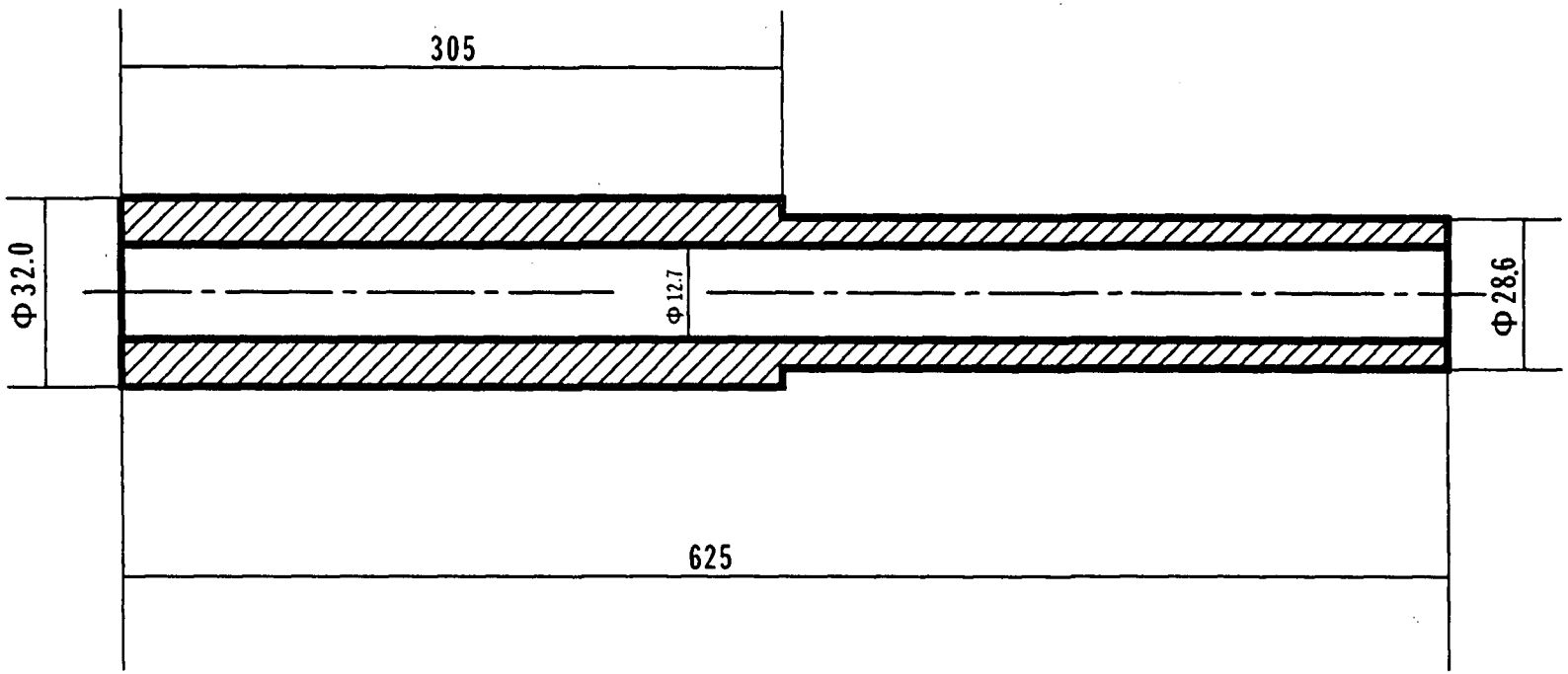

Figure 3.14 Supporting bar for the high temperature erosion test in the combustor (all dimensions are in mm.)

CHAPTER FOUR: TECHNIQUES OF MEASURING EROSION RATE

4.1 Overview of Methods Considered

Good techniques of data measurement are essential to any successful experimental study. In this study, the erosion rates were of the order of only a few micrometers per hundred hours of operation. Therefore, it was critical to have a very accurate and reliable measurement technique. A number of methods were investigated at the beginning, but measuring the weight loss of thin rings was found to be the most reliable, accurate and simple method of determining erosion rates.

The first method tried was a "coating technique". Plexiglass tubes were painted with different colour paints to form ten to twelve layers. In order to make thin and uniform layers, a very fine spray called "air brush" was used to apply the paint. A small DC motor controlled the turning speed of a bar on which the tube was mounted, and the painting time was exactly controlled in the coating process. The painted tubes were then put into the two-dimensional fluidized column to be eroded, and the amount of erosion could then be estimated from the color change of the tube surface. The coating technique was also used in the three-dimensional column to demonstrate the axial and lateral erosion distribution.

Tests showed that the coating method gave satisfactory semi-quantitative results and clear trends. For example, Figure 4.1 shows the erosion rate distribution along the circumference of a 32 mm tube after 40 h in a bed of 1.0 mm sand at $u = 1.2\ m/s$. The results agree quite well with the quantitative results presented later in Chapter 7.

Although paint coating provides excellent direct observations of the erosion rate distribution, the method cannot be used as a quantitative method because: (1) It is impossible to count less than one layer of the coating; (2) the coating shields the base material so that

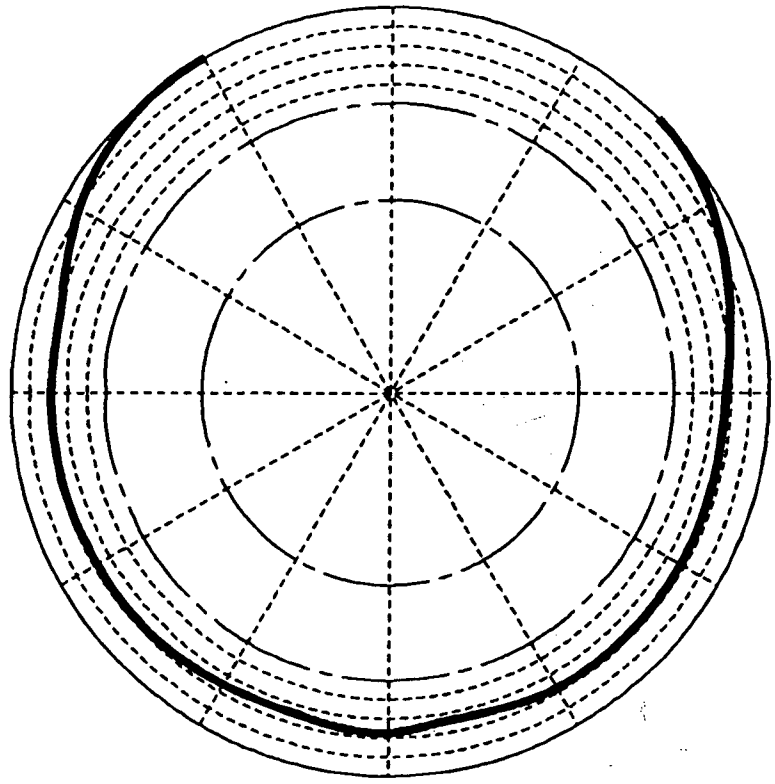

Figure 4.1 Erosion rate along the tube circumference of a plexiglass tube with paint coating (from preliminary experiment performed in the two–dimensional column)

Conditions: air superficial velocity: 1.2 m/s
particles: 1.0 mm silica sand
Operating duration: 40 hours
Tube diameter: 32 mm

(The figure is not to scale; one division represents a layer of paint, about 4.0 μm thick)

the measured erosion rate is not that of the base material.

The second technique tried was the "Talysurf", an instrument which measures surface texture (Figure 4.2). The Talysurf was in Department of Mechanical Engineering at UBC (TALYSURF Model 4). A flat specimen is first mounted on a small horizontal table, and a very fine needle probe is placed on the top of the specimen. As the probe travels over the specimen along a straight line, the up and down movement of the needle probe is transmitted and recorded on a chart in order to show the surface profile of the specimen along that particular path (Figure 4.3). For the erosion test, the surface of a tube section was first "recorded" by the Talysurf. The two ends of the tube section were then protected by tape while the tube was eroded in the fluidized bed. When the test was finished and the pieces of tape were removed, the same section was "traversed" again. By comparing the two charts, the eroded depth along that straight line could be found in principle. However, the method was found to be impractical for two reasons:

(1) Since tubes were round and did not have a flat bottom, it was very difficult to remount them in the Talysurf exactly in the same position before and after the erosion tests. They were often inclined or not parallel to the probe movement. The errors caused by this were of the order of 30 μm, although a good Talysurf may have an accuracy of 1 μm.

(2) The probe was very thin, and it was almost impossible to place it on the same straight line after the specimen was remounted.

A third method investigated involved coating a thin layer of platinum on glass, a technique being used in our laboratory for studying local heat transfer in circulating fluidized beds (Wu 1988). The coated section is placed inside the fluidized bed as part of the tube. It was reasoned that the electrical resistance of the platinum layer would change as the layer

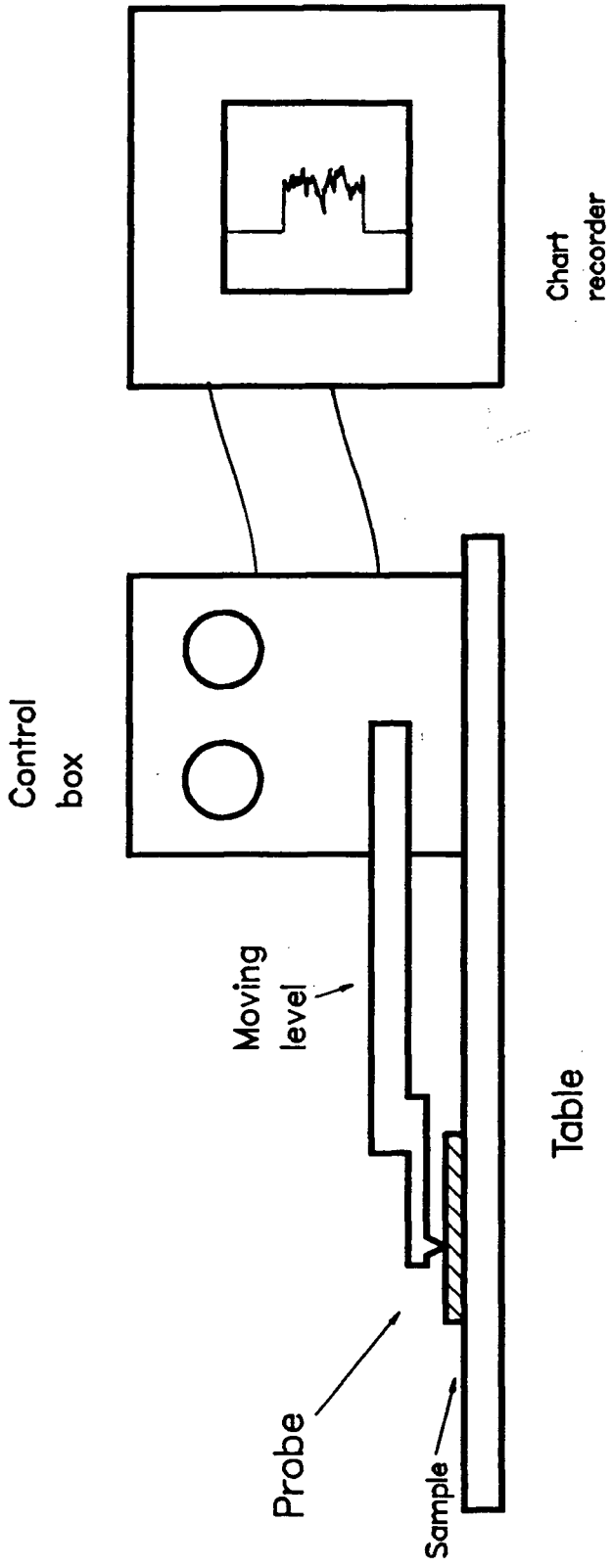

Figure 4.2 Schemetic of Talysurf 4

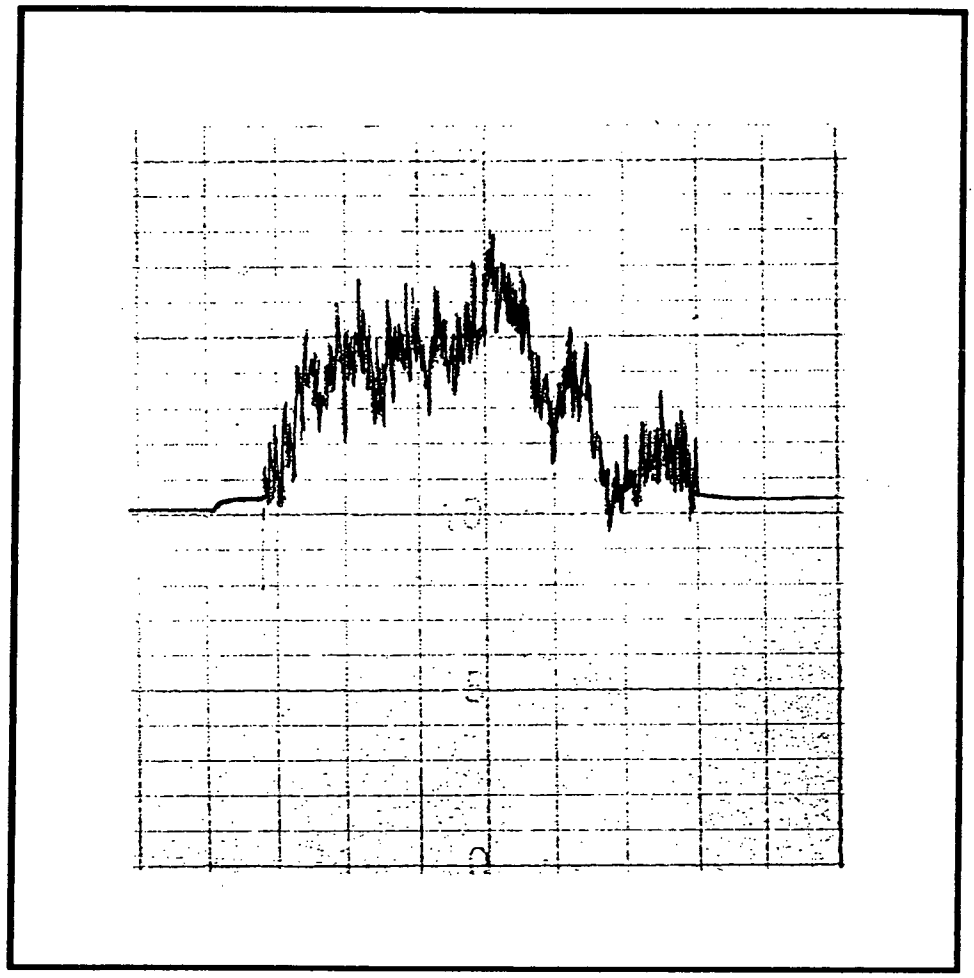

Figure 4.3 Typical surface texture profile recorded by Talysurf

Conditions: air superficial velocity: 0.88 m/s
particles: 1.0 mm silica sand
Operating duration: 5 hours
Tube diameter: 32 mm

was eroded thinner, allowing the layer thickness, and hence the erosion rate, to be measured in situ and continuously by electrical resistance monitoring. However, tests showed that coating layers were very easily cut through totally so that the resistance increased precipitously rather than gradually.

Two techniques of determining particle impacts were considered but not pursued. The first (Rubin et al. 1985) was an acoustic method which measures the sound level caused by the impact of solid particles and correlates the number of impacts and their intensity with erosion rate. The other (Jin 1986) was to use a ceraminator, a transducer which would convert the solid particle impact pressure to an electrical signal. Both of these techniques would require development and calibration, relying on another quantitative measurement technique.

4.2 Weighing Method and Accuracy of Data

The weighing method was very simple. Small sections of tubes (rings), 3.18 *mm* wide and only 1.59 *mm* thick, were mounted in a supporting bar and put into the low temperature and high temperature fluidized beds. The rings were carefully weighed before and after the erosion tests. The weight loss was simply the difference between the two measurements and could be converted to total volume loss by dividing the material density.

The balance (SARTORIOUS Model 1207 MP2A) was a digital balance with an accuracy of 0.05 *mg*. To minimize disturbances, the balance was located on a special heavily loaded table to reduce vibration, and was enclosed in a box to prevent air currents. Two special stainless steel rings were always kept separately and used as standard weights to calibrate the balance every time it was used. These special efforts allowed the balance to reach its maximum available accuracy and helped to give good reproducibility.

To avoid oxidation and dust on their surfaces, the sample rings were removed from the supporting bar immediately after being eroded. They were then wiped clean using very fine tissue paper (KIMWIPES) and put into a desiccator. Weighing was carried out as soon as possible thereafter. The experiments were designed to last long enough to produce a weight loss of at least two significant figures to assure accuracy. Each sample was measured twice, and if the difference of the two measurements did not fall within 0.05 mg of each other, the measurement was repeated until agreement to within this range was attained in successive determinations. Reweighing was required in less than 5% of the cases. The results were then put into a computer program which compared the new weights with the previous weights and calculated the erosion rates of the rings.

The erosion rate utilized here is the volume loss per unit surface area per unit time, or equivalently the eroded depth per unit time in $\mu m^3/\mu m^2 100h$ or $\mu m/100h$.

For the dropping tests described in Section 3.7, the same equipment and procedures were employed to determine the erosion rate of the T shape specimens.

4.3 Mounting of Specimens

For all tests in the low temperature three-dimensional fluidized bed, materials tested were made into small rings which were mounted on a supporting bar which sat in collars on the column walls. The supporting bar for a tube outside diameter of 32.0 mm is shown in Figure 4.4. It was 0.264 m long and 25.4 mm in diameter with the exception of a 0.050 m section at one end having a diameter of 32.0 mm. There was a 9 mm (3/8″) diameter screw hole at the other end of the bar on which a 0.050 m long bar, 32.0 mm in diameter, could be attached. Rings (Figure 4.5) of different materials were 3.18 mm wide sections of a tube of outside diameter 32.0 mm and inside diameter 28.6 mm, with initial mass ranging

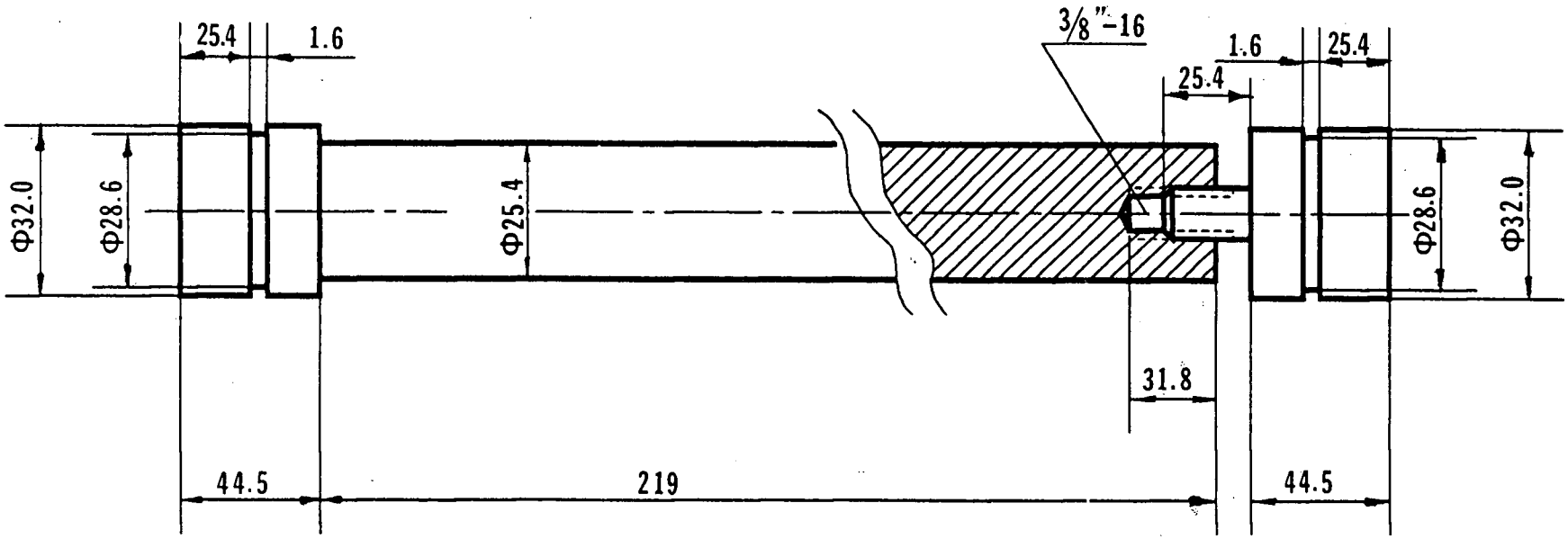

Figure 4.4 Supporting bar for room temperature three-dimensional fluidization column (all dimensions are mm.)

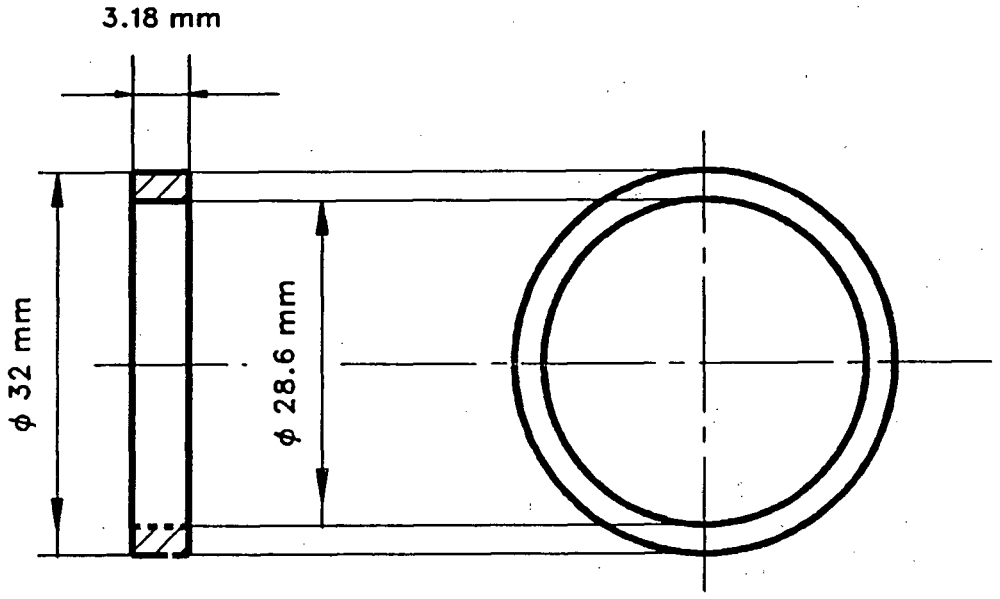

Figure 4.5 Specimen rings

from 1.0 – 4.0 g. Another tube with the same outside diameter but inside diameter of 25.4 *mm* was also made and cut into many small sections with length of 3.18, 6.35, 25.4 and 50.8 *mm*. These sections functioned as spacers to separate sample rings and to keep them in the desired position. After the spacers and rings were all put into position, the screw end of the supporting bar was mounted and tightened in such a way that the outside surface of all rings and spacers formed a smooth single bar (Figure 4.6). The clamping was such that the rings could not rotate during the tests. The rings were marked so that the same point could always be positioned at the bottom for successive mountings. For tests of tubes of smaller outside diameters, supporting bars and sample rings of smaller diameters were made and arranged in the same way.

In order to measure local erosion rates around the circumference, some of the 32.0 *mm* sample rings were cut into 18 – 20 segments. Two coupling tube sections were specially designed to hold these small segments in the same way as if they had been complete rings. The inside and outside dimensions of the coupling sections were the same as the spacers, but the middle of the sections were connected by screws as shown in Figure 4.7. One slot having the same dimension as the rings was machined in each section just beside the screw so that the ring segments could be inserted into the slot and held there by tightening the screws. The masses of the small segments ranged from 0.07 – 0.25 grams. Segments were weighed before and after erosion in the bed in order to determine the circumferential erosion rate distribution.

For the high temperature erosion test, a tube with inside diameter 12.7 *mm* was used as the supporting bar. Part of the tube had an outside diameter of 32.0 *mm*, and the other part 28.6 *mm*. The rings were the same as in the three-dimensional bed, but the spacers had a bigger inside diameter, 28.6 *mm*. The arrangement resembled that in the three-dimensional

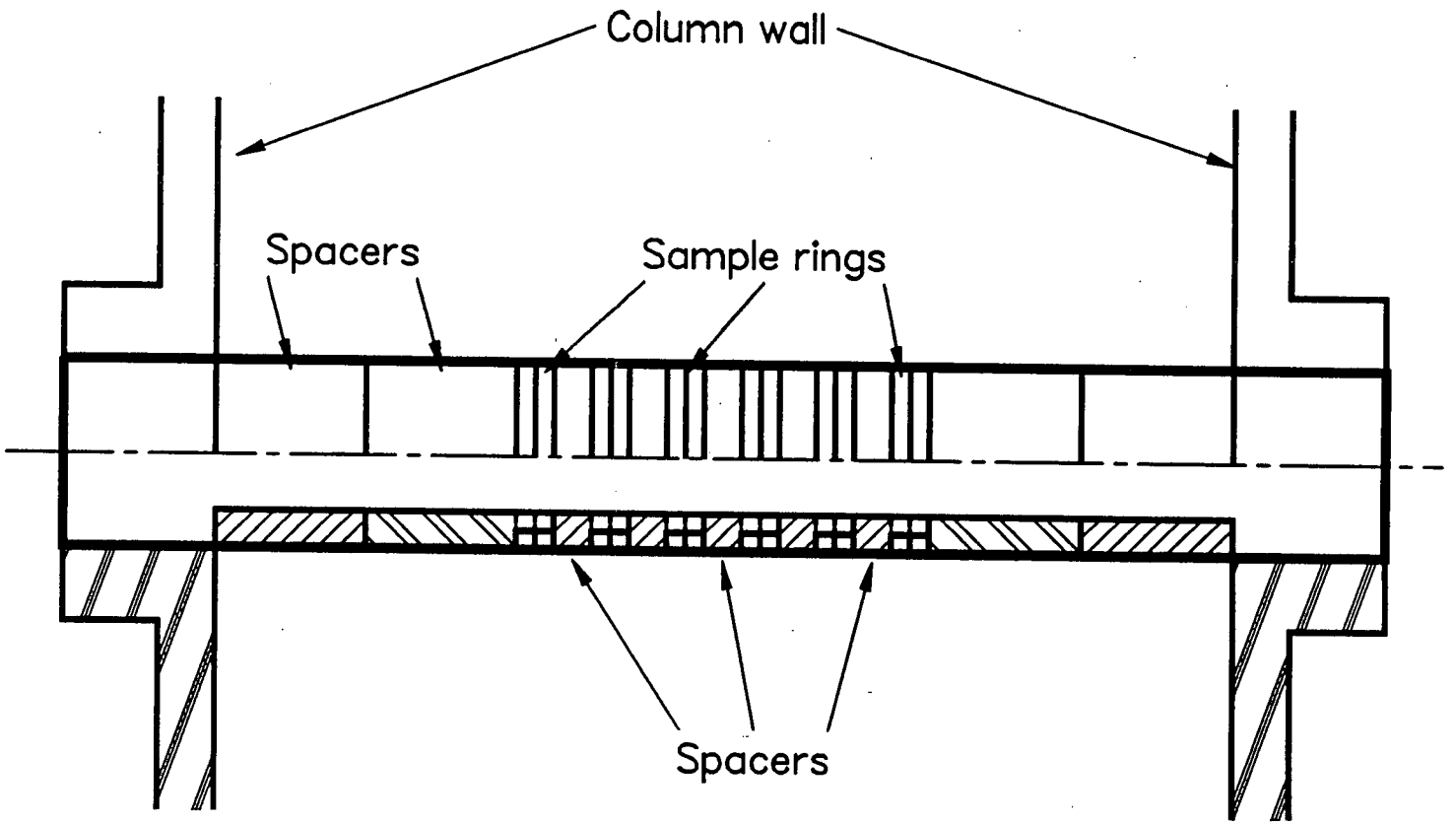

Figure 4.6 Supporting bar and ring assembly for room temperature erosion tests in the three-dimensional fluidization column

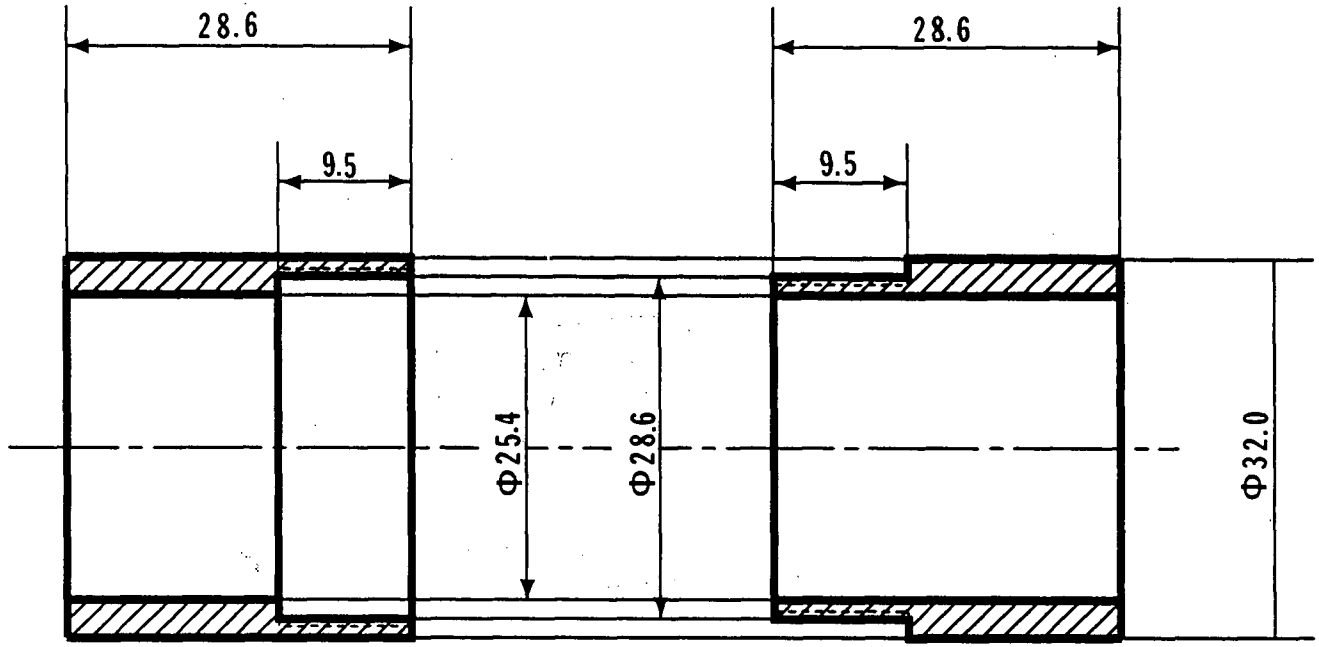

Figure 4.7 Coupling holders for local (segmental) erosion test at room temperature in the three-dimensional fluidization column

low temperature fluidized bed, with a 32.0 *mm* end section screwed on at the other end to secure the rings and spacers.

4.4 Incubation Period

The incubation of fresh rings of the five materials for base conditions were tested before erosion tests were undertaken. The details of these tests are given in Section 7.6. Experimental results showed that the incubation periods for all rings were less than 10 *h* under the base operating conditions. All fresh rings were therefore eroded for at least 20 *h* under the base operating conditions before any measurement for weight loss was made to avoid the incubation effect.

4.5 Statistical Considerations

In Section 4.2, the accuracy of the weighing technique is discussed. In this section we consider the accuracy and reproducibility of the experimental results. Seven experiments were carried out with the base conditions (see Section 3.1) to test the reproducibility. This gave more than 20 data points for each of five materials tested. The results are plotted in Figures 4.8 and 4.9, which show results of 20 hour runs and results of runs longer than 60 hours, respectively. Standard deviations were calculated based on these data. The results for the five materials are summarized in Table 4.1. The maximum error range of erosion rate which could be caused by the error of weighing is also listed in Table 4.1. The data show that the reproducibility is much better and the confidence intervals much smaller for runs of 60 hours or more. However, fluctuations do exist and are much larger than those likely to be caused by errors in weight measurement. To avoid congestion, error bars have not been plotted on later figures. However, all subsequent data are based on tests of duration close to 60 *h* or more, and the error are similar to those indicated in Figure 4.9.

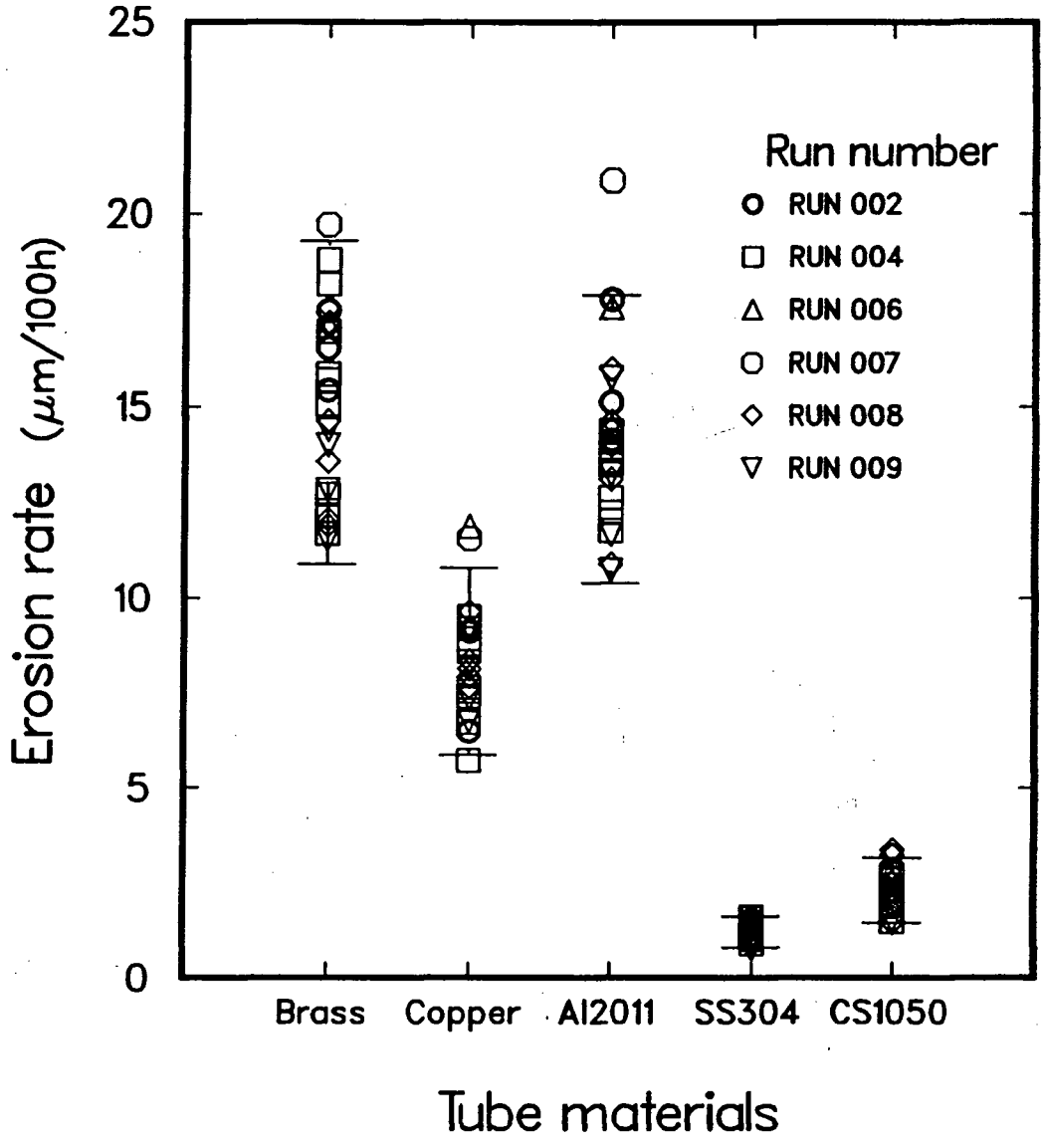

Figure 4.8 Erosion rates of different materials for 1.0 mm silica sand at superficial velocity of 1.87 m/s, for approximately 20 hours (The bars show the 90% confidence interval for the data.)

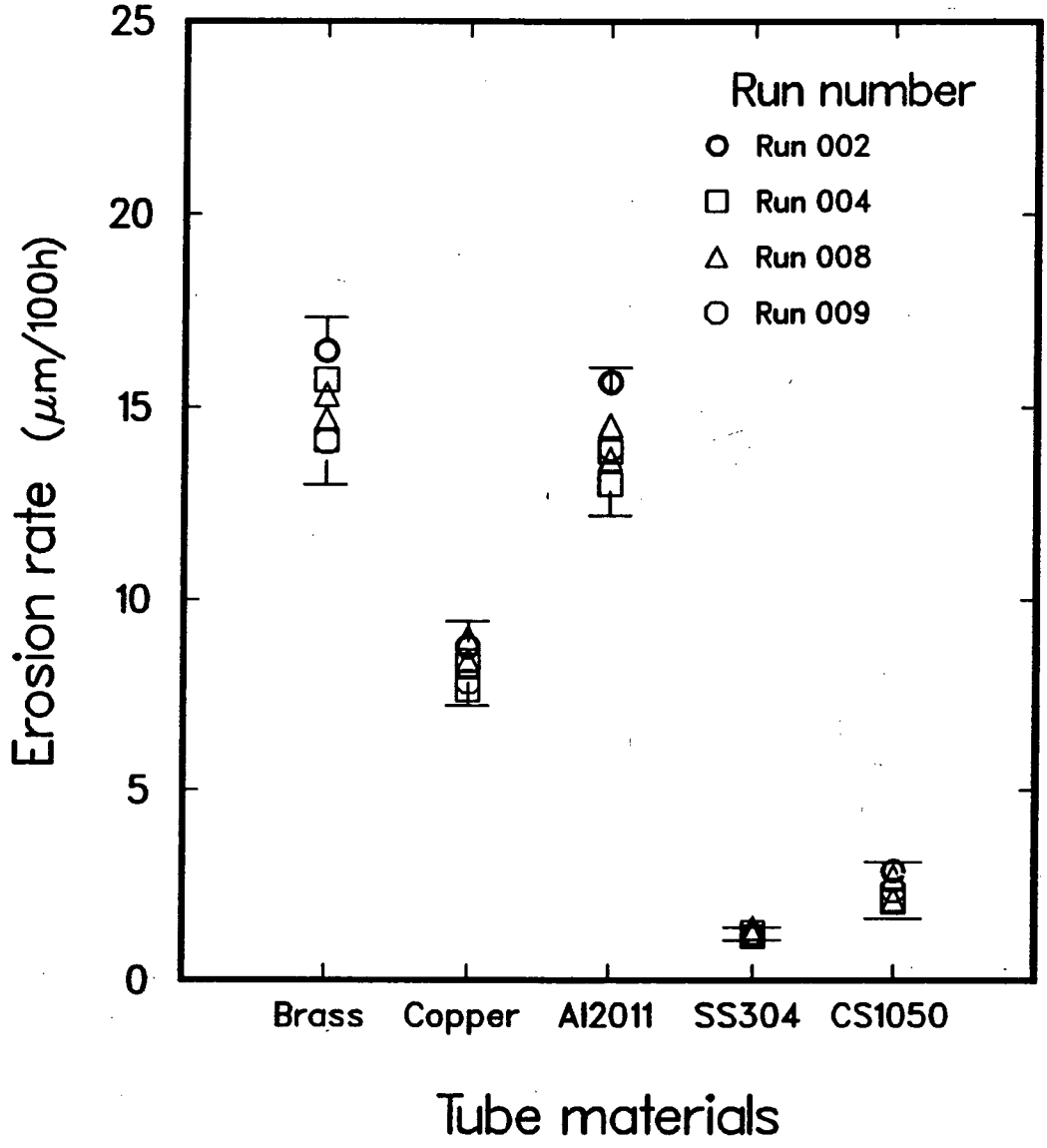

Figure 4.9 Erosion rates of different materials for 1.0 mm silica sand at superficial velocity of 1.87 m/s, for approximately 60 hours (The bars show the 90% confidence interval for the data.)

Table 4.1: (Part I) Deviation of experimental results from the low temperature three-dimensional fluidized bed tests

Conditions: Superficial velocity: 1.88 m/s
Bed material: 1.0 mm silica sand

Data source	Operating hours	Erosion rate (μm/100h) of				
		Brass	Copper	Al2011-T3	SS304	CS1050
Run002	20.0	15.43	6.49	15.12	1.03	2.02
Run002	20.0	16.52	9.11	14.13	1.46	2.67
Run002	20.0	17.48	6.49	17.78	1.06	2.87
Run004	20.0	12.71	8.72	13.58	0.90	2.19
Run004	20.0	16.95	6.73	13.92	1.03	1.98
Run004	20.0	15.06	7.41	13.49	1.30	2.12
Run004	20.0	15.70	5.72	11.78	1.12	1.49
Run004	20.0	18.17	9.51	12.24	1.43	2.45
Run004	20.0	15.85	7.54	14.38	1.31	2.22
Run004	20.0	12.28	8.92	13.85	1.18	1.89
Run004	20.0	11.69	8.70	14.08	1.32	2.25
Run004	20.0	12.18	7.64	12.62	0.90	1.75
Run004	20.0	18.79	8.59	14.32	1.58	2.31
Run006	15.0	17.09	11.88	17.57	1.31	2.58
Run007	20.0	19.71	11.56	20.86	1.47	2.86
Run008	16.0	13.56	9.65	14.61	1.13	1.45
Run008	16.0	17.07	8.34	14.45	1.61	2.79
Run008	16.0	17.18	8.12	10.90	1.35	2.80
Run008	16.0	14.62	7.92	14.40	1.12	2.23
Run008	16.0	17.56	9.23	13.11	1.52	3.37
Run008	16.0	12.05	7.65	13.99	1.13	3.24
Run008	15.0	11.89	9.12	15.98	0.95	1.98
Run009	16.0	12.83	8.17	15.76	1.60	2.28
Run009	44.0	11.54	6.76	13.25	0.98	1.52
Run009	16.0	14.39	9.20	11.67	0.76	2.70
Run009	44.0	14.00	7.35	10.74	1.24	2.26
Mean erosion rate		15.09	8.33	14.18	1.22	2.32
Standard deviation		2.45	1.44	2.19	0.24	0.50
Maximum error due to balance		0.19	0.18	0.60	0.22	0.20

Table 4.1: (Part II) The deviation of experimental results from the low temperature three-dimensional fluidized bed tests

Conditions: Superficial velocity: 1.88 m/s
Bed material: 1.0 mm silica sand

Data source	Operating hours	Erosion rate (μm/100h) of				
		Brass	Copper	Al2011-T3	SS304	CS1050
Run002	60.0	16.46	8.75	15.65	1.18	2.87
Run004	100.0	15.71	7.62	13.00	1.15	2.05
Run004	100.0	14.15	8.28	13.85	1.26	2.08
Run008	80.0	15.32	9.00	14.53	1.37	2.12
Run008	80.0	14.69	8.40	13.65	1.22	2.73
Run009	60.0	14.11	7.84	13.92	1.15	2.38
Mean erosion rate		15.15	8.32	14.10	1.22	2.37
Standard deviation		1.02	0.52	0.90	0.08	0.35
Maximum error due to balance		0.06	0.06	0.20	0.07	0.07

There were several factors which might cause the deviations: (1) The gas superficial velocity tends to cycle somewhat due to pressure fluctuations of the blower. (2) Particle size and sphericity might change due to attrition and elutriation. (3) Temperature and humidity could not be held constant. While these factors may have played a role, the fact that two rings of exactly the same material mounted side by side could have very different erosion rates after the same period of exposure indicates that there must be natural variations due to spatial variations in the fluidized bed. Results of a 100 hour run are tabulated in Table 4.2 showing the erosion rates for each 20 hour time interval where ten rings of five different materials were eroded at the same time. The natural fluctuations can be seen to be much larger than the errors caused by the weight measurements.

Table 4.2: Erosion rate for a 100 hour run in the cold model three-dimensional fluidized bed column

Operating conditions:
Gas superficial velocity: 1.86 m/s
Particles: 1.0 mm Silica sand
Tube outer diameter: 32.0 mm

Erosion Rate* (μm/100h)

	Operating duration (hours)				
Tube materials	20.00	40.00	60.00	80.00	100.00
SS304	0.90	1.03	1.30	1.12	1.43
SS304	1.31	1.18	1.32	0.90	1.58
CS1018	2.19	1.98	2.12	1.49	2.45
CS1018	2.22	1.89	2.25	1.75	2.31
Brass	12.71	16.94	15.05	15.70	18.16
Brass	15.84	12.27	11.69	12.18	18.78
Copper	8.71	6.73	7.41	5.72	9.51
Copper	7.54	8.92	8.70	7.64	8.59
Al2011	13.58	13.91	13.48	11.78	12.24
Al2011	14.38	13.85	14.07	12.61	14.32

* Erosion rate for the last 20 hours measured at the time shown here

CHAPTER FIVE: RESULTS AND DISCUSSION: CONTROLLED DROPPING EXPERIMENTS

The dropping experiments were performed for the purpose of conducting pure erosion tests under controlled conditions. Particles of different properties were dropped freely from various heights onto small specimens of different materials. In the tests, one parameter was varied at a time in order to give a clear picture of the effects of different variables. The conditions of the tests are tabulated in Table 5.1. The experimental set-up was described in Section 3.7.

Before discussing the results, the definitions of low and high impact velocity erosion need to be clarified. Low velocity solid impact erosion here refers to erosion with impact velocities of 0 - 6 m/s, while high velocity solid impact erosion refers to erosion with impact velocities of 30 m/s and above. All tests in this work were for low velocity erosion, since only the lower velocities are of importance for tubes in conventional fluidized beds, providing that good design practice is followed in keeping tubes well away from impinging grid jets.

5.1 Effect of Particle Velocity

The erosion rates of brass at different particle impacting velocities are summarized in Table 5.2 and plotted in Figure 5.1. The particles were silica sand with a mean diameter of 1.0 mm. The particle mass flow rate was held constant at 5.7 kg/m^2s. Figure 5.1 shows clearly that the erosion rate increased rapidly as the particle impact velocity increased. The erosion rate can be fitted with a relationship of the form:

$$E = k_1 V_p^{m_1} \qquad (r = 0.994) \tag{5.1}$$

where E is the erosion rate, V_p is the particle velocity and k_1 and m_1 are constants. It was

Table 5.1: Operating conditions for dropping tests

	M (kg/m^{2}s)	V_p (m/s)	d_p (mm)	Hp (kg/mm^2)	Φ_s	Y_m GPa	H_m (kg/mm^2)	Θ (degree)
Run 1	5.7	5.0	1.00	350.	0.84	97.	155	90
Run 2	5.7	5.0	1.00	350.	0.91	97.	155	90
Run 3	4.4	5.0	1.00	350.	0.91	97.	155	90
Run 4	3.8	5.0	1.00	350.	0.91	97.	155	90
Run 5	2.4	5.0	1.00	350.	0.91	97.	155	90
Run 6	5.7	4.1	1.00	350.	0.91	97.	155	90
Run 7	5.7	3.3	1 00	350.	0.91	97.	155	90
Run 8	5.7	2.2	1.00	350.	0.91	97.	155	90
Run 9	5.7	5.0	1.51	350.	0.86	97.	155	90
Run 10	5.7	5.0	1.31	350.	0.86	97.	155	90
Run 11	5.7	5.0	0.93	40.	0.86	97.	155	90
Run 12	5.7	5.0	1.08	590.	0.86	97.	155	90
Run 13	5.7	5.0	0.89	340.	1.00	97.	155	90
Run 14	5.7	5.0	1.00	350.	0.91	97.	155	68
Run 15	5.7	5.0	1.00	350.	0.91	97.	155	45
Run 16	5.7	5.0	1.00	350.	0.91	97.	155	23
Run 17	5.7	5.0	1.00	350.	0.91	70.	132	90
Run 18	5.7	5.0	1.00	350.	0.91	115.	98	90
Run 19	5.7	5.0	1.00	350.	0.91	190.	327	90
Run 20	5.7	5.0	1.00	350.	0.91	210.	220	90

where:

M - Particle mass flow rate

V_p - Particle impact velocity

d_p - Particle mean diameter

Hp - Particle hardness

Φ_s - Particle sphericity

Y_m - Target material Young's modulus

H_m - Target material hardness

Θ - Angle of impingement

Table 5.2: Influence of particle impact velocity on erosion of brass specimen by 1.0 mm silica sand particles

Particle velocity (m/s)	Average erosion rate (experimental) (μm/100h)	Erosion rate (calculated by equation 5.1) (μm/100h)	Deviation (%)
5.0	238	242	1.1 %
4.1	138	149	7.9 %
3.3	105	92.4	-12.0 %
2.2	35	36.6	4.9 %

Other operating conditions:

Particle mass flow rate: 5.7 kg/m^2s

Particle impingement angle: 90°

Particles: 1.0 mm silica sand (Φ_s=0.91)

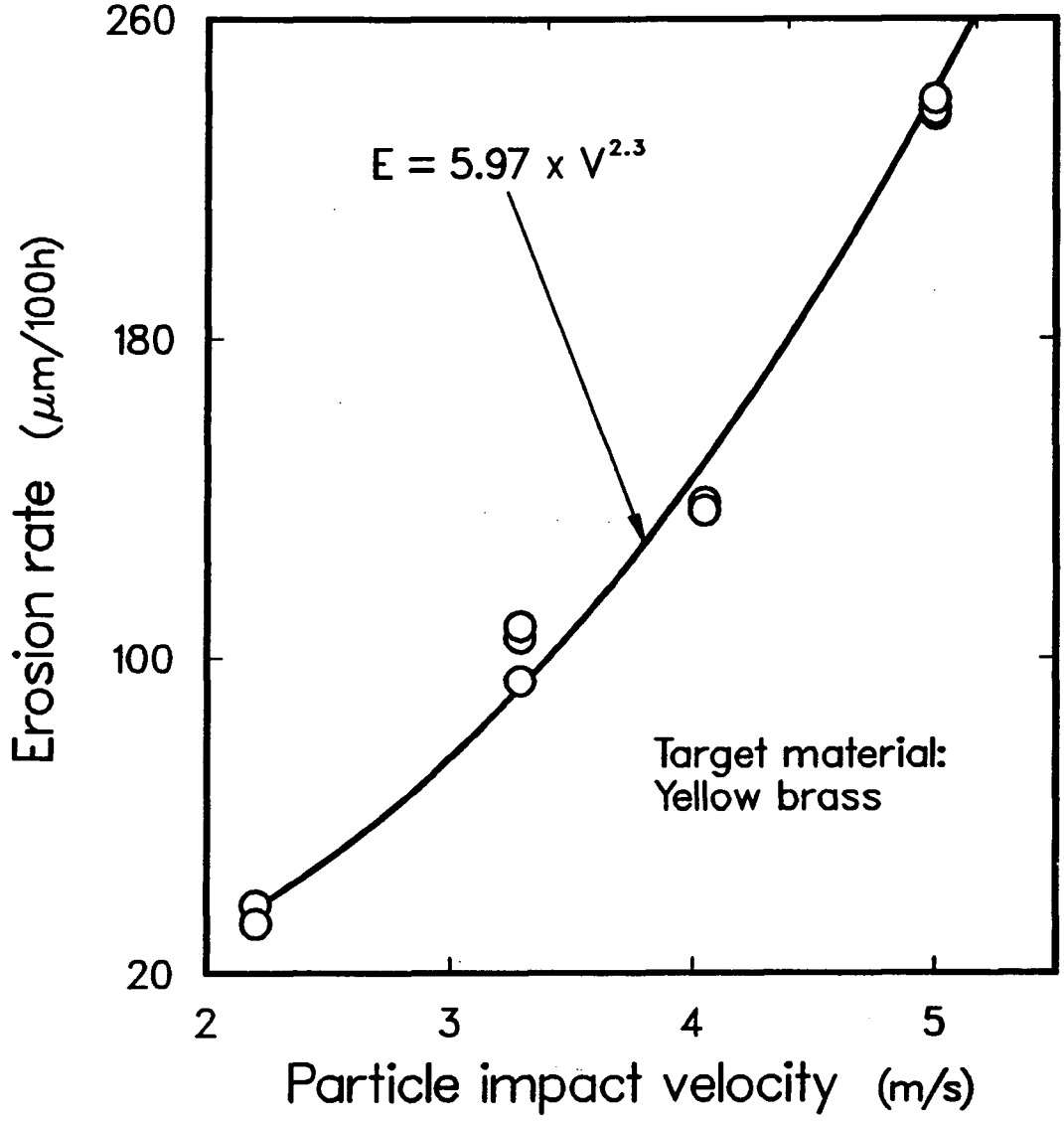

Figure 5.1 Erosion rate vs. particle impact velocity, for 1.0 mm silica sand (φ_s=0.91) with particle mass flow rate of 5.7 kg/m^{2}s at 90° impingement angle.

found by the least squares method that $m_1 = 2.3$ and $k_1 = 5.97$ $(\mu m/100h)/(m/s)^{2.3}$. The fitting results are also shown in Figure 5.1 and Table 5.2.

For high velocity solid impact erosion, as summarized in Section 2.3, erosion rate can be fitted by the same exponential relationship as in equation 5.1. In that case, extensive experimentation indicates that the exponent is between 2.0 and 3.0 (e. g. see Finnie 1979, Schmitt 1980, Tilly 1979, Hutchings 1987). Most of the reported values for the exponent fall between 2.0 - 2.5 (Tilly 1979). The best-fit value in the present experiments of 2.3 falls within the above range, although all tests were conducted at much lower solid impact velocities. This suggests that certain similarities may exist between low and high velocity erosion.

No threshold velocity appears to exist in this experiment below which no erosion occurred. For high velocity solid impact erosion, existence of a threshold velocity has been reported by a number of researchers (see Section 2.3). The suggested threshold velocity is of the order 1.0 – 10 m/s, within the range covered by our experiments. However, the erosion rate for high velocity erosion is of the order 1.0 mm/h (i.e. 10^5 $\mu m/100h$) or more, while the erosion rate in our experiments was only of the order 100 $\mu m/100h$, at least three orders of magnitude smaller. The impact velocity in our experiments may therefore be well below the threshold velocity defined by other researchers, but yet produces erosion which can be measured with a sensitive measurement technique. It is also possible that there is some threshold velocity smaller than the range tested.

5.2 Effect of Particle Mass Flow Rate

The particle mass flow rate was changed from 2.4 kg/m^2s to 5.7 kg/m^2s while all other parameters were kept constant, i.e., particle impact velocity of 5.0 m/s, silica sand of di-

ameter 1.0 mm and brass as the test material. Table 5.3 summarizes the results, which are also plotted in Figure 5.2. A linear relationship was found between the erosion rate and particle mass flow rate, i.e.:

$$E = k_2 M \qquad (r = 0.997) \tag{5.2}$$

where M is the particle mass flow rate and k_2 is a constant, $40.1(\mu m/100h)/(kg/m^2 s)$. It seems reasonable that the erosion rate should be proportional to the particle mass flow, so long as the particles do not interfere with each other. This was the case in this test: Taking the highest mass flow rate, 5.7 kg/m^2s and 1.0 mm particles as an example, the total number of particles dropped per unit target surface area is:

$$\frac{5.7 kg/m^2 s}{2580 kg/m^3 \ (0.001^3 \pi/6) m^3} = 4.2 \times 10^6 \ particles/m^2 s \tag{5.3}$$

The number of particles dropped onto a single particle area therefore is:

$$4.2 \times 10^6 \times 0.001^2 = 4.2 \ particles/s \tag{5.4}$$

while the particle velocity is 5.0 m/s. The vertical space occcupied by the particles is only 0.084% of the available space. Therefore the probability of particle collision is extremely low. Observations indicated that most of the particles which bounce are diverted to the side. A simple statistical estimate shows that the probability of collision between a rebounding particle and falling particles is less than 0.5% (see Appendix A). This explains why there is a linear relationship between erosion and particle mass flow rate. In dense fluidized beds, where the particles are much closer together, this result is different as discussed in Chapter 7.

Table 5.3: Influence of particle mass flow rate on erosion of brass specimen by 1.0 mm silica sand particles

Particle mass flow rate (kg/m^2s)	Average erosion rate (experimental) (μm/100h)	Erosion rate (calculated by equation 5.2) (μm/100h)	Deviation (%)
2.4	94	95.1	1.1 %
3.8	151	153	1.3 %
4.4	172	175	1.7 %
5.7	238	227	-4.6 %

Other operating conditions:

Particle impact velocity: 5.0 m/s

Particle impingement angle: 90°

Particles: 1.0 mm silica sand (Φ_s=0.91)

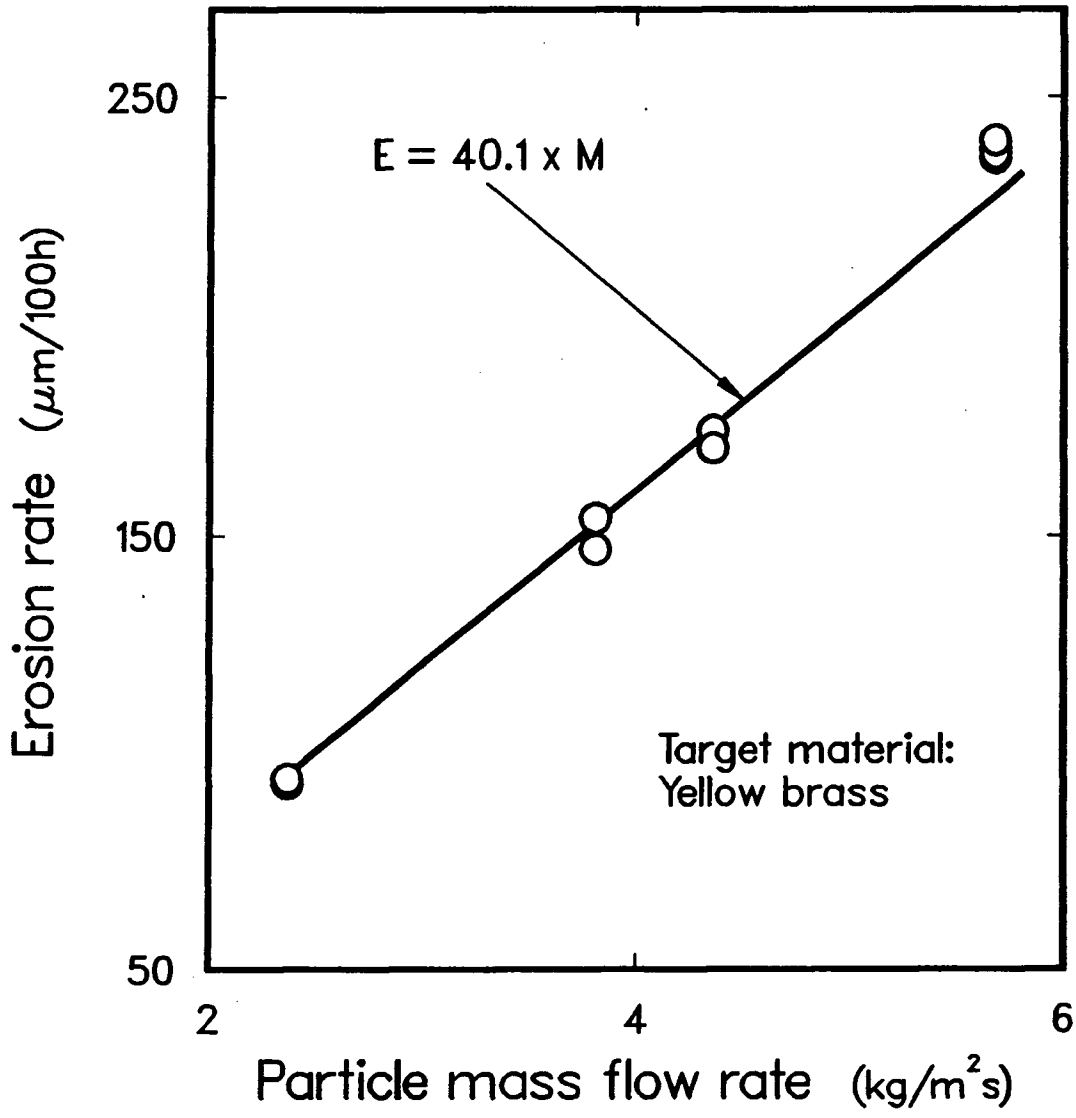

Figure 5.2 Erosion rate vs. particle mass flow rate, for 1.0 mm silica sand (φ_s=0.91) with impact velocity of 5.0 m/s at 90° impingement angle

5.3 Effect of Impingement Angle

In this test, the particles were again silica sand of 1.0 mm and the material was still brass. The particle impact velocity and mass flow rate were kept at 5.0 m/s and 5.7 kg/m^2s, respectively. The impingement angle (angle between particle impact stream and the specimen surface, Figure 5.3) was changed from normal (90°) to a shallow impact angle (22.5°).

In high velocity solid impact erosion, particles impact on the target material individually. For angular tests in those cases (e.g. Tilly 1979), it is generally the number of particles striking the surface that has been kept constant. Therefore the total particle mass flow rate is the same regardless of the angle of impingement. However, in our experiment, it is the particle mass flow density (particle flux) that was kept constant for all tests. The mass flow rate striking the surface is less for lower angles than that for the normal (90°) impact tests because of the reduction in area projected in a horizontal plane. Equation 5.2 was used to correct the experimental data to that which would be expected if the mass flow rate was the same as for the normal impact test. The results are then tabulated and plotted in Table 5.4 and Figure 5.4.

Figure 5.4 shows clearly that erosion rate increases as the impingement angle is reduced, in agreement with the erosion mechanism for ductile materials proposed by Finnie (1958). As summarized in Section 2.3, the relation between erosion rate and impingement angle has been assumed (Tilly 1979) to be of the form:

$$E = A_1 \times (A_3 cos^2\theta + 1) \qquad (22^\circ < \theta < 90^\circ) \tag{5.5}$$

where θ is the impingement angle and A_1 and A_3 are constants. When the data were fitted to this equation using the least squares method, it was found that $A_1 = 232\ \mu m/100h$

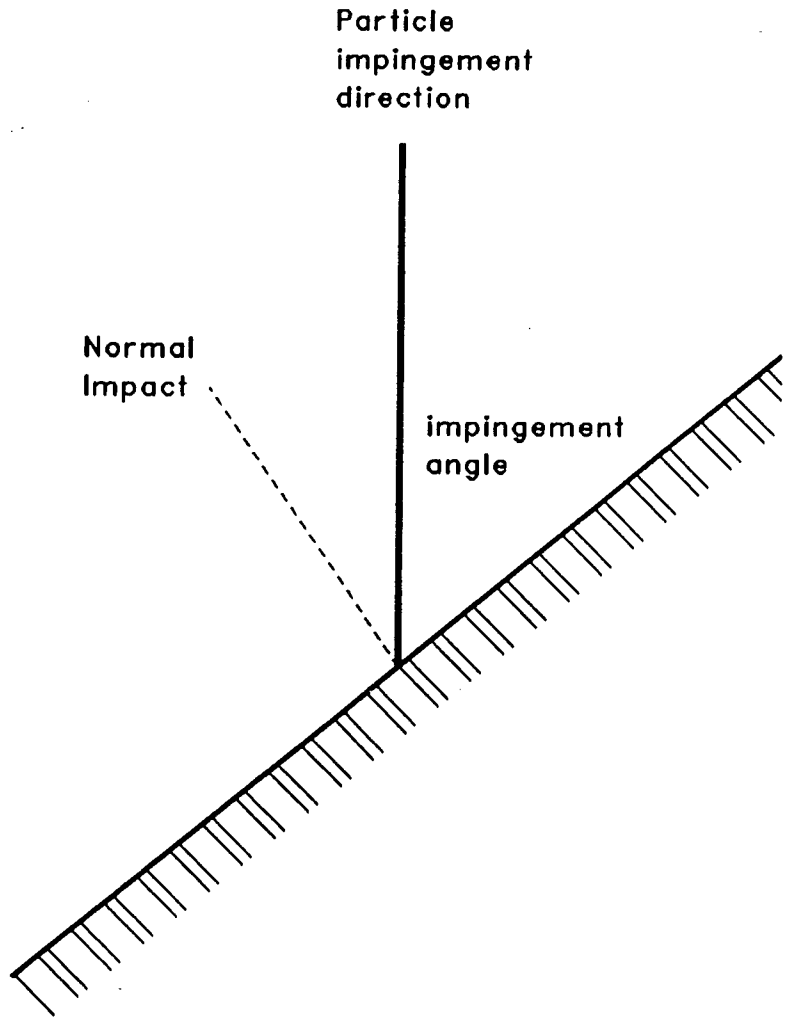

Figure 5.3 Impingement angle for dropping experiments

Table 5.4: Influence of particle impingement angle on erosion of brass specimen by 1.0 mm silica sand particles

Particle impingement angle (degrees)	Average erosion rate (experimental) (μm/100h)	Erosion rate (calculated by equation 5.5) (μm/100h)	Deviation (%)
90	238	232	-2.5 %
68	240	247	2.9 %
45	283	284	0.4 %
23	324	320	-1.2 %

Other operating conditions:

Particle impact velocity: 5.0 m/s

Particle mass flow rate: 5.7kg/m^{2}s

Particles: 1.0 mm silica sand (Φ_s=0.91)

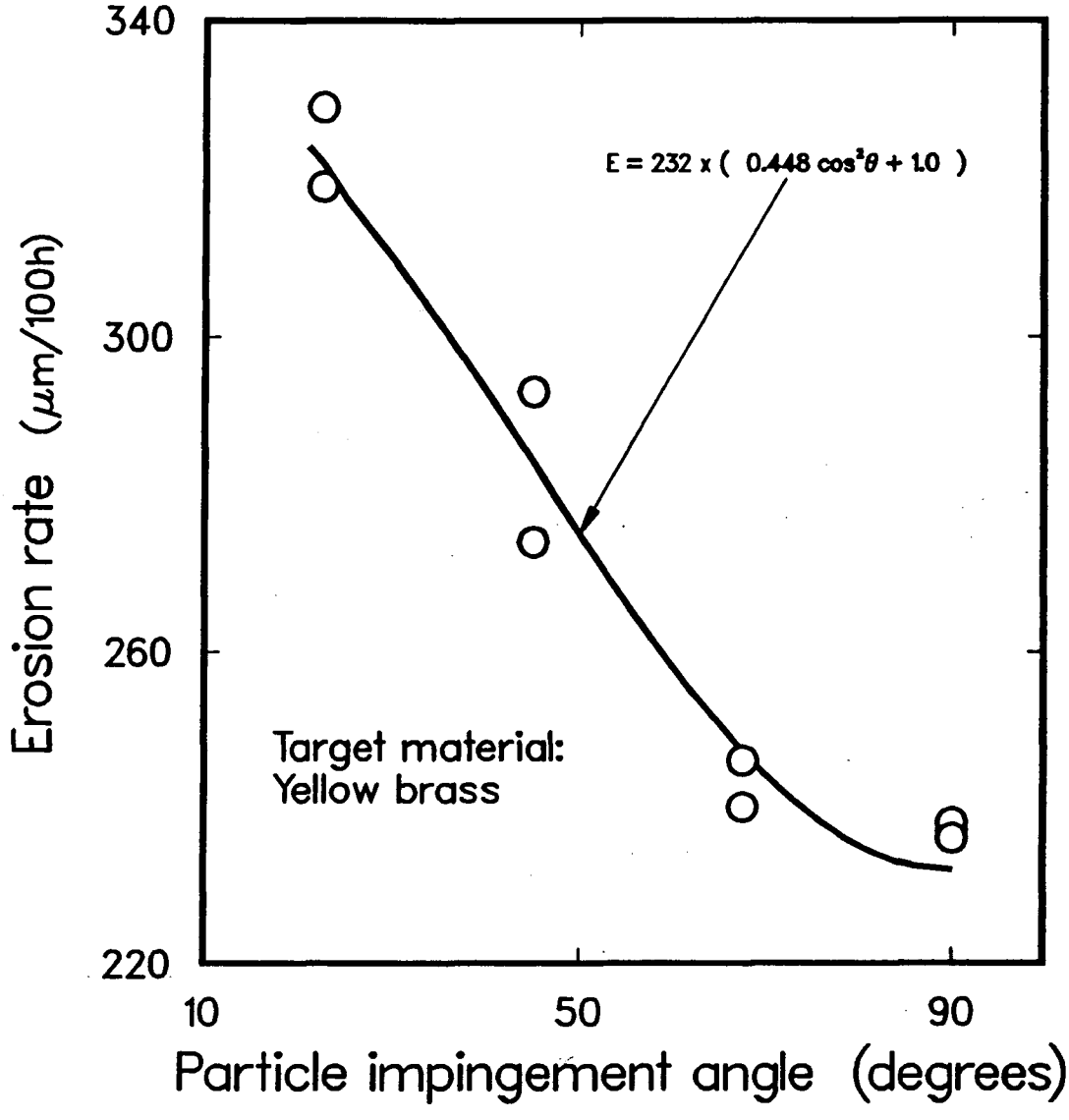

Figure 5.4 Erosion rate vs. particle impingement angle, for 1.0 mm silica sand (φ_s=0.91) with particle mass flow rate of 5.7 kg/m^{2}s and impact velocity of 5.0 m/s

and $A_3 = 0.448$. The results predicted by equation 5.5 are also shown in Table 5.4 and Figure 5.4. The equation form proposed by Tilly (1979) is seen to give a good fit.

However, the ratio of the maximum to minimum erosion for the low velocity results obtained in our work is only 1.4 , compared with 2.0 – 3.0 for high velocity erosion (Tilly 1979). The difference may be due to the fact that brass is less ductile than materials like aluminium and gold which are often used as ductile materials for high velocity erosion. Alternatively, the difference may simply indicate that the mechanisms of low and high velocity erosion are different.

5.4 Effect of Particle Size:

Silica sands of different sizes were tested first. The size distributions of these particles appear in Table 3.4. The size distribution of the 1.0 mm silica sand is plotted in Figure 5.5. Other size distributions were similar in shape. The results of these tests are summarized in Table 5.5. The data for 1.0 mm silica sand is corrected for particle sphericity using equation 5.7. The erosion rate, E, could be correlated with particle diameter, d_p, by an equation of the form:

$$E = k_3 d_p^{m_3} \qquad (r = 0.997) \tag{5.6}$$

where k_3 and m_3 are constants. The least squares method gives the power m_3 as 1.5. The fitted results for $k_3 = 341\ (\mu m)/100h/mm^{1.5}$ and m_3=1.5 are shown together with the original data in Figure 5.6 and Table 5.5.

For high velocity solid impact erosion, a critical particle size has been found to exist, above which the erosion is independent of size (e.g. Finnie 1979, Hutchings 1987). This critical particle size is around 100 μm (Finnie 1979). In the experiments carried out here,

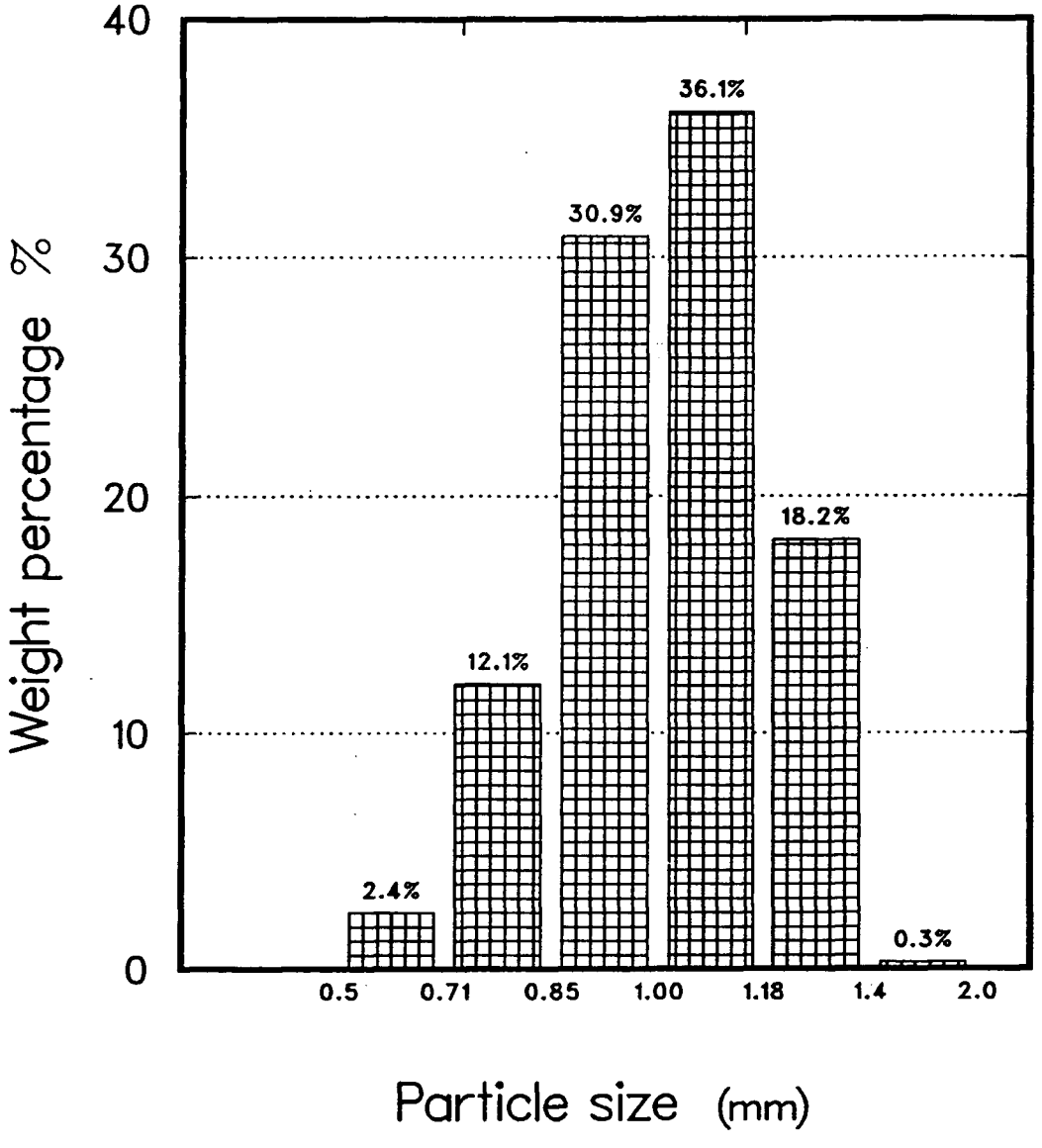

Figure 5.5 Particle size distribution of 1.0 mm silica sand

Table 5.5: Influence of particle diameter on erosion of brass specimen by silica sand particles

Particle mean size (mm)	Average erosion rate (experimental) (μm/100h)	Erosion rate (calculated by equation 5.6) (μm/100h)	Deviation (%)
1.5	638	633	-0.8 %
1.3	520	506	-2.7 %
1.0	330	341	3.3 %

Other operating conditions:

Particle impact velocity: 5.0 m/s

Particle mass flow rate: 5.7 kg/m^2s

Particles: Silica sand (Φ_s=0.86)

Particle impingement angle: 90°

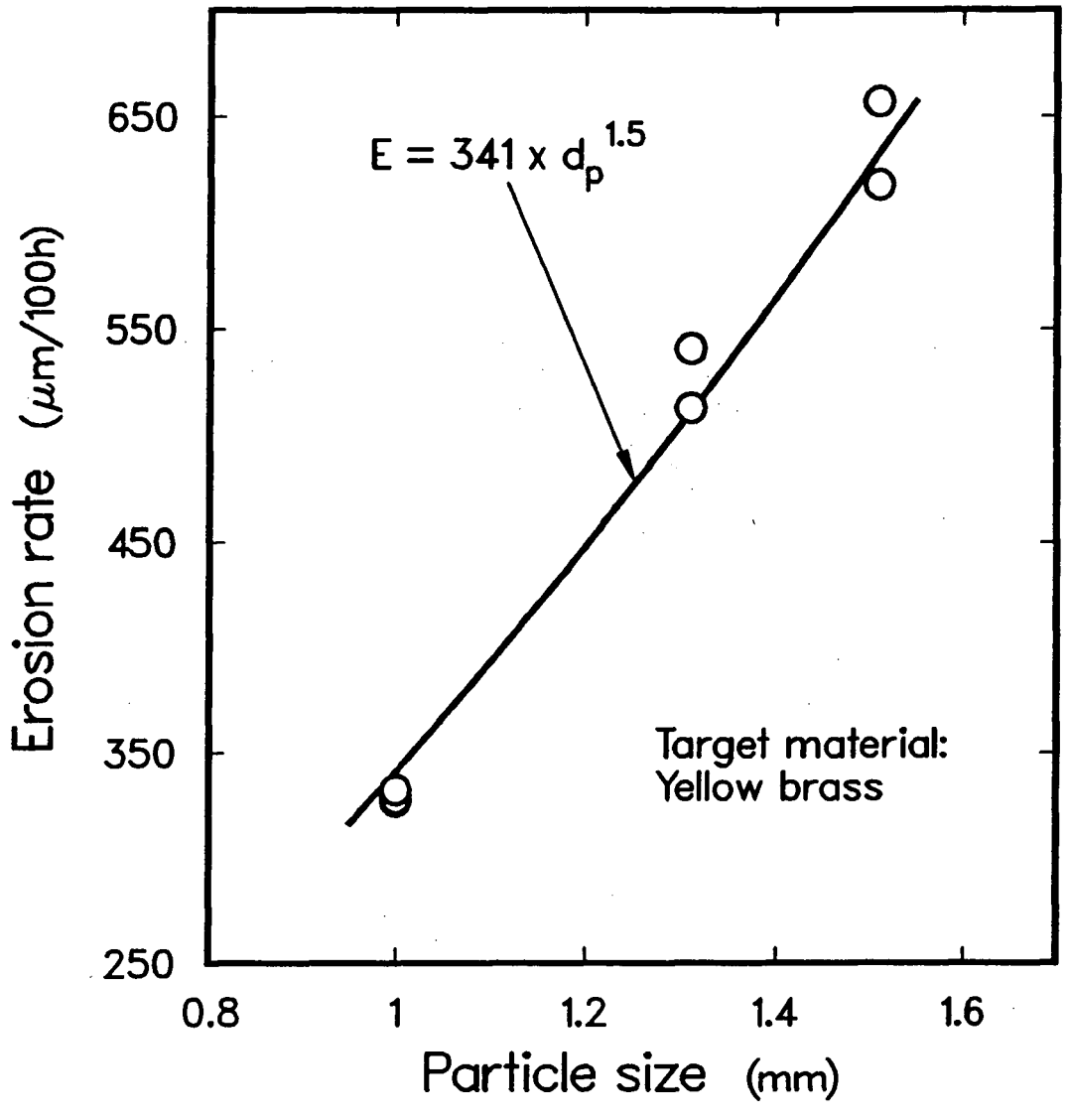

Figure 5.6 Erosion rate vs. particle diameter, for silica sand (φ_s=0.86) with particle mass flow rate of 5.67 kg/m^{2}s and particle impact velocity of 5.0 m/s at 90° impingement angle

all particle sizes were much larger than 100 μm, yet there was a significant influence of particle size on erosion. This suggests that the mechanism of low velocity erosion may be significantly different from that of high velocity erosion.

5.5 Effect of Particle Shape and Hardness

While keeping the impact velocity at 5.0 m/s, the particle mass flow rate at $5.7 kg/m^2$s and brass as the target material, different types of particles were tested. Table 5.6 lists the particles and their properties, together with the erosion rates. The size distributions of these particles are provided in Table 3.4.

For the two runs with silica sand of diameter 1.0 mm, the only difference was that one sand was more angular than the other. The glass beads have roughly the same hardness as the silica sand, and the erosion rate of the 0.89 mm glass beads is corrected to that of glass beads of 1.0 mm using equation 5.6. Recall that equation 5.6 correlated the effect of silica sand particle over the size range of 1.0 – 1.5 mm. Here it is assumed that equation 5.6 can be extended to glass beads over the range from 0.89 to 1.0 mm. Results from the above three runs indicate that the erodability of particles decreases approximately linearly with the increase of particle sphericity for the range investigated. The relationship between particle sphericity, Φ_s, and erosion rate can be expressed by:

$$E = A_4(A_5 - \Phi_s) \qquad (r = 0.999) \tag{5.7}$$

where A_4 and A_5 are constants. The least squares fitting gives $A_4 = 1820\ \mu m/100h$ and $A_5 = 1.04$. The experimental results together with the results predicted by equation 5.7 are listed in Table 5.7 and plotted in Figure 5.7.

The erosion rate for the more angular sand was found to be 1.5 times that of the rounder sand. The difference between the erosion rates for the more angular sand and glass beads

Table 5.6: Influence of particle properties on erosion of brass specimen

Particle type	Particle mean size (mm)	Particle hardness (kg/mm^2)	Particle sphericity	Average erosion rate (experimental) (μm/100h)
Silica sand	1.51	350	0.86	638
Silica sand	1.30	350	0.86	520
Silicon carbide	1.08	590	0.86	424
Silica sand	1.00	350	0.84	358
Silica sand	1.00	350	0.91	238
Glass beads	0.89	340	1.00	62
Limestone	0.93	40	0.86	231

Other operating conditions:

Particle impact velocity: 5.0 m/s

Particle impingement angle: 90°

Particle mass flow rate: 5.7 kg/m^2s

Table 5.7: Influence of particle sphericity on erosion on brass specimen by 1.0 mm particles

	Particle sphericity	Average erosion rate (experimental) (μm/100h)	Erosion rate (calculated by equation 5.7) (μm/100h)	Deviation (%)
Glass beads	1.00	73	73	0.0 %
Silica sand	0.91	238	237	−0.4 %
Silica sand	0.84	358	364	1.7 %

Other operating conditions:

Particle impact velocity: 5.0 m/s

Particle mass flow rate: 5.7 kg/m^2s

Particle impingement angle: 90°

Particle size: 1.0 mm

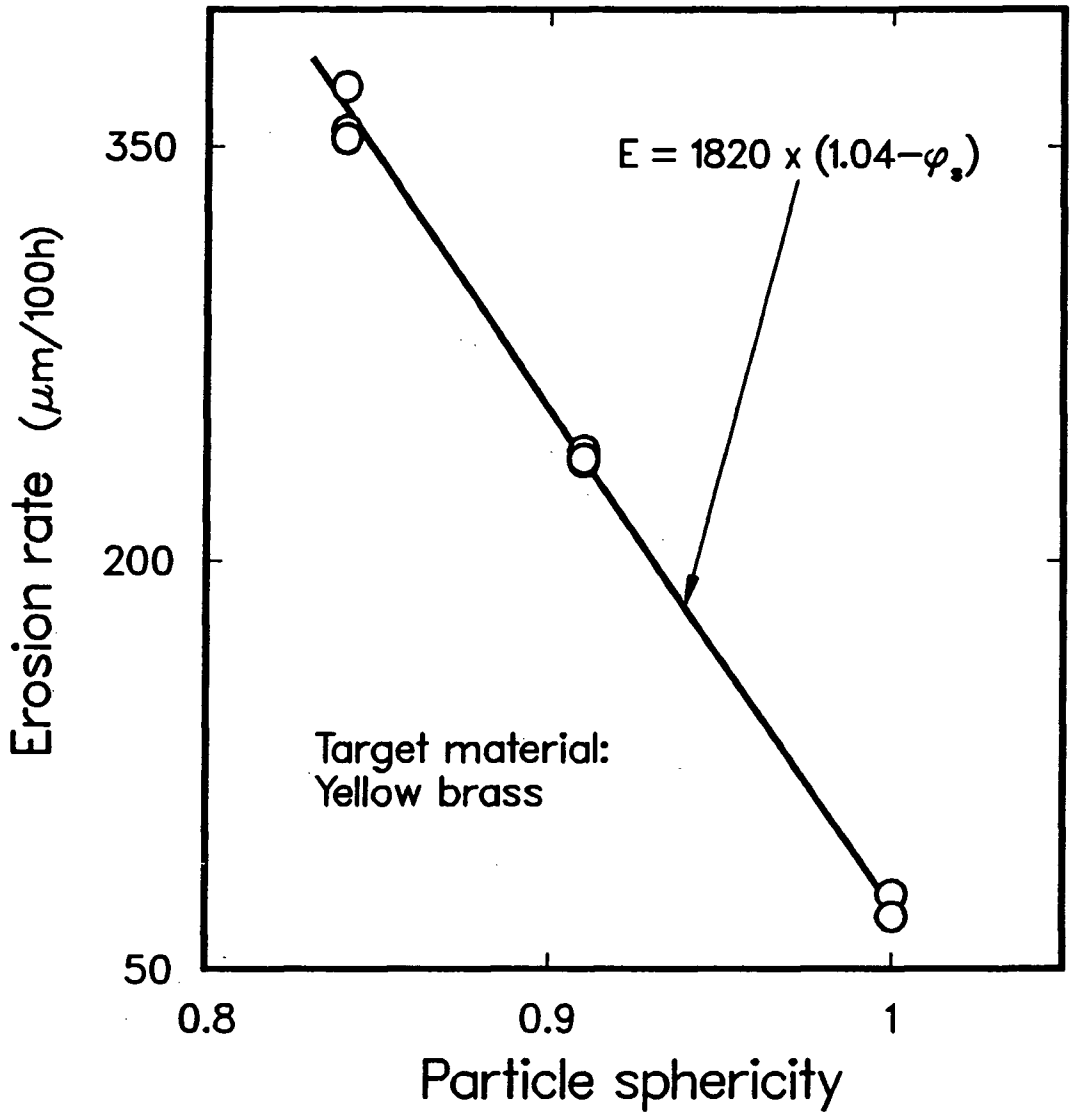

Figure 5.7 Erosion rate vs. particle sphericity, for particle mass flow rate of 5.7 kg/m^{2}s and particle impact velocity of 5.0 m/s at 90° impingement angle

was much larger: 5 times. This phenomenon has been reported previously (see Section 2.3), but no functional relationship appears to have been reported. In addition, the influence of shape appears to have been more pronounced in our work than in high velocity erosion.

The other three runs with 1.0 *mm* silica sand, 1.08 *mm* silicon carbide and 0.93 *mm* limestone also appear to show a significant influence of particle hardness, although other properties (e.g. particle density and strength) may also play some role. The erosion rate of 0.93 *mm* limestone and 1.08 *mm* silicon carbide are corrected to that of 1.0 *mm* particles using equation 5.6. The erosion rate of silica sand is corrected for particle sphericity using equation 5.7. Although equations 5.6 and 5.7 were developed based on silica sand and glass bead, they are used here for limestone and silicon carbide in the absence of any better correlation. The corrected results are plotted in Figure 5.8. Having the same diameter, the hardest particles, silicon carbide, produced the highest erosion rate, while the softest material, limestone, resulted in the smallest erosion rate. The silica sand, with intermediate hardness, gave intermediate results. These observations are in agreement with the results from high impact velocity tests discussed in Section 2.3.

If the form of equation 2.12 is borrowed, i.e.

$$E = k_4 H_p^{m_4} \qquad (r = 0.988) \tag{5.8}$$

where H_p is the Vicker's hardness of the particles and k_4 and m_4 are constants, m_4 and k_4 were found to be 0.20 and 104.8 $(\mu m/100h)/(kg/mm^2)^{0.2}$ respectively by the least squares method. The calculated erosion rates together with the experimental data are listed in Table 5.8. The equation and experimental results are also plotted in Figure 5.8. The exponent in equation 5.8 of 0.20 is very different from the value of 2.3 found by Tilly (1979). This may be because equation 5.8 covers a broad range of hardness values, while equation 2.12 only includes particles of hardness lower than the target hardness.

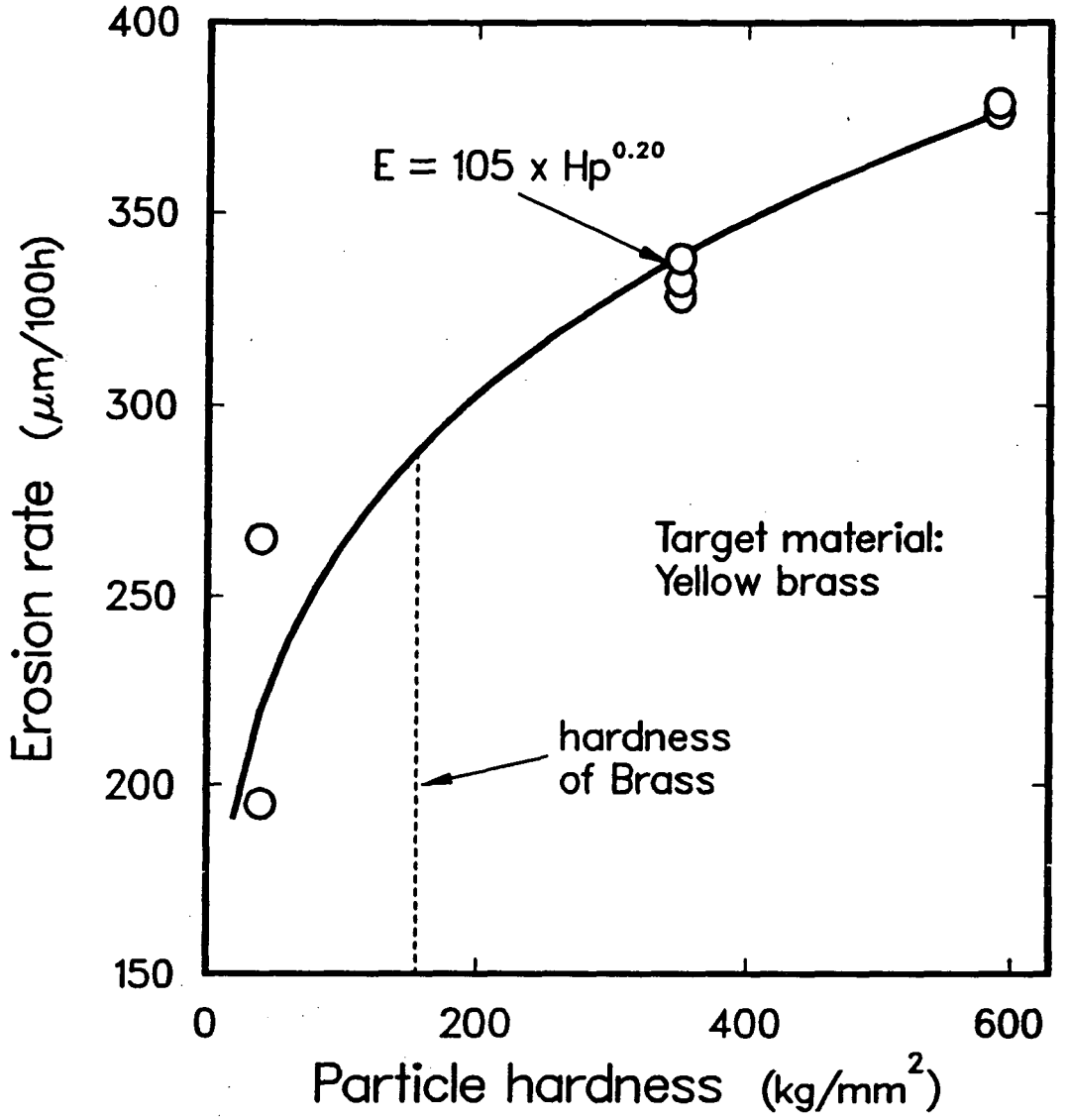

Figure 5.8 Erosion rate vs. particle hardness, for particle mass flow rate of 5.7 kg/m^2s and particle impact velocity of 5.0 m/s at 90° impingement angle

Table 5.8: Influence of particle hardness on erosion of brass specimen by 1.0 mm particles

	Particle hardness (kg/mm^2)	Average erosion rate (experimental) (μm/100h)	Erosion rate (calculated by equation 5.8) (μm/100h)	Deviation (%)
Silicon carbide	590	378	376	-0.5 %
Silica sand	350	330	339	2.7 %
Lime-stone	40	230	220	-4.3 %

Other operating conditions:

Particle impact velocity: 5.0 m/s

Particle mass flow rate: 5.7 kg/m^2s

Particle impingement angle: 90°

Particle size: 1.0 mm

5.6 Effect of Mechanical Properties of Specimen Materials

The erosion rates of different materials are plotted against their hardnesses and Young's moduli in Figures 5.9 and 5.10. The data are also listed in Table 5.9. All the tests were carried out with the 1.0 mm silica sand, an impact velocity of 5.0 m/s and a particle mass flow rate of 5.7 kg/m^2s. Figure 5.9 shows that the erosion rate usually decreased as the material hardness was increased. Figure 5.10 indicates that a higher Young's modulus gives more resistance to erosion.

The dependency of erosion rate on material hardness shown in Figure 5.9 is in agreement with that for high velocity impact erosion (Hutchings 1987). The erosion resistance increased with hardness for most cases, but there were exceptions (see Figure 2.6). It should be noted that the hardness of metals or alloys with exactly the same composition can be dramatically different due to the processing of the materials. However, it is the hardness of the material layer close to the surface that the impacting particles penetrate which likely influences the erosion process most, rather than the material body hardness. Experiments performed in our lab have shown that material Vickers hardness did not change appreciately under extensive erosion (see Section 7.5.1). It should also be noted that the indentation of the Vickers hardness tester reached a depth of approximately 20 – 30 μm. This depth appears to be of the same order as the depth of craters formed on the surface, and hence it can be argued that the Vickers hardness test provides an appropriate measure of hardness. However, it is also possible that the hardness of primary interest is a "surface hardness" pertaining only to a surface layer, perhaps of the order of 1 μm in depth. Microhardness could in principle be measured using the TUKON microhardness tester (see Section 3.3), but this was not suitable for the rough eroded surfaces in this project.

Hardness is in reality a measure of the yield strength of the material, the ability to resist

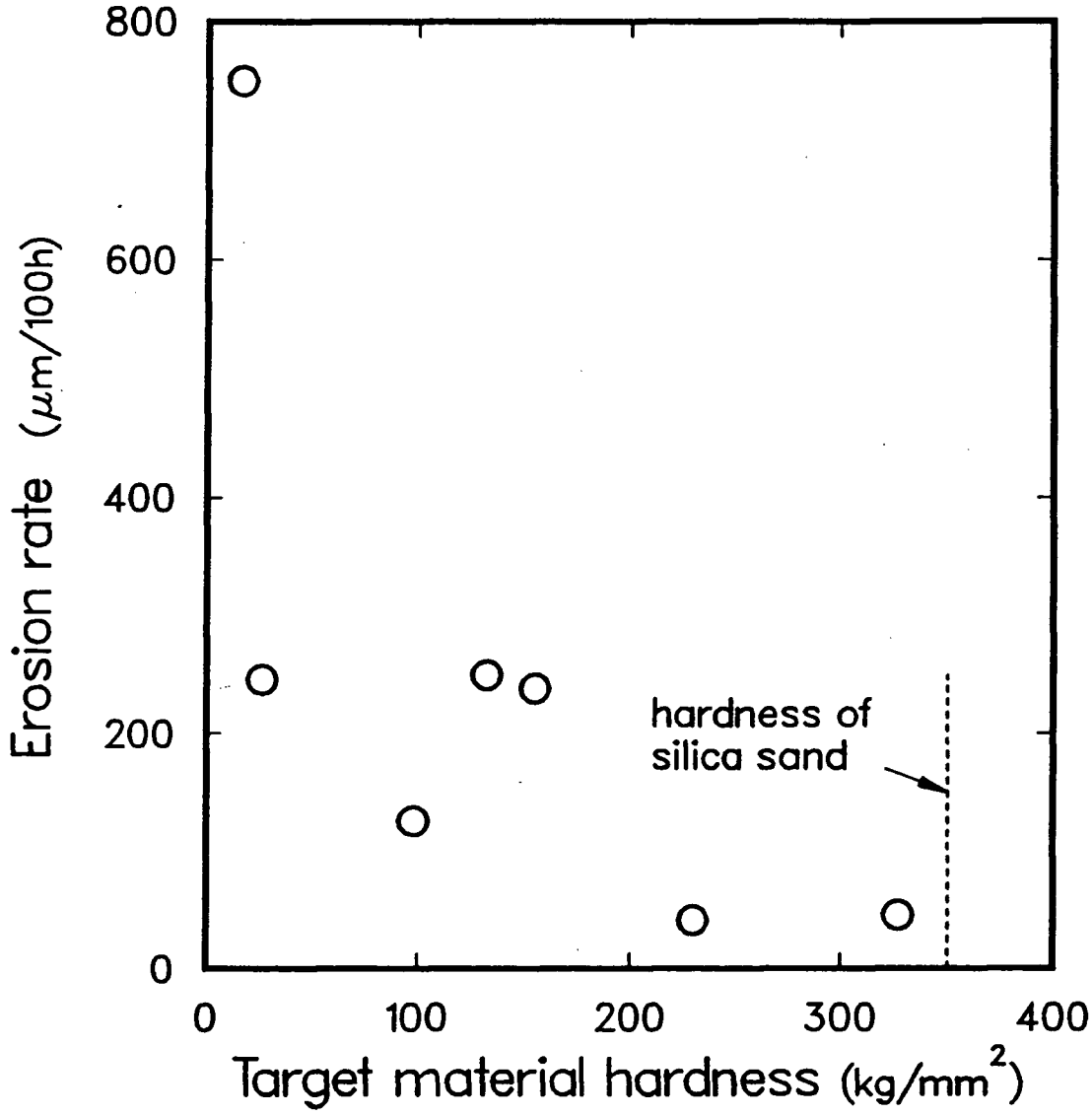

Figure 5.9 Erosion rate vs. target material hardness, for 1.0 mm silica sand (φ_s=0.91) with particle mass flow rate of 5.7 kg/m^{2}s and particle impact velocity of 5.0 m/s at 90° impingement angle

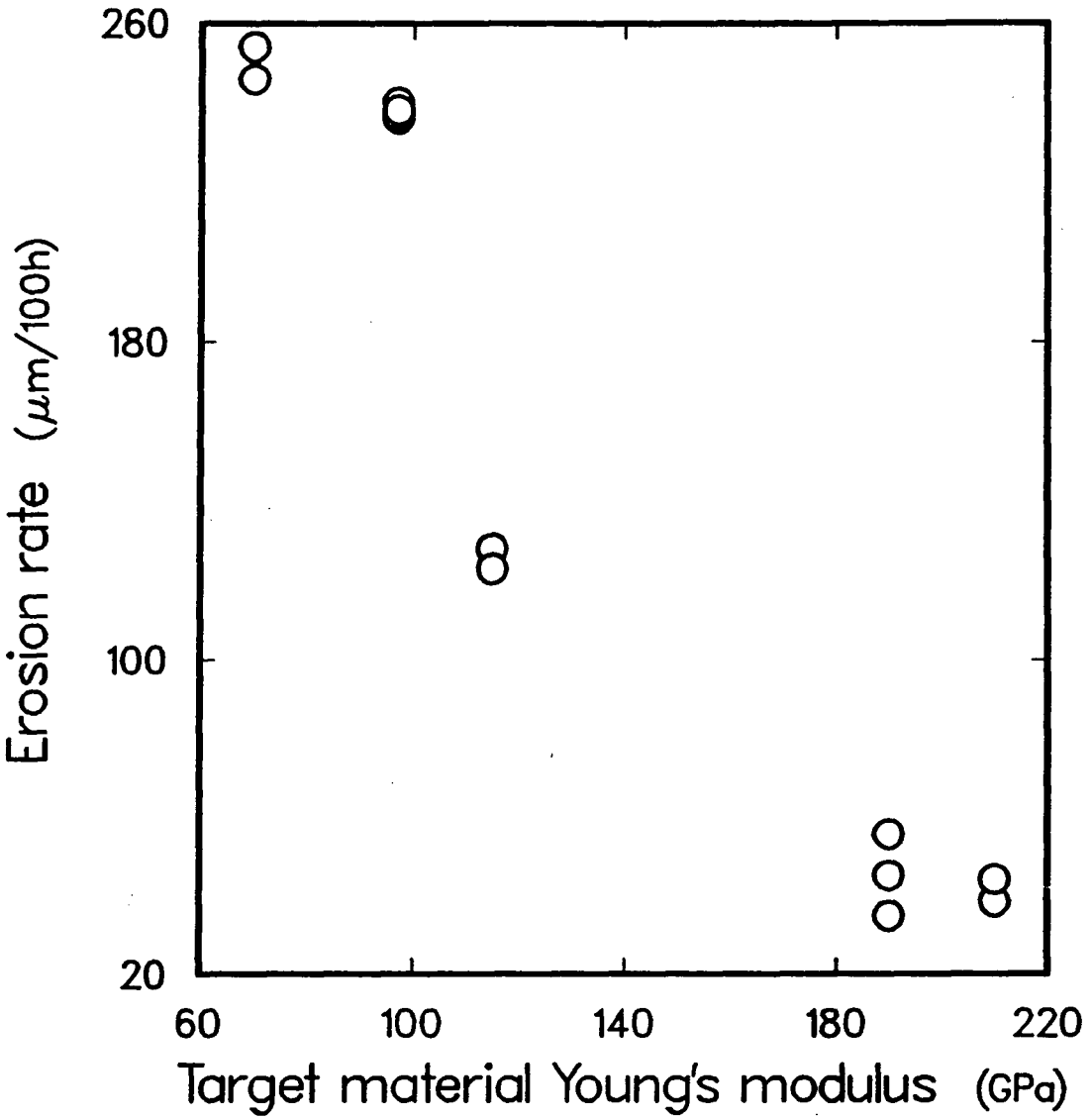

Figure 5.10 Erosion rate vs. target material Young's modulus, for 1.0 mm silica sand (φ_s=0.91) with particl flow rate of 5.7 kg/m^{2}s and particle impact velocity of 5.0 m/s at 90° impingement angle

Table 5.9: Influence of target material Young's modulus hardness on erosion in the dropping experiments

Materials	Material Young's modulus (GPa)	Material Hardness (kg/mm^2)	Average erosion rate (experimental) (μm/100h)
Brass	97.0	155	238
Al2011	70.0	98.0	250
Copper	115	132	126
SS316	190	230	45
CS1050	210	327	41
PVC	*	26.6	246
Plexiglass	*	14.6	750

Other operating conditions:

Particle impact velocity: 5.0 m/s

Particle mass flow rate: 5.7 kg/m^2s

Particle impingement angle: 90°

Particles: 1.0 mm Silica sand (Φ_s=0.91)

* --- Not available.

plastic deformation. For the process of material removal, not only the plasticity but also the elasticity plays an important role. For low velocity impact erosion in particular, elasticity is expected to play a greater role since the lower kinetic energy of the particles at impact produces mainly elastic deformation on the target materials. Taking the highest impact velocity (5.0 m/s) and brass as an example, the Beat and Metz number from Hutchings (1980) is $\rho_s V_p / Y_m = 8500 \times 5.0^2 / 3.3 \times 10^8 = 6.6 \times 10^{-4}$. The number is smaller than 10^{-3}, a value which is said to be the limit of purely elastic behaviour (Hutchings 1980).

Figure 5.10 shows clearly that the erosion rate decreases as the material Young's modulus increases. The results from other sources (see Figure 2.6, Finnie et al. 1967) are replotted also in Figure 5.11 as erosion rate against Young's modulus. Figure 5.11 shows clearly that erosion rate decreases as the target material's Young's modulus increases. Figures 5.10 and 5.11 suggest that Young's modulus may well play a more important role in material erosion than the material hardness. This is further discussed in Section 7.5.

5.7 Conclusions

For the range of conditions studied:

(1) The erosion rate increased with particle impact velocity to the power of 2.3.

(2) The erosion rate increased linearly as the particle mass flow rate increased.

(3) The erosion increased as the angle of impingement became smaller.

(4) The erosion rate increased with the particle size raised to the power of 1.5.

(5) The erosion rate decreased as the material hardness decreased.

(6) Angular particles were found to cause much faster erosion than rounded particles.

(7) Resistance to erosion increased as the material Young's modulus increased, while the influence of material hardness appeared to play a lesser role.

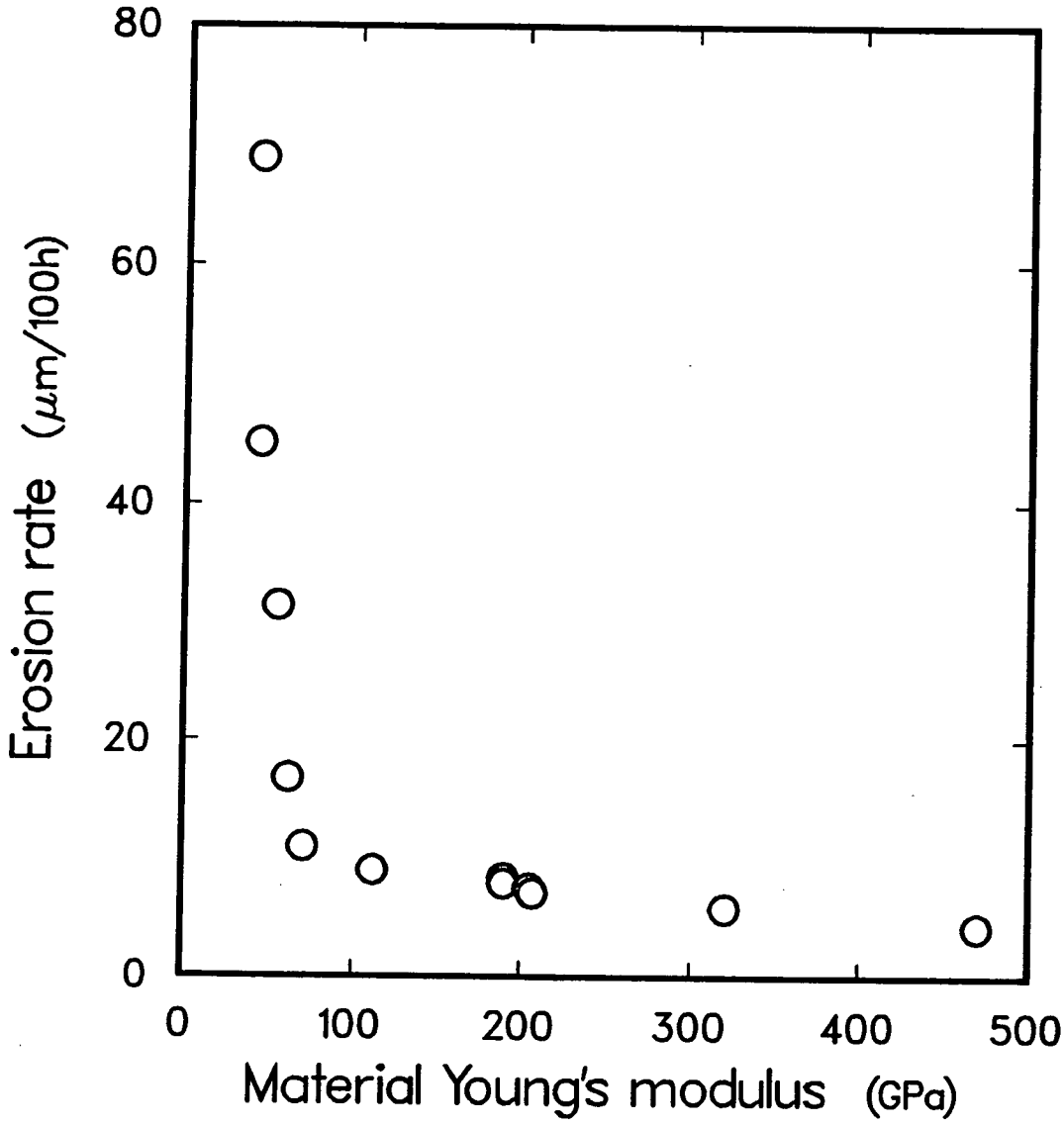

Figure 5.11 Erosion rate vs. material Young's modulus
(Data from Finnie et al. 1967)

A multi-regression fitting was carried out based on all experimental results with brass. The exponents for different variables were found to be the same as those reported above for equations 5.1, 5.2 and 5.5 – 5.8:

$$E = k_5 M V_p^{2.3} d_p^{1.5} H_p^{0.2} \ (1.04 - \Phi_s) \times (0.448 cos^2\theta + 1) \tag{5.9}$$

The constant k_5 was found to be 2.49 $(\mu m/100h)/\{(kg/m^2 s)(m/s)^{2.3} mm^{1.5} (kg/mm^2)^{0.2}\}$ with a standard deviation of 0.19 for yellow brass. The erosion rates calculated from equation 5.9 are plotted against experimental erosion rate in Figure 5.12. The experimental and calculated erosion rates and the errors for brass are also summarized in Table 5.10 together with all operating conditions. Both Figure 5.12 and Table 5.10 show that equation 5.9 works quite well for brass.

In Section 7.1 it is shown that the exponent for particle hardness is also influenced by the mechanical properties of the target materials while the other exponents seem to be independent of material properties. Therefore, we drop the H_p term and suggest the following equation in place of equation 5.9:

$$E = k_6 M V_p^{2.3} d_p^{1.5} \ (1.04 - \Phi_s) \times (0.448 cos^2\theta + 1) \tag{5.10}$$

The k_6 values for different materials are listed in Table 5.11. It is worth noting that the k_6 values listed in Table 5.11, except for brass, should be applied with caution, since only one set of tests were carried out for each material. It is also worth noting that equation 5.10 should be applied with caution when several variables differ at one time from the base conditions. This is because of the multi-axis experimental design, similar to that described in Section 3.1, employed in the dropping experiments. In addition, caution should be exercized when predictions are required for conditions outside the limited ranges of variables covered in our experiments.

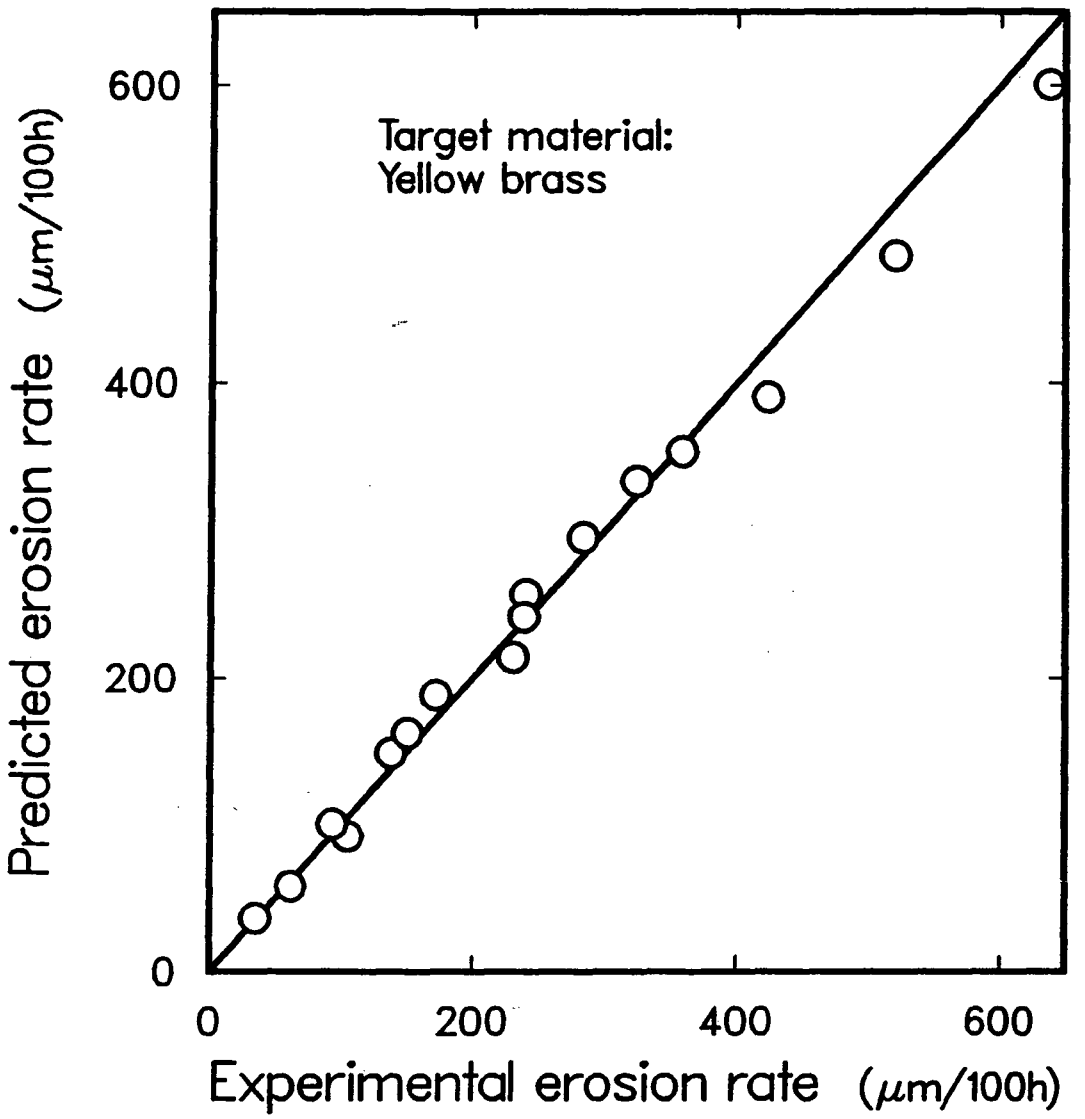

Figure 5.12 Experimental erosion rate vs. calculated erosion rate for all dropping tests with Yellow brass as the target material (Predictions are from equation 5.9.)

Table 5.10: Operating conditions and results of all dropping tests with yellow brass (Y_m = 97.0 GPa) as the target material

	M (kg/m^{2}s)	V_p (m/s)	d_p (mm)	Hp (kg/mm^2)	Φ_s	Θ (degree)	E (μm/100h)	E' (μm/100h)	Error (%)
Run 1	5.7	5.0	1.00	350	0.84	90	358	369	3.0%
Run 2	5.7	5.0	1.00	350	0.91	90	238	240	0.5%
Run 3	4.4	5.0	1.00	350	0.91	90	172	184	7.2%
Run 4	3.8	5.0	1.00	350	0.91	90	150	161	7.1%
Run 5	2.4	5.0	1.00	350	0.91	90	93	100	7.2%
Run 6	5.7	4.1	1.00	350	0.91	90	138	148	7.0%
Run 7	5.7	3.3	1.00	350	0.91	90	105	91.6	-12.8%
Run 8	5.7	2.2	1.00	350	0.91	90	34	36.3	4.0%
Run 9	5.7	5.0	1.51	350	0.86	90	637	616	-3.4%
Run10	5.7	5.0	1.30	350	0.86	90	520	492	-5.4%
Run11	5.7	5.0	0.93	40	0.86	90	230	193	-16.3%
Run12	5.7	5.0	1.08	590	0.86	90	424	414	-2.3%
Run13	5.7	5.0	0.89	340	1.00	90	62	61.6	0.0%
Run14	5.7	5.0	1.00	350	0.91	68	240	256	6.5%
Run15	5.7	5.0	1.00	350	0.91	45	283	294	3.7%
Run16	5.7	5.0	1.00	350	0.91	23	324	331	2.3%

Correlated k value and its deviation: 2.49 ± 0.19

Average error 5.54%

E : experimental erosion rate, E′ : prediction from equation 5.9

Table 5.11: k_6 values for different materials in equation 5.10

Materials	k_6 $\frac{(\mu m/100h)}{(m/s)^{2.3}(mm)^{1.5}\,(kg/m^2 s)}$
Brass	8.04
Al 2011	8.42
Copper	4.23
SS316	1.52
CS1050	1.39

CHAPTER SIX: RESULTS AND DISCUSSION: TWO-DIMENSIONAL EXPERIMENTS

To correlate the erosion rate of immersed tubes with the hydrodynamic behaviour inside fluidized beds, it is necessary to find the relationship between particle flow patterns and the operating conditions. A two-dimensional fluidized bed was employed to provide qualitative and quantitative indications of how particles associated with bubbles interact with immersed tubes. A high speed camera was used to film the particle and bubble movements around tubes in the bed through the transparent wall. The films were then played back and analysed frame by frame to determine bubble velocities, particle velocities, particle velocity distributions, and particle impact angles under different operating conditions.

Although two-dimensional columns may provide qualitative indications and some quantitative results, there are important quantitative differences between two and three dimensional fluidized beds (Grace & Baeyens 1986). For example, there are differences in the rise velocities of isolated bubbles, in bubble coalescence properties, bubble shapes and wake characteristics, and jet stability. In the present experiment, it is the particle motion relative to the bubble movement around the tube that is of interest. While the bubble rise velocity in a two-dimensional column may differ from that in a three-dimensional column under the same fluidizing conditions, it seems likely that the two-dimensional column will give a good qualitative and semi-quantitative picture of the interaction of bubbles and tubes.

Silica sand of 1.0 *mm* diameter was used for all the experiments. 1.04 *mm* silicon carbide (black) particles (approximately 1% by mass) were added as tracer particles for film analysis. The static bed height and tube positions were kept the same as in the three-dimensional fluidized bed. The tube outer diameters were 32 and 29 *mm*. The gas

superficial velocity was kept at 1.87 m/s for most of the tests, and 1.19 m/s for one test to show the effect of gas velocity. A separate experiment was also conducted with the bed held at minimum fluidization and additional air injected into the bed under the tube to form isolated bubbles and bubbles coalescing just beneath the tube. These experiments allowed particle movement around the tube associated with single and coalescing bubbles to be studied. Better correlation of particle impingement velocity with bubble velocity could then be achieved.

The filming speed of the Hycam camera was set at 200 $frames/s$ for most of the tests and 600 $frames/s$ for three tests to allow more detailed views from inside the tube. After the tests, the films were projected onto a large piece of graph paper by a motion analyzer projector which allowed frame by frame viewing. Individual particles were tracked for at least 6 frames before impact with the tube. The (x,y) coordinates of the tracked particles were then entered in a computer program (see Appendix C) which determines the overall average impact velocity, average impact velocity for different groups, and impact angle (i.e. angle between particle trajectory just before impact and tangent to the tube surface). The standard deviations and distributions of all the above variables were also determined.

The analysis of the films consisted of two steps. In the first, every tracer particle which impacted on the tube surface was counted to give the percentage of impact particles for different classifications. The details of the classification scheme are given later in this chapter. In the second step, certain typical sections of the films were chosen in which all particles which could be tracked for 6 consecutive frames before impact were sampled. For viewing from inside the tube, only step two was carried out since the sample size was too small to give an accurate distribution. The requirement for 6 consecutive frames for particle sampling was also discarded due to the limited view from inside the tube.

6.1 Single Bubble Injection

In this experiment, a single tube of diameter 32 mm was placed horizontally in the plexiglass two-dimensional column 408 mm above the air distributor and 308 mm directly above the bubble injection point. The static bed height was 680 mm in order to submerge the tube in the sand. The air superficial velocity was kept at the minimum fluidization velocity, $u_{mf} = 0.72 m/s$ in this case, while bubbles were injected at such intervals that there was only one bubble rising within 200 mm of the tube at any time. The volume of air injected for each bubble was $2.3 \times 10^{-4} m^3$. The bubbles had an average height of 130 mm at the level of the tube position.

Figure 6.1 shows a typical single bubble passing the horizontal tube. Before the bubble was injected, the tube was surrounded by dense phase particles, which were almost stagnant, but there was some tendency to drift with a velocity of the order of 0.01 m/s or smaller. This situation continued after the bubble was injected until the bubble cap arrived within 60 – 80 mm of the tube bottom. Then the velocity of particles in the region below the horizontal tube increased suddenly. However, those particles immediately below the tube remained stagnant until the bubble front reached 10 – 15 mm below the tube bottom. At this level, some of the particles in the bubble cap had enough energy to break through the stagnant layer of particles immediately below the tube and impact on the bottom of the tube.

As the bubble reached the bottom of the tube, there was an increase in the voidage around the tube, and the bubble began to envelope the tube. At this stage, the tube became surrounded by dilute phase. Particle motion in the dilute phase appeared to be somewhat random but predominently downwards due to particles dislodged from the bubble roof. Those raining particles formed a small cap on top of the tube. As the bubble proceeded

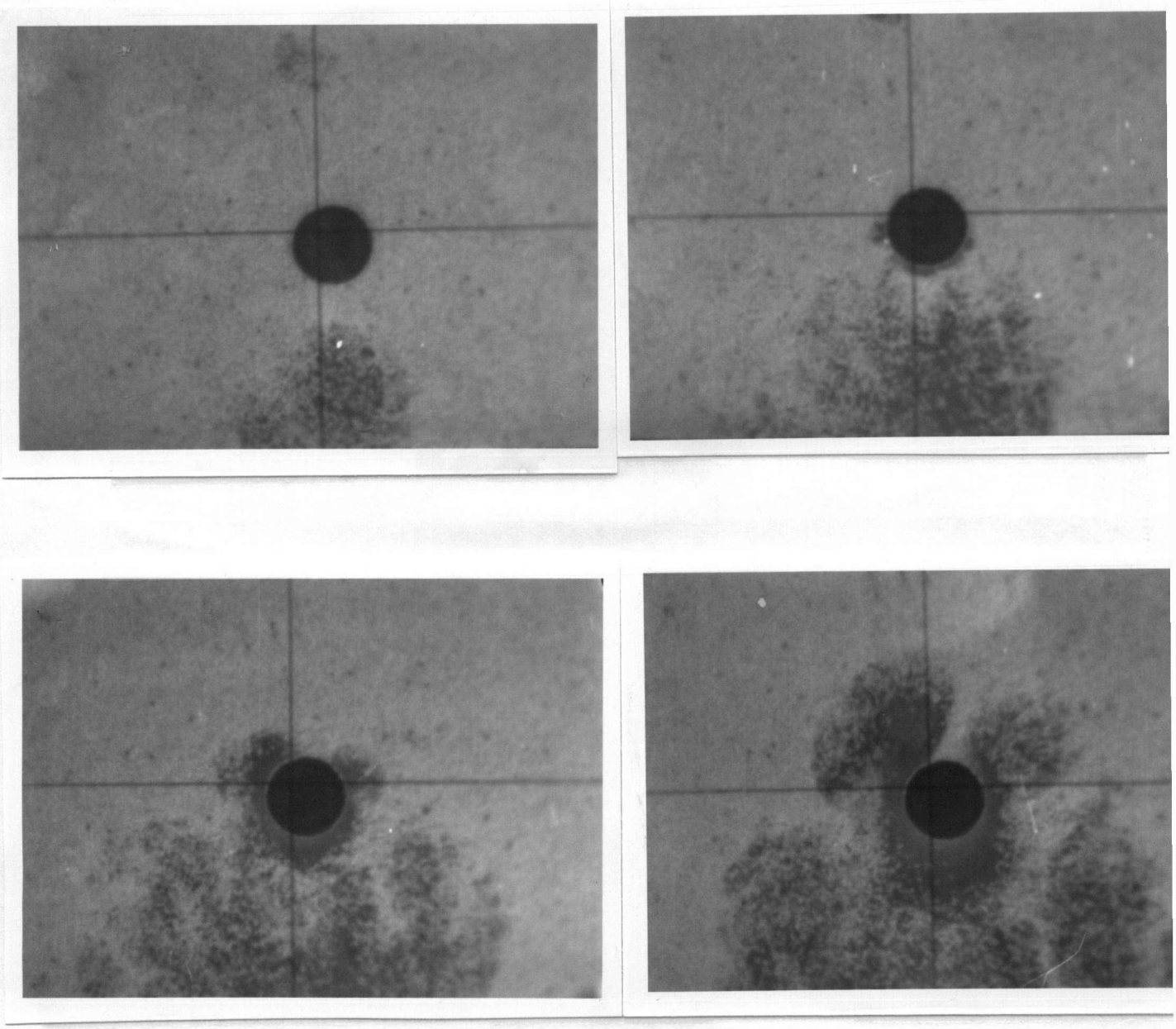

Figure 6.1 Photographs of sequence of a single bubble passing horizontal tube in two-dimensional column

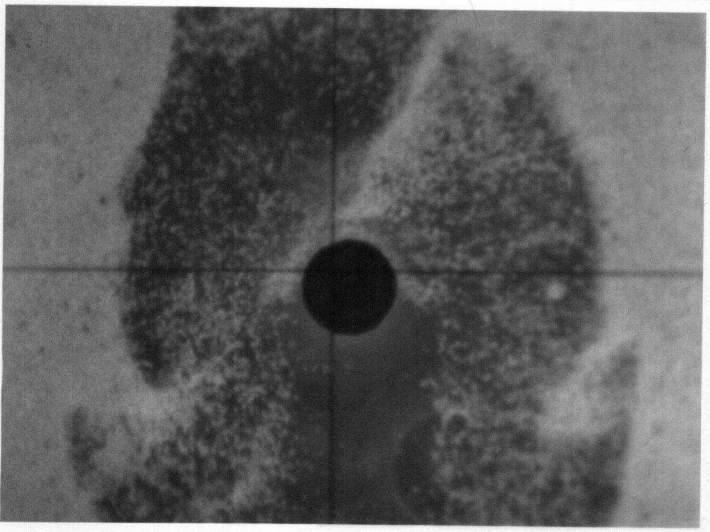

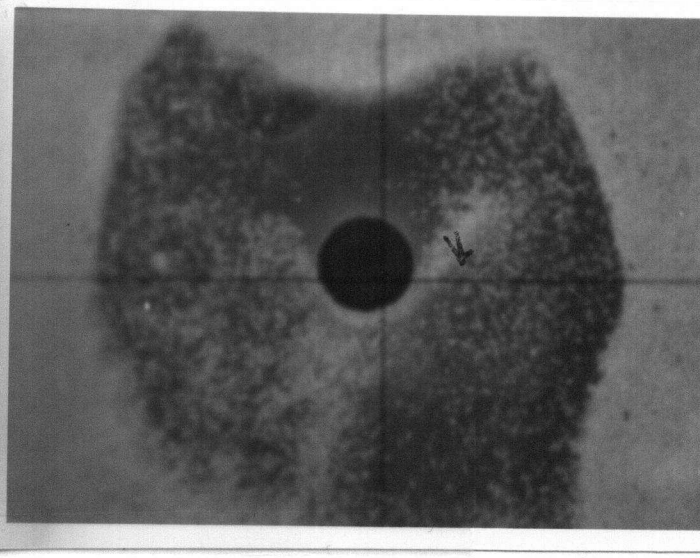

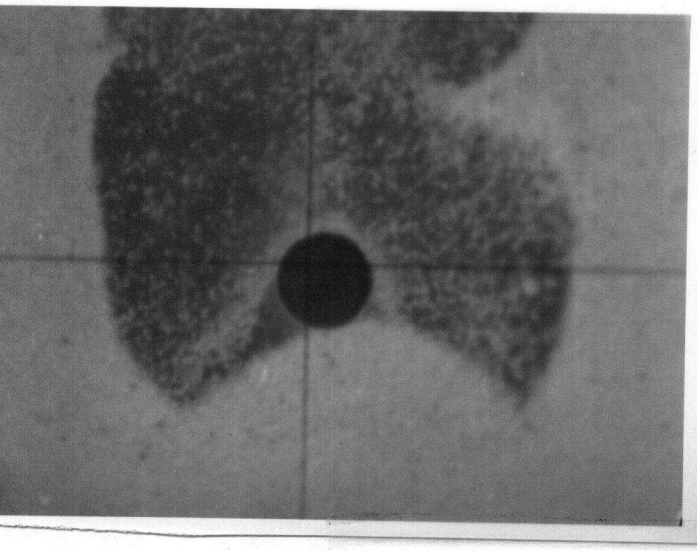

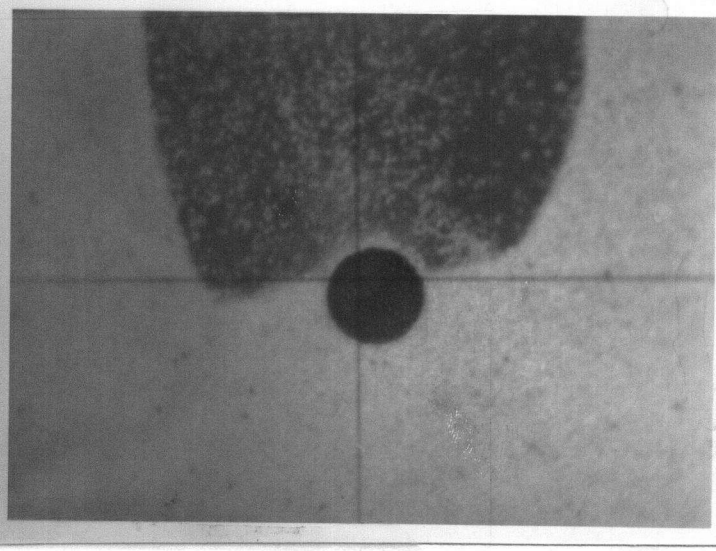

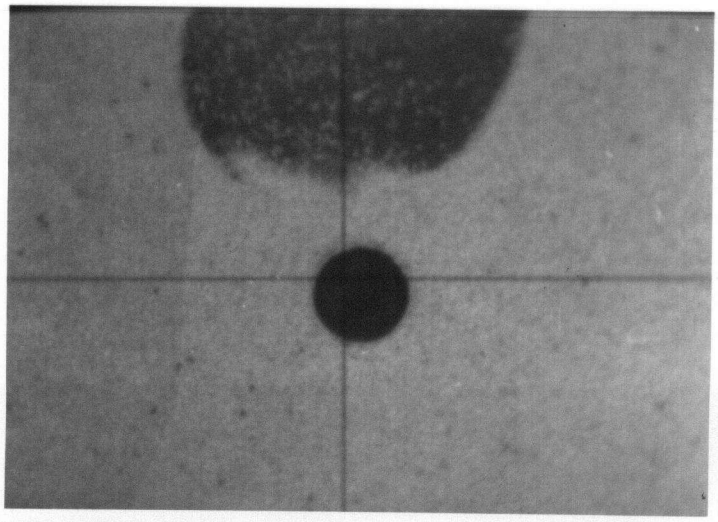

upwards, these particles on top of the tube continuously slid off the upper surface along the sides, falling to the bottom of the bubble.

As the bottom of the bubble approached the tube bottom, the particles in the bubble wake were also carried upwards. For cases where the bubble divided into two parts, one passing to each side of the tube, particles in the wake had less tendency to diverge than the bubble due to inertia. In either case, particles in the bubble wake were thrown against the tube surface when the bottom of the bubble arrived at the tube bottom.

After the impact of wake particles on the tube, most bubbles resumed their original shape and continued upwards, while particles moved in from the sides to fill in the voids and restore the dense phase around the tube. The dense phase then continued to drift about slowly prior to the arrival of the next bubble.

Figure 6.2 shows typical trajectories of particles in bubble caps and wakes just before impact. The dots in the figure represent particle positions in consecutive frames (separated by 0.005 s). As described earlier in this chapter, the coordinates of the positions were entered in a computer program to calculate different variables. Table 6.1 tabulates the results for the single bubble injection tests. Particles striking the tube have been classified into three groups: (1) particles in bubble cap which impact before a bubble arrives at the tube, (2) particles inside the bubble which strike the tube when it is enveloped by a bubble, and (3) particles in bubble wake which strike the tube surface after bubble passage. Between two consecutive bubbles, the particles around the tube were almost stagnant. Their positions did not change appreciably for the tracked 6 – 10 frames, which indicates that the velocities of these particles must have been, if not zero, smaller than about 0.01 m/s. In Chapter 5 it was concluded that erosion is proportional to the 2.3 power of particle velocity. The very low velocities of these particles therefore were considered insignificant and have

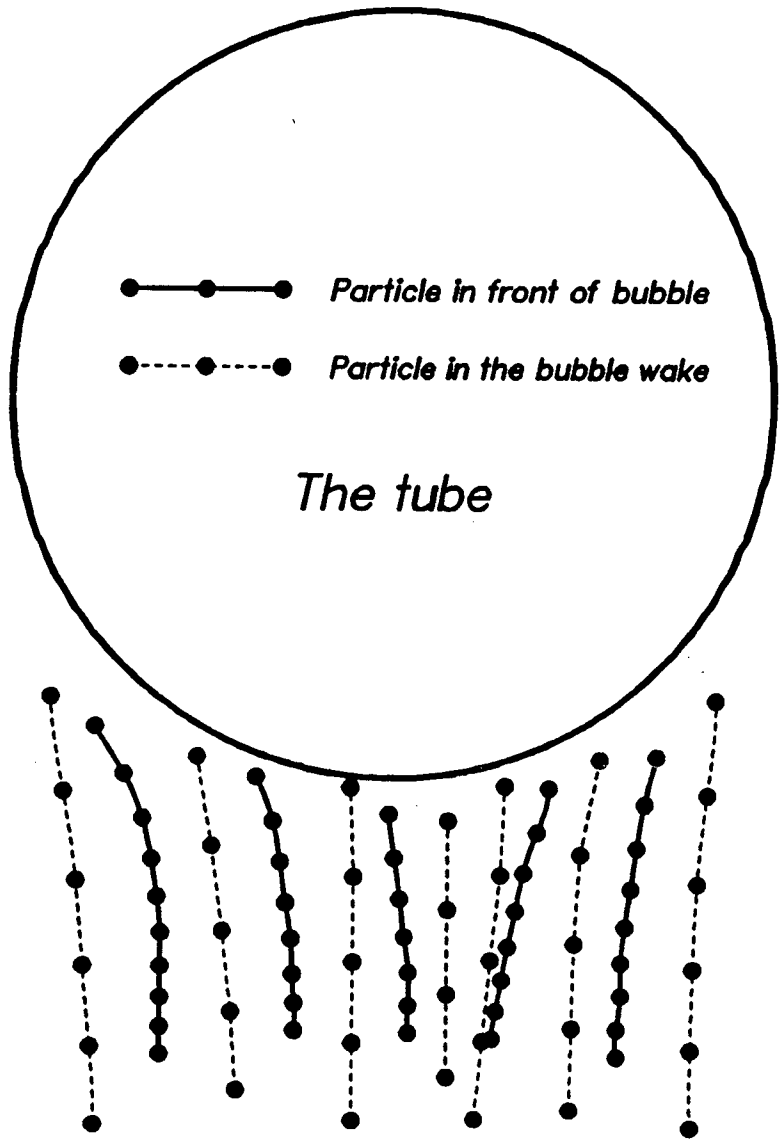

Figure 6.2 Particle trajectory for single bubble injection experiment at minimum fluidization with 1.0 mm silica sand

Table 6.1: Results of film analysis for single bubble injection experiment

Operating conditions:

Sample size:	110 particles 18 bubbles
Background superficial velocity:	0.72 m/s, i.e. u_{mf}
Tube size:	32 mm
Particles:	1.0 mm silica sand
Filming speed:	200 frames/s

	Average velocities (m/s)				
	Mean ± Standard deviation	2.3 power mean	Horizontal Component	Vertical Component	Impact Angle (degrees)
Bubbles	0.62 ± 0.05	0.62			
Particle (overall average)	0.55 ± 0.80	0.56	0.10	0.51	44
Particles (46%) before bubble arrived	0.35 ± 0.08	0.33	0.11	0.30	38
Particles (5%) inside bubbles	0.80 ± 0.20	0.82	0.22	-0.70	39
Particles (49%) after bubble passage	0.70 ± 0.22	0.72	0.08	0.68	50

not been included in the calculation and discussion below.

In Table 6.1, the average impact velocities and impact angles for each of the three classifications, as well as the overall average velocity, are listed. Listed also is the average bubble rise velocity, determined by tracking the interface of bubble voids and bubble wakes from about 40 mm below the tube bottom to about 40 mm above the tube top. Particles in bubble caps had an average impact velocity of 0.35 m/s, much smaller than the average bubble velocity of 0.62 m/s. Since particles in the cap were densely packed, the interaction of particles reduced the impact velocity for cap particles. On the other hand, for particles in bubble wakes, the average impact velocity was 0.70 m/s, very close to the bubble velocity since the tube was surrounded by dilute phase before impact. For the same reason, particles in the bubble wake impacted more directly and had an average impact angle of 50°, larger than the average impact angle of 38° determined for particles in bubble caps. The latter were somewhat diverged due to particle-particle interactions as the nose of the bubble approached. This trend is also apparent in Figure 6.2. The bubble cap and wake particles constituted 95% of total impact particles. Particles inside bubbles only constituted 5% of the total number of impacting particles, although the average velocity of these particles was higher, 0.80 m/s.

The period for significant particle motion around a tube due to passage of a single bubble lasted about 0.15 – 0.35 s. Intensive particle impact in bubble caps or wakes occupied a shorter period, of the order of 0.05 s. Figure 6.3 shows particle impact velocity vs. time. Since few particles inside the bubbles struck the tube, these are not included in the figure. The figure clearly shows two peaks for each bubble passage, with the lower ones representing bubble caps and the higher ones bubble wakes. The average velocity of the bubbles is plotted as a horizontal dotted line.

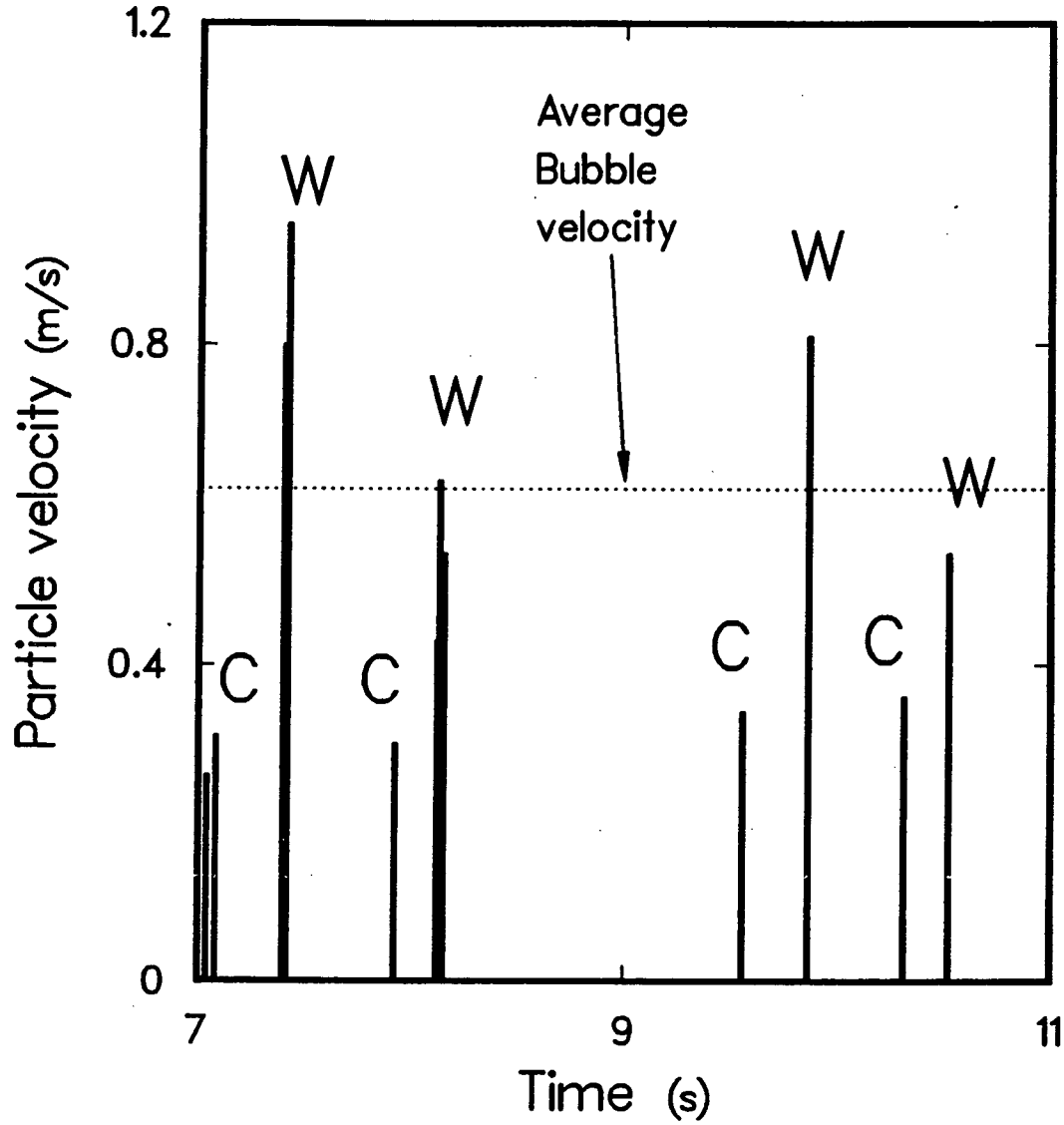

Figure 6.3 Particle velocity vs. time for single bubble injection experiment at minimum fluidization with 1.0 mm silica sand (Filming speed is 200 frames/s.)

C – Bubble caps
W – Bubble wake

As concluded in Chapter 5, impact angle is an important factor in the erosion process. Impact angles are plotted against the angular position on the tube surface where impact occurs in Figure 6.4. As expected, the impact angle decreased as the surface location moved around from the bottom of the tube towards the equator. This is because bubbles in this experiment all rose vertically so that particle trajectories for different bubbles were quite consistent. The impingement angles for impact particles inside the bubble were all larger than 90° since they impacted on the upper surface of the tube. They are not included in Figure 6.4.

Figure 6.5 provides the velocity distribution of all three groups of particles upon impact. There are clearly two peaks corresponding to particles in bubble caps and wakes. Also note that the distribution is wide. As discussed in Chapter 5, erosion rates are proportional to $V_p^{2.3}$. therefore the 2.3 power mean of the impact velocity, defined as $\{\Sigma V_p^{2.3}/n\}^{1/2.3}$, is more meaningful to the erosion process. The overall and 2.3 power mean velocities of particles upon impact for each classification are also listed in Table 6.1, together with the 2.3 power mean velocity of bubbles. The 2.3 power mean values are different from the arithmetic mean impact velocities due to the wide distributions of the particle impact velocities.

6.2 Coalescing Bubbles

In the experiments with coalescing bubble pairs, the conditions were the same as in the single bubble injection experiments, except that the bubbles were injected as pairs at such intervals that the two bubbles in each pair coalesced at or just below the bottom of the horizontal tube. The amount of air injected for each bubble was still $2.3 \times 10^{-4} m^3$, but the bubble shape in the vicinity of the tube was different from that of single bubble due to interaction of the coalescing bubble pair.

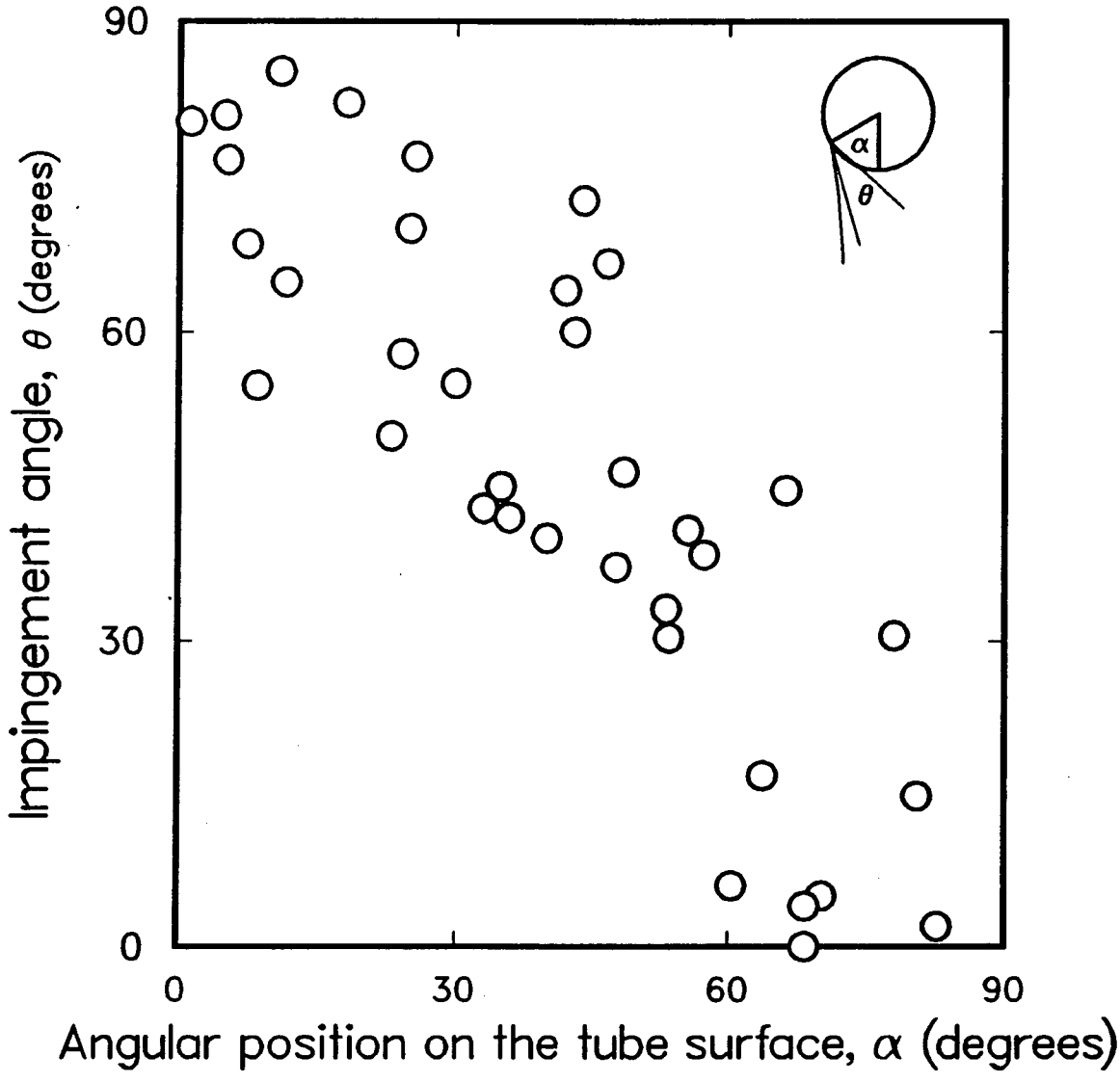

Figure 6.4 Impingement angle vs. angular position on tube for single bubble injection experiment at minimum fluidization with 1.0 mm silica sand

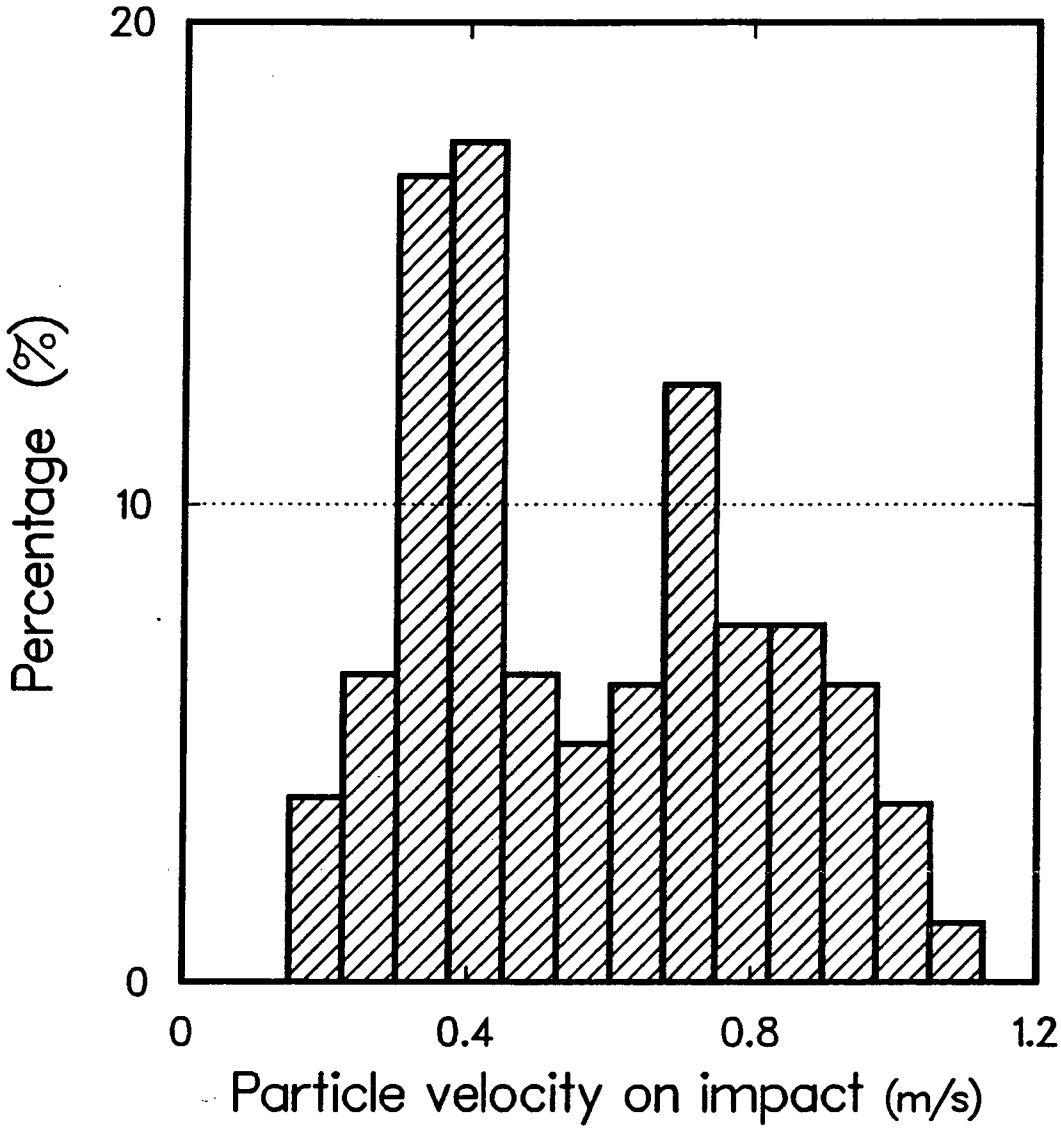

Figure 6.5 Particle velocity distribution for single bubble injection experiment

Table 6.2 summarizes the film analysis results. In this experiment, particles striking the tube were again classified into three groups: particles in first bubble cap, particles in the first bubble wake (also the second bubble cap) and particles in the second bubble wake. Particles inside bubbles reaching the tube surface were very few in number and were not separately classified but were included with the corresponding wake particles. The bubble velocities were determined by tracking the bubble void wake interface from about 40 mm below the tube bottom to the tube bottom or until the bubble wake had been pierced by the lower bubble, whichever came first.

Figure 6.6 provides a detailed view of a pair of coalescing bubbles passing the horizontal tube. Until the bottom of the first bubble reached the tube, the situation was very similar to that for the single bubble experiments. The arrival of the cap of the first bubble caused particles at front to be pushed along the tube bottom as for single bubbles, but with a slightly higher impact velocity, 0.39 m/s, probably due to interaction with the following bubble (Clift & Grace, 1970). The average impact angle is 40°, the same as in the single bubble injection experiment. As the first bubble enveloped the tube, the second bubble followed quickly and elongated. When the wake of the first bubble was about to impact, or was impacting, on the tube bottom, the roof of the second bubble broke through. The thin wall between the two coalescing bubbles just prior to break-through was accelerated upwards, throwing those particles against the tube bottom with an average velocity of 1.30 m/s, much higher than the velocity of either of the original bubbles (see Table 6.2). The average impact angle was 40°, the same as the particles in bubble cap. The acceleration of wake particles for an upper bubble when a second bubble catches up from behind has already been noted at the upper surface of fluidized beds where it can cause vigorous splashes of solids into the freeboard (Do et al. 1972). Evidently, when coalescence takes place near a

Table 6.2: Results of film analysis for bubble coalescence experiment

Operating conditions:

Sample size:	99 particles 9 pairs of bubbles
Background superficial velocity:	0.72 m/s, i.e. u_{mf}
Tube size:	32 mm
Particles:	1.0 mm silica sand
Filming speed:	200 frames/s

	Average velocities (m/s)				
	Mean ± Standard deviation	2.3 power mean	Horizontal Component	Vertical Component	Impact Angle (degrees)
Leading bubbles *	0.75 ± 0.10	0.75			
Overtaking bubbles *	0.96 ± 0.11	0.97			
Particle (overall average)	0.92 ± 1.00	1.09	0.12	0.88	44
Particles (23%) before first bubble arrived	0.39 ± 0.12	0.38	0.11	0.36	40
Particles (43%) between two bubbles	1.30 ± 0.44	1.44	0.18	1.24	40
Particles (34%) after departure of composite bubble	0.79 ± 0.24	0.82	0.03	0.78	51

* Average velocities determined from bubble/wake interface movement in the zone within 30 mm below the tube bottom.

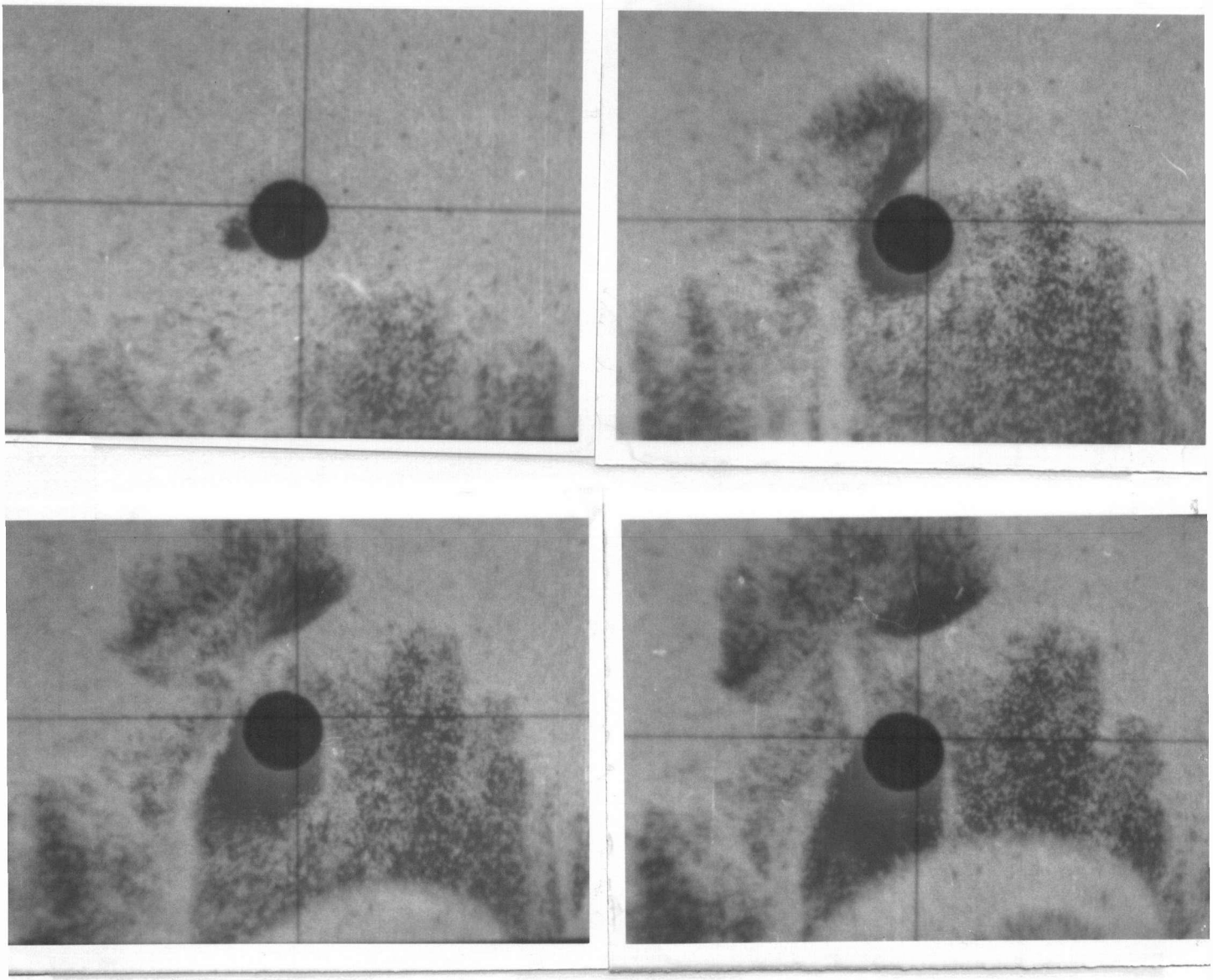

Figure 6.6 Photographs of sequence of two bubbles coalescing just beneath a horizontal tube in two-dimensional column

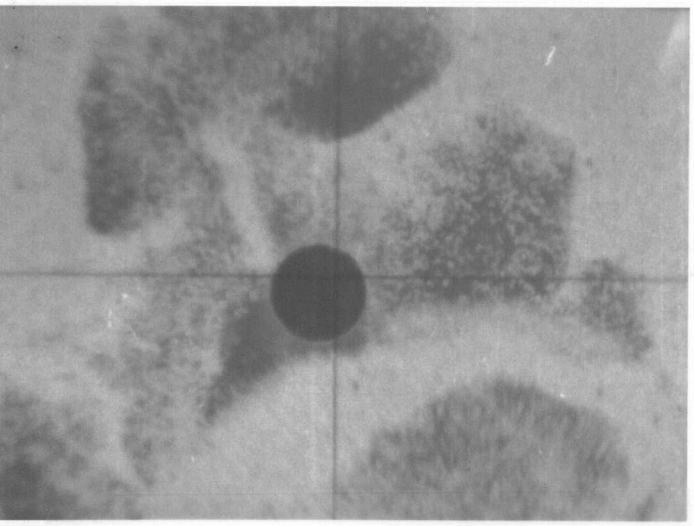

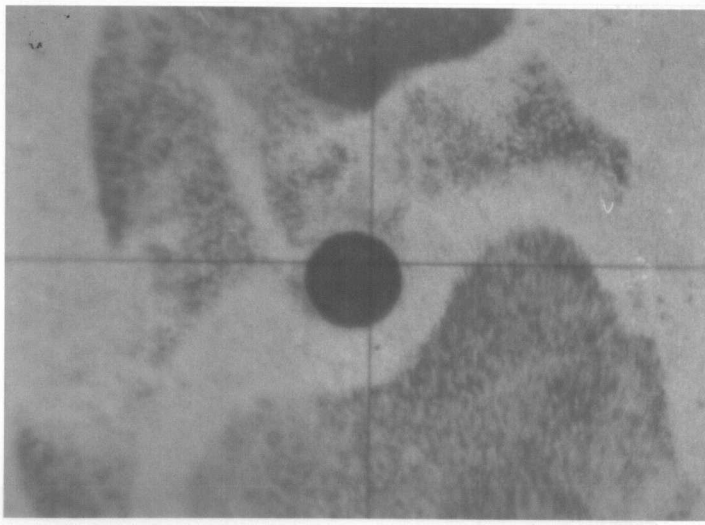

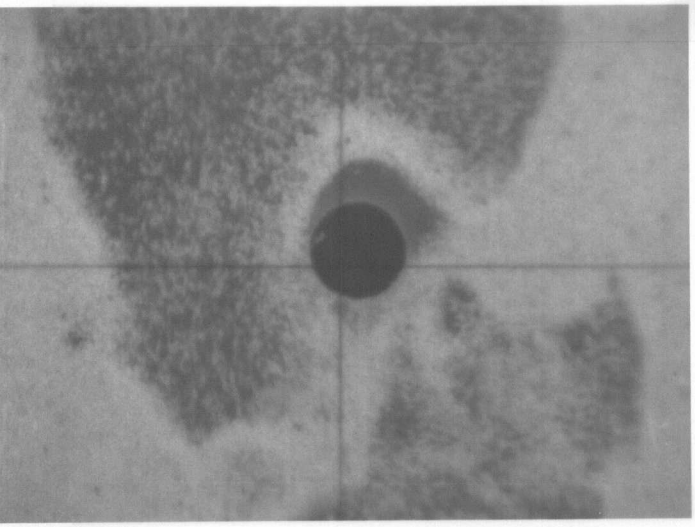

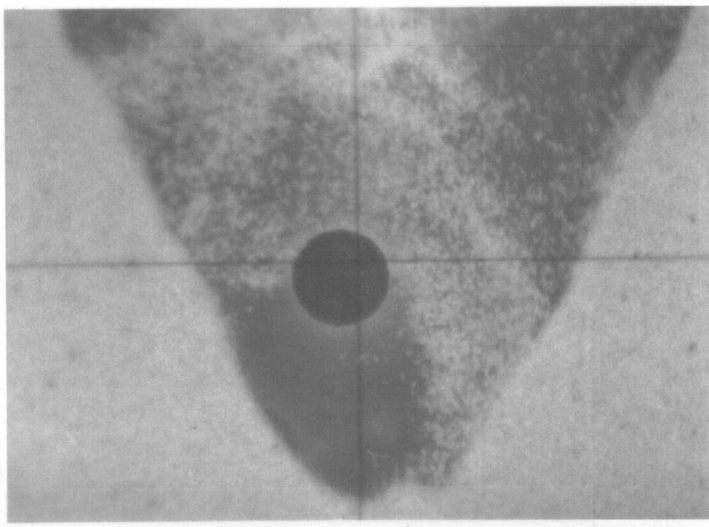

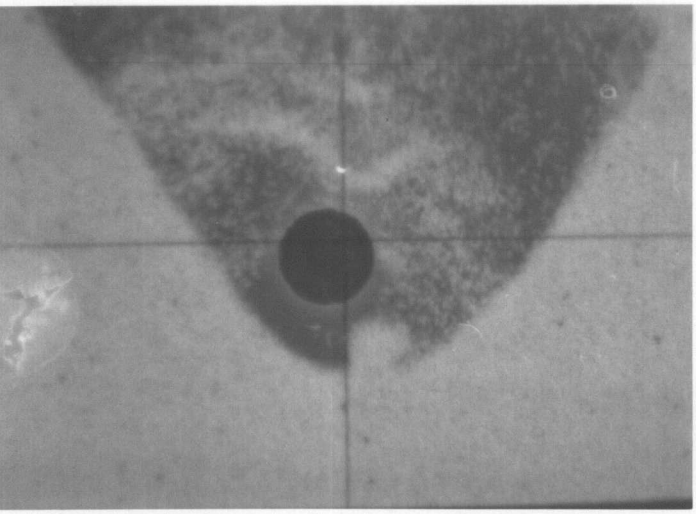

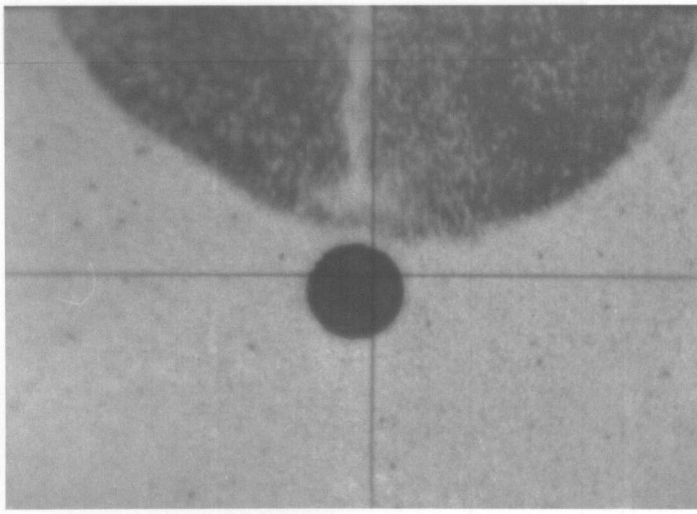

tube, a similar process occurs, causing greatly increased impact velocities with the tube bottom. Since erosion is a strong function of impact velocity, these relatively high velocity impacts due to coalescence may be important in the erosion process in freely bubbbling beds.

The newly formed bubble immediately enveloped the tube, and some particles were dislodged from the bubble roof, forming a small cap on top of the tube as before. As the wake of the second bubble, now the wake of the newly formed composite bubble, arrived at the tube bottom, particles in the wake were carried up too, impacting on the tube bottom. The mean impact velocity of these particles was 0.79 m/s, somewhat larger than that measured in the single bubble injection experiment (see Table 6.1). The average impact angle of wake particles was 51° now, again larger than the average angle for cap particles for the same reason as for single bubbles (see above). After the departure of the second bubble, dense phase reappeared around the tube.

Figure 6.7 shows a plot of particle velocity vs. time for particles which strike the underside of the tube. The duration of the disturbance caused by passage of a pair of coalescing bubbles was only about 0.35 to 0.60 s. The very small number of particles impacting on to the upper surface of the tube when the tube was enveloped by bubbles are excluded. The three sharp peaks for each cluster in the figure represent particles in the bubble cap, the first bubble wake (also second bubble cap) and the second or composite bubble wake. The average velocities of the two bubbles are also shown as horizontal dotted lines. It is clear that particles in the first bubble wake had a much higher mean velocity than the bubble average velocity.

Figure 6.8 gives the velocity distribution of all particles upon impact with the underside of the tube. There are two peaks in this distribution, the first is the combination of particles

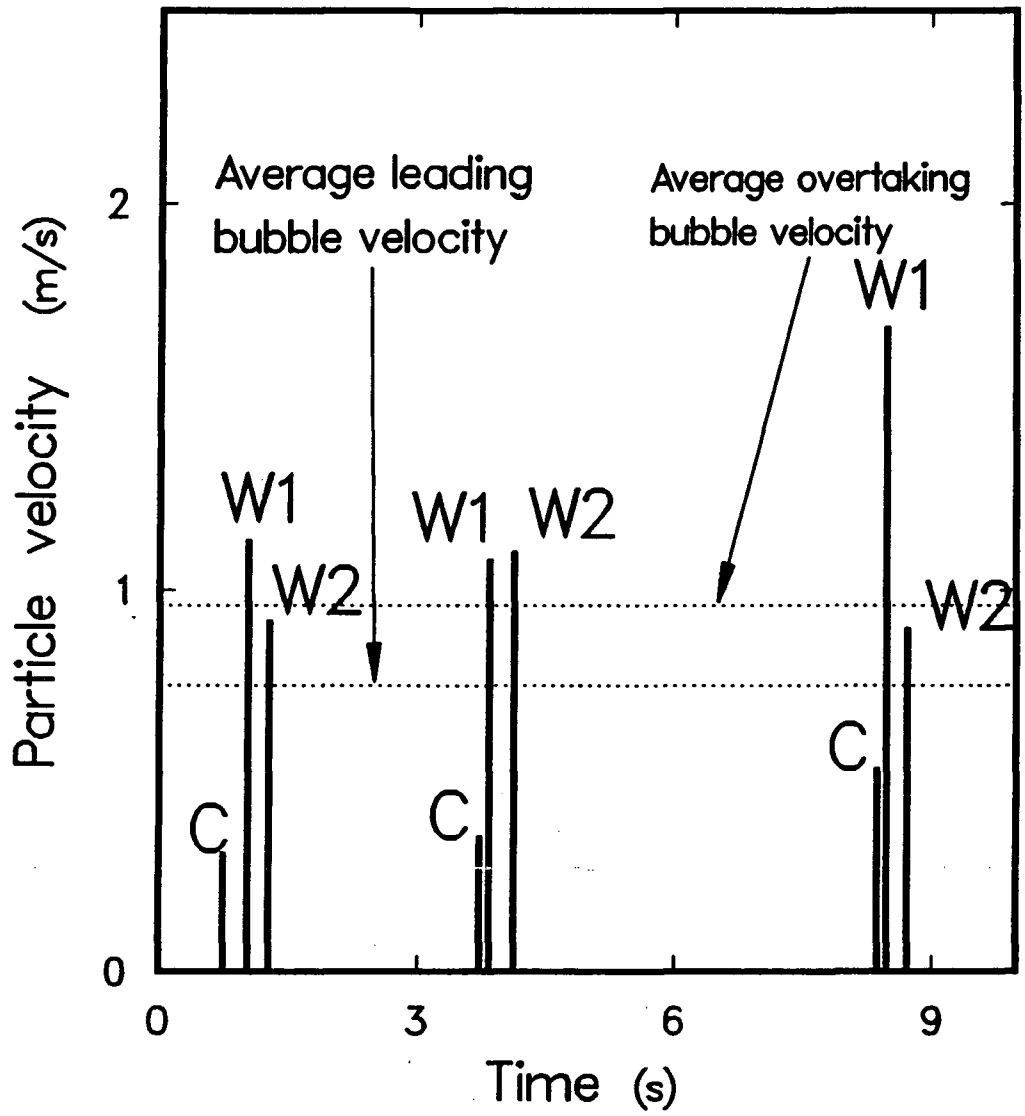

Figure 6.7 Particle velocity vs. time for bubble coalescing experiment at minimum fluidization with 1.0 mm silica sand (Filming speed is 200 frames/s.)

C – Bubble caps
W1 – Wake of first bubbles
W2 – Wake of second bubbles

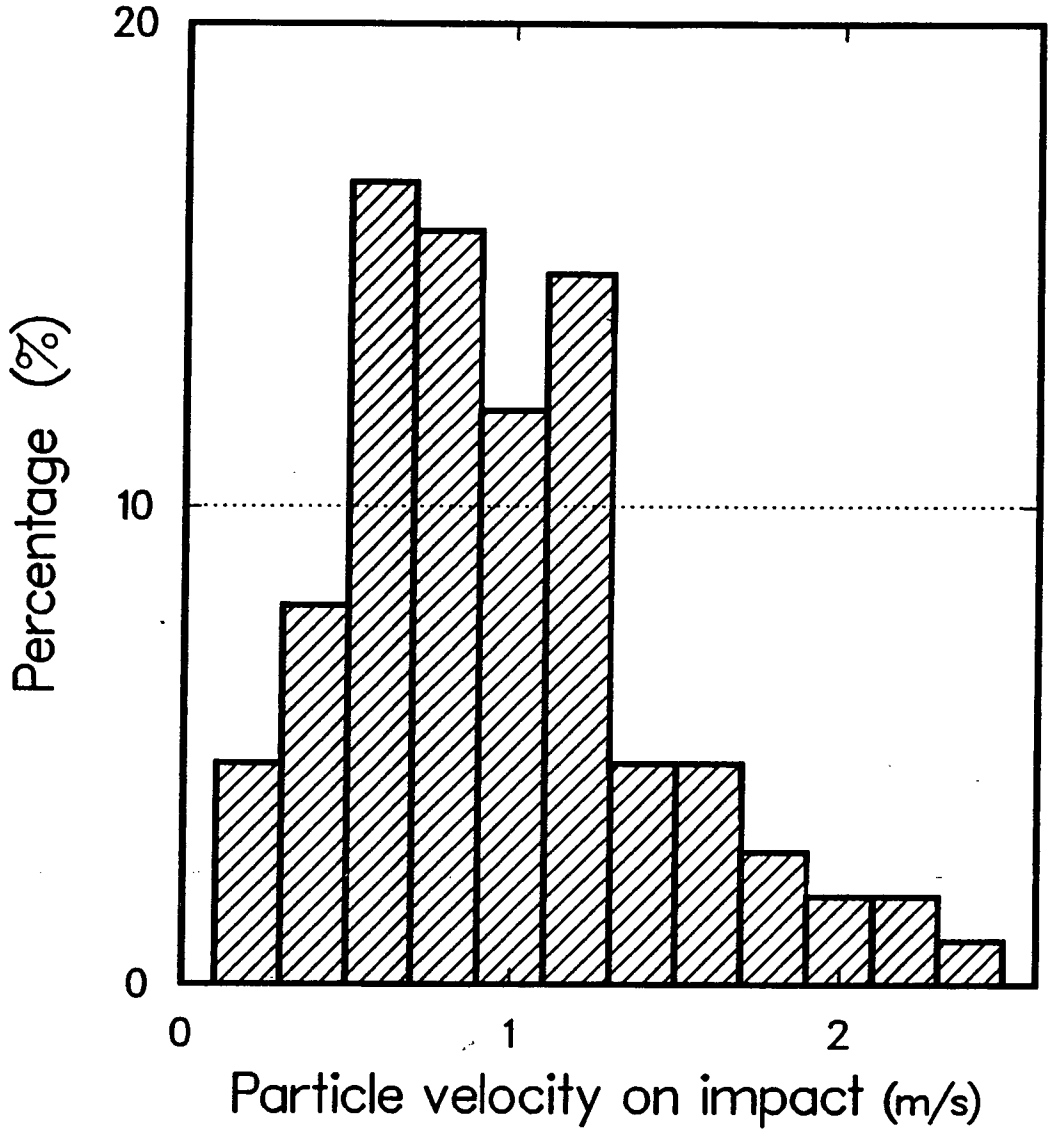

Figure 6.8 Particle velocity distribution for bubble coalesence experiment

in the bubble cap and in the second bubble wake. The second represents particles in the first bubble wake. This distribution had a long tail at the right side, which caused the 2.3 power mean of the velocity to be significantly higher than the mean velocity, as tabulated in Table 6.2.

6.3 Free Bubbling with Single Tube

For the fully bubbling bed experiments, a single tube of outside diameter 32 or 29 mm was installed 308 mm above the air distributor. The static bed height was 320 mm. Air superficial velocities were 1.87 and 1.19 m/s.

Under free bubbling conditions, small bubbles formed immediately above the the multi-orifice plate distributor. These bubbles coalesced and grew quickly as they rose in the bed, and their rising velocity increased as their size increased. The larger bubbles tended to converge to the central part of the bed in the normal manner (Clift & Grace, 1985) where they continued to coalesce vigorously and finally erupted at the bed surface. In the vicinity of the tube, which was at the centre of the bed cross-section, the average solid particle concentration was much smaller than in the rest of the bed due to bubble coalescence. For the $u = 1.19$ m/s test, the tube was surrounded by bubble phase approximately 40 – 50% of the time. For the $u = 1.87$ m/s test, the solid concentration was so small that the tube was actually surrounded by dilute phase most of the time (see Figure 6.9). Voids under these conditions did not have regular shapes as in the single bubble experiment, but were elongated or flattened due to interaction and frequent violent coalescences. At the level of the tube, air passed through the bed in the form of elongated voids or bubble chains. The bubbles or bubble chains also did not rise vertically, but appeared to adopt trajectories with random orientation within about 40° from the vertical.

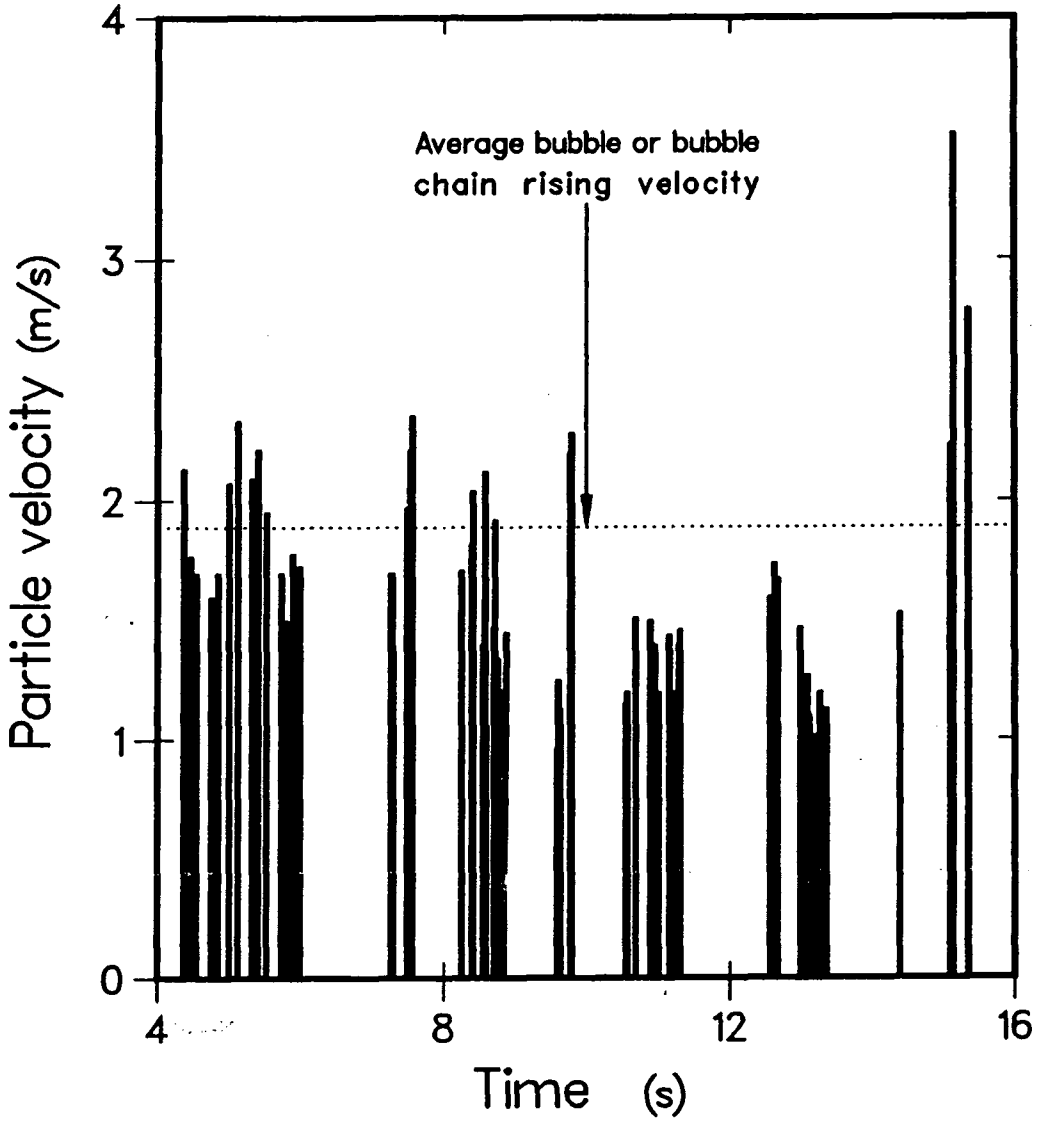

Figure 6.9 Particle velocity vs. time for free bubbling at u = 1.87 m/s with 1.0 mm silica sand (Filming speed is 200 frames/s.)

As a bubble or a chain of bubbles reached the tube, the particles in the bubble caps were pushed over the tube surface as in the case of the single bubbles (see Section 6.1). When bubbles passed the tube, however, they tended not to split and pass around the two sides of the tube. Instead, most of the time a bubble would swerve to pass along one side of the tube causing a thin layer of particles on that side to scrape over the tube surface. As the bubble or bubble chain left the tube, particles in the bubble wake slammed into the lower surface of the tube. The tube was then quickly surrounded or partly immersed by dense phase, but periods of submergence, before the next bubble or bubble chain arrived, were very brief, typically 0.5 to 1 s.

In the film analysis, it was not practical to classify the impacting particles as before in view of the much more chaotic hydrodynamic conditions. Instead, the impacting particles were grouped according to the tube sector in which they impacted, as shown in Figure 6.10. This permitted correlation of local erosion rates with local hydrodynamic conditions. Cases where particles fell onto the upper tube surface were found to be extremely rare and were therefore neglected.

Table 6.3 summarizes the results for the test with $u = 1.87$ m/s. The average bubble velocity is 1.95 m/s, and the overall mean particle velocity is 1.91 m/s. About 4% of the particles impacted in zone 3, while the rest of the particles were distributed more or less equally between zones 1 and 2 (see Figure 6.10). The average impact angle of the particles was 60°. The average impact velocities in zone 1 and zone 2 were 1.98 and 1.85 m/s, close to the bubble or bubble chain average velocity of 1.95 m/s. The average impact velocity in zone 3 was only 1.37 m/s since it was difficult for particles in the bubble cap and wake to impact directly onto that sector of the tube: instead, particles on the bubble sides were pushed against zone 3 when a bubble or bubble chain passed to one side of the tube. Those

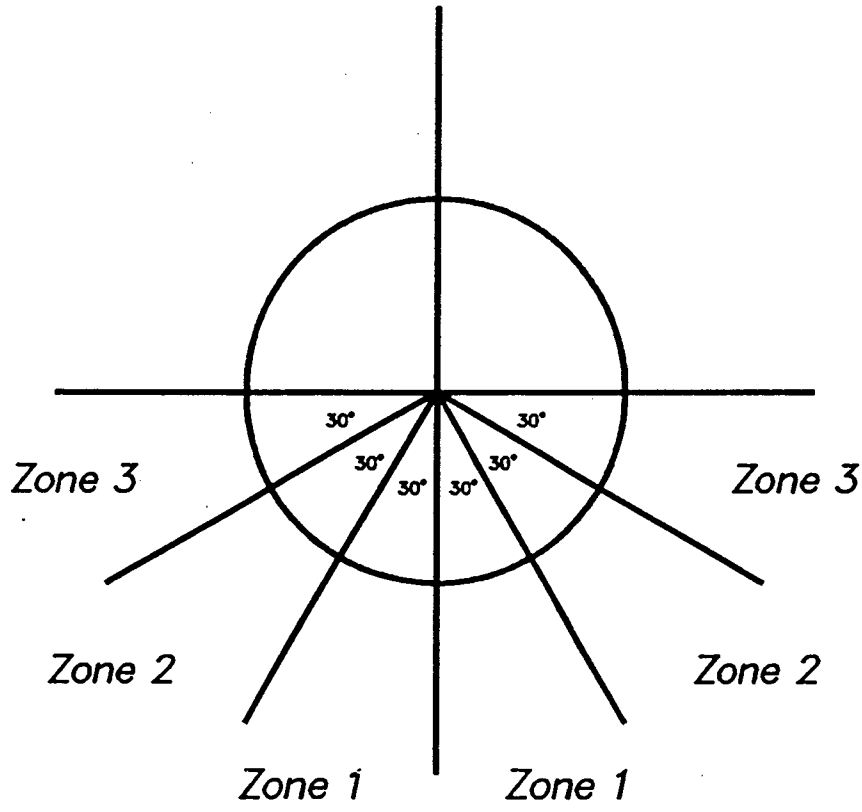

Figure 6.10 Particle classifications for free bubbling experiments

Table 6.3: Results of film analysis for free bubbling with u = 1.87 m/s

Operating conditions:

Sample size:	165 particles
Gas superficial velocity:	1.87 m/s
Tube size:	32 and 29 mm
Particles:	1.0 mm silica sand
Filming speed:	200 and 600 frames/s

	Average velocities (m/s)				
	Mean ± Standard deviation	2.3 power mean	Horizontal Component	Vertical Component	Impact Angle (degrees)
Bubbles *	1.95 ± 0.42	2.09			
Particle (overall average)	1.91 ± 1.50	2.16	0.67	1.73	60
Particles (44%) impact on zone 1	1.98 ± 0.57	2.24	0.64	1.83	64
Particles (52%) impact on zone 2	1.85 ± 0.69	2.15	0.70	1.67	58
Particles (4%) impact on zone 3	1.37 ± 0.35	1.47	0.82	0.92	38

* Average velocities determined from bubble/wake interface movement in the zone within 30 mm below the tube bottom.

particles on the bubble sides may have had smaller impact velocities in zone 3 due to the interaction with other particles in the dense phase which were relatively stagnant. The average impact angle in zone 3 was small because the angle between the tube surface and the vertical is small for this zone. However, particles impacting in zone 2 had roughly the same average impact angle as particles impacting in zone 1. This appears to be due to the fact that bubbles did not rise vertically but with an average angle of 29° from the vertical.

Figure 6.11 shows the impact angle distribution at different tube angular positions for free bubbling at $u = 1.87\ m/s$. The figure indicates that the impact angle tends to decrease as the angle from the bottom of the tube increases, although the distribution of particle impact angles at any position on tube surface was very wide.

The film analysis results for the test with $u = 1.19\ m/s$ are tabulated in Table 6.4. The average particle impact velocity was 0.82 m/s, very close to the average bubble rising velocity measured to be 0.80 m/s. The average velocities of particles impacting on the three zones were, as anticipated, smaller than those for the $u = 1.87\ m/s$ test. The overall average impact angle and average impact angles for the three zones were smaller too. This may be due to the fact that the slower movement of bubbles as they passed the tube allowed more time for particles to alter their flow direction, causing more shallow angles of impact.

From Tables 6.3 and 6.4, it is shown that the average impact particle velocities for both $u = 1.87$ or $u = 1.19\ m/s$ are within 3 % of the corresponding average bubble velocities. The 2.3 power mean values are very close too. This suggests that bubble rise velocity can be used as the approximation for impact particle velocity. Asai et al. (1984) also found that particle velocities in the vicinity of tubes in fluidized bed are close to the bubble rise velocities.

Figures 6.12 and 6.13 give particle impact velocity distributions for the above two

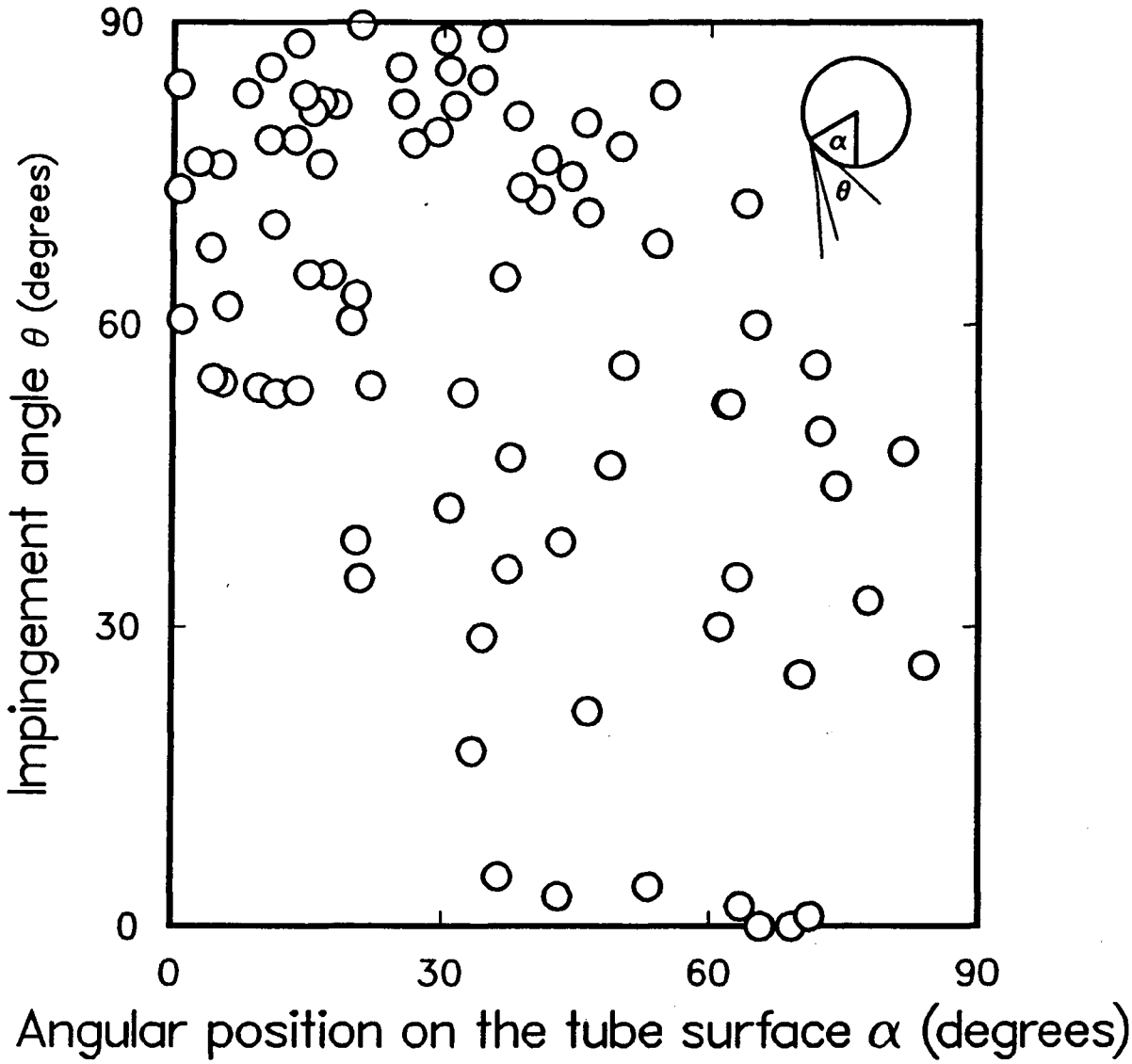

Figure 6.11 Impingement angle vs. angular position on tube for free bubbling experiment at 1.87 m/s air superficial velocity and with 1.0 mm silica sand

Table 6.4: Results of film analysis for free bubbling with u = 1.19 m/s

Operating conditions:

Sample size:	60 particles
Gas superficial velocity:	1.19 m/s
Tube size:	29 mm
Particles:	1.0 mm silica sand
Filming speed:	600 frames/s

	Average velocities (m/s)				
	Mean ± Standard deviation	2.3 power mean	Horizontal Component	Vertical Component	Impact Angle (degrees)
Bubbles *	0.80 ± 0.20	0.86			
Particle (overall average)	0.82 ± 0.97	0.94	0.50	0.53	32
Particles (40%) impact on zone 1	0.92 ± 0.40	1.01	0.59	0.54	40
Particles (40%) impact on zone 2	0.78 ± 0.43	0.91	0.42	0.51	26
Particles (20%) impact on zone 3	0.75 ± 0.29	0.80	0.22	0.65	17

* Average velocities determined from bubble/wake interface movement in the zone within 30 mm below the tube bottom.

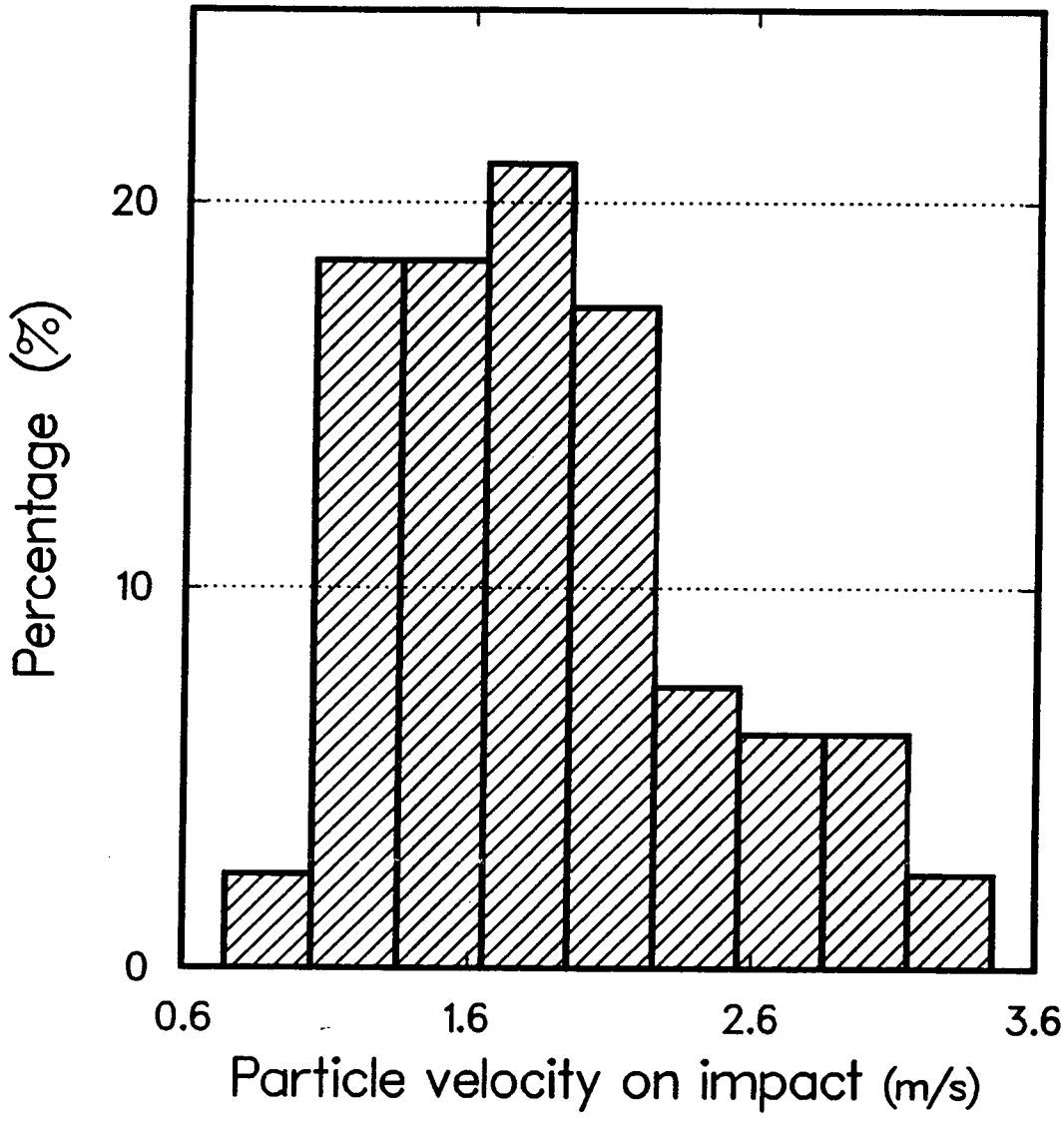

Figure 6.12 Particle velocity distribution for free bubbling with u=1.87 m/s

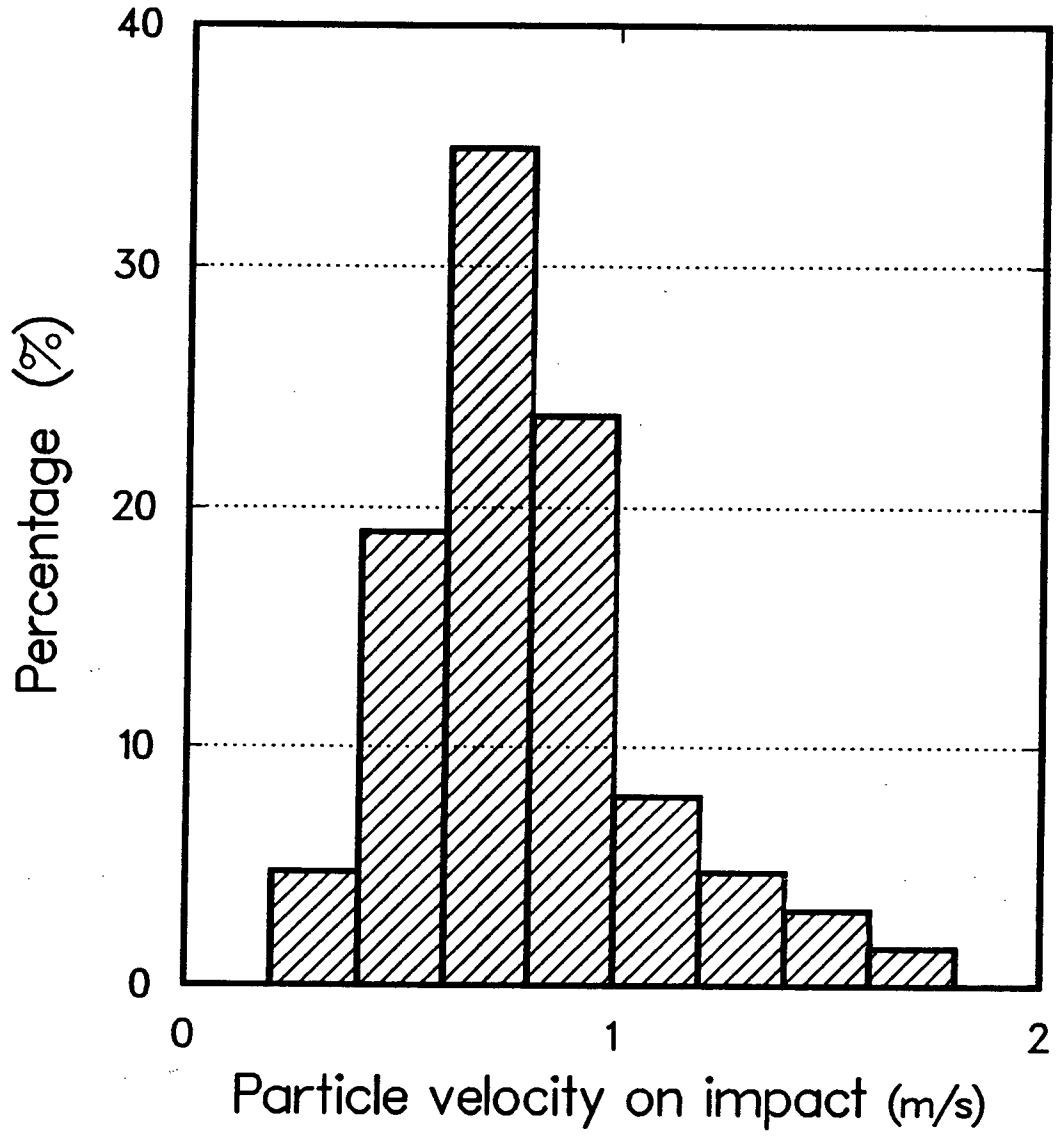

Figure 6.13 Particle velocity distribution for free bubbling with u=1.19 m/s

conditions. Both figures show that the distributions were not normal. Instead, there were a small number of particles having very high impact velocities. This caused the 2.3 power mean of overall impact particle velocities for both tests to be significantly higher than the arithmetic mean velocities. The 2.3 power mean bubble velocities were also higher for both tests (see Tables 6.3 and 6.4).

6.4 Free Bubbling with Tube Bundle

Tests were also conducted with a five-tube bundle having the same configuration as in the three-dimensional column (see Figure 3.9). The operating conditions were the same as for the single tube test with $u = 1.87\ m/s$, except that a bundle of five tubes, the central tube of 29 mm o.d. and four other tubes of 32 mm o.d., was in place instead of a single 32 mm o.d. tube. The bubbles inside the bed behaved in roughly the same way as in the single tube case, but the bubble motion within the tube bundle was retarded dramatically. The four tubes around the test tube acted as barriers, and some bubbles swerved to pass outside the two upstream tubes. For those bubbles which did make their way between these two tubes, the velocity of the bubbles and particles tended to be significantly smaller than for the single tube case. The average bubble velocity inside the tube bundle could not be determined because the bubble shape was not well defined.

Details of the tests and measured particle velocities are provided in Table 6.5. The classification of impact particles is as shown in Figure 6.10. The average particle velocity was 0.87 m/s and the overall average impact angle was 38°. The average impact particle velocities in each of the three groups were smaller too, but the average impact particle velocity for group 3, relative to those for groups 1 and 2, was not as small as that for free bubbling at $u = 1.87 m/s$ with a single tube. The average overall and group impact

Table 6.5: Results of film analysis for free bubbling with u = 1.87 m/s with a five tube bundle

Operating conditions:

Sample size:	71 particles
Gas superficial velocity:	1.88 m/s
Tube size:	29 mm
Particles:	1.0 mm silica sand
Filming speed:	600 frames/s

	Average velocities (m/s)				
	Mean ± Standard deviation	2.3 power mean	Horizontal Component	Vertical Component	Impact Angle (degrees)
Particle (overall average)	0.87 ± 1.00	1.20	0.39	0.65	38
Particles (53%) impact on zone 1	0.93 ± 0.83	1.36	0.39	0.71	51
Particles (36%) impact on zone 2	0.84 ± 0.45	0.98	0.41	0.60	25
Particles (11%) impact on zone 3	0.72 ± 0.50	0.89	0.27	0.58	15

angles were also smaller than those for the single tube test under the same conditions. The above differences may well be because the presence of the four other tubes, especially the upstream pair, alters the particle flow direction and causes more interaction between the particles and tubes.

Figure 6.14 shows the impingement angle distribution for this tube bundle test. Compared with Figure 6.11, the impingement angles were generally smaller than for the single tube case, although still with a very wide scatter. Some particles impacting in zone 3 had a tendency to impact with an impingement angle shallower than 10°. This is of importance since erosion caused by particles impacting with very shallow angles has a different mechanism and tends to be significantly reduced, at least for high velocity erosion (Tilly, 1979).

The impact particle velocity distribution for the tube at the center of the bundle is shown in Figure 6.15. There is only one peak and the distribution is narrower than that for a single tube under the same conditions. This may result from the limitation of particle movement due to presence of the other four tubes.

The fact that some bubbles tended to swerve to miss the tube assembly suggests that different results may have been obtained if the tube bank had extended across the entire cross-section of the column. However, the data obtained from the bubbles which did penetrate the tube bundle should at least give a semi-quantitative indication of what would have occurred if more bubbles had passed through the tube bank, although the number of particle impacts was smaller.

6.5 Viewing from Inside the Tube

Two films were taken from inside the tube with a single tube, 29 *mm* o.d., and gas

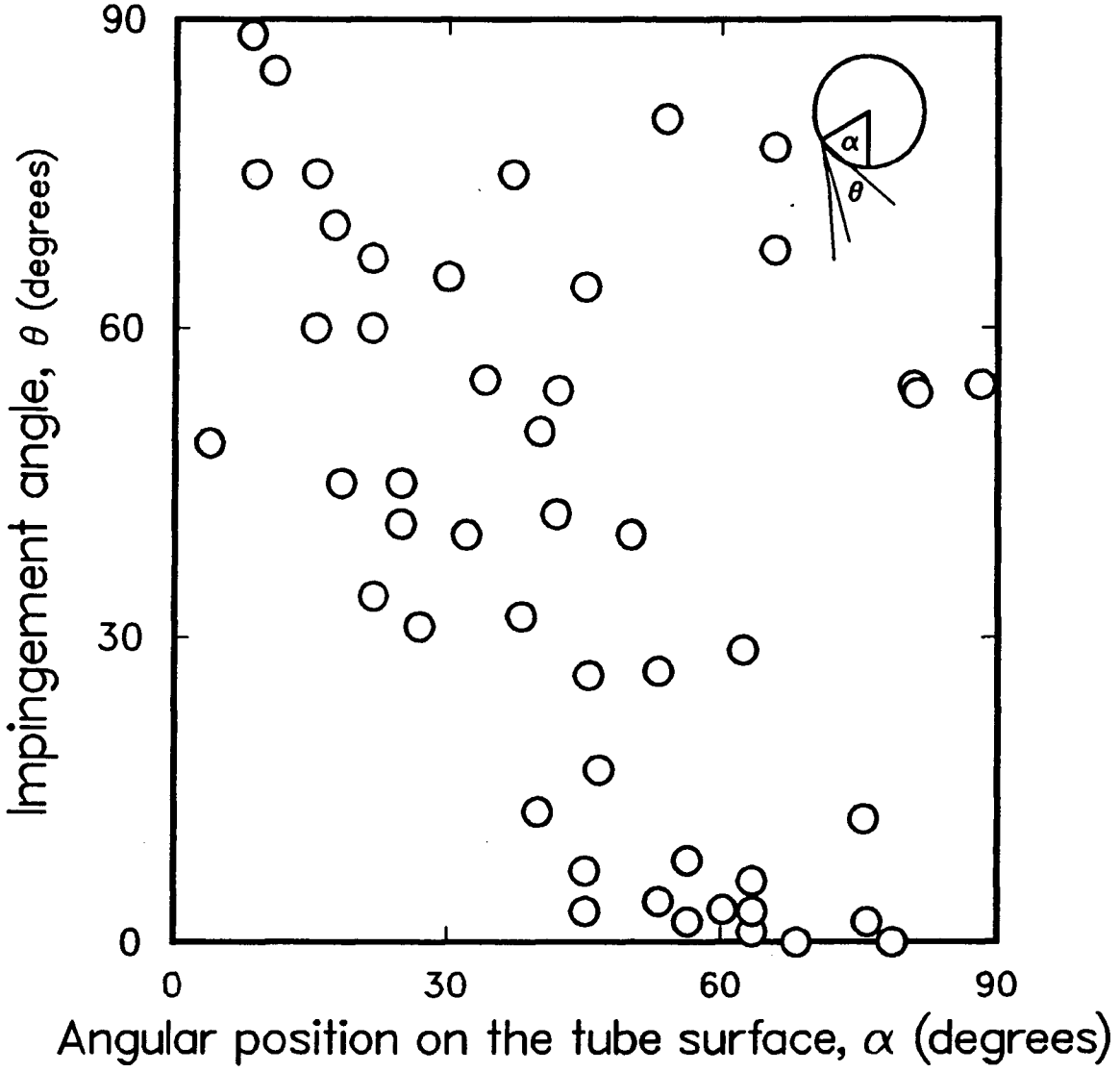

Figure 6.14 Impingement angle vs. angular position on tube for free bubbling experiment at 1.87 m/s air superficial velocity and with 1.0 mm silica sand and tube bundle of five

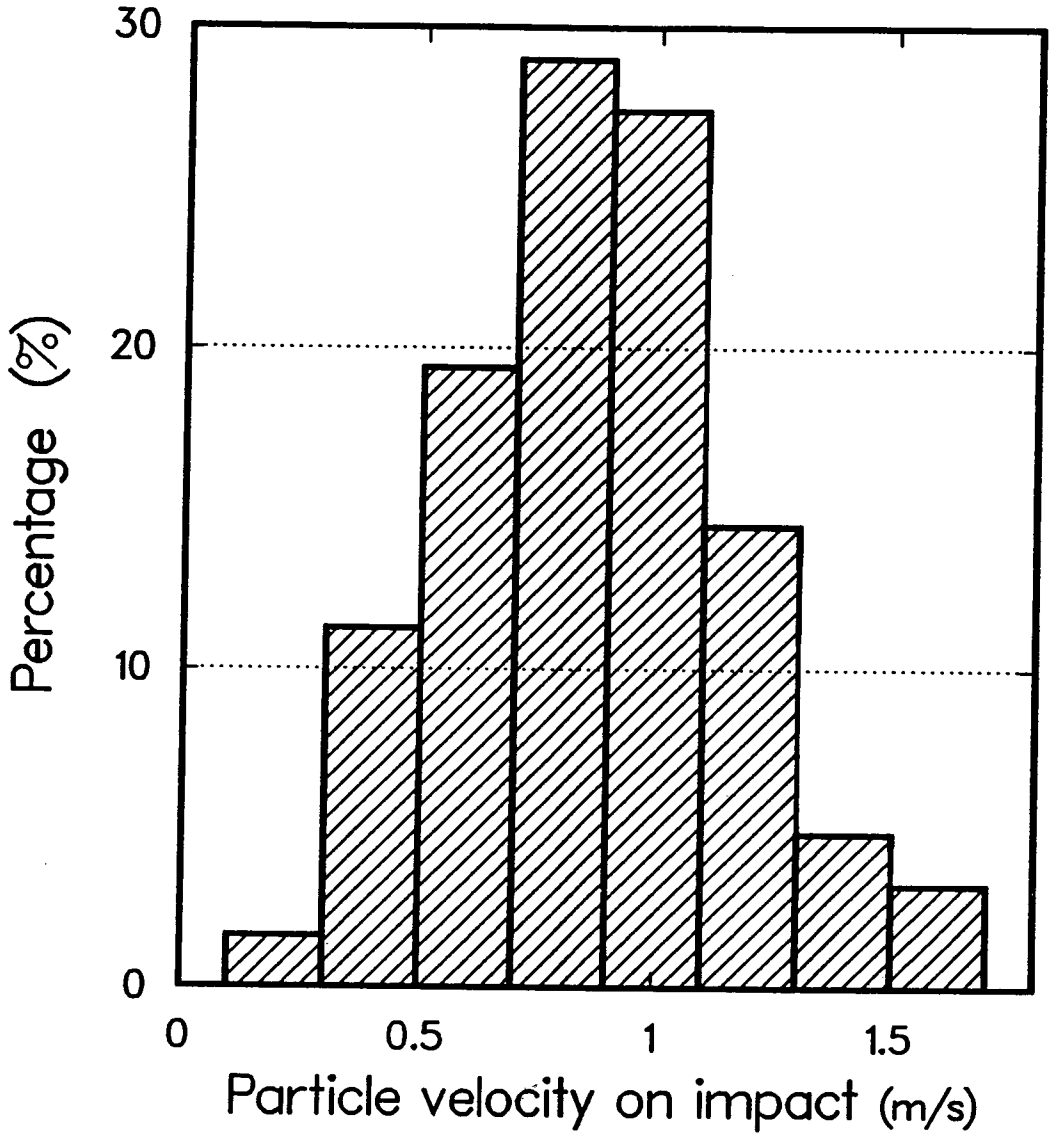

Figure 6.15 Particle velocity distribution for free bubbling with u=1.87 m/s with tube bundle

superficial velocities of 1.19 m/s and 1.87 m/s. The operating conditions were the same as those described in Section 6.3. The films showed clearly the particle movement on the tube surface. The four mirrors inside the tube were labelled as shown in Figure 6.16.

Table 6.6 details the results obtained from these two films. Compared with Tables 6.3 and 6.4, the average particle velocities for the right and left sides were very close to the average velocities of particles impacting in zone 3 of the two corresponding tests. However, the particle velocities determined for the top and bottom quarters were significantly smaller.

The results in Table 6.6 can only be treated as a qualitative or, at best, semi-quantitative indication of particle movement. They cannot be considered to be accurate quantitative results because: (1) The particle path sometimes tended to be distorted when it was projected onto the mirror surface, since it was not possible to distinguish totally between particles travelling against the tube surface from particles travelling some distance away from the tube (Figure 6.17). This tends to lead to overestimates of the particle velocity. This was particularly significant for particles moving over the top and bottom quarters. (2) The view was very restricted so that both the sample size and the accuracy of each sample were limited. Notwithstanding these limitations, Table 6.6 gives the order of magnitude of the velocities of particle scraping along the tube surface.

For the two-dimensional column considered in this chapter, viewing from inside the tube provides little or no information which could not be obtained by filming the outside of the column. However, viewing from the outside is not an option for the interior of a three-dimensional column. In that case, the results presented here indicate that viewing from the inside provides the order of magnitude of particle velocities at the surface, but that caution is needed when making quantitative measurements, especially at the top and bottom of the tube where the particles have appreciable components of velocity normal to

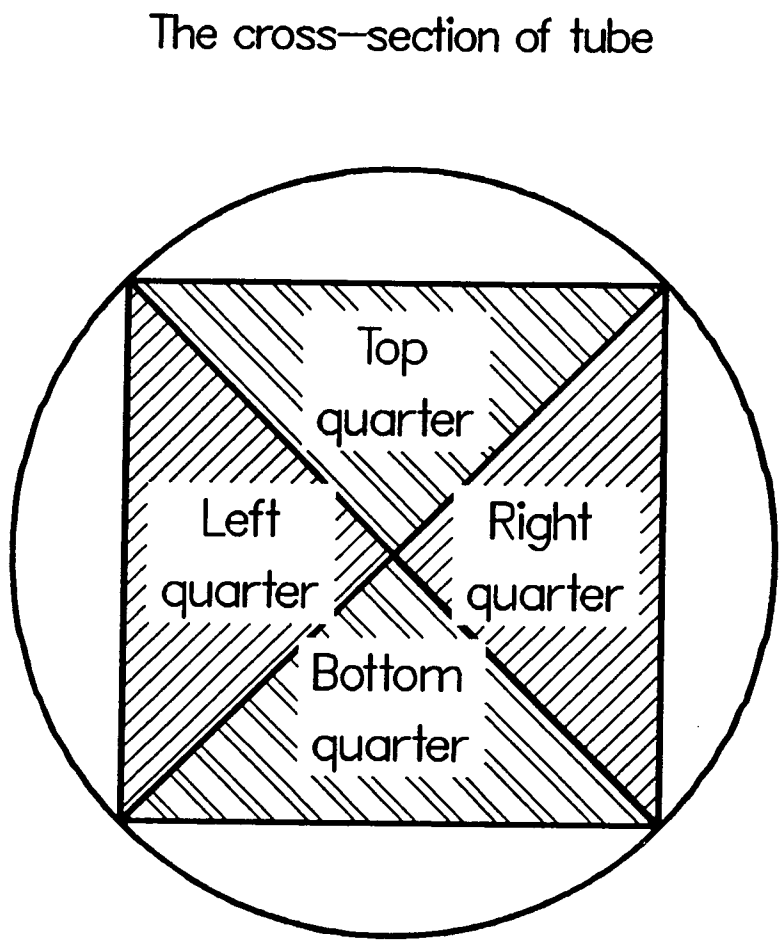

Figure 6.16 Impact particle classifications for viewing from inside the tube

Table 6.6: Results of film analysis for free bubbling at u = 1.19 and 1.87 m/s for view from inside tube

Operating conditions:

Total sample size:	26 and 43 particles
Gas superficial velocity:	1.19 and 1.87 m/s
Tube size:	29 mm
Particles:	1.0 mm silica sand
Filming speed:	600 frames/s

	Average particle velocities and their standard deviations (m/s)	
	(1.19 m/s run)	(1.87 m/s run)
Top quarter view *	0.53 ± 0.24	1.29 ± 0.56
Bottom quarter view *	0.87 ± 0.62	0.89 ± 0.43
Right quarter view *	0.93 ± 0.24	1.38 ± 0.86
Left quarter view *	0.78 ± 0.32	1.51 ± 0.76

* See Figure 6.16

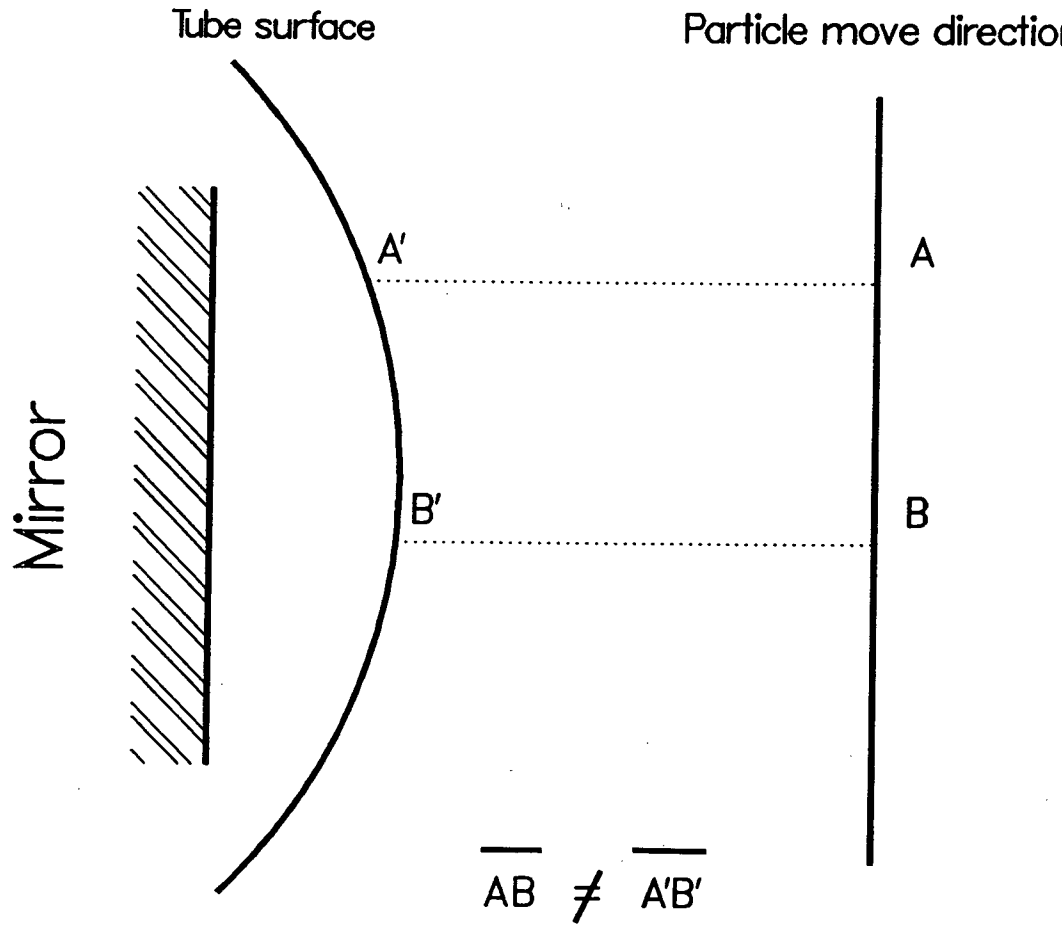

Figure 6.17 Distortion of distance due to mirror projection

the surface. The chief value of viewing from the inside is therefore likely to be qualitative. It is notable that cine photos taken from the inside by earlier workers (Peeler & Whitehead 1982, Webb 1986) appear to have been mainly used in this manner.

6.6 Conclusion

Table 6.7 summarizes the arithmetic and 2.3 power average bubble velocities, average particle velocities and average impact angles for all the two-dimensional experiments. The table shows clearly that average particle velocities are closely related to average bubble velocities. This indicates that particle motion in the vicinity of a tube is mainly caused by bubbles, not a surprising conclusion. When the bubble velocity decreased, not only did the impact velocity decrease, but the average impact angle also decreased. Increases in bubble velocity due to coalescence in the neighbourhood of the tube caused a significant increase in the impact velocity. The presence of two upstream and two downstream tubes effectively reduced particle impact velocities inside the tube bundle and caused more shallow impacts. Filming from inside the tube gave some estimate of particle scraping velocity on the tube surface and provides qualitative information about particle motion on the tube surface.

Table 6.7: Summary of results for film analysis of all experiments

Operating conditions:

Particles: 1.0 mm Silica sand
Tube sizes: 29 & 32 mm

	Average bubble velocity (m/s)	2.3 power mean bubble velocity (m/s)	Average particle velocity (m/s)	2.3 power Mean particle velocity (m/s)	Average impact angle (degrees)
Single bubble injection:	0.62	0.62	0.55	0.56	44
Bubble coalescence:	0.86	0.89	0.92	1.09	44
Free bubbling 1.19 m/s:	0.80	0.86	0.84	0.94	32
Free bubbling 1.87 m/s:	1.95	2.09	1.91	2.16	60
Tube bundle 1.87 m/s:	(*)	(*)	0.85	1.20	38

* Not available

CHAPTER SEVEN: RESULTS AND DISCUSSION: THREE-DIMENSIONAL ROOM TEMPERATURE EXPERIMENTS

As detailed in Section 3.1, the three-dimensional cold model (room temperature) fluidization column, equipped with a multi-orifice distributor plate, was used to measure the erosion rate under different operating conditions. The base case was silica sand of 1.0 *mm* mean diameter operated at a gas superficial velocity of 1.87 m/s with a single tube of diameter 32 *mm* containing rings of five tube materials - SS304, CS1050, Brass, Copper and Al2011. The tube was placed horizontally 308 *mm* above the distributor, and the static bed height was 320 *mm*. All rings were mounted in the central 70 *mm* section of the tube. Nine variables were changed, one at a time, to test the effect of different parameters. The conditions of the tests are tabulated in Table 7.1. The erosion rates were calculated from ring weight losses as described in Section 4.2. The rings were usually weighed after each 16 – 20 hours of operation to monitor the erosion process, while the overall duration of most of the runs was usually more than 50 hours to ensure the reliability of results.

7.1 Effects of Fluidizing Conditions

As discussed in Chapter 5, particle impact velocity, particle mass flow rate and particle properties can each have a very significant influence on erosion. In fluidized beds, these are determined by the fluidizing conditions.

7.1.1 Gas Superficial Velocity

With the 1.0 *mm* silica sand in place, the gas superficial velocity was varied from 0.88 m/s to 2.5 m/s. The results are shown in Figure 7.1. It is clear that the erosion rate increased as the superficial velocity increased for each of the materials.

Table 7.1: Operating conditions for tests in the low temperature three-dimensional bed

Run	Particles	Particle size d_p (mm)	Particle hardness H_p (kg/mm^2)	Particle Sphericity Φ_s	Excess air velocity $u-u_{mf}$ (m/s)	Tube diameter D_t (mm)	Operating duration (h)
1	Silica sand	1.02	350.	0.83	0.32	32.0	250.0
2	Silica sand	1.00	350.	0.83	1.32	32.0	60.0
3	Silica sand	1.00	350.	0.83	1.57	32.0	14.1
4	Silica sand	1.00	350.	0.84	1.30	32.0	120.1
5	Silica sand	1.00	350.	0.84	1.47	32.0	40.0
6	Silica sand	1.00	350.	0.84	1.31	32.0	15.0
7	Silica sand	1.00	350.	0.84	1.31	32.0	20.0
8	Silica sand	1.00	350.	0.84	1.31	32.0	79.3
9	Silica sand	1.00	350.	0.84	1.31	32.0	60.0
10A	Silica sand	1.10	350.	0.86	1.31	32.0	64.3
10B	Silica sand	1.04	350.	0.86	1.31	32.0	63.8
11A	Silica sand	1.30	350.	0.86	1.31	32.0	61.0
11B	Silica sand	1.30	350.	0.86	1.31	32.0	110.5
12	Silica sand	1.30	350.	0.86	1.31	32.0	64.0
13	Silica sand	0.67	350.	0.86	1.31	32.0	70.3
14A	Silica sand	0.31	350.	0.86	1.31	32.0	62.0
14B	Silica sand	0.30	350.	0.86	1.31	32.0	68.6
15A	Silica sand	1.51	350.	0.86	1.31	32.0	85.4
15B	Silica sand	1.51	350.	0.86	1.31	32.0	61.2
16	Silica sand	1.00	350.	0.86	1.30	32.0	122.0
17	Silica sand	1.00	350.	0.86	1.31	25.0	54.4
18	Silica sand	1.00	350.	0.86	1.31	25.0	46.7
19	Silica sand	1.00	350.	0.89	0.33	32.0	64.7
20	Silica sand	1.00	350.	0.89	1.31	15.0	65.5
21	Silica sand	1.00	350.	0.89	0.82	32.0	55.2
22	Silica sand	1.00	350.	0.89	1.31	32.0	87.0
23	Silica sand	1.00	350.	0.89	1.42	32.0	36.1
24	Silica sand	1.00	350.	0.89	1.31	32.0	45.0
25	Silica sand	1.00	350.	0.89	1.96	32.0	22.8
26	Silica sand	1.00	350.	0.89	1.66	32.0	51.5
27	Silica sand	1.00	350.	0.89	1.31	32.0	44.1
28	Silica sand	1.00	350.	0.89	1.31	32.0	44.4
29	Silica sand	1.00	350.	0.89	1.31	20.0	65.1
30	Silica sand	1.00	350.	0.89	1.67	32.0	28.3
31	Silica sand	1.00	350.	0.91	1.32	32.0	55.0
32A	Silica sand	1.00	350.	0.91	1.31	32.0	61.8
32B	Silica sand	1.00	350.	0.91	1.31	62.0	141.5
33	Silica sand	1.00	350.	0.91	1.32	32.0	46.1
34	Silica sand	1.00	350.	0.91	1.32	32.0	55.0
35	Silicon carbide	1.08	590.	0.86	1.31	32.0	56.6
36	Silica sand	1.00	350.	0.91	1.33	15.0	16.5
38	Silica sand	1.30	350.	0.86	1.31	32.0	47.6
40	Glass beads	0.89	340.	1.00	1.31	32.0	41.1

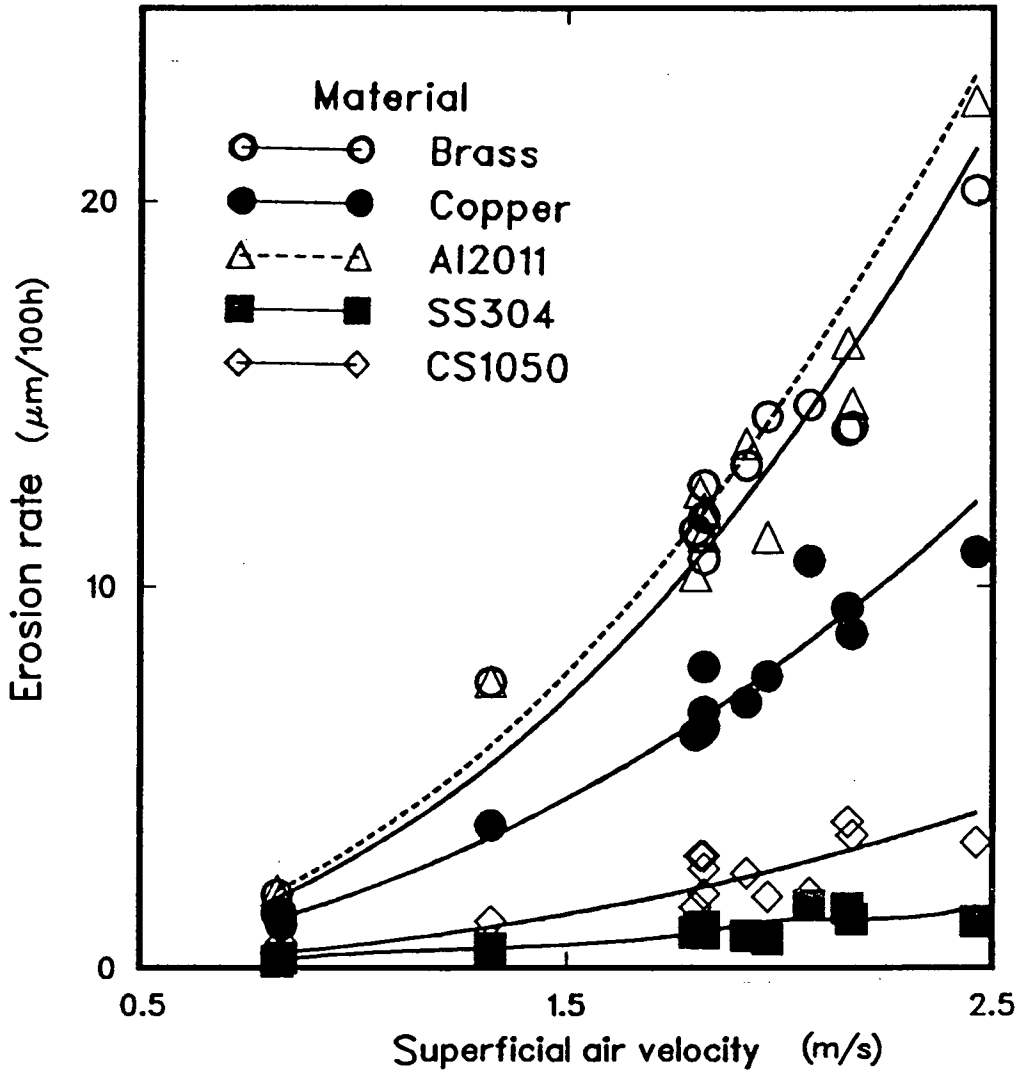

Figure 7.1 Erosion rate vs. superficial air velocity

Operating conditions:

Particles: *1.0 mm silica sand*
Particle sphericity: *0.89*
Tube: *32 mm single tube*
Duration: *20 – 250 h*

As discussed in Chapter 6, the particle impact velocity is not proportional to the gas superficial velocity, but it is approximately equal to the void rising velocity for bubbling conditions. The bubble velocity can be estimated from equation 2.12, if the bubble size is known. The average bubble size can be estimated from the correlation due to Darton et al. (1977) as modified by Bar-Cohen et al. (1980), equation 2.4, or that due to Mori and Wen (1975), equation 2.8. For larger particles, similar results are given by the recent predictive method of Horio et al. (1987). The calculated results are shown in Table 7.2, together with the ratio of bubble size to column mean diameter. As discussed in Section 2.1, if the bubble size is larger than about 1/3 of the column diameter, the bubble rising velocity is not determined by bubble size but rather by the column size. When the ratio (D_e/D) is equal to or larger than about 0.5, slug flow occurs. As also shown in Table 7.2, D_e/D for all tests was larger than 0.5. Therefore all the runs were in the slug regime. The slug rising velocity can then be calculated from equation 2.18. Values of u_s calculated in this manner are also listed in Table 7.2.

The bed height in these experiments was not deep enough to permit a train of several slugs to form in series. Therefore the bed was not in the usually defined slug regime, but in the so-called apparent slug regime in which slugs do not have well established forms (Canada et al. 1978). In this regime the large diameter voids resulting from bubble coalescence produce large bed oscillations and cyclic heaving of the bed surface (Canada et al. 1978).

Void rise velocities calculated from equation 2.12 based on the Darton et al. and Mori and Wen prediction for bubble size are also listed in Table 7.2. These are close to u_s from equation 2.18. Therefore u_s can be considered to represent the void rise velocity in the correlations considered below.

In Figure 7.2, the erosion rate is plotted against the calculated void velocity. The

Table 7.2: Calculated void mean diameters and rise velocities

		Darton equations (Equations 2.4 & 2.14)			Mori & Wen equations (Equations 2.8 & 2.14)			Slug equation (Eq'n 2.18)	
	u (m/s)	D_e (m)	D_e/D	u_b (m/s)	D_e (m)	D_e/D	u_b (m/s)	u_s (m/s)	f_v * (HZ)
Run 19	0.89	0.084	0.40	0.82	0.110	0.53	0.82	0.83	1.9
Run 21	1.38	0.121	0.58	1.31	0.159	0.76	1.29	1.32	2.0
Run 22	1.87	0.146	0.70	1.79	0.191	0.92	1.75	1.81	2.3
Run 23	1.98	0.152	0.72	1.90	0.198	0.95	1.85	1.92	2.2
Run 05	2.03	0.153	0.73	1.94	0.200	0.95	1.90	1.97	2.2
Run 03	2.13	0.158	0.75	2.06	0.207	0.99	1.99	2.09	2.2
Run 26	2.22	0.161	0.77	2.14	0.211	1.01	2.08	2.17	2.3
Run 25	2.52	0.171	0.82	2.42	0.225	1.08	2.36	2.46	2.3

* The slug frequency was measured in the experiments

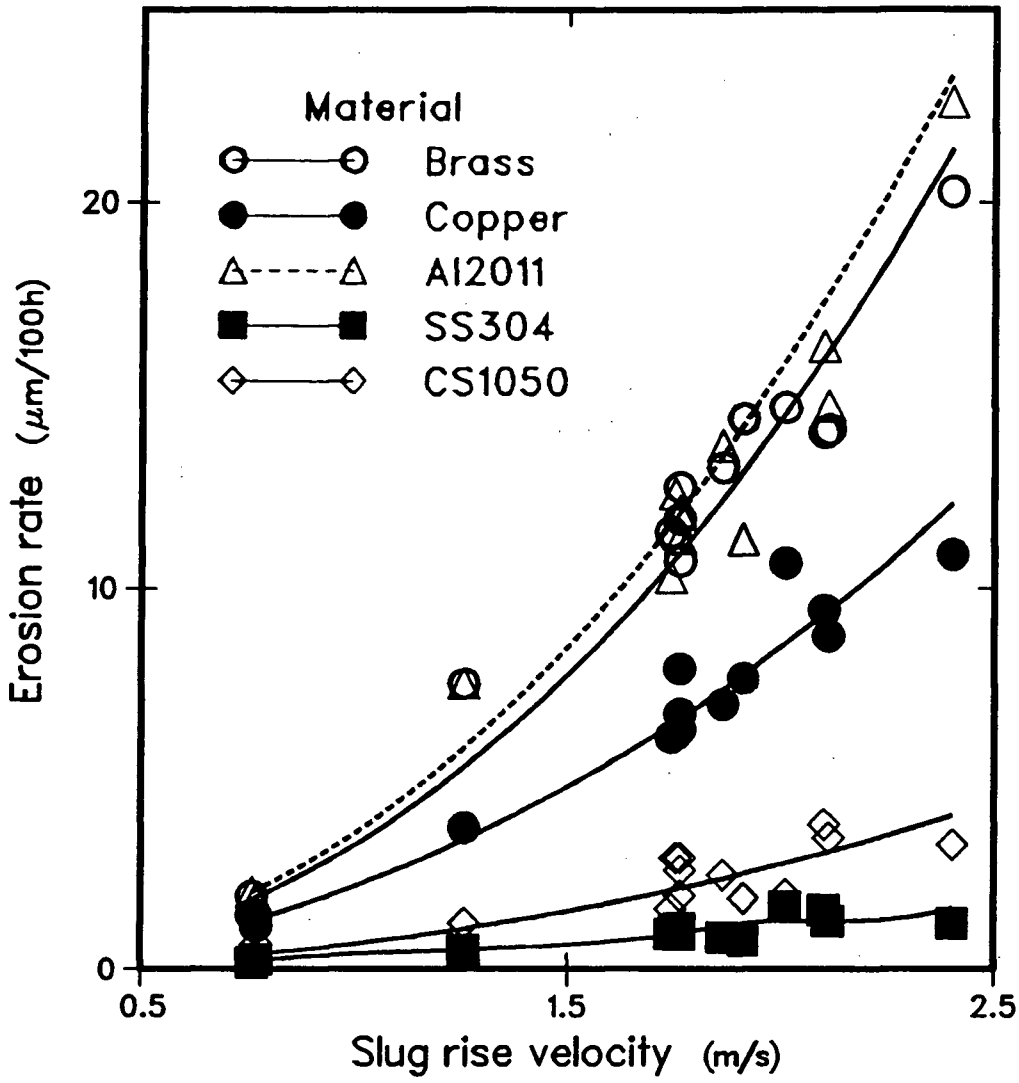

Figure 7.2 Erosion rate vs. void (slug) rise velocity

Operating conditions:

Particles: 1.0 mm silica sand
Particle sphericity: 0.89
Tube: 32 mm single tube
Duration: 20 – 250 h

erosion rate, E, can be fitted using least squares with an equation of the form:

$$E = C_1 u_s^{n_1} \tag{7.1}$$

where u_s is the slug velocity. The values of the constants n_1 and C_1 for different materials are listed in Table 7.3. The fitting results are also shown in Figure 7.2.

The average value of n_1 was found to be 2.1, slightly lower than the value of 2.3 obtained from the dropping tests. The difference is probably not significant in view of the approximate values of the void velocities.

Particle movement and impacts are closely associated with void movement. Only those particles in the immediate region of the void cause significant erosion (see Chapter 6). Assuming that V_c and V_w are the effective void cap volume and the effective void wake volume all particles in which are able to impact on the tube, the particle mass flow rate impacting on unit area is then:

$$M \propto f_v M_b \propto f_v(1-\epsilon_{mf})\rho_s(V_c + V_w)/\pi D_e^2 \tag{7.2}$$

where f_v is the frequency of voids in the bed, M_b is the impact particle mass flow for a single void passage, ρ_s is the particle density and D_e is the void mean diameter. The term $(1-\epsilon_{mf})(V_c + V_w)/\pi D_e^2$ is approximately the total volume of particles which may be able to strike the tube for each passing void.

Large bed oscillations and cyclic heaving of the bed surface associated with void movement could be clearly observed. The number of oscillations in each test was counted during a period of time to determine the average void frequency. The results are also shown in Table 7.2. It is clear that the void frequency was not sensitive to the void velocity and gas superficial velocity, except for the lowest u_s, where $(u - u_{mf})$ was very small. Hence, the frequency in equation 7.2 remained nearly unchanged as $(u - u_{mf})$ changed over the range

Table 7.3: Constants from least square curve fitting of equation 7.1

Material	C_1 $\left[\frac{\mu m/100h}{(m/s)^{n_1}}\right]$	n_1	Correlation coefficient
Brass	2.96	2.23	0.98
Copper	1.94	2.04	0.99
Al2011	3.02	2.22	0.97
SS304	0.31	1.83	0.95
CS1020	0.59	2.14	0.91
Mean value		2.1	
Standard deviation		0.17	

Conditions:

Sample size: 26 data points for every material

Particles: 1.0 mm silica sand

Particle sphericity: 0.89

investigated. For the other terms on the right side of equation 7.2, while the front cap and wake volume of void increased with void size, the ratio $(V_c + V_w)/\pi D_e^2$ remained almost the same. Therefore, the impact particle mass flow rates for all the tests were nearly the same. The estimation of M_b will be discussed in Chapter 9.

7.1.2 Particle Size

Six kinds of silica sand with different sizes were used in the tests, while the excess superficial velocity, $(u - u_{mf})$, was kept at 1.31 m/s. The other conditions were the same as the base conditions. The results are shown in Figure 7.3.

It was found that the erosion rate increased significantly as particle size increased. The dependence of erosion rate on particle size can be fitted by least squares with a relationship of the form

$$E = C_2 d_p^{n_2} \tag{7.3}$$

where C_2 and n_2 are constants. The fitted values of C_2 and n_2 for different materials are listed in Table 7.4.

The average value of n_2 was 1.2, somewhat smaller than 1.5 from the dropping experiments. This may arise from the fact that the bubble wake volume fraction decreases when particle size increases at the same $(u - u_{mf})$ (Clift & Grace 1985).

7.1.3 Other Particle Properties

Experiments were carried out five times at base conditions over the period of all erosion tests with the same 1.0 mm silica sand for all five tests. As shown in Figure 7.4, the particles became more rounded as a result of the repeated tests. Results from these tests are plotted in Figure 7.5 with sphericity as the abcissa.

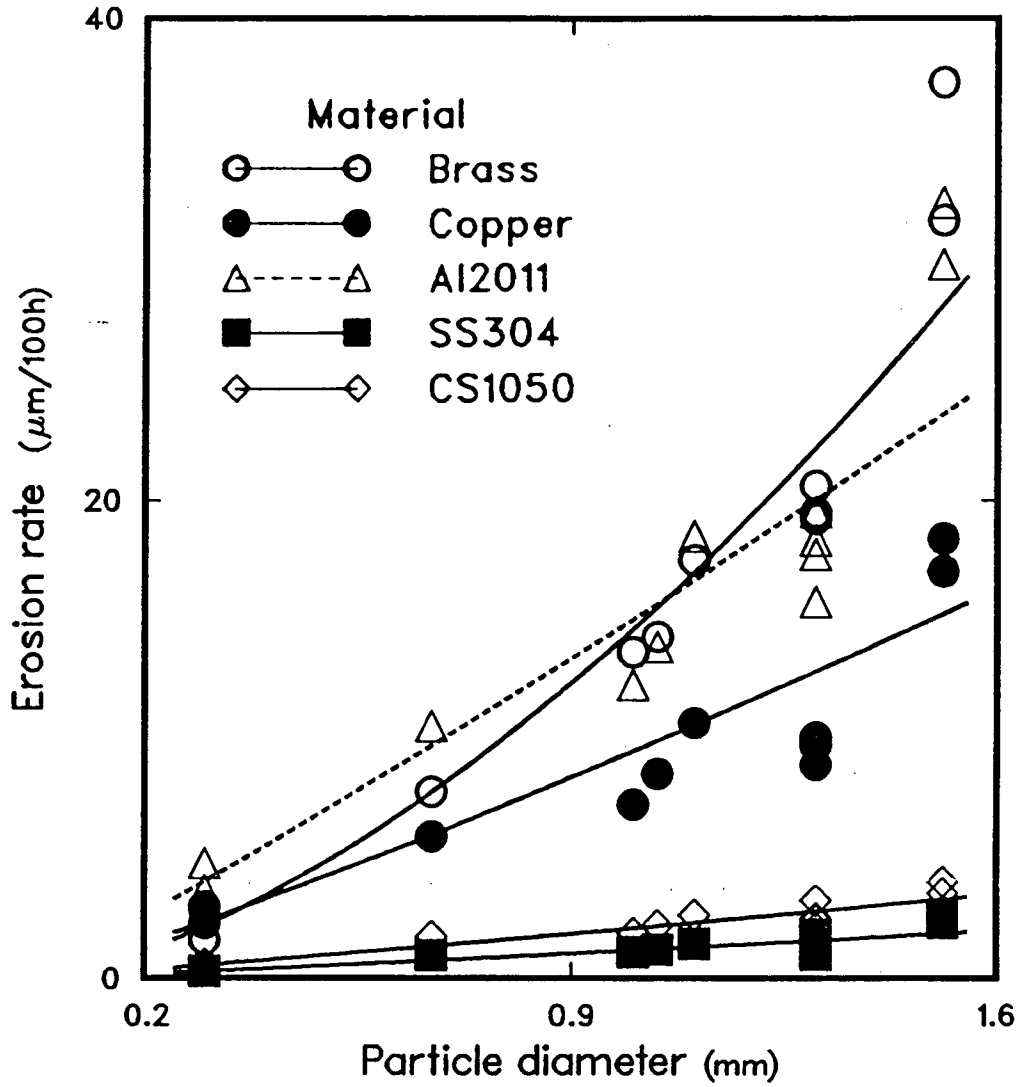

Figure 7.3 Erosion rate vs. particle diameter

Operating conditions:

Particles: *silica sand*
Particle sphericity: *0.89*
Excess air velocity: *1.31 m/s*
Tube: *32 mm single tube*
Duration: *60 – 110 h*

Table 7.4: Constants from least square curve fitting of equation 7.3

Material	C_2 $\left[\frac{\mu m/100h}{(mm)^{n_2}}\right]$	n_2	Correlation coefficient
Brass	14.42	1.58	0.98
Copper	9.50	1.15	0.96
Al2011	15.05	1.09	0.96
SS304	1.18	1.13	0.94
CS1020	2.10	1.09	0.97
Mean value		1.2	
Standard deviation		0.21	

Conditions:

Sample size: 24 data points for every material

Excess air velocity: 1.31 m/s

Particles: silica sand

Particle sphericity: 0.89

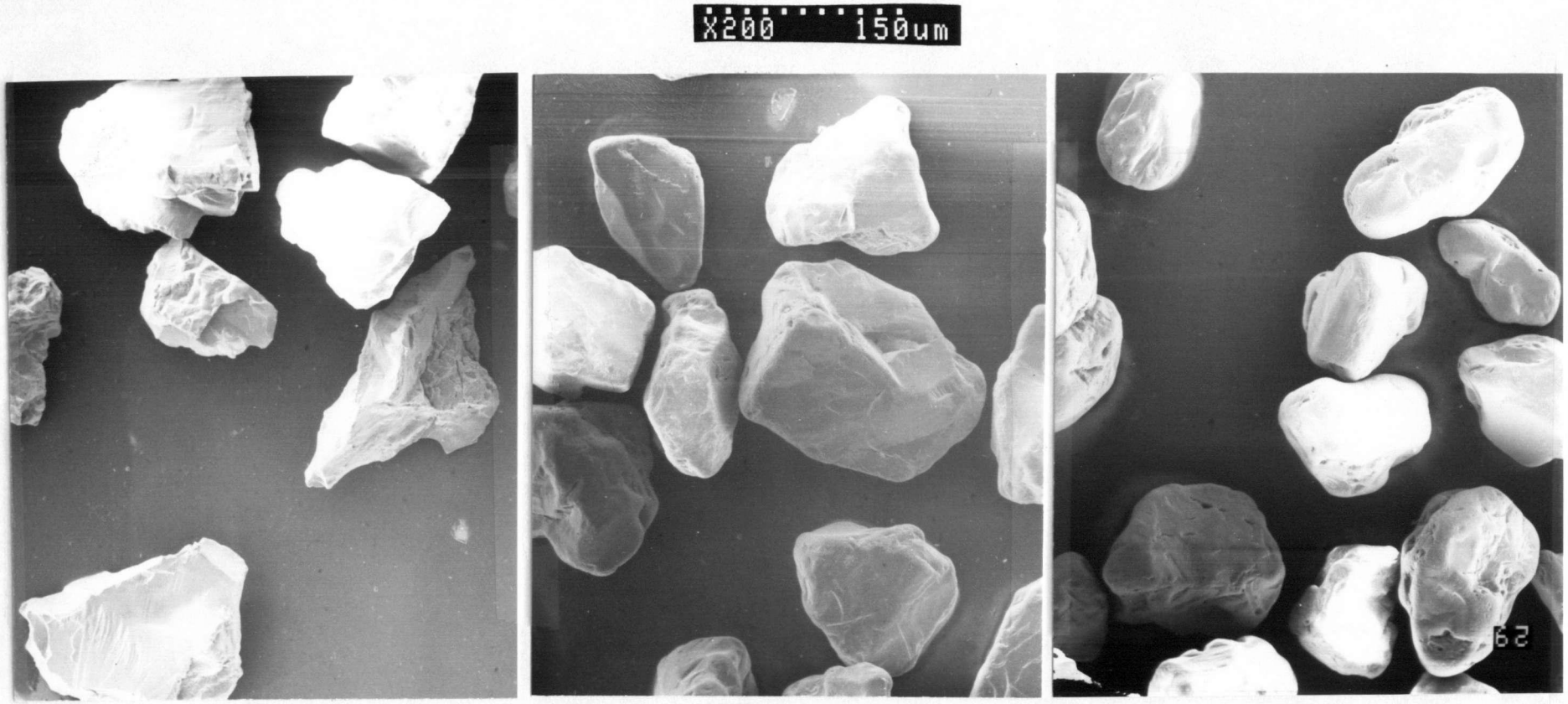

(a) fresh particle (b) after 900h (Run 9) (c) after 2000h (Run 34)

Figure 7.4 Photograghs of 1.0 mm silica sand taken before and after erosion test in the three-dimensional cold model fluidized bed

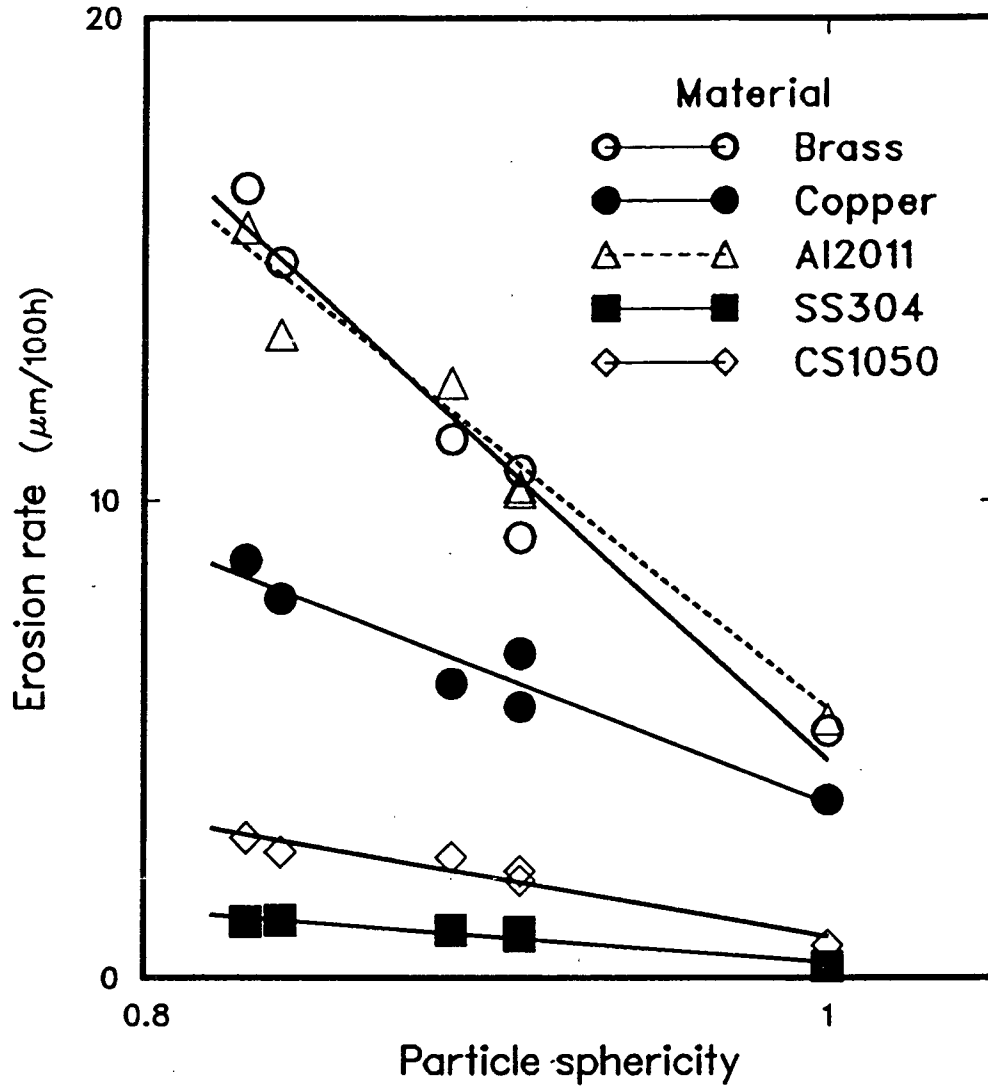

Figure 7.5 Erosion rate vs. particle sphericity

Operating conditions:

Particles: *1.0 mm silica sand and glass beads*
Excess air velocity: *1.31 m/s*
Tube: *32 mm single tube*
Duration: *41 – 120 h*

Another test using 0.89 *mm* glass beads was also carried out. The glass beads have a hardness of 340 kg/mm^2, very close to that of the silica sand (350 kg/mm^2). The particle densities are also very similar. The results of this run were corrected for particle size using equation 7.3 to give the erosion rate of 1.0 *mm* glass beads. The correlated results are also plotted in Figure 7.5.

Figure 7.5 shows clearly that the erosion rate decreased significantly as the particle sphericity increased. As in Chapter 5 the erosion rate can be correlated against the particle sphericity, Φ_s, by an equation

$$E = C_3(C_4 - \Phi_s) \tag{7.4}$$

where C_3 and C_4 are constants. The C_3 and C_4 values and correlation coefficients obtained from the least square fitting of equation 7.4 are tabulated in Table 7.5. The fitted equations are also plotted in Figure 7.5. The high correlation coefficients as well as Figure 7.5 suggest a linear relationship between erosion rate and Φ_s over the range covered.

One species of very hard and heavy particles, silicon carbide, was also used as the bed material to test the effect of particle hardness. Results of this test and average results from the 1.0 *mm* silica sand tests are plotted versus tube material hardness in Figure 7.6. These data were corrected to the same sphericity (Φ_s=0.86), particle size (1.0 mm) and void velocity using equations 7.4, 7.3 and 7.1 respectively. The particle hardnesses are also shown in Figure 7.6 for reference purpose.

It was noted above that erosion produced by silicon carbide was higher than produced by silica sand. As stated in Chapter 5, the erosion rate in the dropping tests was proportional to the particle mass flow rate, but in the fluidized bed the mass flow is dependent on the bubble volume and the particle density. It seems logical that the erosion rate should be proportional to the particle density. The data in Figure 7.6 were corrected for the effect of

Table 7.5: Constants from least square curve fitting of equation 7.4

Material	C_3 [μm/100h]	C_4	Correlation coefficient
Brass	65.1	1.07	0.98
Copper	28.0	1.13	0.91
Al2011-T3	56.4	1.10	0.95
SS304	5.5	1.06	0.96
CS1020	12.5	1.07	0.92
Mean value		1.1	
Standard deviation		0.03	

Conditions:

Sample size: 12 data points for every material

Particles: 1.0 mm silica sand and 1.0 mm glass beads

Excess air velocity: 1.31 m/s

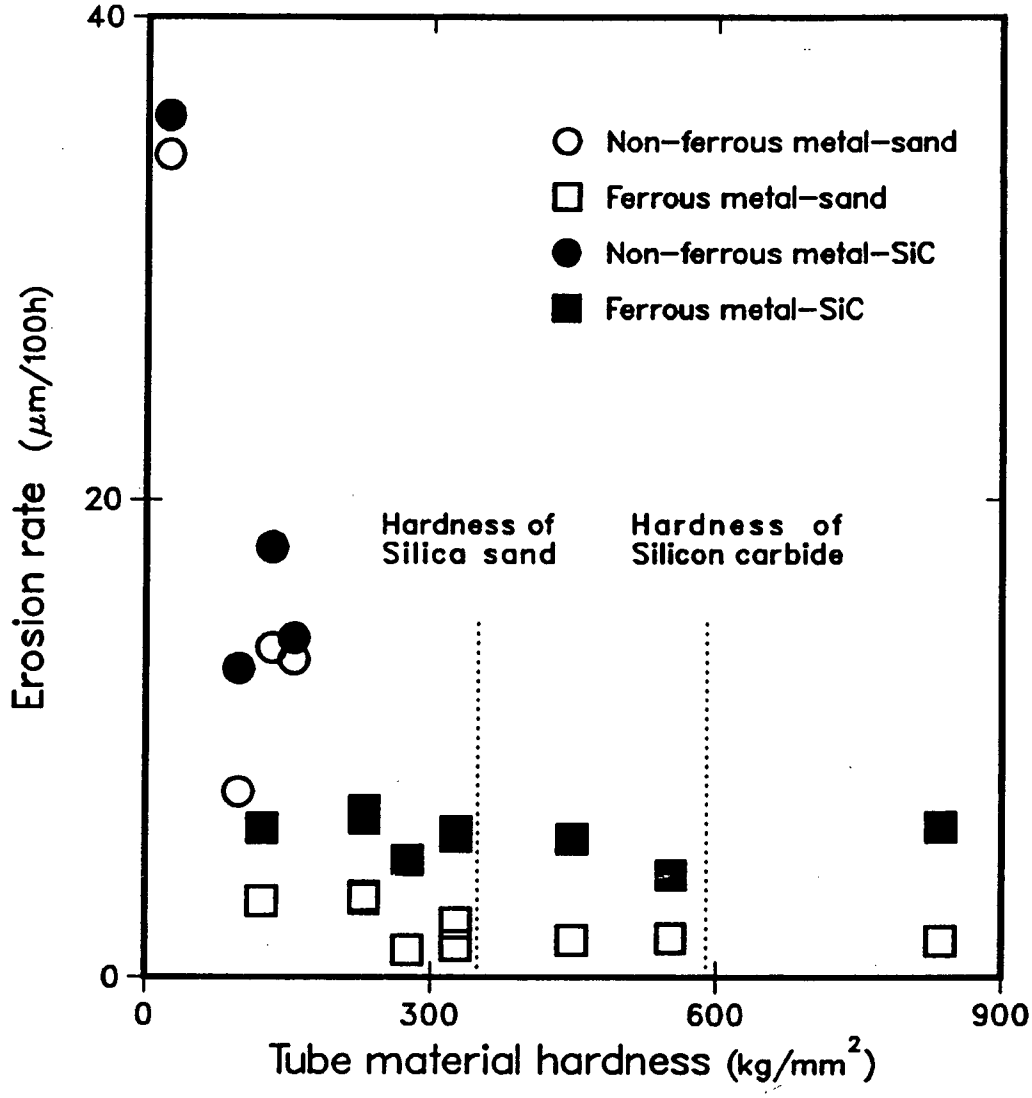

Figure 7.6 Erosion rate of different materials with silica sand and silicon carbide particles

Operating conditions:

Particles: 1.0 mm silica sand
Particle sphericity: 0.89
Excess air velocity: 1.31 m/s
Tube: 32 mm single tube
Duration: 35 – 120 h

density and are replotted in Figure 7.7.

Figure 7.7 indicates that there may be a different behaviour for the two groups of materials. For the non-ferrous materials, the particle hardness did not appear to affect the erosion rate appreciably. However, for the ferrous metals an increase of particle hardness caused an increase in the erosion rate of the materials tested. This finding may be due to the fact that ferrous metals generally have high hardness values, close to the hardness of silica sand, so that silica sand can not readily erode these metals. However, pure iron has the same hardness as Al2011 while the erosion behaviour was quite different, suggesting that there may be some other factor or property of ferrous metals that leads to the difference in erosion rate.

It was noted also that for either of the particles, the erosion rate of ferrous metals appeared to remain constant regardless of whether the particle hardness, H_p, is greater or smaller than the ring material hardness, H_m. This is contrary to the finding reported by Hutchings (1987) for high velocity solid impact erosion that there is a sharp change of erosion rate at $H_p = H_m$.

7.2 Effect of Tube Diameter

Four tube sizes were tested while other operating conditions were kept constant (1.0 *mm* silica sand, 1.88 m/s superficial air velocity and single tube 308 *mm* above the distributor). The four tubes had outer diameters of 15 (Runs 20 and 36), 20 (Run 29), 25 (Run 18) and 32 *mm*.

The results are plotted in Figure 7.8. For tube sizes of 20, 25 and 32 *mm*, the erosion rate increased slightly as the tube size became smaller. For a tube size of 15 *mm*, the erosion rate increased dramatically for brass and Al2011, while the erosion rate for the other three

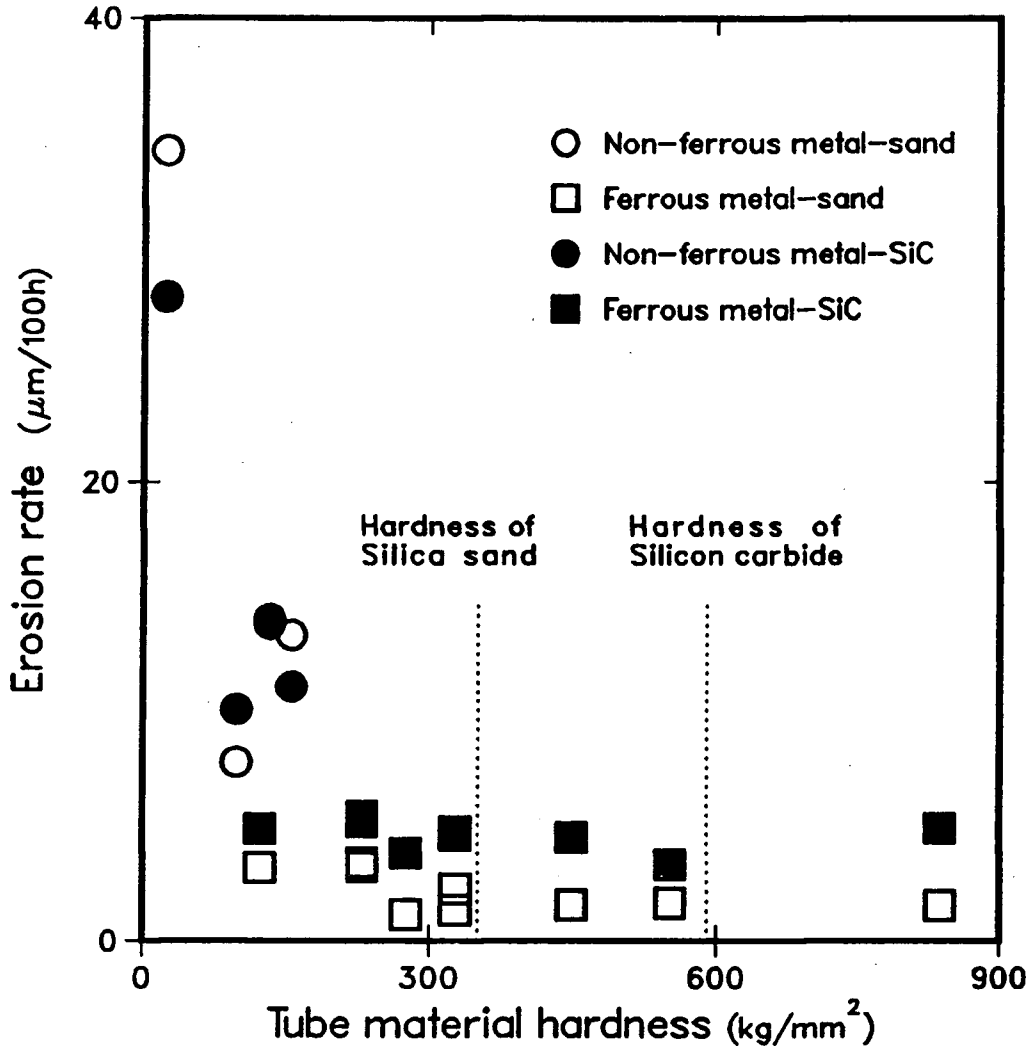

Figure 7.7 Erosion rate of different materials with silica sand and silicon carbide particles (corrected for particle density)

Operating conditions:

Particles: 1.0 mm silica sand
Particle sphericity: 0.89
Excess air velocity: 1.31 m/s
Tube: 32 mm single tube
Duration: 60 – 120 h

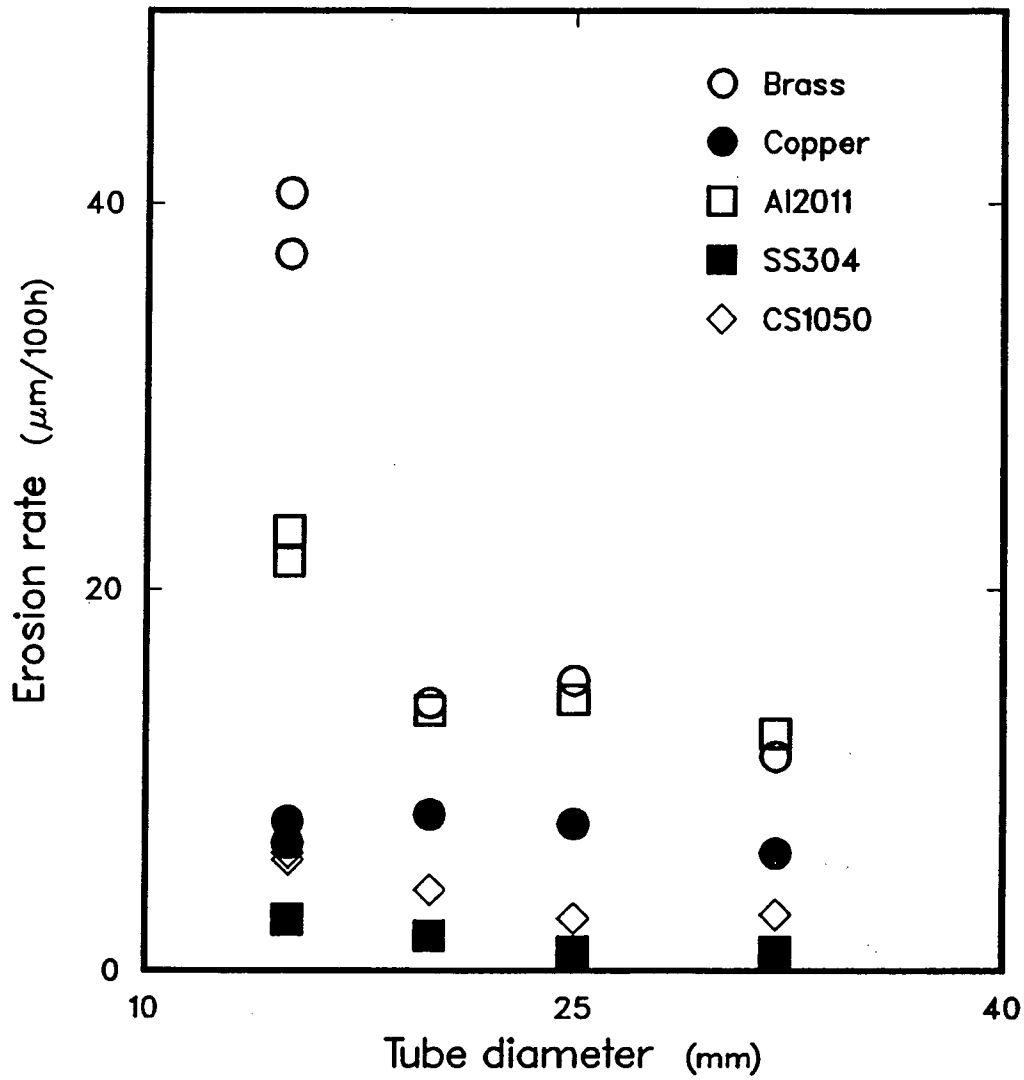

Figure 7.8 Erosion rate vs. tube diameter

Operating conditions:

Particles: 1.0 mm silica sand
Particle sphericity: 0.89
Excess air velocity: 1.31 m/s
Duration: 46 – 65 h

materials remained relatively constant. These findings may be explained as follows:

(1) As discussed in Chapter 5 and Section 7.1, the erosion of a tube is proportional to the mass flow rate of impacting particles. For bubbling or slugging, this mass flow rate is expected to depend on the wake volume. However, the wake is somewhat thicker near the axis of the bubble than at the outside. Bubbles are more likely to swerve to avoid larger tubes than smaller ones (Harrison & Grace 1971). Therefore the impact particle mass flow rate per unit area tends to be somewhat higher for smaller tubes than for larger tubes.

(2) As tube size decreases, the volume of the de-fluidized cap appearing from time to time on top of the tube (Glass & Harrison, 1964) decreases relative to the tube size, since the angle of repose for the particle was the same while the tube surface became more curved. This provides more chance for particles to impact on the top part of the tube, hence increasing the average erosion rate there.

(3) When the tube diameter was smaller, particles impacting on the tube surface were able to leave the tube more quickly, providing less protection against the next batch of impacting particles.

The above arguments may explain the small increase of erosion rate for a change in tube diameter from 32 to 20 mm, but not the sharp increase for the 15 mm brass and Al2011 tubes. A possibility for the outstandingly high erosion rate for the 15 mm tubes could be that the 15 mm tubes tended to vibrate slightly, which may have enhanced the erosion rate. However, it is notable that Hosny (1982), Hosny and Grace (1983) and Grace and Hosny (1985) with the same column found that rms (root mean square) forces were proportional to tube diameter for tube diameters of 15, 25 and 32 mm when $u - u_{mf}$ is larger than about 0.3 - 0.5 m/s. The full reason is not clear.

7.3 Effect of Tube Location and Configuration

As noted in Section 1.1, tubes in fluidized beds do not erode uniformly. Clearly it is the local erosion rate, not the average rate, which is of concern when avoiding failure of the tubes. Therefore it is critical to know the spatial distribution of erosion and to know how the tube location affects erosion. Experiments were therefore performed with brass and Al2011 to test the erosion rate at different locations in the bed and to determine the erosion rate distribution along the tube length and around the circumference. For these tests other operating conditions were maintained at the base conditions, i.e. with a 1.88 m/s superficial velocity, 1.0 *mm* silica sand and 32 mm tube diameter.

7.3.1 Circumferential Distribution of Erosion

Small segments of brass and Al2011 rings were mounted on the test tube to determine the erosion variation around the circumference of the tube, as discussed in Section 4.3. The length of these segments ranged from 4 to 6 *mm*, which corresponded to 15 to 20 degree intervals of the tube surface. The erosion rates calculated from weight loss measurements were taken as the average erosion rate over that segment. The results are shown in Figure 7.9.

Local erosion rates were also determined from the ring thickness change after a total of about 1400 *h* of exposure to the bed. During this period the rings underwent tests with silica sands of different sizes operated at different superficial velocities (Runs 1 - 15 in Table 7.1). Hence the erosion rates can only give some indication of magnitude, but the relative erosion rate distributions are of interest given the longer period of operation. Four rings in all, two each of brass and Al2011, were tested in this manner. Since the left and right sides of the rings were determined separately, this provided four sets of data for each material. The average results are plotted in Figure 7.10.

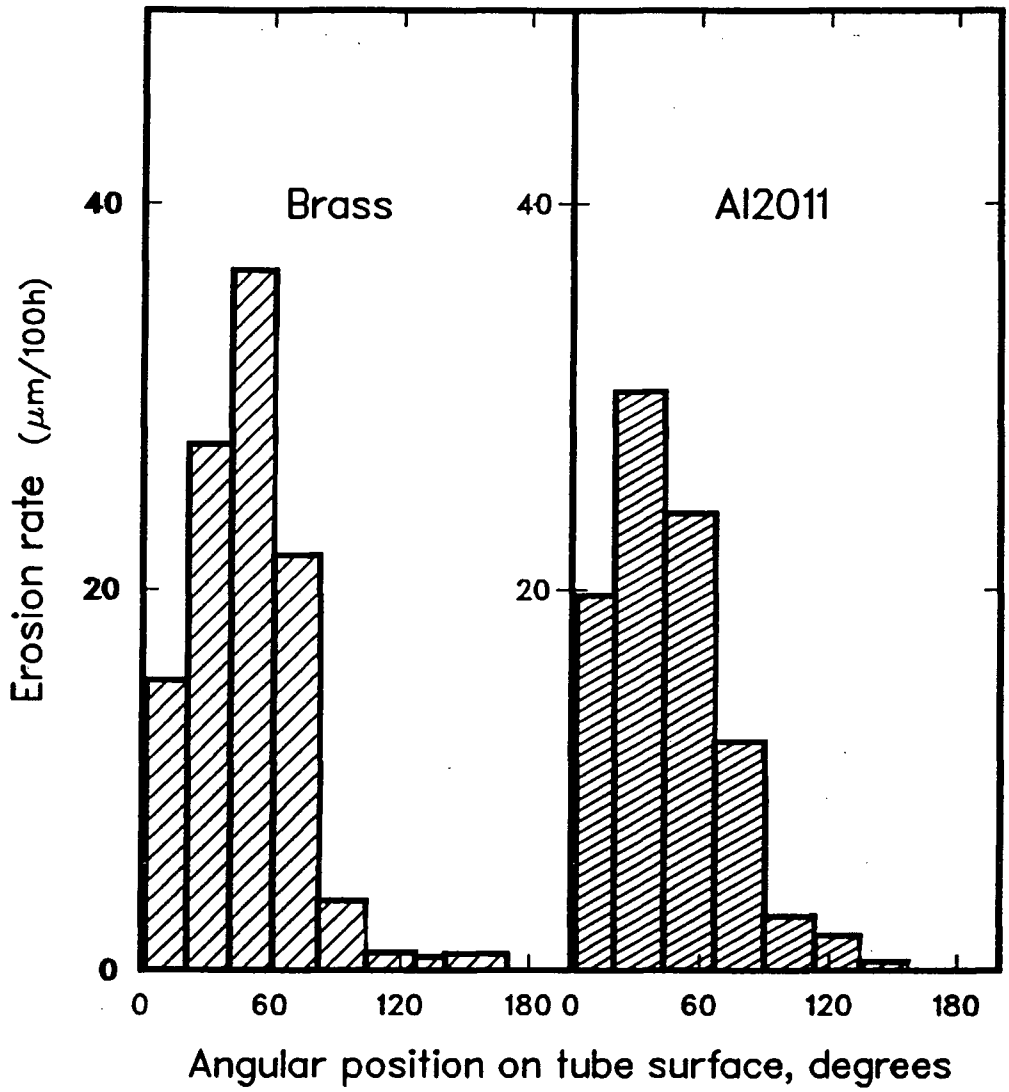

Figure 7.9 Circumferential erosion rate distribution

Operating conditions:

Particles: 1.0 mm silica sand
Particle sphericity: 0.89
Excess air velocity: 1.31 m/s
Tube: 32 mm single tube
Duration: 20 – 250 h

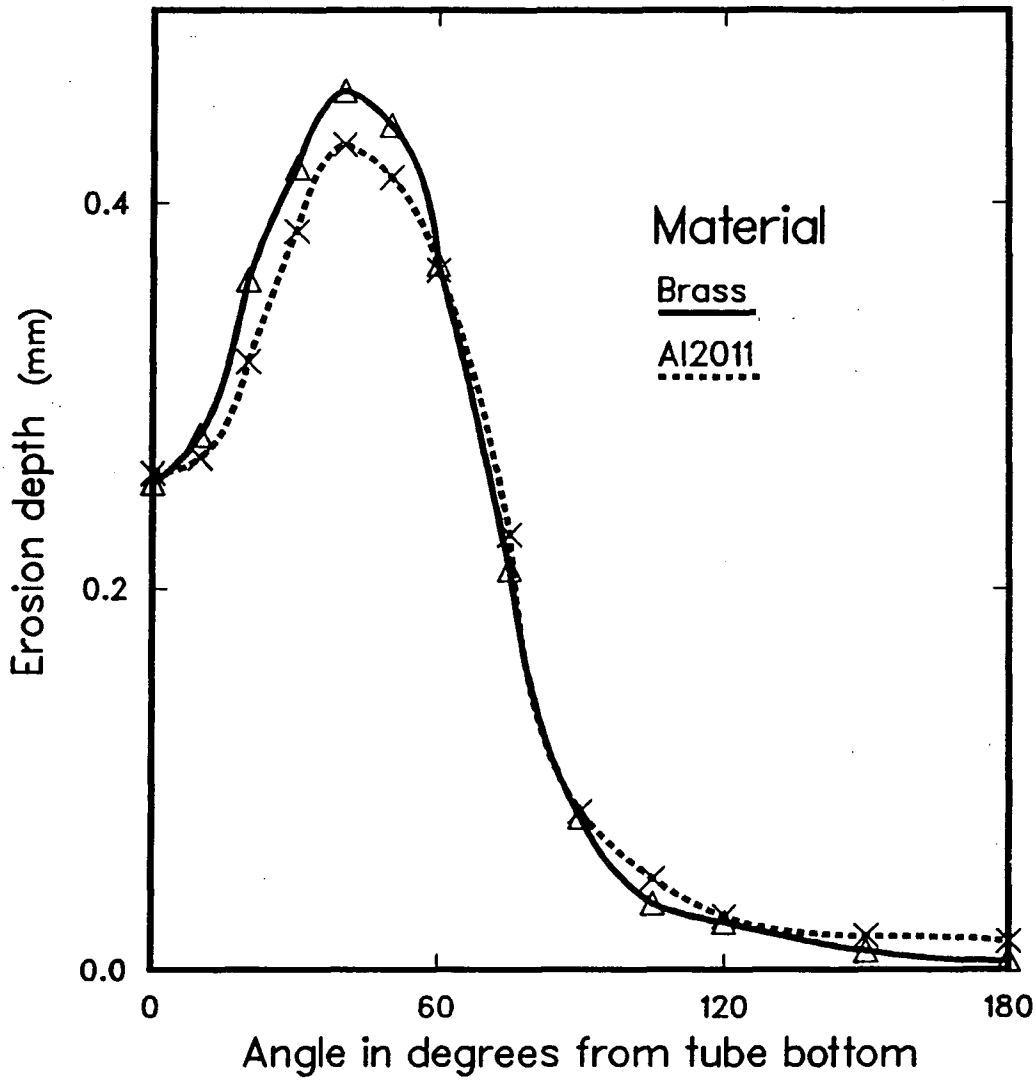

Figure 7.10 Eroded depth as a function of angle around the tube

Operating conditions:

Particles: *1.0 mm silica sand*
Tube: *32 mm single tube*
Duration: *about 1400 h*
Conditions: *various*

Both Figures 7.9 and 7.10 show that for brass and Al2011, more than 95% of the material (weight) loss occurred over the lower half of the tube. Most of the material loss was over the bottom 120°, with the maximum erosion occurring at 40° to 50° from the bottom of the tube. The erosion rate dropped dramatically near the equator to almost zero over the top half of the tube. The results indicate that overall average erosion rates underestimate the maximum local erosion rate by a factor of about 3. The above finding was in agreement with the results from the two-dimensional fluidized bed photography discussed in Chapter 6. As shown in Table 6.3, the number of particle impacts over the bottom 120° of the tube constituted 96% of the total number of paticle impacts.

The local erosion rates plotted in Figure 7.9 were also integrated over the tube circumference to give average erosion rates based on the small segment tests. The integrated erosion rates, 13.5 and 12.7 $\mu m/100h$ for brass and Al2011, respectively, agreed quite well with the average erosion rates from tests with complete rings of the same materials under the same conditions, namely 14.1 $\mu m/100h$ for brass and 13.1 $\mu m/100h$ for Al2011. This suggests that the small segment method was reliable.

7.3.2 Axial Distribution of Erosion

Eight brass rings were mounted at four positions in pairs along the tube (Run 24). They were located symmetrically, 19 *mm* and 57 *mm* on either side of the middle. The erosion rates of these rings, together with average erosion rates of brass under the same conditions, are listed in Table 7.6. The pairs of rings located 19 *mm* away from the centre had erosion rates very similar to the brass rings in the earlier tests where the rings were close to the middle. However, the two pairs located further away from the centre had significantly smaller erosion rates. This is probably due to the tendency for bubbles, due to coalescence patterns, to naturally tend towards the centre of the column (Grace & Harrison, 1968).

Table 7.6: Erosion rates of brass at different positions along the tube

Ring location *	Erosion rate (μm/100h) Horizontal tube (Run 24)	Tube near distributor (Run 28)	Inclined tube (Run 27)
57 mm left	8.0 8.2	22.8 13.1	7.4 9.1
19 mm left	11.2 12.5	22.8 22.6	9.9 13.4
19 mm right	11.4 12.1	7.67 13.4	11.5 10.4
57 mm right	8.4 7.5	23.3 38.6	6.8 7.3

* Measured horizontally from centre of the tube

The results of this test are also shown graphically in Figure 7.11. Table 7.6 suggests that erosion was symmetrical in the bed along the horizontal tube.

One further test (Run 33) was carried out with test rings mounted on the tube at positions at least 44 *mm* away from their usual positions. The results of this test and the location of the rings are tabulated in Table 7.7 together with the results of two runs with identical conditions where the rings were at their usual positions. There was no sign of significant differences between Run 33 and the other two runs. This indicates that the erosion was uniform within about 44 *mm* from the centre on both sides.

7.3.3 Tube near Distributor, Inclined Tube and Tube close to Bed Surface

Similar to the test Run 24, discussed in Section 7.3.2, eight brass rings were mounted at four positions in pairs along the tube, symmetrically 19 *mm* and 57 *mm* away from the middle. One run (Run 28) was conducted with the tube horizontally placed only 30 *mm* above the distributor plate. In addition, a further test (Run 27) was carried out with the tube inclined at 15° from the horizontal with its centroid 308 *mm* above the distributor.

The experimental results of these runs are listed in Table 7.6. For the inclined tube (Run 27) the overall erosion rate and its distribution were similar to that of a horizontal tube (Run 24). This similarity suggests that the 15 degree inclination of the tube did not change the gas-solid flow pattern in the bed significantly. The two results are also shown graphically in Figure 7.11.

For Run 28, the tube was just 30 *mm* above the distributor. Details of the distributor are provided in Section 3.2. The lower half of the tube was within the jet zone, which extended 29 *mm* above the distributor according to the jet penetration correlation of Merry (1975):

$$L_j = 5.2 d_{or} (\frac{\rho_f d_{or}}{\rho_s d_p})^{0.3} \{1.3 (\frac{u_{or}^2}{g dor})^{0.2} - 1\} \tag{7.5}$$

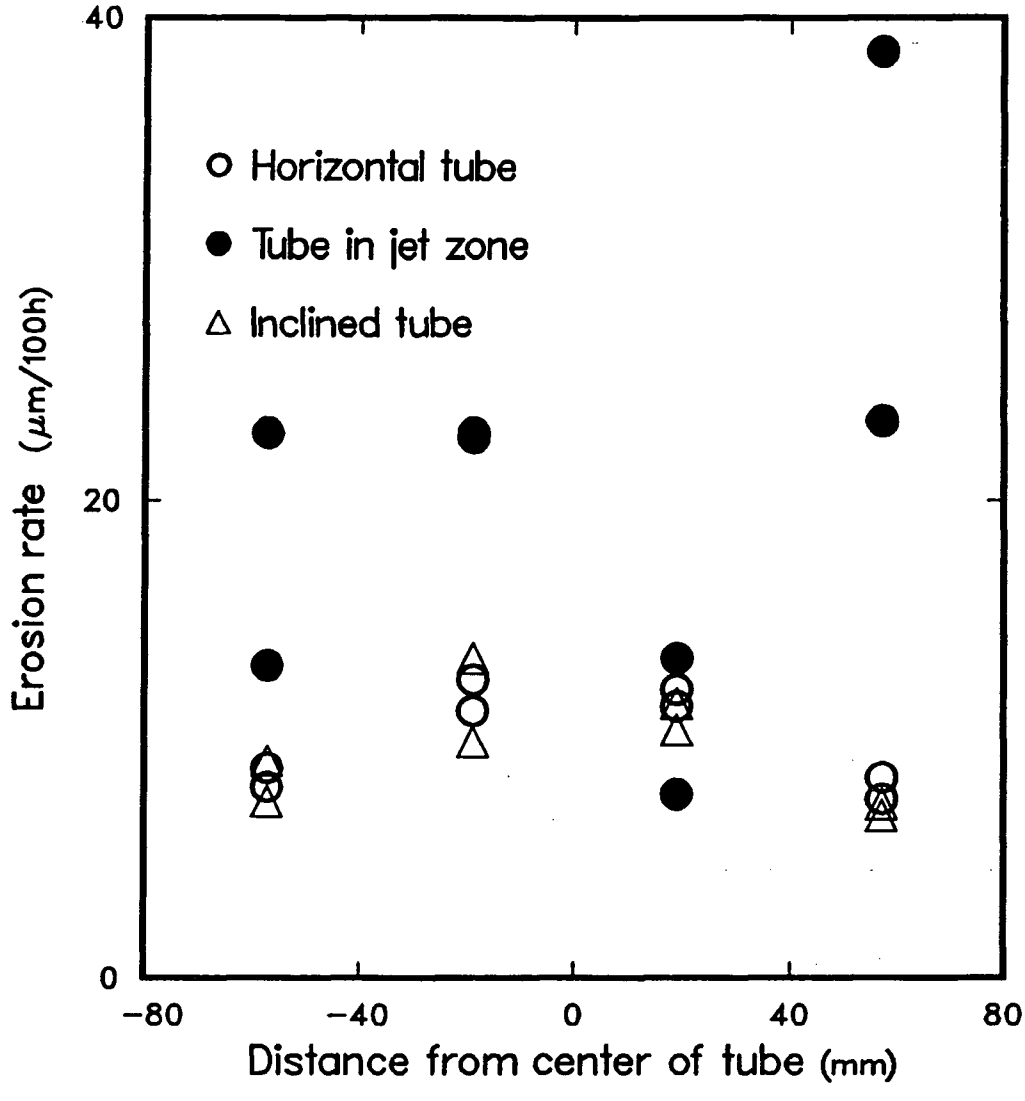

Figure 7.11 Erosion rate at different locations and for different orientation

Operating conditions:

Particles: 1.0 mm silica sand
Particle sphericity: 0.89
Excess air velocity: 1.31 m/s
Tube: 32 mm single tube
Duration: 44 – 45 h

Table 7.7: Erosion rates (μm/100h) of different materials located at different positions along the tube

	Brass	Copper	Al2011	SS304	CS1020	SS316	CS1050	Iron	Pure Al
Ring position:*	L30mm	L22mm	L14mm	R21mm	R40mm	R14mm	R30mm	L46mm	L40mm
Run 22	12.05	5.94	11.58	0.95	3.05	1.05	2.66	3.07	29.85
	10.47	6.41	13.30	1.07	2.81	1.05	2.77	2.13	29.02
Run 31	12.70	6.10	11.52	1.16	2.88	1.16	2.77	2.75	31.91
	10.86	6.50	11.05	0.99	2.96	1.39	3.47	2.55	24.74
Ring position:*	R21mm	R29mm	R37mm	L24mm	L10mm	L30mm	L14mm	R5mm	R11mm
Run 33	11.66	6.93	10.71	0.95	2.39	1.05	2.67	3.25	33.08
	9.73	7.85	13.11	1.09	2.79	1.22	2.54	2.55	29.14

Operating conditions:

Superficial air velocity: 1.88 m/s

Particles: 1.00mm Silica sand

Particle sphericity: 0.89

* From the centre of the tube, L = left, R = right

valid only for

$$u_{or} > 0.52(gd_{or})^{0.5} \tag{7.6}$$

where L_j is the jet penetration depth, d_{or} is the orifice diameter and u_{or} is the mean gas velocity through the orifices. The distribution of erosion is also plotted in Figure 7.11. Erosion was not uniform along the tube due to the non-uniformity of the jet zone (Massimilla, 1985). The measured average erosion rate was 20.5 $\mu m/100h$, about 1.8 times higher than the erosion for tubes located 308 mm above the distributor. The increase is no doubt due to the high particle impact velocities caused by jets from the small orifices of the distributor. Note that the erosion rate for one of the rings was much higher than for the others, indicating that jets may produce pronounced local erosion.

A further test (Run 17) was conducted in conjunction with Run 18 to test the effect of static bed height. In Runs 17 and 18, all other conditions were kept the same as the base conditions (1.0 mm silica sand, 1.88 m/s superficial velocity and single tube, 308 mm above the distributor), but with slightly smaller rings, 25 mm o.d.. For Run 17, the static bed height was lower, about 180 mm, so that the tube was immersed close to the bed surface when fluidized, while for Run 18, the static bed height was 320 mm (normal condition).

The results of these two runs are tabulated in Table 7.8. For the materials tested, the erosion rate decreased in Run 17 due to the reduction in bed height. The lower bed height likely reduced the amount of bubble coalescence in the vicinity of the tube and the number of particles striking the tube surface (solids mass flow rate), thereby reducing the erosion rate (see Chapters 5 and 6).

7.3.4 Tube within Tube Bundle

With the tube to be tested still located parallel to and midway between two walls of the column and 308 mm above the distributor, four other tubes of the same size were placed

Table 7.8: Comparison of erosion rate between beds of 320 mm and 180 mm static bed depth

Ring material	Erosion rate (μm/100h) Static bed height 320mm (Run 18)	Static bed height 180mm (Run 17)	Ratio
SS 304	0.98	0.95	0.97
	1.07	0.95	0.89
CS1050	2.75	2.39	0.87
	2.72	2.49	0.92
Brass	16.6	7.85	0.47
	13.9	7.74	0.56
Copper	7.24	5.76	0.80
Al2011	14.9	8.84	0.59
	13.5	7.90	0.58

around it with their axes 64 *mm* from the axis of the central tube (see Section 3.2 and Figure 3.6). This configuration was found to give the most uniform distribution of voidage and to reduce the defluidized cap on the top of the tube effectively (Sitnai & Whitehead, 1985). It was also found (Hosny 1982, Hosny & Grace 1984) to result in a reduction in rms (root square mean) transient forces caused by bubbles.

The erosion rates were found to be effectively reduced by the presence of the four shielding tubes. The average erosion rates of complete rings are tabulated in Table 7.9 in comparison with two runs for a single tube under the same conditions carried out just before and immediately after the tube bundle test. On average, the tube in the bundle suffered only about 0.6 times the erosion of the single tube. As discussed in Chapter 6, the presence of other tubes reduced the particle impact velocity inside the tube bundle, thereby reducing the erosion rate.

The lateral erosion distribution was also tested in the same run using the same small segment technique as employed for the single tube. The erosion distributions for brass and Al2011 around the tube circumference are shown in Figure 7.12. The spatial distribution of erosion differed somewhat from that of the single tube: (1) The maximum erosion occurred at the very bottom of the tube instead of at about 40° to 50° from the bottom. This probably arises because the particle flow is channelled by the two upstream tubes, leading bubbles to impinge directly from below. (2) The erosion rate was still quite low for the top half of the tube, but the erosion loss over this region now constituted more than 15% of the total, much larger than the proportion ($< 5\%$) for the single tube. This difference may be due to the fact that the particles are forced to converge more as they are pushed or carried past the central tube in order to pass between the two downstream tubes (Chapter 6). Downflow of particles through the tube bundle after bubble passage will also be more

Table 7.9: Comparision of erosion rate between tube in bundle and single tube

Erosion rate (μm/100h)

	Brass	Copper	Al2011	SS304	CS1020	SS316	CS1050
Run 31	11.44	5.49	10.38	1.05	2.59	1.04	2.49
Single tube	9.79	5.86	9.95	0.89	2.67	1.25	3.12
Run 33	10.05	6.84	9.23	0.82	2.06	0.90	2.30
Single tube	8.39	6.77	11.30	0.94	2.41	1.05	2.19
Run 32	5.95	4.01	6.31	0.52	1.44	0.62	1.27
Tube in bundle	6.83	4.29	7.29	0.60	1.45	0.56	1.49
% reduction	34	33	33	39	41	44	45

Operating conditions:

Superficial air velocity: 1.8 m/s

Particles: 1.0 mm Silica sand

Particle sphericity: 0.91

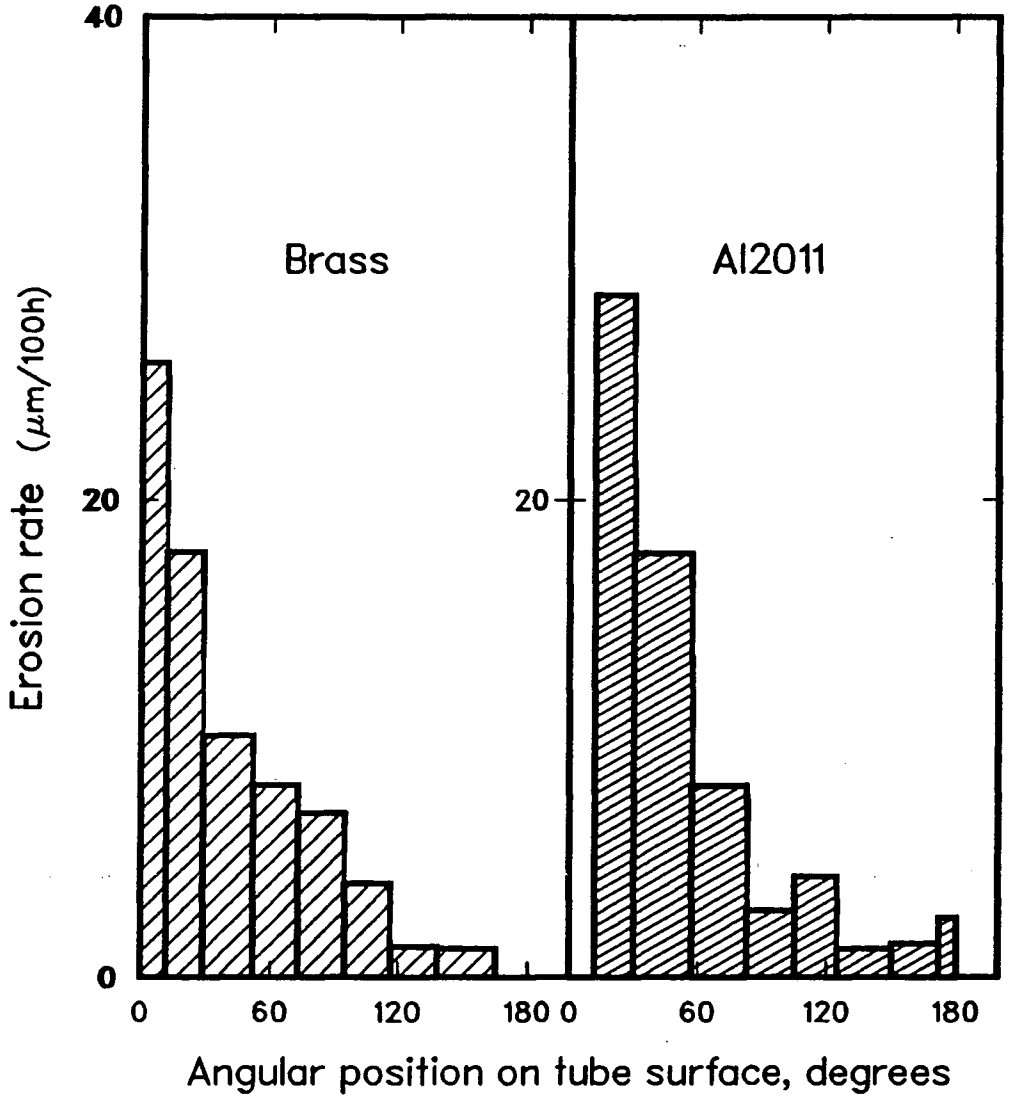

Figure 7.12 Circumferential erosion rate distribution for tube inside tube bundle

Operating conditions:

Particles: 1.0 mm silica sand
Particle sphericity: 0.89
Excess air velocity: 1.31 m/s
Tube: 32 mm tube bundle
Duration: 141.5 h

complex for a multi-tube bundle, leading to more abrasion on the upper tube surface.

The local erosion rates were integrated to give the average erosion rate over the tube circumference. The averages were determined to be 7.50 $\mu m/100h$ and 7.66 $\mu m/100h$ for brass and Al2011 respectively, in satisfactory agreement with the results from the complete rings, 6.83 $\mu m/100h$ for brass and 6.80 $\mu m/100h$ for Al2011. The maximum local erosion rates were 25.7 and 28.6 $\mu m/100h$ for brass and Al2011, 4 times higher than the average erosion rate of the complete rings. This indicates that the average erosion rate in a tube bundle can underestimate the danger of local rupture by at least a factor of four.

7.3.5 Square Tube

A square tube was put into the bed under the base operating conditions for 311 h to test separately the erosion rates due to impact and scraping of solid particles. The tube was installed so that the bottom surface of the tube was parallel to the distributor. Four flat rectangular cuboid brass pieces were mounted on a square plexiglass holder in the same way as the segments used for circumferential erosion distribution tests (see Section 4.3). The four specimens were placed only in the central region of each surface and the four corners were rounded off. The gaps between specimens were filled with plexiglass pieces to make the surface smooth.

The average erosion rates for the two side surfaces of the square tube were 1.12 and 1.14 $\mu m/100h$, only 11% of the 10.5 $\mu m/100h$ rate measured for the bottom surface. The erosion at the tube bottom was considered to be caused only by particle impact while the erosion at the two sides was considered to be caused mainly by particle scraping. The erosion rate for the top surface was very low, only 0.27 $\mu m/100h$. This suggests that erosion caused by impact is much more severe than that caused by abrasion, and that erosion of all horizontal tubes is mainly due to solid impact erosion.

It was also noted that the erosion rate for the square tube bottom surface (10.5 $\mu m/100h$) was somewhat smaller than that at the round tube bottom (15.2 $\mu m/100h$). This suggests that the square tube may have retarded the particle impact mass flow rate and/or particle impact velocity on the tube bottom.

7.4 Effect of Distributor Geometry

Two tests (Runs 52 and 59) were carried out at room temperature with the same operating conditions in the circulating fluidized bed combustion unit. These provided some indication of the effect of a different distributor. The conditions were nearly the same as the base conditions in the main column used in this work, but the particle size was 0.92 mm, slightly smaller than 1.0 mm because some smaller sand used in previous CFBC runs remained in the L-valve when the dense bed was drained. The air distributor of the combustor consisted of three tuyeres, each with six orifices sloping downwards at an angle of 30° to the horizontal, as presented in Section 3.8. The combustor also had a somewhat smaller cross-sectional area (152 x 152 mm) than the cold model column (203 x 216 mm).

The results are shown in Figure 7.13 in comparison with the average results of five runs (Runs 2, 4, 22, 31, 33), which were conducted at essentially the same conditions except that a multi-orifice distributor was used in the low temperature three-dimensional column. The results for Runs 52 and 59 were corrected for particle size using equation 7.1. The comparison shows that erosion rates changed by a factor of up to 2.3 for some materials, with the multi-orifice distributor leading to much more severe erosion than the tuyere distributor. This dramatic change in erosion rate must have resulted from a change of gas and particle flow conditions in the vicinity of the tube. The tuyeres in the combustor discharged air nearly horizontally. This may have reduced the initial bubble rise velocity

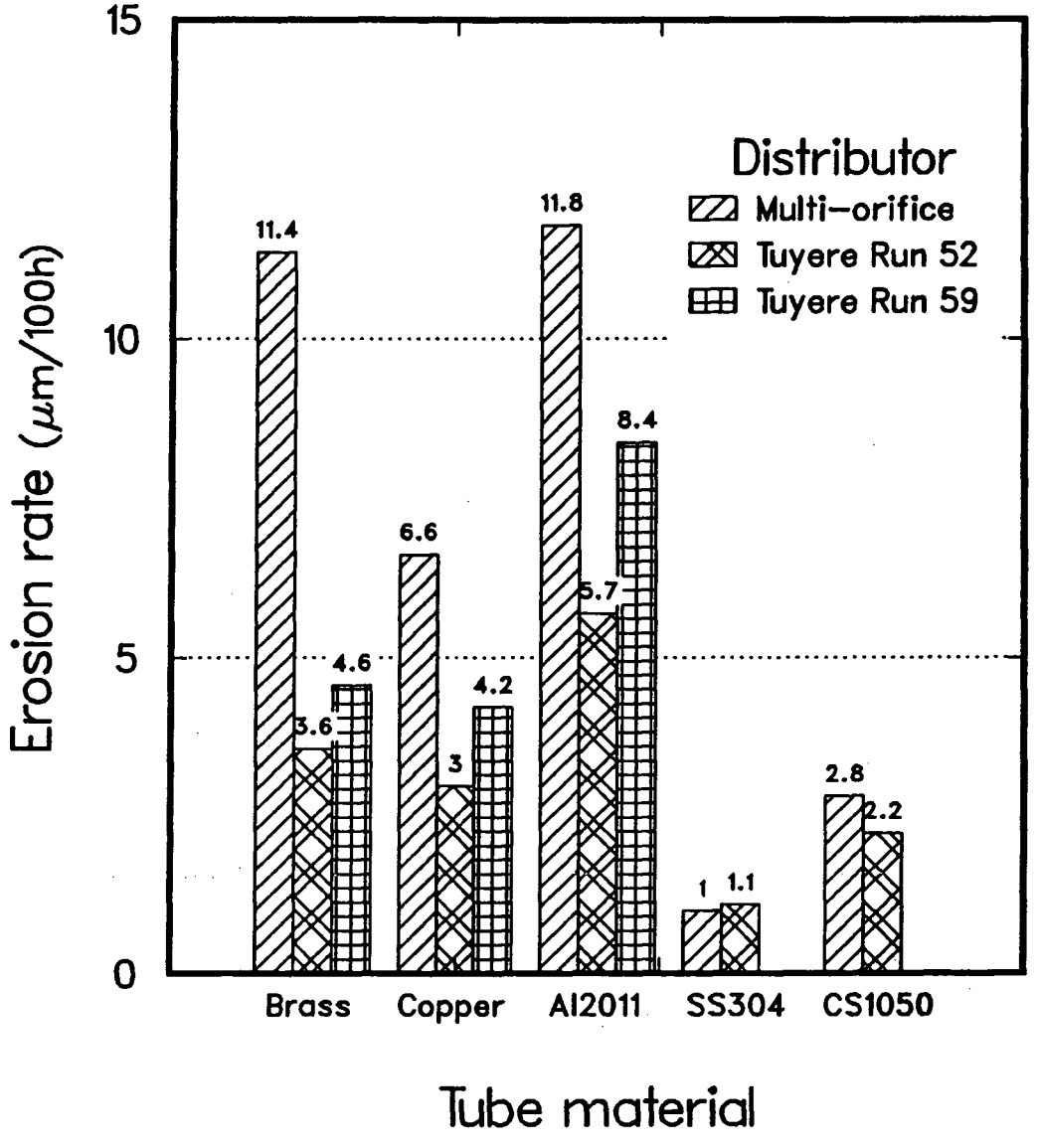

Figure 7.13 Effect of distributor on erosion rate

Operating conditions:

Particles: 1.0 mm silica sand
Particle sphericity: 0.89
Excess air velocity: 1.31 m/s
Tube: 32 mm single tube
Duration: 40 – 100 h

and bubble coalescence, hence reducing the bubble size and therefore the bubble or particle velocity at the level of the tube. Also, more of the bubble gas may have been distributed to the wall region, resulting in fewer bubbles in the centre of the column. Moreover, the smaller column cross-section will cause about 5% reduction in the limiting (slug) velocity according to equation 2.18. As discussed in Section 7.1, erosion is proportional to the particle velocity to the 2.1 power, so that a 5% reduction in the void (and hence the particle impact) velocity would result in about a 10% decrease in erosion rate.

7.5 Effect of Mechanical and Thermal Properties of the Tube Materials

Under the same operating conditions, rings of different materials suffered different erosion rates, with some materials being eroded up to 30 times faster than others. There are many material properties which may affect the erosion rate. As reviewed in Section 2.3, the mechanical properties are most likely to influence the erosion rate directly. The mechanical properties of the materials tested are listed in Table 3.6. The effects of these mechanical properties are discussed in this section.

7.5.1 Hardness

The most commonly quoted mechanical property is hardness. During the erosion test runs, the Vickers hardnesses of eroded rings were measured several times. Table 7.10 summarizes the results of these measurements. It was found that the hardness of all the materials did not change appreciably due to erosion.

The average erosion rates for six runs (Runs 2, 4, 22, 31, 33 and 34) at the base operating conditions are plotted in Figure 7.14 against the hardness of ten different ring materials. While erosion appears to generally decrease with increasing hardness, the trend is unclear, especially for the materials in the 50 - 60 kg/mm^2 hardness range.

Table 7.10: Material hardness measured at different times during the overall test period

Ring material	Hardness (kg/mm^2) Fresh	after 300 h	after 1480h	after 1870h	after 2240h
Brass	158	164	156 156		155 154
Copper	106	108	97 95		96 100
Al2011	139	133	135 135		130 131
CS1050	254	237	234 237	229 234	226 234
SS304	241	235	256 252	257 260	264 289

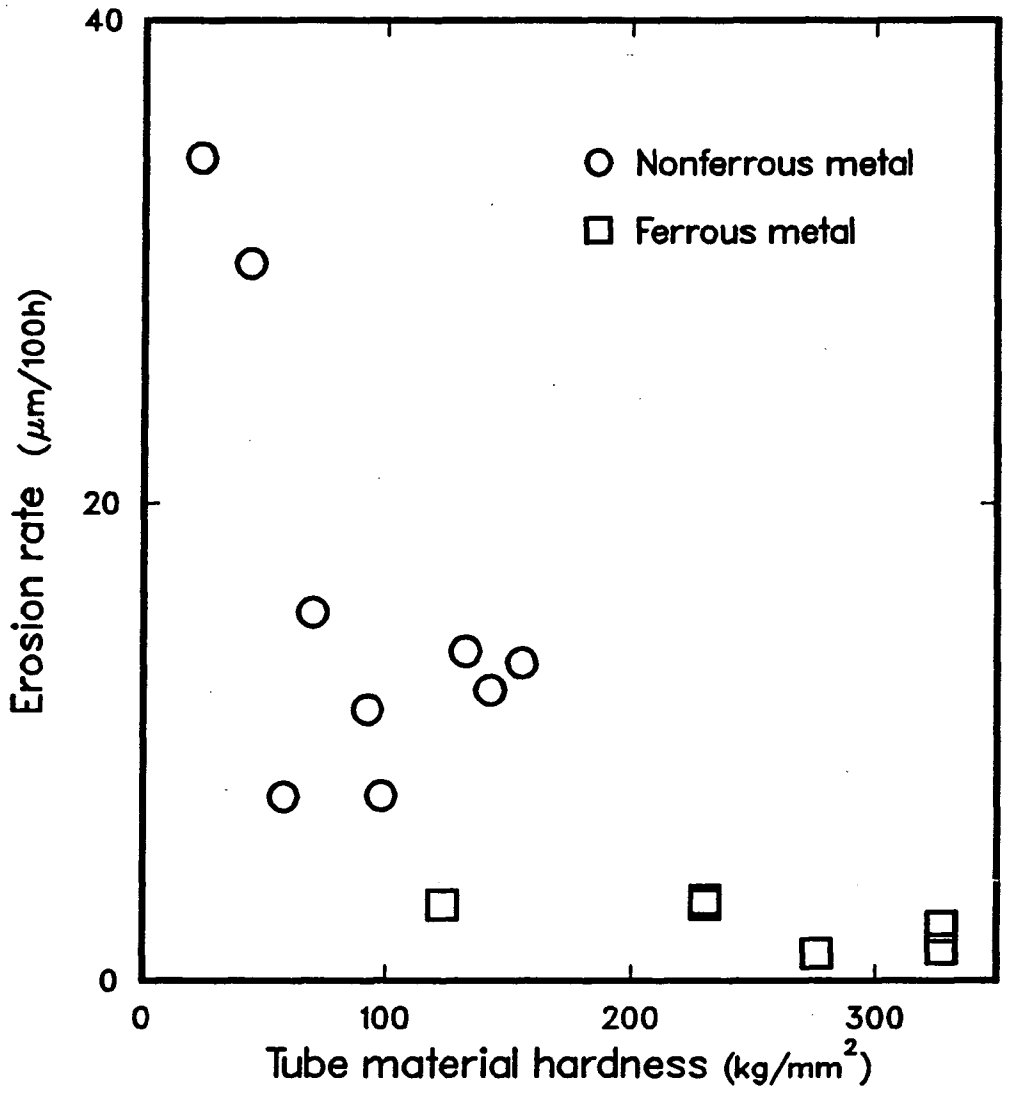

Figure 7.14 Erosion rate vs. material hardness for different materials

Operating conditions:

Particles: 1.0 mm silica sand
Particle sphericity: 0.89
Excess air velocity: 1.31 m/s
Tube: 32 mm single tube
Duration: 35 – 120 h

To investigate the influence of hardness further, several materials were heat-treated to change their hardness. The hardnesses of these nine heat-treated rings and the conditions of treatment are tabulated in Table 7.11. Four Keewatin rings were hardened to four different hardnesses covering a wide range. Figure 7.15 shows the erosion rates of these four rings as well as of other ferrous metal rings. It is clear that the erosion rate of Keewatin rings was unaffected by hardness. Two rings each of brass, copper and Al2011 were annealed under different conditions. The erosion rates of these annealed rings are plotted together with those of the original cold-drawn rings in Figure 7.16. This figure indicates that erosion was insensitive to the hardness change, except for one Al2011 ring, the hardness of which was so low that the particle impact may have overcome the material's yield point as discussed later.

The above findings suggest that tube material hardness may not be a major factor influencing erosion rate. Since the heat-treatment of materials also changed the tensile strength and yield strength of the materials and there was very little change in erosion, these factors also appear to be excluded as major factors.

7.5.2 Young's Modulus

The Young's modulus (elasticity) of a material is determined by the bonding structure and does not change with heat-treatment. The erosion rates of the same six runs conducted under the base conditions are plotted again in Figure 7.17. This time the Young's modulus of the ten ring materials is the abscissa. The results with silicon carbide particles (Run 35) are plotted against material Young's modulus in Figure 7.18.

As shown in Figure 7.17, there exists a clear trend, with erosion rate decreasing as the Young's modulus (elasticity) increased. The erosion rate changes smoothly except for pure Al, where the erosion rate unexpectantly increased to a high value. A similar behaviour is

Table 7.11: Hardness and heat treatment of rings

Ring material	Hardness before treatment (kg/mm^2)	Hardness after treatment (kg/mm^2)	Heat treatment conditions (*)
Brass #71	155	142	57.5 h at 400/120 C (**)
Brass #72	154	92.3	30.0 h at 400/120 C, 27.5 h at 750/145 C,
Al2011 #75	130	69.6	57.5 h at 400/120 C
Al2011 #76	131	43.6	30.0 h at 400/120 C, 27.5 h at 750/145 C,
Copper #73	98	57.8	57.5 h at 400/120 C
Keewatin steel #19	not avail.	320	Oil quenched from 800 C in saltpot, tempered at 600 C for one hour
Keewatin steel #20	not avail.	480	Oil quenched from 800 C in saltpot, tempered at 480 C for one hour
Keewatin steel #21	not avail.	551	Oil quenched from 800 C in saltpot, tempered at 310 C for one hour
Keewatin steel #22	not avail.	836	Oil quenched from 800 C in saltpot, tempered at 105 C for one hour

* Many of the rings underwent erosion in the combustor at high temperature, which changed their hardness. In these cases, the history of the rings is given instead of the heat treatment conditions.

** For details of the temperature conditions, see Chapter 8.

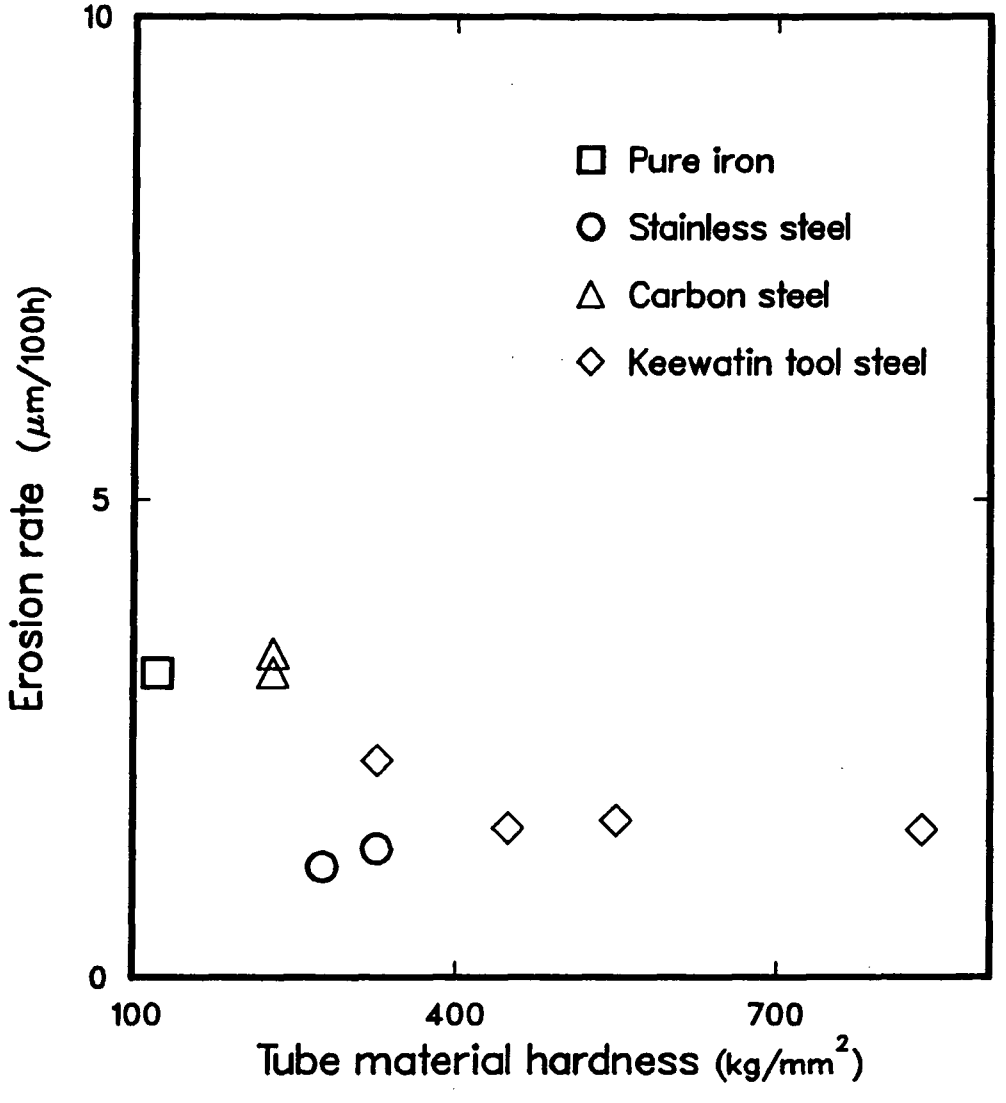

Figure 7.15 Erosion rate vs. material hardness for ferrous metal materials

Operating conditions:

Particles: 1.0 mm silica sand
Particle sphericity: 0.89
Excess air velocity: 1.31 m/s
Tube: 32 mm single tube
Duration: 35 – 120 h

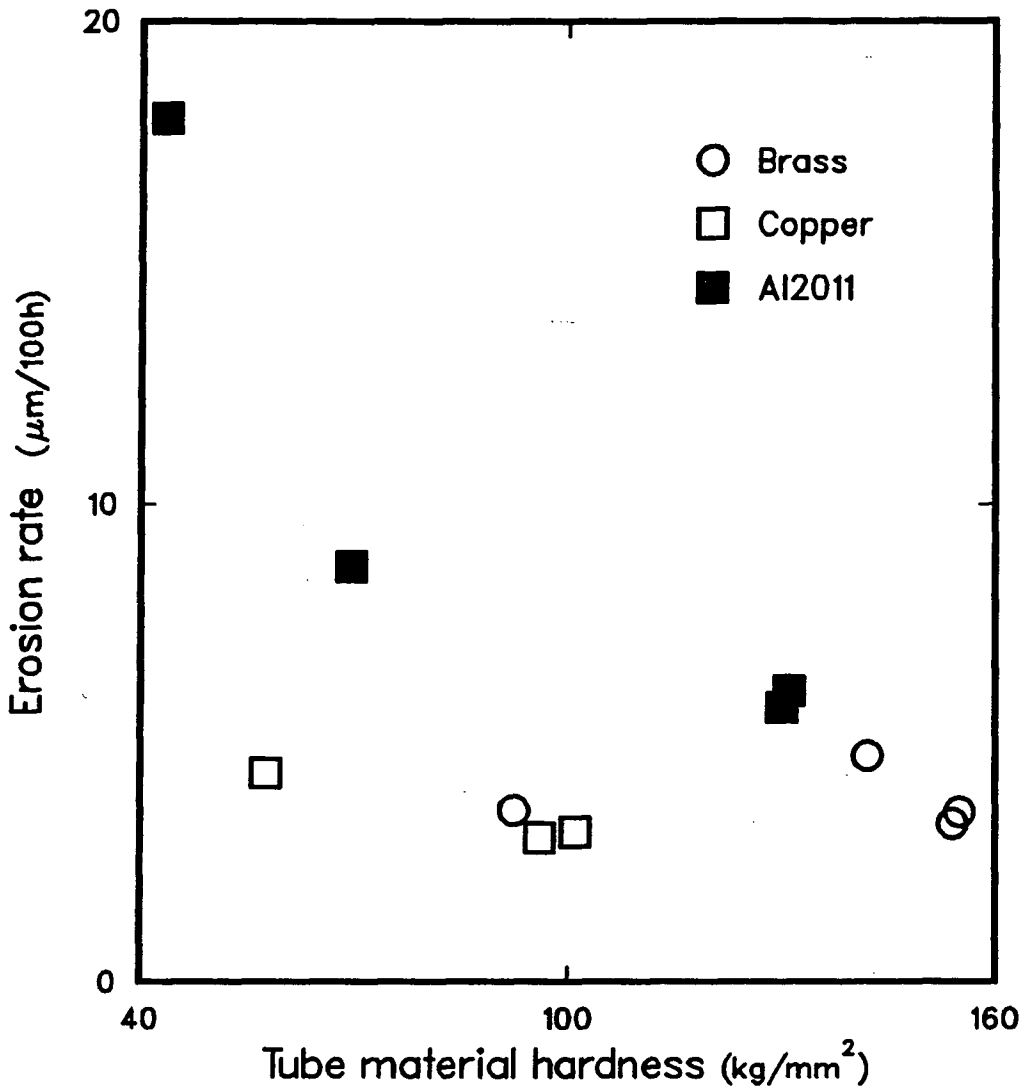

Figure 7.16 Erosion rate vs. material hardness for non–ferrous metals before and after heat treatment

Operating conditions:

Particles: 1.0 mm silica sand
Particle sphericity: 0.89
Excess air velocity: 1.31 m/s
Tube: 32 mm single tube
Duration: 35 – 120 h

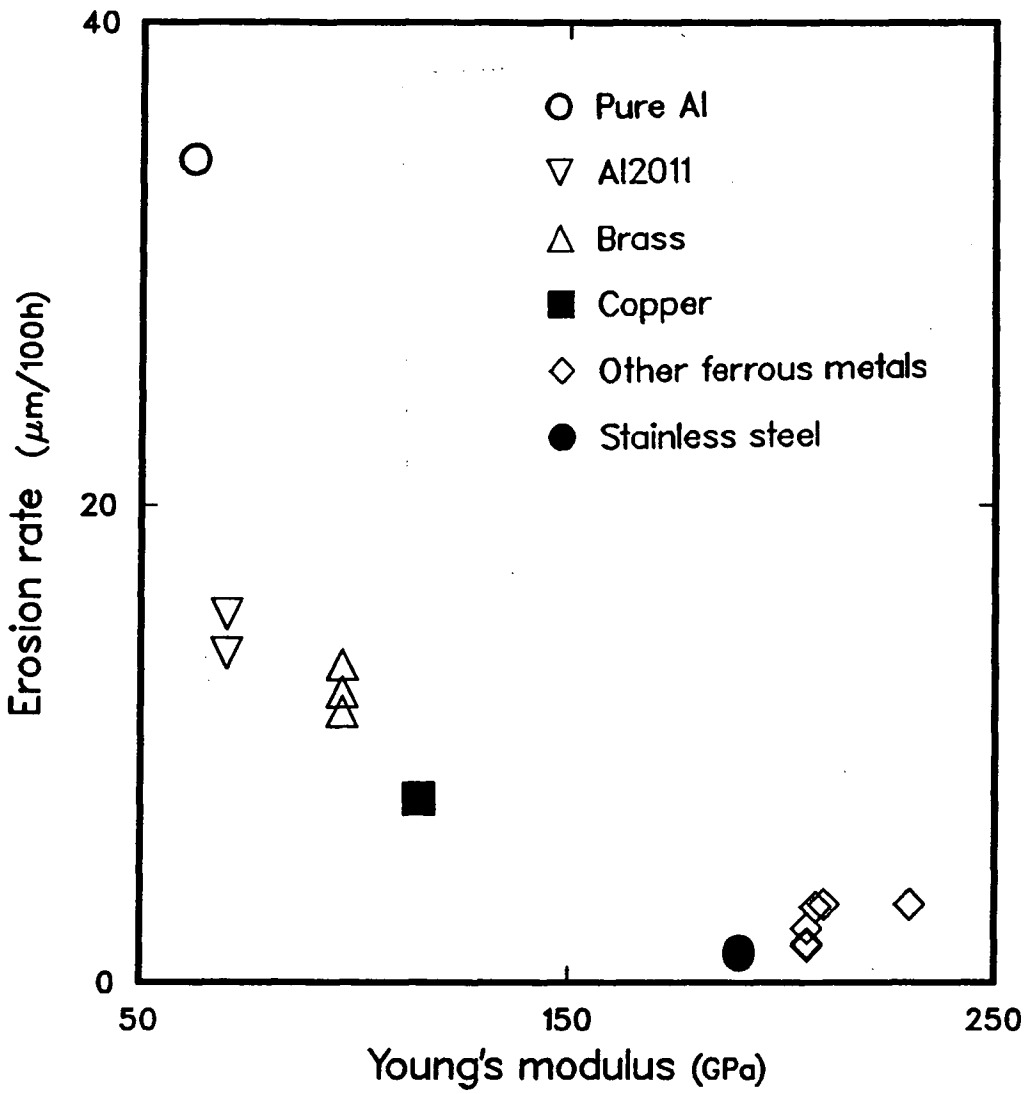

Figure 7.17 Erosion rate vs. tube elasticity for silica sand particles

Operating conditions:

Particles: 1.0 mm silica sand
Particle sphericity: 0.89
Excess air velocity: 1.31 m/s
Tube: 32 mm single tube
Duration: 60 – 120 h

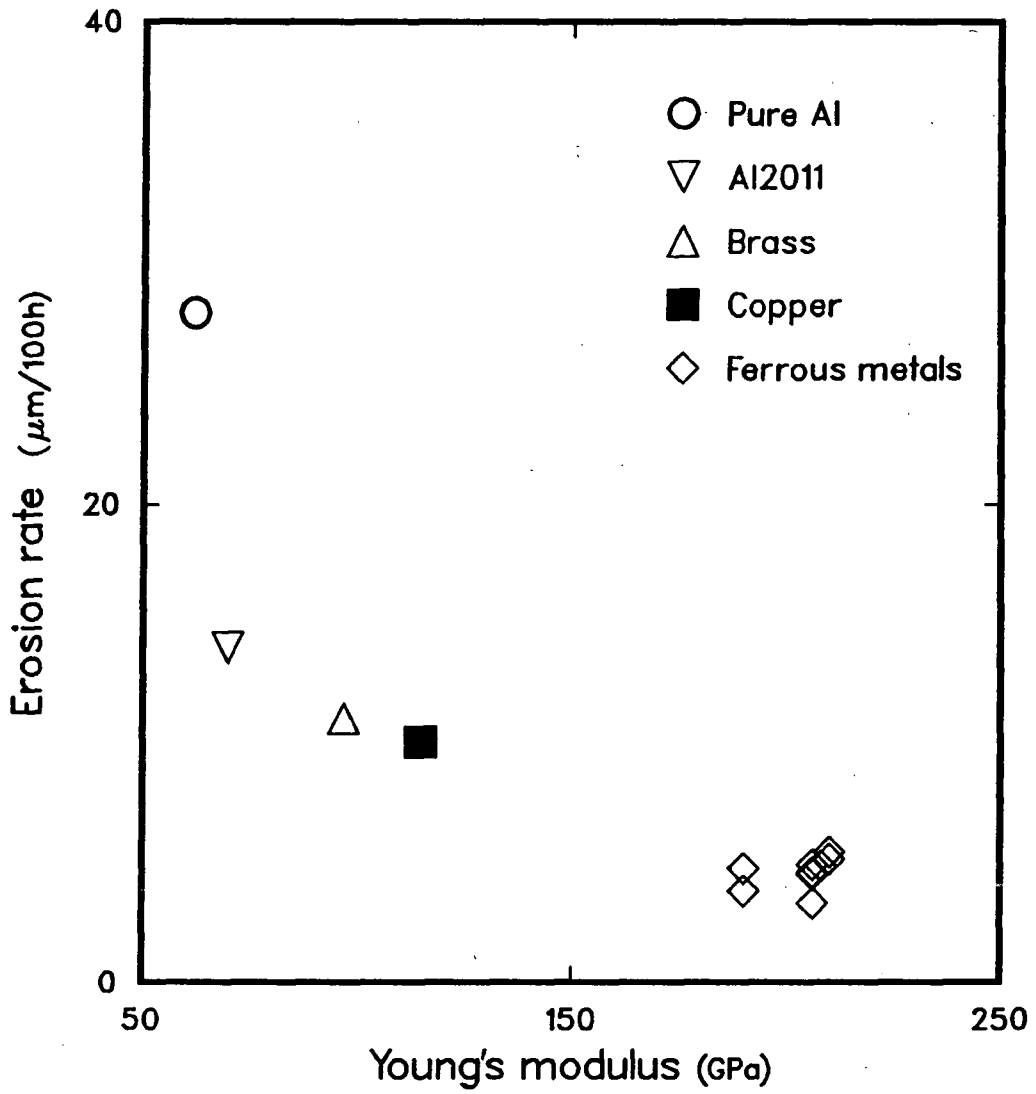

Figure 7.18 Erosion rate vs. tube elasticity for silicon carbide particles

Operating conditions:

Particles:	*1.0 mm silicon carbide*
Particle sphericity:	*0.89*
Excess air velocity:	*1.31 m/s*
Tube:	*32 mm single tube*
Duration:	*55 h*

found in Figure 7.18. The reason for the very high erosion rate for pure Al may be because the yield strength of pure Al is very low (29.6 MPa) so that the particle impacts on the tube surface may cause a significant amount of plastic deformation. For other materials the fact that erosion is a strong function of material Young's modulus suggests that the kinetic energy of the particles at impact was low and produced mainly elastic deformation as discussed in Section 5.6. The results from the fluidized bed agree with those from the dropping tests, suggesting that elasticity is a major factor influencing erosion.

7.5.3 Other Mechanical Properties

The relationship between erosion rate and Young's modulus was generally smooth, but with three outlying points for pure Al and two stainless steels. There appear to be secondary factors affecting erosion.

As stated earlier in this section, tensile strength and yield strength change due to heat treatment. The insensitivity of erosion to heat treatment suggests that erosion is insensitive to tensile and yield strength.

Another factor which could be important is ductility. Ductility is also altered by heat treatment, although the changes are not as dramatic as changes in the tensile and yield strength (ASM 1983). The results suggest that the influence of ductility is probably small. However, stainless steel had an extremely high ductility (more than 50% elongation), much more than the other ferrous materials (20-25% elongation). This high ductility may have resulted in the unusually low erosion rates of the two stainless steels shown in Figure 7.17 compared with the other ferrous metals.

Although erosion was insensitive to yield strength, there may be a threshold value of yield strength below which the impact of particles would cause mainly plastic deformation, hence increasing the erosion rate dramatically. This threshold value seems to exist in the

Vickers hardness 44 – 57 kg/mm^2 range, or between yield strengths of 143 and 162 MPa. This could explain the high erosion rate of pure Al (Figures 7.14 7.17 and 7.18) and the heavily annealed Al2011 alloy (Figure 7.16). The original yield strengths of the ten materials are plotted in Figure 7.19.

There are other mechanical properties which may also influence the erosion rate. Since erosion is believed to be a fatigue process (see Chapter 9), the surface fatigue resistance and surface toughness may play important roles in the process. However, there are no standard methods to measure these properties and no applicable data available from other sources. Therefore, these properties are not considered in the model proposed in Chapter 9.

7.5.4 Thermal Properties

Some thermal properties of the ring materials such as the thermal conductivity, thermal diffusivity, thermal capacity and the coefficient of thermal expansion are also considered. The values of these thermal properties are listed in Table 3.7. No clear relationship was found between these thermal properties and erosion rate of the ring materials. This finding is in agreement with the statement by Rickerby (1983) that the mechanical properties rather than thermal properties are more important in erosion caused by solid particle impact.

7.6 Incubation of Fresh Materials

For fresh materials, there may exist an incubation period during which the erosion rates differ from the erosion rates for previously eroded materials. Prior to Run 4, fresh rings of the five materials of base conditions were put into the three-dimensional cold model column together with five previously eroded rings of the same materials under the base operating conditions to test the incubation effect.

The volume losses of the ferrous and non-ferrous materials are plotted against operating

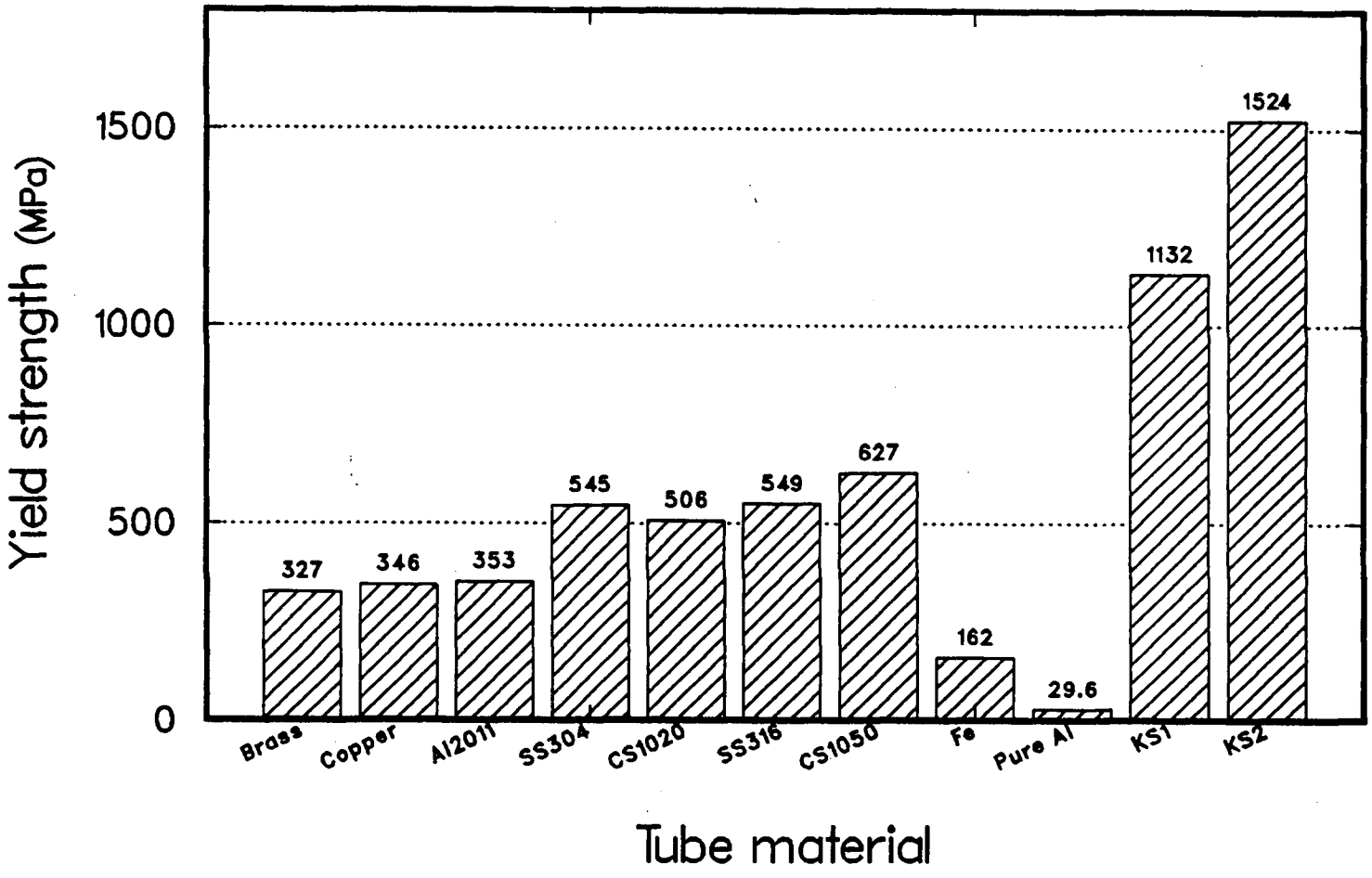

Figure 7.19 Yield strength of different tube materials

duration in Figures 7.20 and 7.21. For the three non-ferrous metals, the slopes of the cumulative volume loss vs. time curves are constant, indicating that there is little sign of incubation. On the other hand, for ferrous metals, the slopes of the same curves are smaller at the beginning of the erosion process, suggesting that an incubation period exists. As shown in Figure 7.21, the incubation period of fresh SS304 ring is about 10 h, while the incubation period for fresh CS1050 ring is about 5 h. Both ferrous materials show a critical volume of about 0.02 mm^3 below which the erosion rates are lower than normal. The 0.02 mm^3 volume loss represents a thickness of 0.064 μm for the rings tested, suggesting that the erosion rate for the first 0.064 μm depth of fresh surface is lower than the normal erosion rate due to an incubation effect. Since the erosion rates for non-ferrous metals are high and a 0.064 μm depth will be eroded away in only about half an hour, the incubation effect for these materials would be negligible. Even for ferrous materials, the incubation periods are less than 10 h, a period too brief to be considered important for erosion of tubes in real fluidized bed processes.

The mechanism of the incubation is not very clear. It may be due to initial formation of craters and platelets. Alternatively, it may be due to the adherance or deposition of very fine fragments from particle attrition and collision with the tube, leading to smaller apparent erosion rates determined from weight losses. Energy Dispersion X-ray (EDX) tests have shown that about 30 – 50% of the tube surface is covered by silica after 20 h operation, while the silica concentration on a fresh ring surface is zero. However, the deposition of fine silica fragments does not appear to be the only factor affecting the incubation behaviour of different materials since the incubation periods for different materials are not identical. Which factor contributes more to the incubation of fresh materials was not further investigated since the incubation period was found to be short and therefore of limited practical

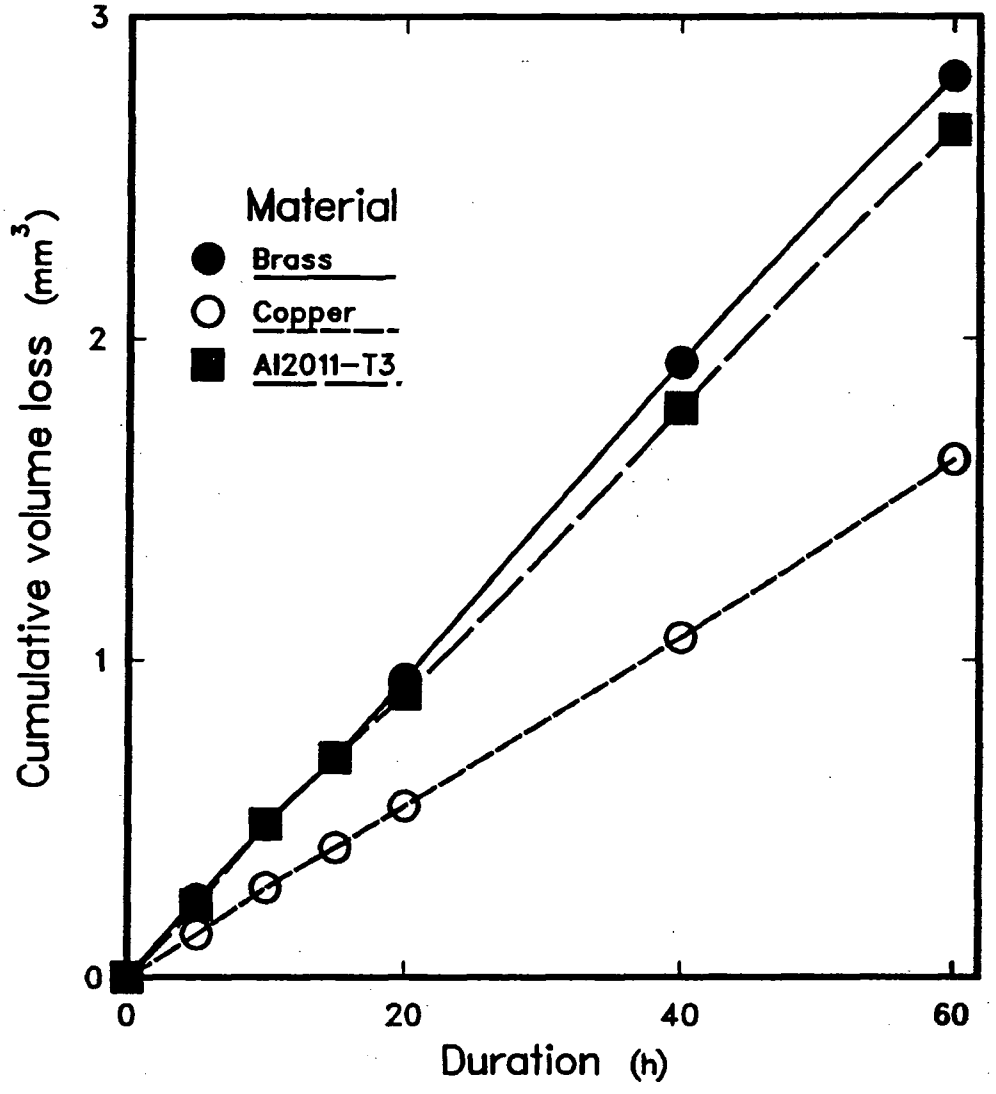

Figure 7.20 Cumulative volume loss vs. duration for non-ferrous metals

Operating conditions:

Particles: 1.0 mm silica sand
Particle sphericity: 0.84
Excess air velocity 1.31 m/s
Tube: 32 mm single tube

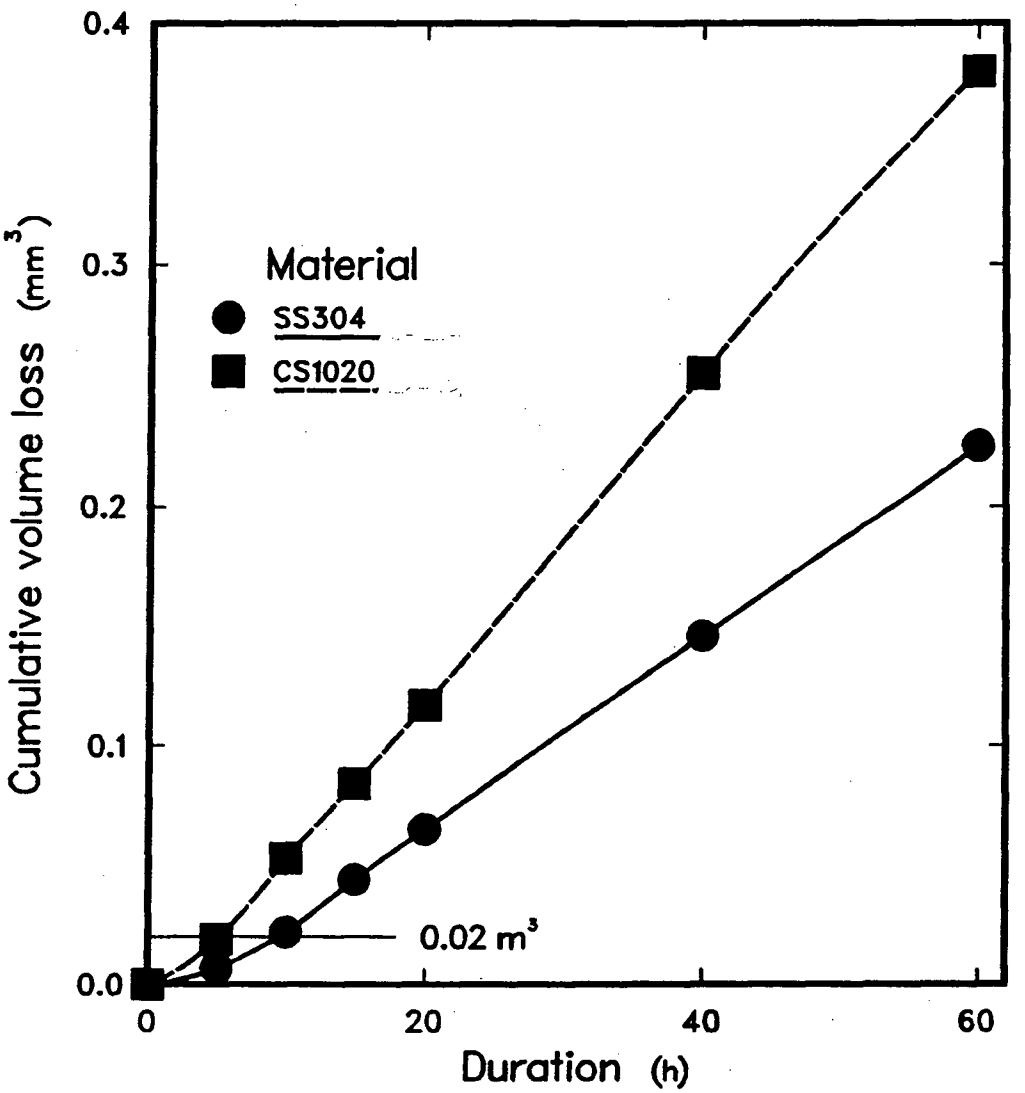

Figure 7.21 Cumulative volume loss vs. duration for ferrous metals

Operating conditions:

Particles: 1.0 mm silica sand
Particle sphericity: 0.84
Excess air velocity 1.31 m/s
Tube: 32 mm single tube

interest.

7.7 Conclusions

For the range of conditions tested:

(1) The erosion rate in the cold model fluidized bed increased with the void velocity to the power of 2.1 and with the particle size to the power of 1.2.

(2) Increasing the particle hardness augmented the erosion rate of ferrous metals, but did not appreciably affect the erosion rate of non-ferrous metals.

(3) Angular particles caused much faster erosion than rounded ones.

(4) The erosion rate increased slightly with a reduction in the tube diameter. There appeared to be a critical diameter below which the erosion rate of some materials increased dramatically.

(5) Erosion did not occur uniformly around the circumference and axis of a tube. More than 95% of the material loss occurred over the lower half of a single tube, and erosion was higher in the middle of the bed than close to the walls.

(6) Erosion was very dependent on tube location and configuration. A tube in the interior of a tube bundle suffered much less average erosion, but increased relative erosion over its upper surface. A tube in the jet zone endured higher erosion. An inclination of 15° from the horizontal did not appreciably affect the erosion rate. Reduction of static bed height led to decrease of erosion rate.

(7) Erosion of tubes was mainly caused by particle impact, erosion due to particle abrasion or scraping was less than 11% of the total weight loss.

(8) There were indications that the gas distributor can influence the erosion rate substantially.

(9) Young's modulus appeared to be the major mechanical property of the target material that influences the erosion rate, with higher Young's modulus producing higher resistance to erosion. The erosion rate was not sensitive to changes in material hardness, yield strength and tensile strength. However, there appeared to be a threshold value of hardness (and yield strength) below which the erosion rate increased dramatically.

(10) Incubation periods for fresh materials were short and appear to be of limited importance for erosion in real fluidized beds.

CHAPTER EIGHT: RESULTS AND DISCUSSION: ELEVATED TEMPERATURE EXPERIMENTS

Nine tests were conducted in the lower part of the CFB (circulating fluidized bed) combustor described in Chapter 3 at four different tube temperatures to test the effect of temperature on the erosion of different materials. Seven materials, i.e. brass, copper, Al2011, SS304, SS316, CS1020 and CS1050, were tested. All tubes were of 32 *mm* o.d.. The superficial gas velocity was 1.83 m/s; 0.92 *mm* silica sand particles (Φ_s=0.89) were employed as the bed material, and the static bed height was 410 *mm* in all cases. Details of the apparatus and its operation are presented in Section 3.8.

All high temperature tests lasted about 30 hours except for Run 58 for which the duration was 74 hours. Longer runs were not possible because of the limited availability of the equipment and of operating personnel. Because of the limited number and duration of the tests, they must be regarded as preliminary in nature. For convenience in comparing the results at high temperature with those at room temperature, the erosion rates reported in this Chapter have all been corrected for particle size using equation 7.9. The original data appear in Appendix D.

The temperature and other operating conditions for each run are given in Table 8.1. The four temperatures used were room temperature, a bed temperature of 400 C with a tube temperature, measured by a thermocouple embedded in the tube positioned at the side, of 120 C to 130 C, a bed temperature of 750 C with a tube surface temperature of 145 C and a bed temperature of 780 C or 750 C with a tube surface temperature of 520 C. For the sake of brevity, these temperatures are separated by a slash in this chapter. For example 400/120 C refers to a case where the bed temperature was 400 C and the tube

Table 8.1: Temperature and other operating conditions for erosion tests in the combustor

Run No.	Materials tested	Operation duration (h)	Coolant	Temperatures (C) Tube surface	Bed	Coolant in	Coolant out
051	all 7	41.8	n/a	25	25	n/a	n/a
052	all 7	43.2	n/a	25	25	n/a	n/a
059	all 7	34.9	n/a	25	25	n/a	n/a
053	all 7	30.0	water	120	400	23	92
054	all 7	27.3	water	130	402	21	98
055	all 7	30.0	water	145	750	16	22
056	S304, SS316	28.7	air	520	751	29	141
057	S304, SS316	28.6	air	520	780	27	131
058	S304, SS316	73.8	air	520	750	30	137

Other operating conditions:

Excess air velocity: 1.31 m/s

Particles: 0.92 mm silica sand

Particle sphericity: 0.89

temperature was 120 C. The erosion behavior of ferrous and non-ferrous metals under these conditions was found to be totally different.

8.1 Non-Ferrous Metals

The three non-ferrous metals (brass, copper and aluminum alloy) were tested under the first three temperature conditions. The results of these tests are presented in Table 8.2. It is clear from this table that the erosion rate for these three materials increased as the tube and bed temperatures increased, although the increments for the different materials were different.

A distinct oxidized layer was not observed for any of the three materials at 400/120 C, nor for the brass and Al2011 at 750/145 C. However, copper was heavily oxidized to form a very friable black layer about 0.01 - 0.1 *mm* thick in the 750/145 C test.

For copper, the erosion rate increased by a factor of 8 from room temperature to 400/120 C and appeared to remain unchanged as the temperature was further increased. This might be because copper was already softened under the temperature conditions 400/120 C to be lower than the threshold hardness values discussed in Section 7.5. The relatively constant measured erosion rate at the two higher temperatures could also be caused by a balance between increasing real erosion rate and increased oxidation of the surface.

For the brass and aluminum alloy, the erosion rate increased much more smoothly as the temperature increased. As discussed in Sections 5.6 and 7.5, elasticity appears to play a major role in erosion. Mechanical properties at the tube temperature affect erosion rate. Young's modulus of metals and alloys decreases with increasing temperature (ASM Handbook 1983). If elasticity is important in erosion at the test temperature, some contribution to increased erosion might be expected from this source. However, it is unlikely

Table 8.2: Erosion rates of non-ferrous metals at different temperatures

Bed temperature (C)	25	400	750
Tube surface temperature (C)	25	120	145
	Erosion rate (μm/100h)		
Brass	4.57 3.43 3.68	7.95 9.79	13.2
Copper	2.91 3.03 4.22	23.5	22.8
Al2011	5.55 5.88	6.86 8.14	17.8

Other operating conditions:

Excess air velocity: 1.31 m/s

Particles: 1.00 mm silica sand

Particle sphericity: 0.89

that Young's modulus will experience more than a 10% reduction over the temperature interval of interest (Lund 1987). On the other hand, the hardness and yield strength of metals can be substantially lower at elevated temperatures. As noted in Chapter 7, there may be a threshold yield strength below which plastic deformation plays an important role in erosion. It was suggested there that heavily-annealed Al may have a yield strength below this threshold value at 20 C. At higher temperatures, it is here suggested that the yield strength of copper and brass may also be below the threshold values. The hardness of non-ferrous metals measured before and after the high temperature tests are listed in Table 8.3. It is clear that hardness decreased significantly with increasing temperature. The hardness of these materials must have been even lower during the tests when the surface of the rings was in contact with the bed. This hardness change appears to be the major reason for the increase of erosion rate.

8.2 Ferrous Metals

Four ferrous metals (SS304, SS316, CS1020 and CS1050) were tested under different temperature conditions. The results for these ferrous metals were totally different from those for non-ferrous metals. As shown in Figures 8.1 and 8.2, the erosion rate, measured from weight loss, decreased as the bed and tube surface temperatures increased, and when the temperatures were at 780/520 C, the apparent erosion rate of stainless steel was close to zero or even negative.

It was observed that all of the ferrous metal rings were oxidized after being heated up in the bed. Carbon steel rings were oxidized slightly under the 400/120 C temperature conditions, while stainless steel rings showed no sign of apparent oxidation under the same conditions. After the run with temperature conditions of 750/145 C, the surface of the

Table 8.3: Hardness of non-ferrous metals before and after high temperature erosion tests

Ring material	Hardness (kg/mm^2) Original	after 400/120 C run	after 750/145 C run
Brass #71	155	142	
Brass #72	154	145	92.3
Al2011 #75	130	69.6	
Al2011 #76	131		43.6
Copper #73	96	45.1	
Copper #74	101	46.7	<< 10

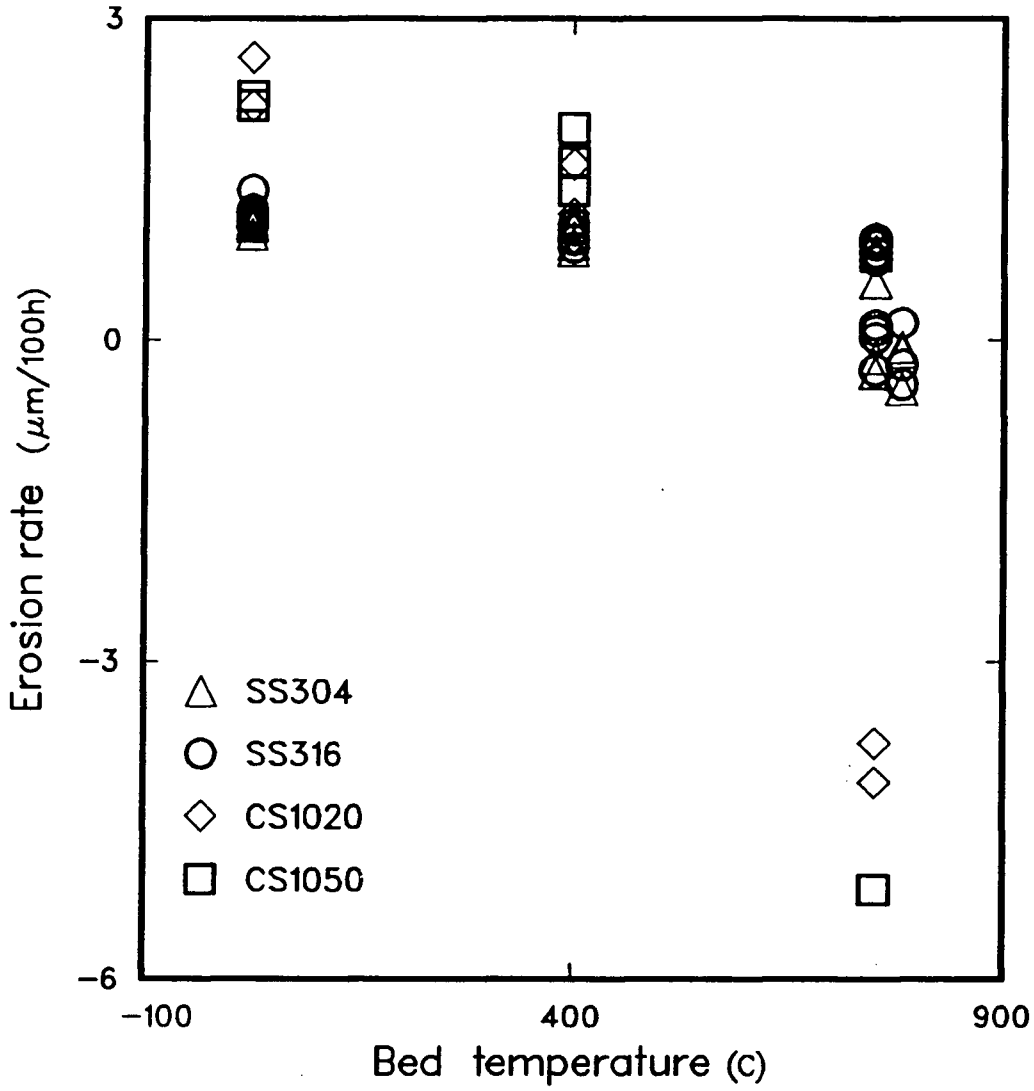

Figure 8.1 Erosion rate vs. bed temperature for 1.00 silica sand particles with 32 mm tube at $u - u_{mf} = 1.31$ m/s

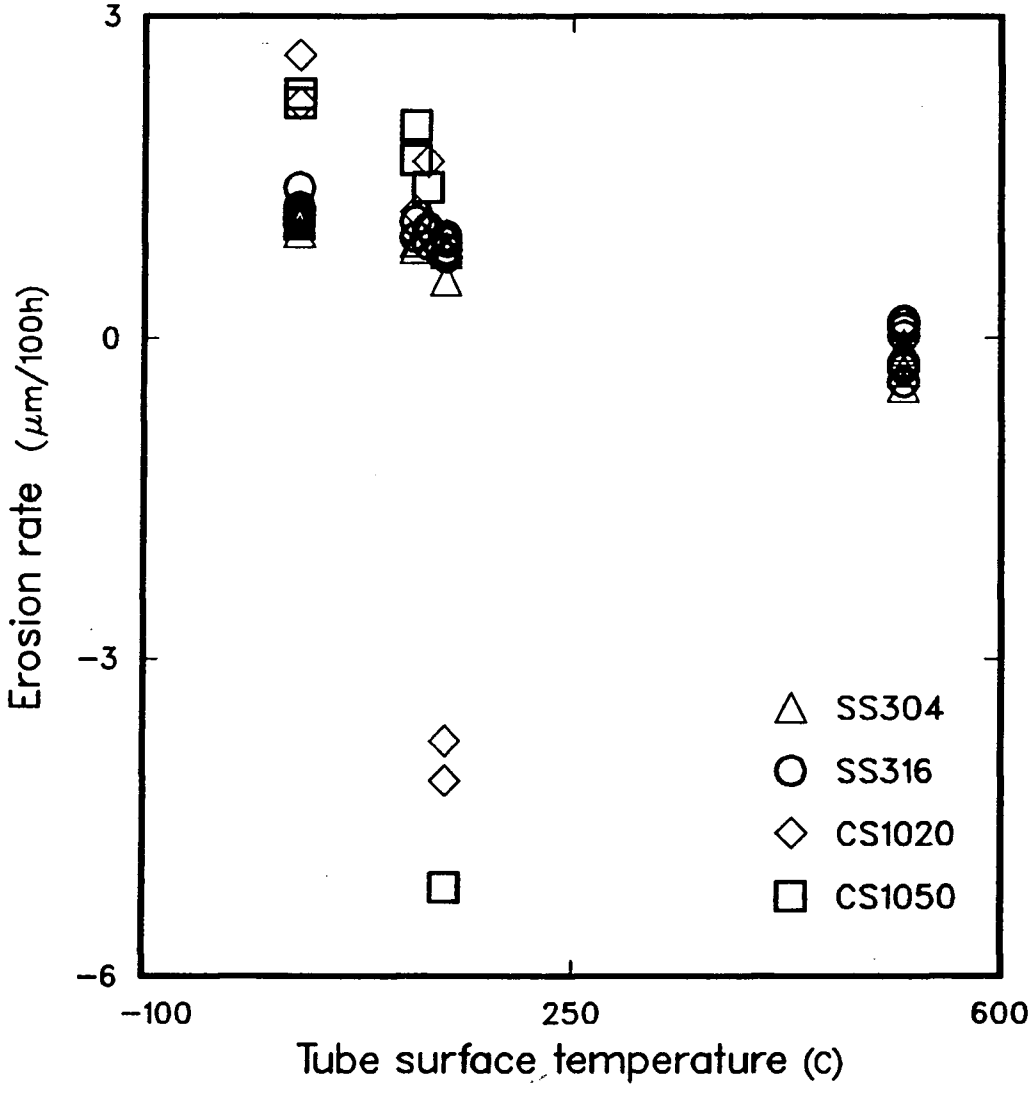

Figure 8.2 Erosion rate vs. tube surface temperature for 1.00 silica sand particles with 32 mm tube at $u - u_{mf} = 1.31$ m/s

carbon steel rings was totally blackened and appeared to be brittle, whereas the surface of stainless steel rings was just light gray. After the final run with 780/520 C temperatures, the surfaces of the stainless steel rings were also heavily oxidized to form thin layers of shiny dark brown surface.

Since the melting points of steel are much higher than those of non-ferrous metals, it seems likely that the hardnesses of the steels under the operating temperatures remained much higher than the threshold hardness. This is supported by the finding that the hardnesses of the tested steels, measured at room temperature after the tests, did not change significantly (Table 8.4), contrary to the non-ferrous metals (Table 8.3). The results for the ferrous alloys under different operating temperatures are believed to be strongly influenced by surface oxidation. In the presence of surface oxidation, the apparent erosion rate calculated from ring weight loss is actually the difference between material loss due to erosion and material gain due to oxidation or corrosion.

For carbon steels, the measured erosion rate at 400/120 C was only about 65% of that at room temperature, probably due to the surface oxidation. At a higher temperature, 750/140 C, the apparent erosion rate was even negative (Figures 8.1 and 8.2) since the heavily oxidized surface layer increased the ring weight. In a later run (Run 59), the oxidized surface layer was found to be very vulnerable to erosion at room temperature. This suggests that the erosion rate might have been very high if the carbon steel rings had been exposed in the bed at 750/140 C for a longer duration. Stringer et al. (1985) and Mann et al. (1987) have indicated that low grade materials, such as carbon steel, would suffer severe erosion in fluidized bed combustors and are not commercially acceptable. No difference has been noticed between the two carbon steels tested.

For stainless steel, the oxidation rate of the ring surface appeared to be slower than that

Table 8.4: Hardness of ferrous metals before and after high temperature erosion tests

Ring material	Hardness (kg/mm^2)			
	Original	after 400/120 C run	after 750/145 C run	after 780/520 C run
SS304	296	307	310	286
SS316	327	372	364	356
CS1020	230	238	201	n/a
CS1050	220	250	232	n/a

of the carbon steel rings. This is, of course, a property of stainless steels that makes them valuable in elevated temperature applications. Figure 8.2 shows that the apparent erosion rate of stainless steels decreased slightly with the increase of tube surface temperature and approached zero at 520 C. At the temperature conditions 400/120 C, where little sign of oxidation was observed, the erosion rates of both stainless steels were slightly reduced, to about 88% of that at room temperature. When the temperatures were increased to 750/140 C, where the light gray surface of the rings showed some sign of oxidation, the erosion rate of both stainless steel rings decreased to about 80% of that at room temperature, apparently due to the surface oxidation. In the final runs with the temperatures 750/520 C, where heavily oxidized layers were observed on the ring surface, the apparent erosion rate was nearly zero. In other words, no significant erosion was noticed. Also, there was no distinct difference between the behaviour of the two types of stainless steels tested.

After the three runs at temperatures 750/520 C, some of the heavily oxidized stainless steel rings were tested again at room temperature with all other operating conditions kept constant. The average erosion rate of these rings was 2.53 $\mu m/100h$, while the average erosion rate of the same rings under the same operating conditions before any high temperature tests was 1.14 $\mu m/100h$. It was also noted that the oxidized layer was not eroded away after 34.9 h of operation at room temperature, which indicates that the average thickness of the oxidized layer is not less than 2.53 $\mu m/100h \times 34.9\ h = 0.88\ \mu m$. The findings suggest that the erosion rate of the stainless steel rings, or rather the oxidized layer, at 750/520 C may actually have been higher than the erosion rate under room temperature conditions. Apparently the oxidation rate balanced the erosion rate at 750/520 C and led to an apparent erosion rate near zero.

The erosion rate of stainless steel rings at temperatures 750/520 C changed from an

average of -0.97 $\mu m/100h$ in Run 56 to -0.18 $\mu m/100h$ in Run 57 and -0.12 $\mu m/100h$ in Run 58. There appeared to be some incubation time for the oxidized layer to be fully developed, although the rings had been put into the temperature conditions 750/520 C for incubation for about 20 h before Run 56. The oxidizing rate seems to have been higher before the end of this incubation period. The change of erosion rate through the three runs also appears to suggest that the apparent erosion rate may eventually become positive after the oxidized layer is fully developed.

8.3 Erosion/Corrosion

Whether the erosion rate of the oxidized layer of the tested stainless steel rings at high temperature is greater or less at room temperature is unknown. The situation is further complicated in fluidized bed combustors due to the presence of possible sulfidation/corrosion (Stringer & Minchener 1984 and Mann et al. 1987). The presence of different corrosion/sulfidation processes may enhance or reduce the oxidized layer or even replace it with other deposits. The erosion rate under those circumstances therefore has to be considered on a case by case basis.

Other experimental erosion results reported at high temperatures, e.g. Stringer et al. (1985), Jansson (1985) and Mann et al. (1987), all involve coal combustion. Stringer et al. (1985) reported maximum erosion rates of 42 $\mu m/100h$ and 9 $\mu m/100h$ respectively for in-bed tube banks of two commercial prototype fluidized bed boilers installed by Gibson Wells Limited operated for 2,300 and 3,400 hours at bed temperatures in the range 800 – 950 C. The size of the boilers, the fluidizing conditions and the tube materials were not reported. The erosion rates reported are 2 – 10 times higher than those in our experiments at room temperature. Mann et al. (1987) utilized a 0.041 m^2 AFBC unit to investigate the

erosive and/or corrosive properties of four different coals with six steels (one carbon steel, four stainless steels and one other alloy) at specimen surface temperatures ranging from 41 C to 843 C. The bed temperature was controlled at 843 C, the superficial air velocity was kept at 2.3 m/s with 25% of excess air and the duration for all four tests was 1,000 hours. Of the four types of coal tested, only one showed measurable erosion of in-bed tube banks. This erosion occurred on the sides of the tube adjacent to the leading edge facing the gas flow, but no quantitative information was provided. The other three tests showed deposit build-up on the in-bed tubes, while significant corrosion was occurring under deposit pitting and sulfide attack.

Gilmour et al. (1985) reported some preliminary results of the 10,000 h AFBC material test carried out in Point Tupper, Nova Scotia. The combustor was 1×1 m with a bed depth of 1.2 m. The specimen sections were connected to form a smooth tube of 50 mm o.d. located in the bubbling bed. The tube temperature had a gradient from 450 to 650 C along the tube length while the bed temperature was maintained at 850 C. An average metal loss for five ferrous metals for the first 1,000 h is estimated to be the order of 10 $\mu m/100h$ due to the combined effect of corrosion and erosion. No simple relationship between temperature and corrosion rate was found. Erosion was pointed out to be playing a major part in the attack and caused "higher than expected metal loss" at the tube bottom.

Jansson (1985) reviewed the problem of erosion/corrosion in fluidized bed combustors and pointed out that oxide films can indeed protect tube materials from erosion in FBC systems and that protection can also result from other deposits on the tube surface. The results of our brief experiment seem to suggest, however, that it is not only the shielding of the oxidized film/deposits on the tube surface, but more important, the substitution of those film/deposits for the base metal and rapid renewal of the oxidized film/deposits which

"protect" the base tube materials from erosion.

There are many papers dealing with the combined effect of corrosion and erosion. Stringer has reviewed this in several papers (Stringer & Minchener 1984, Stringer 1986, Stringer & Wright 1986). A summary of high temperature tests from 13 sources over the last 17 years has recently been published (Natesan et al. 1987). Some of these sources and many other papers all mention erosion as a problem, but quantitative data for erosion are seldom reported due to experimental difficulties and the presence of corrosion and deposits. Further tests are necessary before conclusive statements can be made regarding tube erosion in fluidized bed combustors.

8.4 Conclusions

(1) For non-ferrous metals, the erosion rate increased with temperature due to a decrease of Young's modulus and of material hardness. No oxidation was observed due to the temperature increase except for copper when the tube surface temperature was 145 C in a bed at 750 C.

(2) For ferrous metals, the apparent erosion rate decreased with temperature because oxidation of the ring surface increased the ring's weight, partially counteracting or even more than offsetting the weight loss due to material loss. The presence of this layer made it impossible to obtain accurate measurements of true erosion in the limited time available for the high temperature experiments. However, the data obtained here and data from other studies appear to indicate that the actual erosion rate at high temperature is higher than that at room temperature under the same operating conditions.

(3) More tests are clearly needed to clarify the influence of high temperature on erosion and on joint erosion/corrosion of ferrous metal surfaces.

CHAPTER NINE: EROSION MECHANISM AND PREDICTION

9.1 Mechanisms of Erosion

The mechanism of high velocity solid impact erosion, as defined in Chapter 5, has been studied in depth (see Section 2.3). The principal mechanism appears to be the one proposed by Levy (1982) who suggests a combined forging-extrusion mechanism or the platelet mechanism of erosion based on a series of careful experiments on the microscopic level. His experiments showed that the impact of solid particles first formed platelets and craters on the tube surface. The impact of subsequent solid particles further extruded/forged some of the platelets, and those extruded-forged platelets were fractured by further solid impact (Bellman & Levy 1981, Levy 1983).

In the low velocity solid impact erosion dropping experiments of the present work, "craters" were also observed by scanning election microscopy on the eroded surface of the tested materials, but the craters were much smaller than those seen by others after high velocity impact erosion. For example, Figure 9.1.a shows the surface of a yellow brass specimen struck by 1.0 mm silica sand particles in the dropping apparatus with an impact velocity of 1.82 m/s and a particle mass flow rate of 5.7 kg/m^2s at normal (i.e. perpendicular) incidence for 2 h. In the present study, the craters in Figure 9.1.a have diameters of the order of 10 μm. Figure 9.1.b shows a crater created by impact of a single 600 μm SiC particle at an impact velocity of 30.5 m/s with an impingement angle of 30° (Bellman & Levy 1981). The material is Al alloy 7075-T6. The crater in Figure 9.1.b has a diameter of the order of 100 μm, much bigger than those in Figure 9.1.a. Data from another source (Cousens & Hutchings 1983) indicate that the erosion rate for an aluminum alloy is of the order of 100 mm/h for 1.0 mm silicon carbide with a particle mass flow rate of 5.7 kg/m^2s

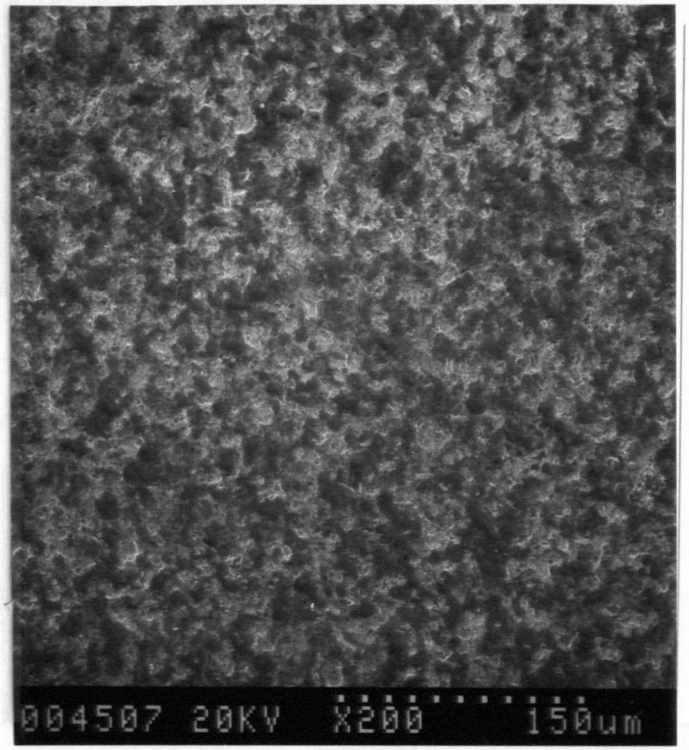

(a)

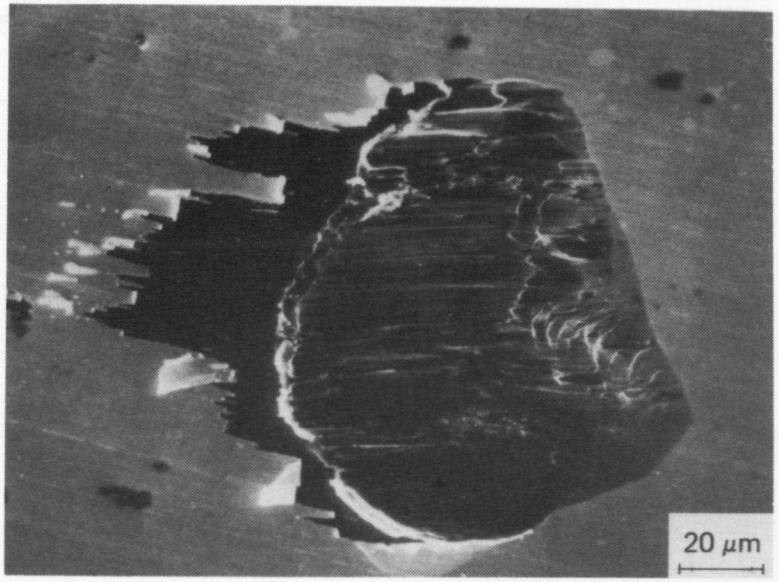

(b)

Figure 9.1 Surface of (a) brass (b) Al7075–T6 after erosion

Conditions:

(a) 1.0 mm silica sand with mass flow rate of 5.7 kg/m^{2}s at impact velocity of 1.8 m/s with normal incidence for 2 hours

(b) single impact by 600 μm silicon carbide particle (Bellman & Levy 1981)

at an impact velocity of 30 m/s for normal incidence. This value is about 24,000 times as large as the value for brass with the same mass flow rate of SiC particles at an impact velocity of 5.0 m/s in our dropping experiment, and about 220,000 times larger than that in our fluidized bed experiments under base operating conditions.

This enormous difference between erosion rates and crater dimensions on the target surface appears to suggest that the mechanisms of high and low velocity solid impact erosion may be different. It is apparent from the present work that even below the so-called "threshold" impact velocity of the order of 6 – 30 m/s (Tilly 1979, Finnie 1979) for high velocity solid impact erosion, erosion still occurs, although at a much lower rate for a given number of striking particles. It is postulated that material loss at low particle impact velocities is due to a surface fatigue process. In this process, cyclic loads are largely elastic and reach levels sufficient to cause local yielding or dislocation on a microscopic scale (Suh 1979, Liu et al. 1984). For materials of high Young's modulus, a greater proportion of the local deformation is likely to have been elastic in nature with plastic deformation only occurring locally or slowly, compared with materials of lower elasticity where a greater proportion of the local deformation is likely to have been plastic. The role of Young's modulus, discussed in Chapters 5 and 7, is therefore consistent with the proposed mechanism. Under the recurrent impact of solid particles in the experiments performed, the repeated cyclic deformation on the target surface is postulated to have led to the initiation and growth of minute fatigue cracks due to microscopic plastic damage, at or just below the target surface. It is further postulated that growth of these cracks led to separation of small pieces of target material. Woodford and Wood (1983), based on their experiments, also suggested that wear in fluidized beds is produced by fatigue damage.

Figure 9.2 shows the surfaces of brass specimens before and after erosion in the dropping

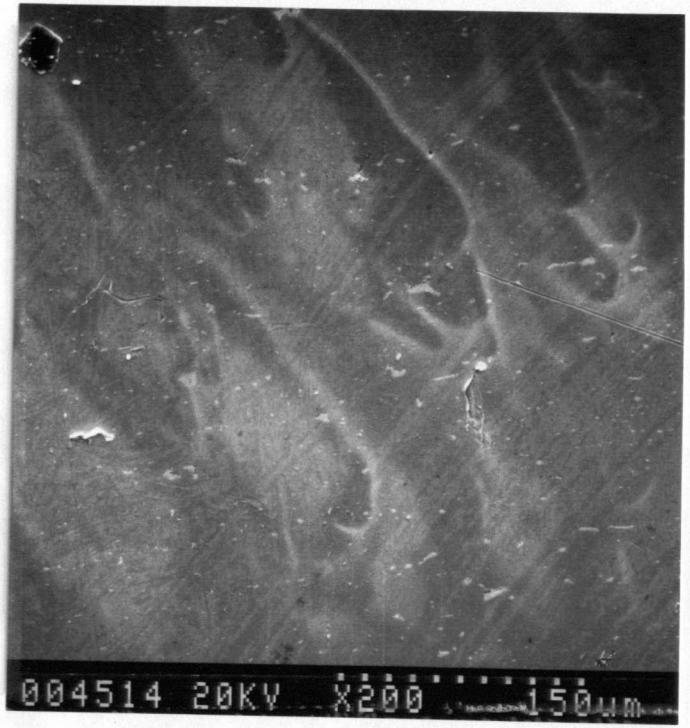

(a) fresh surface

(b) after 5 s

Figure 9.2 Surfaces of brass specimens before and after erosion for 1.0 mm silica sand with mass flow rate of 5.7 kg/m^{2}s at impact velocity of 1.8 m/s for normal incidence

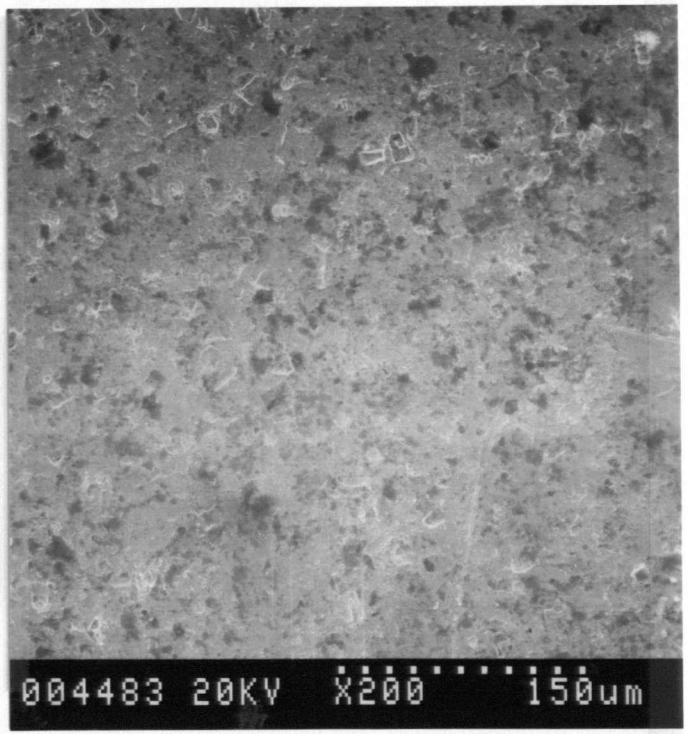

(c) after 1 min.

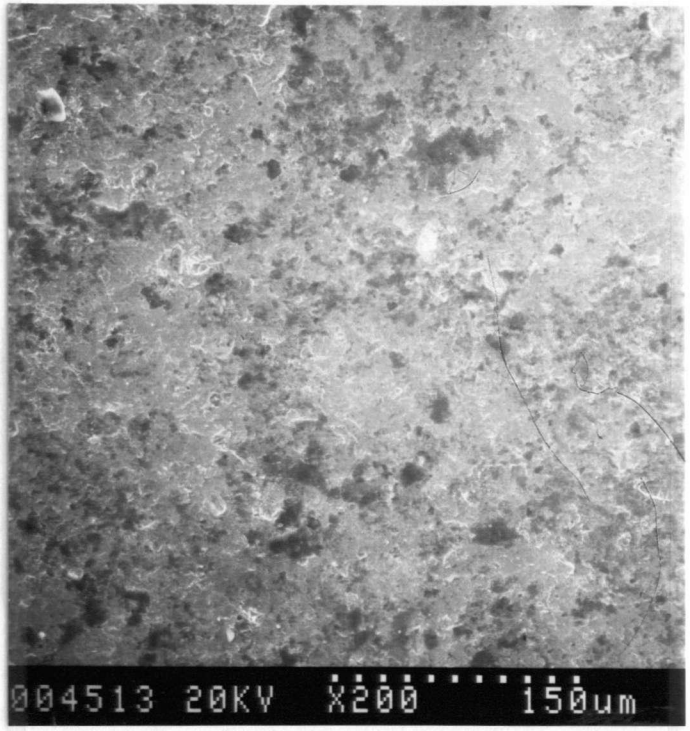

(d) after 2 min.

Figure 9.2 Surfaces of brass specimens before and after erosion for 1.0 mm silica sand with mass flow rate of 5.7 kg/m^{2}s at impact velocity of 1.8 m/s for normal incidence

test. The four specimens were polished at the same time and then eroded for different durations before their surfaces were examined under the electron scanning microscope. The particle impact velocity was 1.8 m/s and the particle mass flow rate of 1.0 mm silica sand was 5.7 kg/m^2s. Figure 9.2.a shows the fresh surface before erosion. Figure 9.2.b shows the eroded surface after 5 seconds of solid impact. Markings believed to be very shallow craters are seen on the surface. After particles had continued to strike the target for about 1 minute, linear traces of the order of 10 μm in length appeared on the surface (Figure 9.2.c). It is believed that these were traces of target cracks. Figure 9.3 shows typical cracks with higher magnification for the same conditions as Figure 9.2.c. The sequence of observation suggests that localized plastic deformation occurred, at least at the beginning of the erosion process. However, material removal seems to be related to cracking; the sizes of these "cracks" in Figure 9.2.c are of the same order of magnitude as the craters in Figures 9.1.a and 9.2.d.

Figure 9.4 shows the bottom surface of brass rings after erosion in the three-dimensional fluidized bed subject to superficial air velocities of 0.88 and 1.87 m/s for 250 and 100 hours, corresponding to average gas void rise velocities of 0.82 and 1.81 m/s. It shows that the crater dimension for erosion at $u = 1.87$ m/s is about 2 - 4 times that for $u = 0.88$ m/s, while the erosion rate for $u = 1.87$ m/s is about 5 - 6 times that for $u = 0.88$ m/s. Figure 9.4 also shows the bottom surface of a CS1020 ring after erosion in the fluidized bed at a superficial air velocity of 1.87 m/s for 100 hours of operation. The crater dimension on the brass surface is about 6 - 8 times the crater dimension on the CS1020 surface, while the erosion rate of brass under identical conditions is 6 - 7 times that of CS1020. The relative size of the craters appears to correspond to the relative erosion rate.

The surfaces at different angular positions on a SS304 ring after erosion in the fluidized bed under the same conditions are shown in Figure 9.5. It was found that the crater

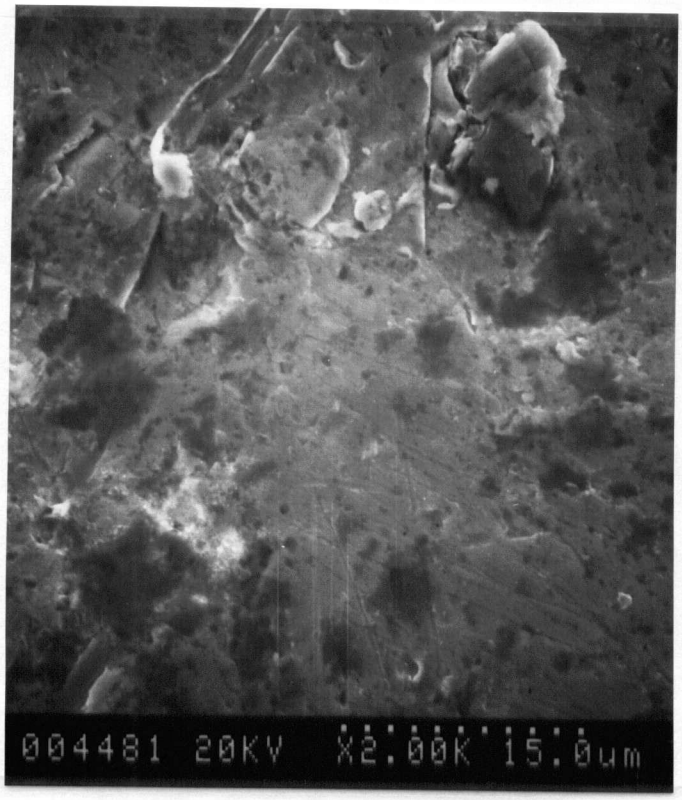

Figure 9.3 Surface of a brass specimen after erosion for 1 min. for 1.0 mm silica sand with mass flow rate of 5.7 kg/m^{2}s at impact velocity of 1.8 m/s for normal incidence

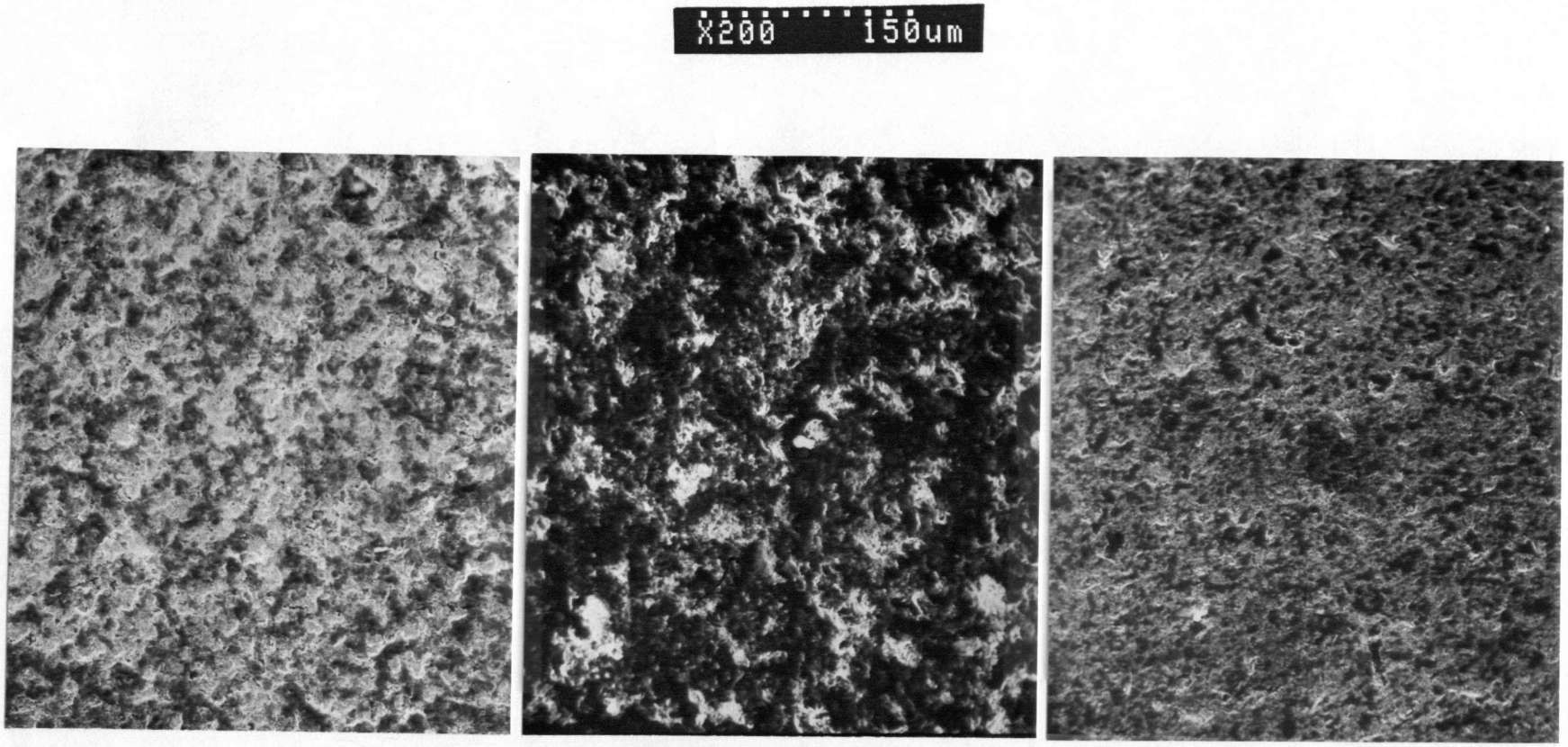

(a) (b) (c)

Figure 9.4 Surfaces of brass and CS1050 rings after erosion in the room temperature three-dimensional fluidized bed

(a)	Brass	at	u=0.88	m/s	for	250	h
(b)	Brass	at	u=1.88	m/s	for	100	h
(c)	CS1050	at	u=1.88	m/s	for	100	h

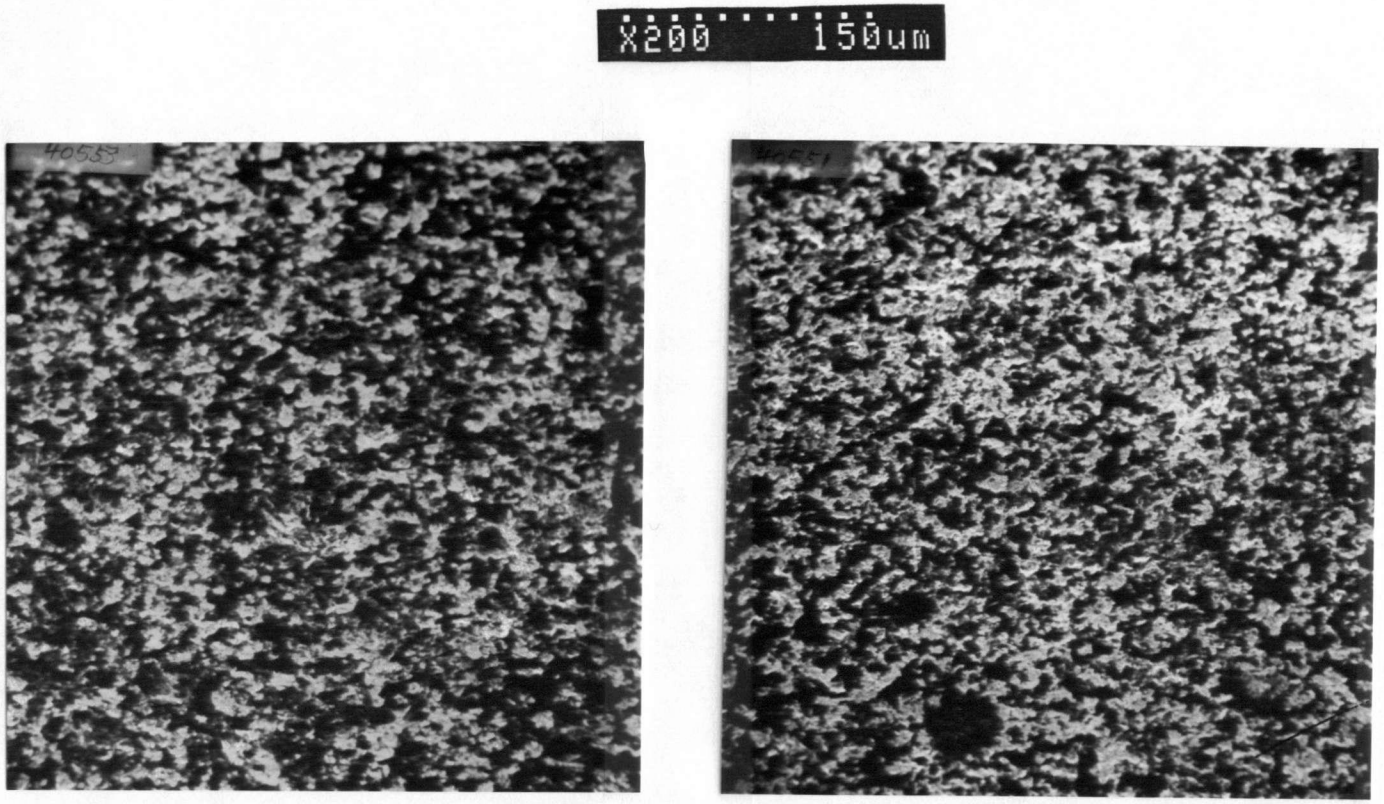

(a) 0° (b) 40°

Figure 9.5 Surfaces at different angular positions on a SS304 ring 100 h erosion at u = 1.87 m/s with 1.0 mm silica sand particles in the the room temperature three-dimensional fluidized bed (Angles are measured in degrees from the tube bottom and the photos are negative.)

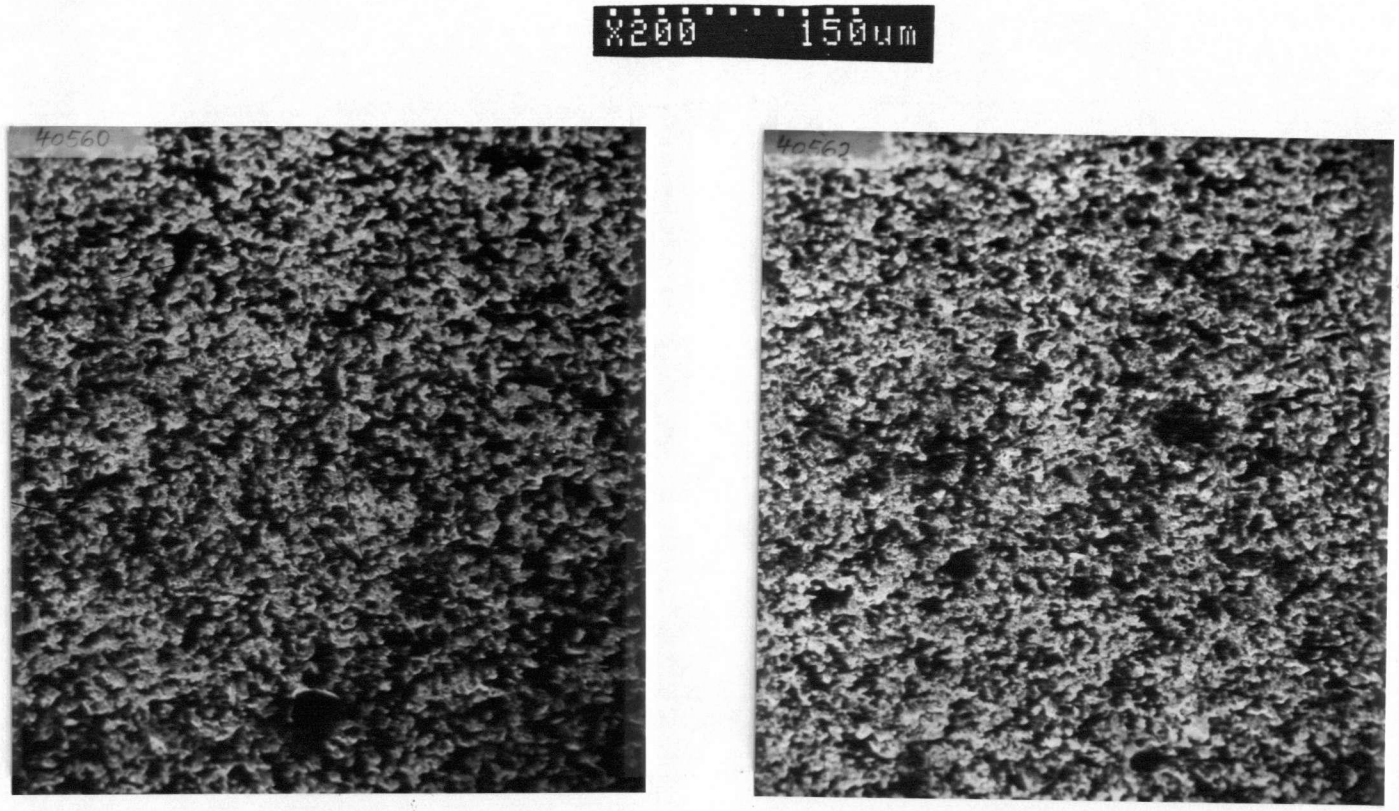

(c) 60° (d) 90°

Figure 9.5 Surfaces at different angular positions on a SS304 ring 100 h erosion at u = 1.87 m/s with 1.0 mm silica sand particles in the the room temperature three-dimensional fluidized bed (Angles are measured in degrees from the tube bottom and the photos are negative.)

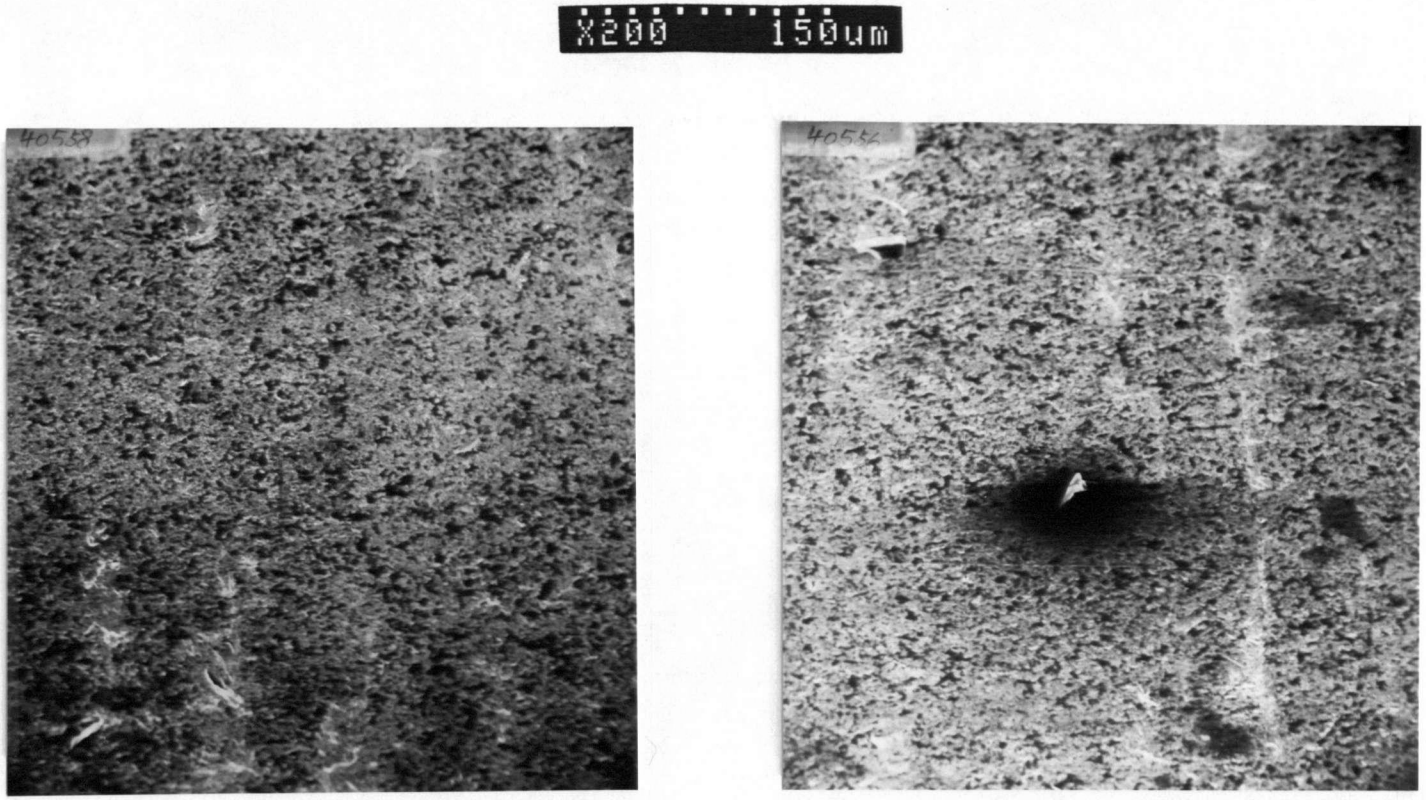

(e) 120°

(f) 180°

Figure 9.5 Surfaces at different angular positions on a SS304 ring 100 h erosion at u = 1.87 m/s with 1.0 mm silica sand particles in the the room temperature three-dimensional fluidized bed (Angles are measured in degrees from the tube bottom and the photos are negative.)

dimensions were very similar on the bottom surface and at 40° and 60° from the bottom where the erosion rate is high. The crater dimensions were observed to decrease quickly with increasing angle as the erosion rate dropped near the equator and approached zero at the top. Again, the dimensions of the craters correspond to the erosion rate.

9.2 Model for Low Velocity Particle Impacts

Many predictive models have been developed to estimate erosion rates, e.g. Soo (1977), Finnie and McFadden (1978) and Lyczkowski (1987) for high velocity solid impact erosion. All of these models involve plastic flow of the target, and all contain some parameters which cannot be measured directly. A simple model for low velocity solid impact erosion is required.

Four highly simplifying assumptions are made for the model developed here:

(1) Material loss is assumed to occur by a surface fatigue phenomenon.

(2) Local plastic deformation which leads to material losses by surface fatigue is directly related to the degree of elastic deformation. The magnitude of material loss due to surface fatigue is in turn directly proportional to the volume of target material which undergoes substantial elastic deformation as a result of particle impacts.

(3) The erosion rate is assumed to be proportional to the cube of the maximum elastic deformed depth, h, associated with a particle impact. This is equivalent to an assumption that the volumes of target material, stressed enough to be eventually removed by the fatigue crack initiation and growth process, are geometrically similar.

(4) All impact particles striking the surface at a given angle transfer the same fraction of their kinetic energy to the target surface regardless of their size, velocity or density.

By energy conservation, the kinetic energy transferred to the target, i.e. the kinetic

energy of a particle, E_k, upon impact multiplied by an energy transfer coefficient, k', equals the work done on the target material by the particle, ΔW. Therefore,

$$k' E_k = \Delta W \tag{9.1}$$

It is recognized that k' is likely to be a function of the impingement angle, particle sphericity and particle hardness. The kinetic energy of a particle before impact is

$$E_k = \frac{1}{2}(\pi\, d_p^3 \rho_s / 6)\, V_p^2 \tag{9.2}$$

The work done on the target is (see Appendix B):

$$\Delta W \;\propto\; \frac{\pi}{6} E_y d_p h^3 \tag{9.3}$$

Combining equations 9.1 to 9.3 and rearranging, we have:

$$h^3 \;\propto\; \frac{1}{2} k'\, d_p^2 \rho_s V_p^2 / E_y \tag{9.4}$$

If, as noted above, we assume that the erosion rate is proportional to h^3, then

$$E \;\propto\; nh^3 \;\propto\; \frac{1}{2} k'\, n d_p^2 \rho_s V_p^2 / E_y \tag{9.5}$$

where n is the number of particles striking unit surface area per second. If we let k be the new coefficient of proportionality (itself a function of impingement angle, particle sphericity and particle hardness), then

$$E = k n d_p^2 \rho_s V_p^2 / E_y \tag{9.6}$$

Equation 9.6 suggests that the erosion rate is proportional to the number of striking particles, the particle density, the square of the particle diameter, the square of the impact velocity, and inversely proportional to the Young's modulus of the target material.

Equation 9.6 may be compared with the empirical equation 5.10 based on least square curve fitting for the "dropping experiment":

$$E = k_6 M V_p^{2.3} d_p^{1.5} \ (1.04 - \Phi_s) \ (0.448 cos^2\theta + 1) \tag{5.10}$$

The mass flow rate for a given particle diameter is proportional to n and ρ_s, which leads to the same dependence of erosion rate on n and ρ_s for the two equations. The powers of V_p and d_p in equation 5.10 are slightly different from those in equation 9.6, but are quite close considering the limited data available and the highly simplified nature of the physical model. Unlike equation 9.6, the dependence of Young's modulus is not included in equation 5.10. However, as shown in Figures 5.10, 5.11 and 7.17, the erosion rate is apparently related to Young's modulus, although no simple empirical equation involving E_y was found, probably due to the fact that elasticity is not the only significant mechanical property which influences the material's resistance to erosion. As discussed in Chapters 5 and 7, other mechanical properties, such as hardness and yield strength may also play some role in erosion resistance.

The particle hardness, particle sphericity and particle impingement angle are also not explicitly considered in equation 9.6. Therefore k may be expressed as:

$$k = F(\Phi_s, H_p, \theta, H_m, Y_m \ldots) \tag{9.7}$$

The combination of equations 9.6 and 9.7 results in

$$E = F(\Phi_s, H_p, \theta, H_m, Y_m \ldots) \ n d_p^2 \rho_s V_p^2 / E_y \tag{9.8}$$

which reveals the complexity of the erosion process. More intensive experiments are needed to further address the effects of material mechanical properties on erosion, and to verify the dependence of erosion on particle sphericity, hardness and impingement angle. The validity

of the simple physical model of erosion by surface fatigue, and the assumption that erosion rate is proportional to h^3 also need to be proven with more precise experiments.

9.3 Tentative Model for Horizontal Tubes in Fluidized Beds

In fluidized beds, erosion of internal tubes is caused by the particle movement associated with gas void motion. Our experiments (see Section 7.3.5) indicate that material loss due to abrasive erosion is less than 12% of the total loss, and that impact erosion is the dominant factor.

In a fluidized bed, the particle velocity at impact is not directly related to the superficial gas velocity, but is very close to the bubble or slug rise velocity (Chapter 6) for operation in the bubbling or slugging regime. The erosion rate was correlated with void velocity in Section 7.1.1. The power exponent was found to be 2.1, lying between the theoretical value of 2.0 of equation 9.6 and the empirical value of 2.3 of equation 5.10. For particle diameter the power exponent is 1.2, smaller than the values in both equations 5.10 and 9.6. It is notable that Yates (1987) proposed an equation which would lead to a much higher index by assuming that all wake particles impacted on the tube. This assumption is not justified for reasons discussed later in this Chapter. The dependence of erosion on particle sphericity was found to be similar to that of equation 5.10 (Section 7.1.3). The impact particle mass flow rate is proportional to the void frequency (Section 7.1.1). A correlation may be obtained for predicting the erosion rate for a horizontal tube in a fluidized bed by a multi-regression analysis of the experimental results for the cold model three-dimensional column of the form

$$E = C' f_v M_b u_s^{n_1} d_p^{n_2} \ (1.1 - \Phi_s) \tag{9.9}$$

where C' is a constant for given mechanical properties of the particles and tube materials.

The exponents for u_s and d_p for different materials obtained in this manner are listed in Table 9.1.

If M_b is proportional to ρ_s, which seems likely, and average exponents for the various materials are assumed to apply, then equation 9.9 may be rewritten as

$$E = Cf_v\rho_s u_s^{2.1}\, d_p^{1.2}\ (1.1 - \Phi_s) \tag{9.10}$$

where C is a constant and the exponents have been rounded off to two significant figures. C can be called the erosion coefficient. C values for the different materials can now be calculated from equation 9.10, with $f_v \approx 2.2\ Hz$ from Table 7.2 and u_s from equation 2.18, for each of the experimental tests described in Chapter 7 and listed in Appendix D. The resulting values of C can then be averaged for a given tube material and particulate material. The C values for all 13 ring materials tested with silica sand obtained in this manner are listed in Table 9.2. The standard deviations of these C values are also listed in Table 9.2. The operating conditions and experimental results for the five materials of the base operating conditions with silica sand are tabulated in Table 9.3, together with the calculated results from equation 9.10 using the averaged values of C given in Table 9.3.

Clearly C in equation 9.10 is related to the volume of particles striking the underside of the tube for each bubble and the angle at which impingement occurs. Some estimate of this volume may be made based on the dropping experiments (Chapter 5) where the mass flow rate of particles striking the specimen was known for each case. The exponents and other constants in this Chapter differ somewhat from those in Chapter 5 (eg. compare equations 5.10 and 9.9). In order to be able to compare the data, the data in Chapter 5 for one target material (yellow brass) and silica sand particles were fitted to an equation of the form consistent with equation 9.9, i.e.

$$E = k_7 M\, V_p^{2.1}\, d_p^{1.2}\ (1.1 - \Phi_s)\ (0.448 cos^2\theta + 1) \tag{9.11}$$

Table 9.1: Exponents in equation 9.9 for different materials obtained from multi-regression analysis

Material	Exponent for u_s	Exponent for d_p
Brass	2.3	1.4
Al 2011	2.1	1.1
Copper	2.1	1.1
SS304	1.8	1.2
CS1050	2.0	1.1
Average	2.1	1.2

Table 9.2: C values for different materials in equation 9.10 with silica sand as the particular material

Material	C $\left(\frac{\mu m/h \ s^{3.1}}{kg \ m^{0.3}}\right)$	Standard deviation $\left(\frac{\mu m/h \ s^{3.1}}{kg \ m^{0.3}}\right)$
Brass	0.115	0.0022
Al 2011	0.119	0.0046
Copper	0.0683	0.0029
SS316	0.0097	0.0016
CS1050	0.0199	0.0010
SS304	0.0101	0.0001
CS1020	0.0257	0.0009
Iron	0.0239	0.0008
Pure Al	0.237	0.0330
Keewatin steel 1	0.0146	0.0004
Keewatin steel 2	0.0110	0.0005
Keewatin steel 3	0.0105	0.0002
Keewatin steel 4	0.0103	0.0001

Table 9.3: Operating conditions and results of all tests with silica sand in the cold model three-dimensional fluidized bed

(a) For Brass

The average absolute error is: 13.17%

	$u - u_{mf}$ m/s	u_t m/s	d_p mm	D_t mm	H_p kg/mm^2	Φ_t	T h	Erosion rate ($\mu m/100h$) Measured Results	Predicted Results	Error (%)
Run 01	0.32	0.82	1.02	32.	350.	0.83	250.0	2.8	3.0	9.0
Run 02	1.32	1.82	1.00	32.	350.	0.83	60.0	16.5	15.7	-4.8
Run 03	1.57	2.07	1.00	32.	350.	0.83	14.1	19.2	20.5	7.1
Run 04'	1.30	1.80	1.00	32.	350.	0.84	100.1	14.9	14.7	-1.2
Run 05	1.47	1.97	1.00	32.	350.	0.84	40.0	18.8	17.8	-5.2
Run 10	1.31	1.81	1.10	32.	350.	0.86	64.3	17.5	15.4	-11.9
Run 10+	1.31	1.81	1.04	32.	350.	0.86	63.8	14.3	14.4	1.0
Run 11	1.31	1.81	1.30	32.	350.	0.86	61.0	19.5	18.9	-3.1
Run 11+	1.31	1.81	1.30	32.	350.	0.86	110.5	19.3	18.9	-2.4
Run 12	1.31	1.81	1.30	32.	350.	0.86	64.0	19.2	18.9	-1.8
Run 13	1.31	1.81	0.67	32.	350.	0.86	70.3	7.8	8.5	9.2
Run 14	1.31	1.81	0.31	32.	350.	0.86	62.0	3.0	3.4	12.6
Run 14+	1.31	1.81	0.30	32.	350.	0.86	68.6	2.6	3.2	24.4
Run 15	1.31	1.81	1.51	32.	350.	0.86	85.4	37.3	22.6	-39.5
Run 15+	1.31	1.81	1.51	32.	350.	0.86	61.2	31.6	22.6	-28.6
Run 19	0.33	0.83	1.00	32.	350.	0.89	64.7	1.6	2.3	44.7
Run 21	0.82	1.32	1.00	32.	350.	0.89	55.2	7.5	6.2	-17.2
Run 22	1.31	1.81	1.00	32.	350.	0.89	87.0	11.3	12.1	7.0
Run 23	1.42	1.92	1.00	32.	350.	0.89	36.1	13.1	13.6	3.9
Run 25	1.96	2.46	1.00	32.	350.	0.89	22.8	20.3	23.0	13.2
Run 26	1.66	2.16	1.00	32.	350.	0.89	51.5	14.0	17.5	24.4
Run 30	1.67	2.17	1.00	32.	350.	0.89	28.3	14.1	17.6	24.9
Run 31	1.32	1.82	1.00	32.	350.	0.91	35.0	10.6	11.0	4.0
Run 33	1.32	1.82	1.00	32.	350.	0.91	46.1	9.2	11.0	19.6
Run 38	1.31	1.81	1.30	32.	350.	0.86	47.6	20.6	18.9	-8.4

Table 9.3: Operating conditions and results of all tests with silica sand in the cold model three-dimensional fluidized bed

(b) For Copper

The average absolute error is: 14.41%

	$u - u_{mf}$ m/s	u_t m/s	d_p mm	D_t mm	H_p kg/mm^2	Φ_s	T h	Erosion rate ($\mu m/100h$) Measured Results	Predicted Results	Error (%)
Run 01	0.32	0.82	1.02	32.	350.	0.83	250.0	1.9	1.8	-3.4
Run 02	1.32	1.82	1.00	32.	350.	0.83	60.0	8.8	9.3	6.5
Run 03	1.57	2.07	1.00	32.	350.	0.83	14.1	13.9	12.2	-12.2
Run 04'	1.30	1.80	1.00	32.	350.	0.84	100.1	7.9	8.8	10.2
Run 05	1.47	1.97	1.00	32.	350.	0.84	40.0	10.0	10.6	6.2
Run 10	1.31	1.81	1.10	32.	350.	0.86	64.3	10.7	9.2	-14.1
Run 10+	1.31	1.81	1.04	32.	350.	0.86	63.8	8.6	8.6	0.3
Run 11	1.31	1.81	1.30	32.	350.	0.86	61.0	9.7	11.2	15.2
Run 11+	1.31	1.81	1.30	32.	350.	0.86	110.5	9.9	11.2	13.6
Run 12	1.31	1.81	1.30	32.	350.	0.86	64.0	10.1	11.2	11.1
Run 13	1.31	1.81	0.67	32.	350.	0.86	70.3	5.9	5.1	-14.8
Run 14	1.31	1.81	0.31	32.	350.	0.86	62.0	2.9	2.0	-30.8
Run 14+	1.31	1.81	0.30	32.	350.	0.86	68.6	2.3	1.9	-16.1
Run 15	1.31	1.81	1.51	32.	350.	0.86	85.4	18.4	13.4	-27.1
Run 15+	1.31	1.81	1.51	32.	350.	0.86	61.2	17.1	13.4	-21.3
Run 19	0.33	0.83	1.00	32.	350.	0.89	64.7	1.1	1.4	23.3
Run 21	0.82	1.32	1.00	32.	350.	0.89	55.2	3.7	3.7	-1.1
Run 22	1.31	1.81	1.00	32.	350.	0.89	87.0	6.2	7.2	16.1
Run 23	1.42	1.92	1.00	32.	350.	0.89	36.1	6.9	8.1	16.6
Run 25	1.96	2.46	1.00	32.	350.	0.89	22.8	10.9	13.6	25.5
Run 26	1.66	2.16	1.00	32.	350.	0.89	51.5	9.4	10.4	10.1
Run 30	1.67	2.17	1.00	32.	350.	0.89	28.3	8.8	10.5	19.8
Run 31	1.32	1.82	1.00	32.	350.	0.91	35.0	5.7	6.6	15.6
Run 33	1.32	1.82	1.00	32.	350.	0.91	46.1	6.8	6.6	-3.6
Run 38	1.31	1.81	1.30	32.	350.	0.86	47.6	8.9	11.2	25.7

Table 9.3: Operating conditions and results of all tests with silica sand in the cold model three-dimensional fluidized bed

(c) For Al2011

The average absolute error is: 13.30%

	$u - u_{mf}$ m/s	u_s m/s	d_p mm	D_t mm	H_p kg/mm^2	Φ_s	T h	Erosion rate ($\mu m/100h$) Measured Results	Predicted Results	Error (%)
Run 01	0.32	0.82	1.02	32.	350.	0.83	250.0	3.2	3.1	-1.8
Run 02	1.32	1.82	1.00	32.	350.	0.83	60.0	15.6	16.2	3.3
Run 03	1.57	2.07	1.00	32.	350.	0.83	14.1	18.0	21.2	17.7
Run 04'	1.30	1.80	1.00	32.	350.	0.84	100.1	13.4	15.2	13.4
Run 05	1.47	1.97	1.00	32.	350.	0.84	40.0	14.7	18.4	25.1
Run 10	1.31	1.81	1.10	32.	350.	0.86	64.3	18.5	15.9	-13.9
Run 10+	1.31	1.81	1.04	32.	350.	0.86	63.8	13.9	14.9	7.3
Run 11	1.31	1.81	1.30	32.	350.	0.86	61.0	19.5	19.5	-0.2
Run 11+	1.31	1.81	1.30	32.	350.	0.86	110.5	18.3	19.5	6.2
Run 12	1.31	1.81	1.30	32.	350.	0.86	64.0	17.8	19.5	9.7
Run 13	1.31	1.81	0.67	32.	350.	0.86	70.3	10.6	8.8	-16.7
Run 14	1.31	1.81	0.31	32.	350.	0.86	62.0	4.8	3.5	-27.4
Run 14+	1.31	1.81	0.30	32.	350.	0.86	68.6	3.7	3.4	-8.7
Run 15	1.31	1.81	1.51	32.	350.	0.86	85.4	32.3	23.3	-27.9
Run 15+	1.31	1.81	1.51	32.	350.	0.86	61.2	29.8	23.3	-21.8
Run 19	0.33	0.83	1.00	32.	350.	0.89	64.7	1.9	2.4	28.6
Run 21	0.82	1.32	1.00	32.	350.	0.89	55.2	7.5	6.4	-14.7
Run 22	1.31	1.81	1.00	32.	350.	0.89	87.0	12.4	12.4	-0.0
Run 23	1.42	1.92	1.00	32.	350.	0.89	36.1	13.7	14.1	2.7
Run 25	1.96	2.46	1.00	32.	350.	0.89	22.8	22.6	23.7	4.8
Run 26	1.66	2.16	1.00	32.	350.	0.89	51.5	16.3	18.0	10.8
Run 30	1.67	2.17	1.00	32.	350.	0.89	28.3	14.7	18.2	23.6
Run 31	1.32	1.82	1.00	32.	350.	0.91	35.0	10.2	11.4	11.9
Run 33	1.32	1.82	1.00	32.	350.	0.91	46.1	10.3	11.4	10.8
Run 38	1.31	1.81	1.30	32.	350.	0.86	47.6	15.8	19.5	23.4

Table 9.3: Operating conditions and results of all tests with silica sand in the cold model three-dimensional fluidized bed

(d) For SS304

The average absolute error is: 18.80%

	$u - u_{mf}$ m/s	u_t m/s	d_p mm	D_t mm	H_p kg/mm^2	Φ_s	T h	Erosion rate ($\mu m/100h$) Measured Results	Predicted Results	Error (%)
Run 01	0.32	0.82	1.02	32.	350.	0.83	250.0	0.3	0.3	-12.5
Run 02	1.32	1.82	1.00	32.	350.	0.83	60.0	1.2	1.3	12.0
Run 03	1.57	2.07	1.00	32.	350.	0.83	14.1	2.1	1.7	-19.5
Run 04′	1.30	1.80	1.00	32.	350.	0.84	100.1	1.2	1.2	2.7
Run 05	1.47	1.97	1.00	32.	350.	0.84	40.0	1.0	1.5	51.8
Run 10	1.31	1.81	1.10	32.	350.	0.86	64.3	1.4	1.3	-10.2
Run 10+	1.31	1.81	1.04	32.	350.	0.86	63.8	1.2	1.2	0.6
Run 11	1.31	1.81	1.30	32.	350.	0.86	61.0	1.0	1.6	60.7
Run 11+	1.31	1.81	1.30	32.	350.	0.86	110.5	1.1	1.6	39.5
Run 12	1.31	1.81	1.30	32.	350.	0.86	64.0	1.8	1.6	-13.1
Run 13	1.31	1.81	0.67	32.	350.	0.86	70.3	1.0	0.7	-26.0
Run 14	1.31	1.81	0.31	32.	350.	0.86	62.0	0.3	0.3	-5.1
Run 14+	1.31	1.81	0.30	32.	350.	0.86	68.6	0.3	0.3	-5.6
Run 15	1.31	1.81	1.51	32.	350.	0.86	85.4	2.6	1.9	-26.5
Run 15+	1.31	1.81	1.51	32.	350.	0.86	61.2	2.3	1.9	-17.9
Run 19	0.33	0.83	1.00	32.	350.	0.89	64.7	0.3	0.2	-24.0
Run 21	0.82	1.32	1.00	32.	350.	0.89	55.2	0.5	0.5	2.6
Run 22	1.31	1.81	1.00	32.	350.	0.89	87.0	1.0	1.0	0.6
Run 23	1.42	1.92	1.00	32.	350.	0.89	36.1	0.8	1.1	36.9
Run 25	1.96	2.46	1.00	32.	350.	0.89	22.8	1.2	1.9	61.3
Run 26	1.66	2.16	1.00	32.	350.	0.89	51.5	1.6	1.5	-5.0
Run 30	1.67	2.17	1.00	32.	350.	0.89	28.3	1.3	1.5	17.1
Run 31	1.32	1.82	1.00	32.	350.	0.91	35.0	1.0	0.9	-4.1
Run 33	1.32	1.82	1.00	32.	350.	0.91	46.1	0.9	0.9	5.7
Run 38	1.31	1.81	1.30	32.	350.	0.86	47.6	1.5	1.6	8.9

Table 9.3: Operating conditions and results of all tests with silica sand in the cold model three-dimensional fluidized bed

(e) For CS1050

The average absolute error is: 19.23%

	$u - u_{mf}$ m/s	u_s m/s	d_p mm	D_t mm	H_p kg/mm^2	Φ_s	T h	Erosion rate ($\mu m/100h$) Measured Results	Predicted Results	Error (%)
Run 01	0.32	0.82	1.02	32.	350.	0.83	250.0	0.4	0.5	15.9
Run 02	1.32	1.82	1.00	32.	350.	0.83	60.0	2.5	2.7	7.8
Run 03	1.57	2.07	1.00	32.	350.	0.83	14.1	2.5	3.6	40.1
Run 04'	1.30	1.80	1.00	32.	350.	0.84	100.1	2.1	2.6	24.1
Run 05	1.47	1.97	1.00	32.	350.	0.84	40.0	2.4	3.1	28.2
Run 10	1.31	1.81	1.10	32.	350.	0.86	64.3	2.6	2.7	2.1
Run 10+	1.31	1.81	1.04	32.	350.	0.86	63.8	2.2	2.5	14.2
Run 11	1.31	1.81	1.30	32.	350.	0.86	61.0	2.1	3.3	56.5
Run 11+	1.31	1.81	1.30	32.	350.	0.86	110.5	2.4	3.3	36.3
Run 12	1.31	1.81	1.30	32.	350.	0.86	64.0	3.2	3.3	1.2
Run 13	1.31	1.81	0.67	32.	350.	0.86	70.3	1.7	1.5	-15.2
Run 14	1.31	1.81	0.31	32.	350.	0.86	62.0	0.6	0.6	-2.4
Run 14+	1.31	1.81	0.30	32.	350.	0.86	68.6	0.5	0.6	14.9
Run 15	1.31	1.81	1.51	32.	350.	0.86	85.4	4.0	3.9	-2.4
Run 15+	1.31	1.81	1.51	32.	350.	0.86	61.2	3.5	3.9	11.2
Run 19	0.33	0.83	1.00	32.	350.	0.89	64.7	0.7	0.4	-38.4
Run 21	0.82	1.32	1.00	32.	350.	0.89	55.2	1.2	1.1	-10.3
Run 22	1.31	1.81	1.00	32.	350.	0.89	87.0	2.9	2.1	-28.7
Run 23	1.42	1.92	1.00	32.	350.	0.89	36.1	2.5	2.4	-4.3
Run 25	1.96	2.46	1.00	32.	350.	0.89	22.8	3.3	4.0	21.3
Run 26	1.66	2.16	1.00	32.	350.	0.89	51.5	3.8	3.0	-20.3
Run 30	1.67	2.17	1.00	32.	350.	0.89	28.3	3.4	3.1	-11.4
Run 31	1.32	1.82	1.00	32.	350.	0.91	35.0	2.6	1.9	-27.3
Run 33	1.32	1.82	1.00	32.	350.	0.91	46.1	2.2	1.9	-14.3
Run 38	1.31	1.81	1.30	32.	350.	0.86	47.6	2.5	3.3	31.9

The resulting values of k_7 is 7.45 $(\mu m/100h)/\{(kg/m^2 s)\ (m/s)^{2.1}\ (mm)^{1.2})\}$ or 297 $(\mu m/h)/\{kg\ m^{1.3}/s^{3.1}\}$. If, as discussed in Chapter 6, the average impingement angle on the underside of the tube is about 60°, then comparison of equations 9.9 and 9.11, with $V_p \approx u_s$ and $M \approx f_v M_b$, yields

$$\begin{aligned} C' &\approx k_7\ (0.448 cos^2\theta + 1) \\ &= k_7\ (0.448 cos^2 60^\circ + 1) \\ &= 330\ (\mu m/h)/\{kg\ m^{1.3}/s^{3.1}\} \end{aligned} \tag{9.12}$$

Comparison of equation 9.9 and 9.10, with $C = 0.115(\mu m/h)/\{kg\ m^{0.3}/s^{3.1}\}$ for brass, shows that

$$M_b = C\rho_s/C' = 0.115 \times 2600/330 = 0.906\ kg/m^2 bubble \tag{9.13}$$

However, the M_b value from equation 9.13 is the average for the whole ring. As discussed in Section 7.3.1, erosion on the top half of the ring was less than 5%. Therefore M_b is about $0.906 \times 0.95 \times 2 = 1.72\ kg/m^2 bubble$ based on the surface area of the lower half ring. The mass flow rate of more interest here is the mass flow rate carried by a single void based on the projected area of the ring in a horizontal plane, $M_b = 1.72 \times (\pi/2) = 2.70\ kg/m^2 bubble$. If ϵ_{mf} is assumed to be 0.5, a typical value, the actual thickness of the layer of particles which undergoes impact causing erosion of the tube is then only

$$M_b/\rho_s(1 - \epsilon_{mf}) = \frac{2.70 \times 1000}{2600 \times (1 - 0.5)} = 2.1\ mm/bubble \tag{9.14}$$

This suggests that only about two layers of particles take part in the erosion process, which is consistent with the findings from the two-dimensional bed observations (see Chapter 6). This further indicates that erosion may be independent of the wake volume fraction of bubbles provided that the wake is large enough to cover the ring area.

The term $H_p^{0.2}$ in equation 5.9 is not included in equation 9.10 since the exponent 0.2 for brass cannot be applied to ferrous metals (Section 7.1.3). This exponent is likely to be influenced by the mechanical properties of both the particle and the target materials. The erosion coefficient C is therefore a function of particle hardness, target material hardness, Young's modulus etc.. C also represents the erodability of one material by another material and is determined *only* by the mechanical properties of both the particulate and target materials.

For fluidized beds operating at other fluidizing conditions, the slug rise velocity used in equation 9.10 can be replaced by the void (i.e. bubble or slug) rise velocity. C values may be estimated from experiments in a fluidized bed at the desired temperature and any other operating conditions. With the C value of a given material, the average erosion rate of a single horizontal tube of this material may then be estimated from equation 9.10, keeping in mind that the maximum local erosion rate is usually at least $2 - 3$ times the average erosion rate. In principle, one could also use dropping tests to predict fluidized bed erosion, but the construction of high temperature dropping equipment and the uncertainties in applying the data suggest that this would be a less desirable method.

The calculated erosion rates from equation 9.10 for the five materials of the base operating conditions are plotted against the experimental results obtained from our three-dimensional cold model fluidized bed in Figures 9.6 to 9.10. Equation 9.10 is seen to fit well in the ranges tested.

Woodford and Wood (1983) conducted erosion tests in a fluidized bed with 0.93 and 1.9 *mm* silica sand on ten different tube materials. Their data for copper and SS316 are listed in Table 9.4, together with the predictions from equation 9.10. Since not all values needed to apply the equation were provided by the authors, some parameters have had to

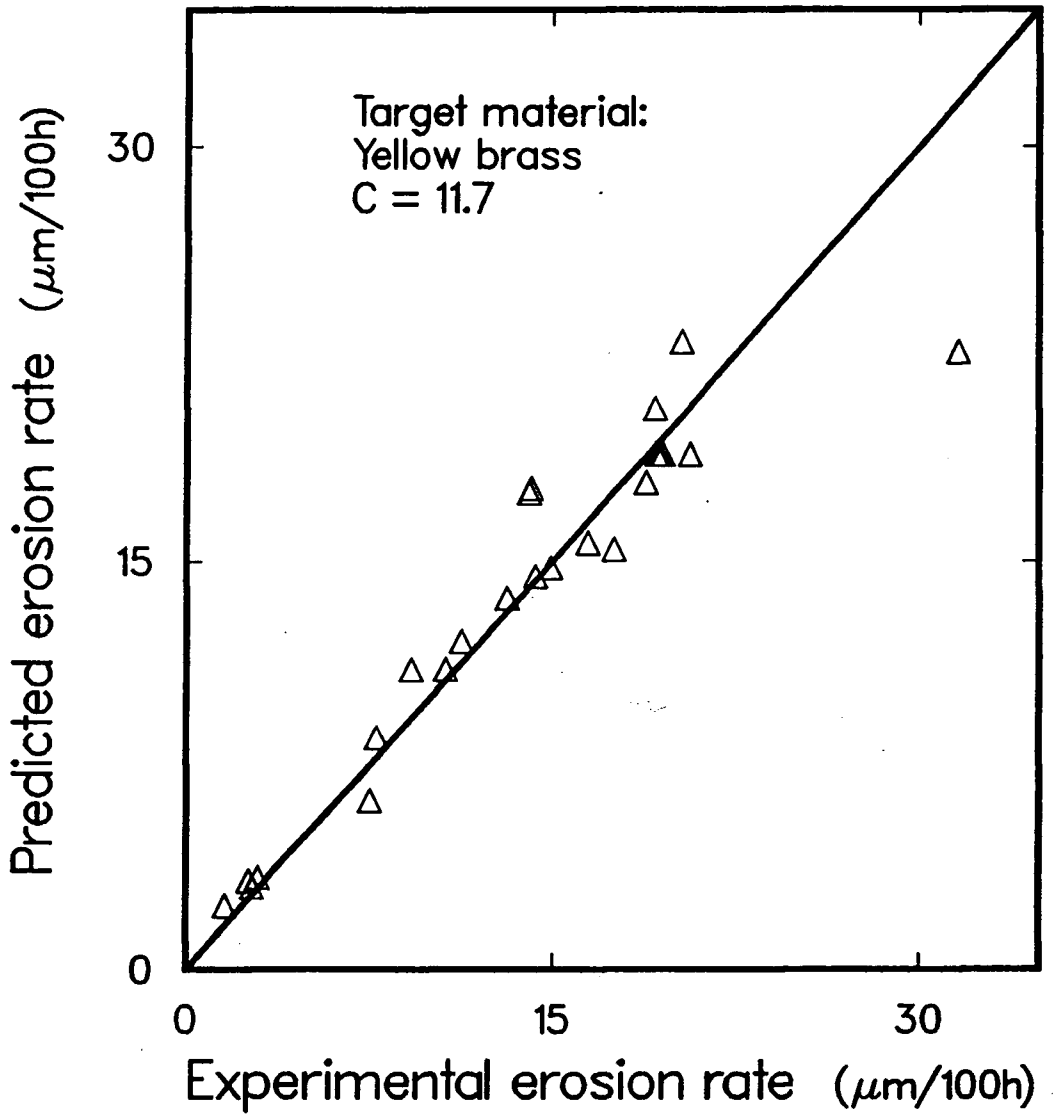

Figure 9.6 Predicted erosion rate vs. experimental erosion rate for erosion tests with silica sand and brass as tube material in the three–dimensional cold model fluidized bed (Predictions are from equation 9.10.)

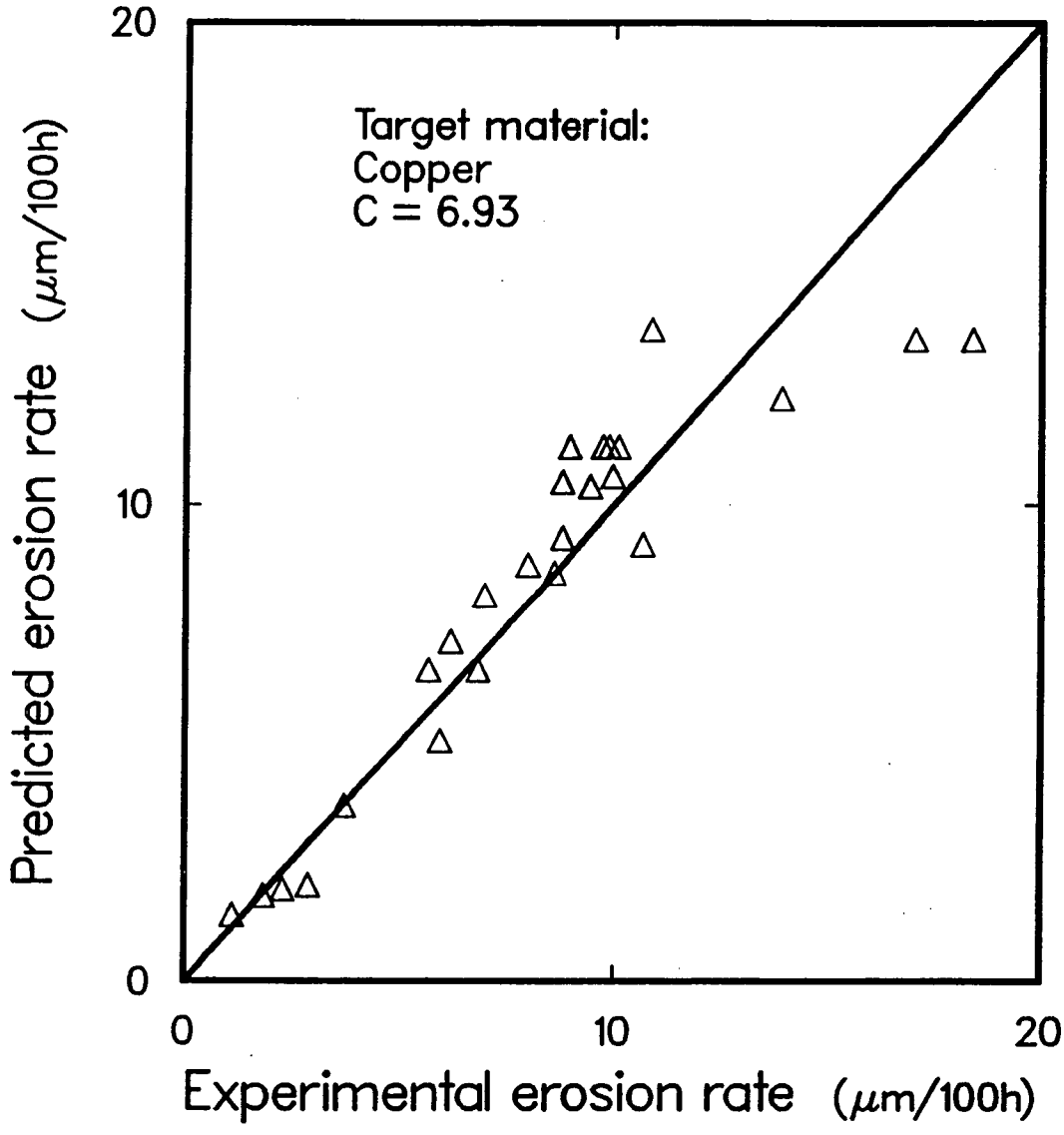

Figure 9.7 Predicted erosion rate vs. experimental erosion rate for erosion tests with silica sand and copper as tube material in the three–dimensional cold model fluidized bed (Predictions are from equation 9.10.)

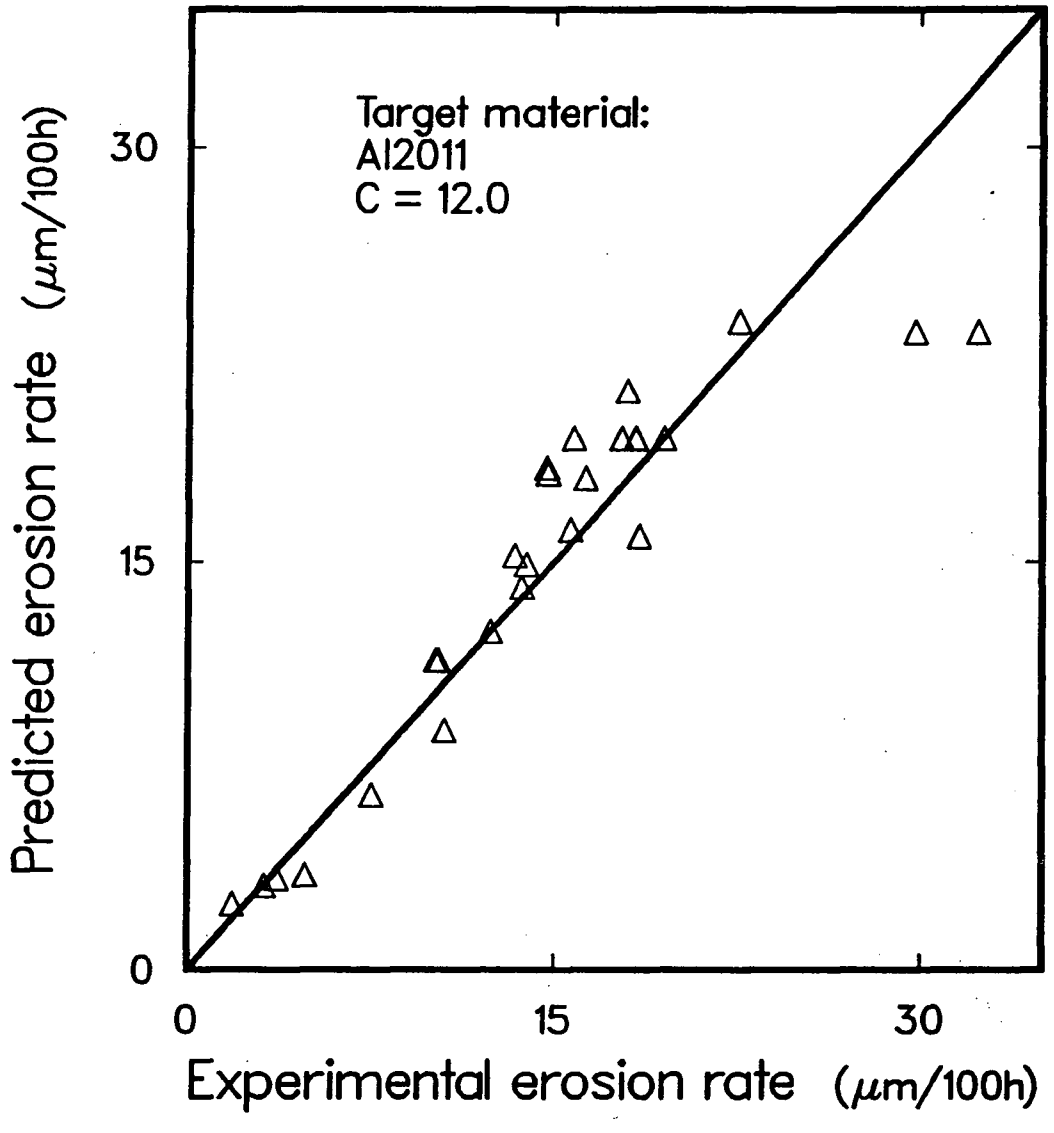

Figure 9.8 Predicted erosion rate vs. experimental erosion rate for erosion tests with silica sand and Al2011 as tube material in the three-dimensional cold model fluidized bed (Predictions are from equation 9.10.)

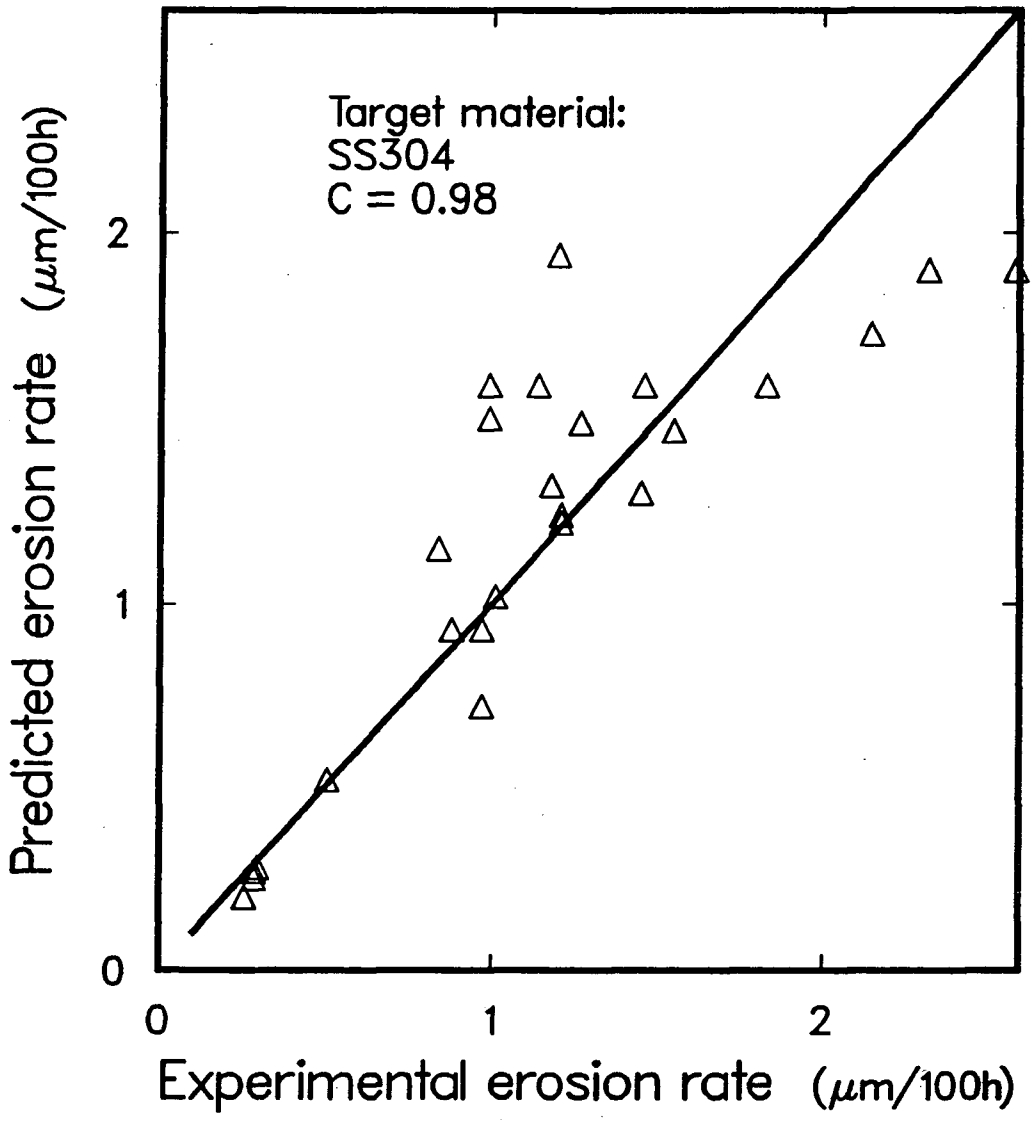

Figure 9.9 Predicted erosion rate vs. experimental erosion rate for erosion tests with silica sand and SS304 as tube material in the three–dimensional cold model fluidized bed (Predictions are from equation 9.10.)

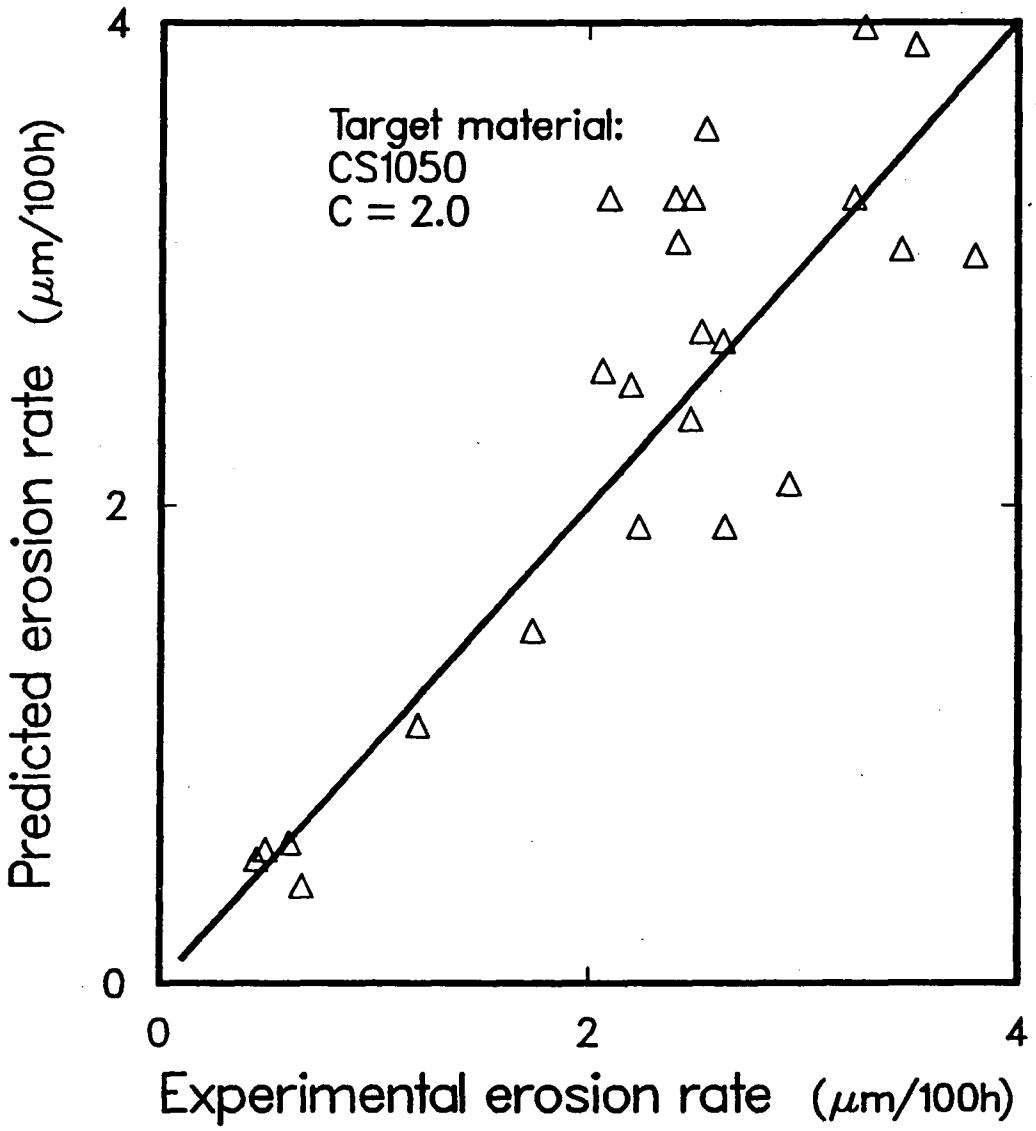

Figure 9.10 Predicted erosion rate vs. experimental erosion rate for erosion tests with silica sand and CS1050 as tube material in the three-dimensional cold model fluidized bed (Predictions are from equation 9.10.)

Table 9.4: Comparison of the results from Woodford and Wood (1983) with predictions from equation 9.10

Tube material	Particle diameter (mm)	Erosion rate (μm/100h) Experimental results*	Calculated results
Copper	1.9	17	19
SS316	1.9	3.0	2.8
Copper	0.93	6.7	8.2
SS316	0.93	1.8	1.2

* Values have been converted to average erosion rate along the circumference without tube banks.

** Assumed values:

Particle sphericity: 0.89

Void rise velocity: 2.0 m/s

Void frequency: 2.2 /s

be estimated. We assumed a particle sphericity of 0.89, a void rise velocity of 2.0 m/s and a void frequency of 2.2 Hz. It is shown that equation 9.10 gives very good predictions for these two materials with these reasonable parameter values.

Notwithstanding the satisfactory predictions obtained from equation 9.10 for our data and for the Woodford and Wood data and the consistency of the interpretation with the dropping experiments and two-dimensional observations, the model must be regarded as tentative in nature. This is because:

(1) The number of experimental data and ranges of some of the variables are severely limited.

(2) The multi-axes experimental design (see Section 3.1) means that many combinations of variables remote from the "base case" were not explored.

(3) The model is highly simplified. For example, any losses due to abrasion, combined corrosion/erosion or local high velocity grid jets (which should, in any case, be absent if good design practices are followed) are ignored. In addition, while the observed surface fatigue process is consistent with the observations in this thesis, the process is complex, and other mechanisms may also contribute.

9.4 General Discussion

As discussed in earlier chapters, the repeated impact of low velocity particles in fluidized beds can produce substantial erosion on horizontal tubes which endangers the life and proper performance of heat exchange tubes, even though the kinetic energy of individual particles is very low. The erosion rate is closely related to the particle movement in the vicinity of the tubes/internals.

Particle impact velocity has a very strong influence on erosion rate and is closely related

to gas void rise velocity, and hence to the void size, in fluidized beds. Therefore control of gas void size inside fluidized beds is very important. An increase of superficial air velocity generally increases the gas void size up to the point where turbulent fluidization is achieved. The presence of tube banks usually limits the gas void size inside the tube banks and therefore reduces the particle velocity. The erosion rate is smaller for tubes inside a tube bundle than for a single isolated tube. The lowest two rows of tubes in a bundle, however, are likely to suffer more severe erosion than the rest when the tube bank begins well above the distributor such that the bubble size entering the bank is much greater than the intertube spacing. Swift et al. (1984) have reported an erosion rate for the first row of tubes 1.25 times as high as that of other tubes inside tube bundle in the IEA Grimethorpe $2\ m \times 2\ m$ PFBC unit. Similarly Hosny and Grace (1984) reported that the lowermost row is subject to larger transient forces than higher tubes within tube bundles providing that bubbles have grown to be much larger than the intertube spacing before entering the tube bundle.

Localized high particle velocity caused by jets just above the distributors, at bends in internal tubes or baffles and near feed points are extremely susceptible to wear. Regions of high velocity impact should be avoided when heat exchanger tubes are designed and installed. In practice, it has proved useful to weld small knobs on tube surface or rods along the tube bottom and near tube turning points to reduce erosion (Zhang 1982, Jin 1984, Monenco 1987).

Turbulent fluidization may be desirable because of the reduced void size. The presence of internal baffles or tube banks can induce turbulent flow at smaller gas velocities (Staub & Canada 1978, Jin et al. 1986). Installation of one or two rows of dummy tubes or other baffles below the tube banks may be used to reduce the erosion of tubes in the first two rows of tubes without changing the flow conditions or overall heat transfer very much. Horizontal

tubes in circulating fluidized beds are generally not feasible due to the much higher particle velocities.

Particle size also influences the erosion rate, smaller particles producing much less erosion. This is probably why there are so many reports of erosion in fluidized bed combustors, where relatively coarse particles ($> 600\mu m$) are used, but few reports of serious erosion in other fluidized bed reactors, where much smaller particles are usually employed. The heat exchange tubes and other internals in fluidized bed facilities with small particles ($< 600\mu m$) are likely to be safe from erosion to a commercially acceptable level. Angular particles cause much more severe erosion than rounded ones. The use of angular particles should therefore be avoided whenever possible. Increases of particle density and hardness also increase the danger of erosion.

Ferrous metals and alloys have higher resistance to erosion than non-ferrous metals and alloys. Stainless steels suffer much less erosion than carbon steels at room temperature. At high temperatures, there are examples where carbon steel has been used in small fluidized bed combustors (Zhang 1980, Zhang 1982), but caution has to be exercised in large facilities. Stainless steel is superior at high temperatures due to its resistance to oxidation/corrosion. Alloys which have high resistance to oxidation/corrosion and yet have high ductility are most desirable.

In some fluidized bed combustion systems where heavy deposits on tube surfaces are produced, it may be useful to purposely introduce a certain amount of erosion to balance the deposition rate to keep the tubes clean from deposits for best heat transfer. This, however, must be applied with caution and considered on a case by case basis.

CHAPTER TEN: CONCLUSIONS AND RECOMMENDATIONS

10.1 General Conclusions

Several major conclusions can be drawn based on this study:

(1) Low velocity ($< 6m/s$) particle impact can cause substantial erosion, even though the velocities of impact are well below the threshold velocity given by investigators studying high velocity solid impact erosion.

(2) Erosion of horizontal tubes in fluidized beds is caused by particle motion around the tube and is mainly due to impact of these particles on the lower tube surface, lesser amounts of wastage occurring due to abrasion on the upper surface. The erosion rate is strongly influenced by the particle impact velocity, which is caused by the rise and interaction of voids in the bed. Localized high gas velocities may lead to higher particle impact velocities in given regions, which can cause premature failure of the tube or internal baffles.

(3) Particle diameter affects the erosion rate, with larger particles producing a higher erosion rate. The erosion rate is also dependent on particle hardness and particle density. Angular particles cause more erosion than rounded ones.

(4) The erosion rate is strongly dependent on the mechanical properties of the target materials. Young's modulus plays a more important role in erosion than hardness, with the erosion rate increasing as the Young's modulus decreases.

(5) The erosion process in a fluidized bed appears to occur mostly by a surface fatigue process. The removal of materials is then caused by repeated impact of low energy particles, which only cause elastic deformation on the target for each particle impact, but eventually produce small cracks on or underneath the target surface. Over a period

of time this process leads to the material loss.

(6) At high temperatures, the erosion problem becomes more complicated due to the involvement of oxidation, corrosion and deposition. The presence of an oxidized layer or deposits may reduce the apparent erosion rate in some cases.

Recommendations

(1) Further tests with more types of particles and target materials should be performed in the cold model three-dimensional fluidized bed or in the dropping equipment to elucidate the influence of mechanical properties of both particles and materials on the erosion coefficient C.

(2) Experiments in fluidized beds operating in regimes other than slugging are needed to generalize the application of the tentative erosion model.

(3) Many more tests at high temperature are required to adapt our model to erosion in fluidized bed combustors and other units at high temperature and to make allowance for corrosion, deposition and hydrodynamic factors.

NOMENCLATURE

A	cross-sectional area of bed
$A_1 - A_5$	constants used in equations 2.19, 5.5 and 5.7
A_b	cross-sectional area of the tensile test beam
A_c	contact area of the indenter with tested material
A_{cap}	the bottom area of the sphere cap indented by impact particle
A_D	area of distributor plate per orifice
B	Beat & Metz number, $\rho_s V_p / Y_m$
C	erosion coefficient, defined in equation 9.10
$C_1 - C_4$	constants used in Chapter 7
C_o	constant in equation 2.13
C'	constant in equations 9.9, 9.11 and 9.12
D	bed mean diameter
D_e	bubble mean diameter
$D_{e,0}$	diameter of bubbles formed at distributor
$D_{e,\infty}$	bubble diameter in isolation
D_h	horizontal mean path of a rebounding particle
D_t	tube diameter
d_1	diagonal of indentation for hardness tests
d_2, d_3	length and width of the specimen used in dropping tests
d_{or}	distributor orifice diameter
d_p	particle mean diameter
d_{p_i}	mean particle diameter for the interval i during screening

E	erosion rate
E_k	kinetic energy of a single particle upon impact
E_y	Young's modulus of target material
f_b	bubble frequency
f_v	gas void frequency
G_b	visible bubble flow rate
g	acceleration due to gravity
H	height of fluidized bed
H_m	target material hardness
H_{mf}	height of fluidized bed at minimum fluidization
H_p	particle hardness
H_v	Vickers hardness
h	depth of maximum deformation of target material caused by particle impact
h_x	depth of deformation of target material caused by particle impact
k	constant defined in equation 9.6
$k_1 - k_6$	constants in Chapter 5
k_7	constant in Chapter 9
k'	energy transfer coefficient of a particle upon impact
k''	constant defined in equation 2.2
L	length of a tensile test beam
ΔL	length change of a tensile test beam
L_j	jet penetration depth of grid jet
M	mass flow rate of particles undergoing impact
M_b	mass flow rate of particles impacting due to one bubble

$m_1 - m_4$	constant indices defined in Chapters 2 and 5
n	number of particles striking unit target surface area per second
$n_1 - n_4$	constant indices defined in Chapters 7 nad 9
P	tension in the tensile specimen
R	bed mean radius
r'	radius of curvature of the leading edge of a bubble
r	correlation coefficient of regression
T	duration of operation
u_b	bubble rise velocity
$u_{b,\infty}$	isolated bubble rise velocity
u_{mf}	minimum fluidization velocity
u_{ms}	minimum slugging velocity
u_{or}	air velocity through each distributor orifice
u_s	slug rise velocity
$u_{s,\infty}$	single slug rise velocity
u_T	terminal velocity of spherical particles of diameter $2.7d_p$
u_t	terminal velocity of particles
V_b	volumetric flow rate due to bubble displacement
V_c	effective void cap volume
V_p	particle impact velocity
V_w	effective void wake volume
W	mechanical energy density
ΔW	work done by a particle on the target material due to impact
x	height above distributor

x_i	weight fraction of particles
Y_m	target material yield strength

Greek Letters

α	angular position on the tube surface, as shown in Figure 6.4
Φ_s	particle sphericity
ϵ	strain
$\bar{\epsilon}$	average strain of target material due to particle impact
ϵ_b	total (bubble) void fraction in the bed
ϵ_{mf}	voidage at minimum fluidization
θ	impingement angle, as shown in Figure 6.4
ρ_s	particle density
σ	stress
σ_u	ultimate tensile stress
σ_y	yield stress

REFERENCES

Andersson, S., "Report for EPRI Materials Workshop", Nova Scotia, July, 1985.

Anthony, E., J., Combustion Research Laboratory, CANMET, Personal Communications, 1988.

Asai, M., Aoki, K. and Tsuji, S., "Particle Behaviour in the Vicinity of Tubes in Fluidized Bed Boilers", in *Fluidized Combustion: Is It Achieving Its Promise?* Inst. of Energy, London, 1984.

ASM Handbook Committee, *Metal Handbook,* B. P. Bardes and H. Baker eds., American Society for Metals, Ninth Edition, 1983.

Baeyens, J. and Geldart, D., "An Investigation into Slugging Fluidized Beds", *Chem. Eng. Sci.,* 29, 255-265, 1974.

Bao, D. and Ruan, Y., "Research and Development of Coal-fired Fluidized-Bed Boiler", *Preprints of Papers,* American Chemical Society, Divison of Fuel Chemistry, Vol 27(1), 196-203, 1982.

Bar-Cohen, A., Glicksman, L. R. and Hughes, R. W., "Semi-Empirical Prediction of Bubble Diameter in Gas Fluidized Bed", *Int. J. Multiphase Flow,* 7, 101-113, 1981.

Bellman, R. Jr. and Levy, A., "Erosion Mechanism in Ductile Metals", *Wear,* 70, 1-27, 1981.

Bonds, T., General Electric Company, Personal Communication, 1983.

Byam, J. W., Madsen, M. M. and Nazemi, A. H., "Analysis of Metal Loss from Heat Exchangers in Fluidized-bed Combustors", *Proc. 8th Int. Conf. on Fluidized Bed Combustion,* Vol 2, Houston, 1985.

Canada, G. S., McLaughlin, M. H. and Staub, F. W., "Flow Regimes and Void Fraction Distribution in Gas Fluidization of Large Particles in Beds without Tube Banks", *AIChE. Symp. Ser.,* No.176, Vol.74, 14-26, 1978.

Ĉatipović, N. M., Jovanović, C. and Fitzgerald, T. J., "Regimes of Fluidization for Large Particles", *AIChE Journal,* 24, 543-547, 1978.

Cherrington, D. C., Golan, L. P. and Hammitt, F. G., "Industrial Application of Fluidized Bed Combustion – Single Tube Heat Transfer Studies", *Proc. 5th Int. Conf. on Fluidized Bed Combustion,* Washington, D. C., Vol. 3, 184-210, 1977.

Clift, R. and Grace, J. R., "Bubble Interactions in Fluidized Beds", *Chem. Eng. Progr. Symp. Series,* 66, No. 105, 14-27, 1970.

Clift, R. and Grace, J. R., "Continuous Bubbling and Slugging", Chapter 3 in *Fluidization, (2nd ed.),* J. F. Davidson, R. Clift and D. Harrison eds, Academic Press, 73-132, 1985.

Clift, R., Grace, J. R. and Weber, M. E., *Bubbles, Drops and Particles,* Academic Press, New York, 1978.

McClintock, F. A. and Argon A. S., "Hardness", Chapter 13 in *Mechanical behaviour of Materials,* Addison-Wesley Publishing Company, 1966.

Cousens, A. K. and Hutchings, I. M., "Influence of Erodent Particle Shape on the Erosion of Mild Steel", *Proc. 6th Int. Conf. on Erosion by Liquid and Solid Impact,* 41.1-41.8, 1983.

Cranfield, R. R. and Geldart, D., "Large Particle Fluidization", *Chem. Eng. Sci.,* 29, 935-947, 1974.

Darton, R. C., LaNauze, R. D., Davidson, J. F. and Harrison, D., "Bubble Growth due to Coalescence in Fluidized Beds", *Trans. Inst. Chem. Eng.,* 55, 274-280, 1977.

Davidson, J. F. and Harrison, D., *Fluidised Particles,* Cambridge Univ. Press, London and New York, 1963.

Davidson, J. F., Paul, R. C., Smith, M. J. S. and Duxbury, H. A., "The Rise of Bubbles in a Fluidized Bed", *Trans Inst. Chem. Engrs.,* 37, 323-328, 1959.

Do, H. T., Grace, J. R. and Clift, R., "Particle Ejection and Entrainment for Fluidized Beds", *Powder Tech.,* 6, 195-200, 1972.

Fakhimi, S. and Harrison, D., "The Voidage Fraction Near a Horizontal Tube Immersed in a Fluidized Bed", *Trans. Inst. Chem. Engrs.,* 58, 125-131, 1980.

Finnie, I., "The Mechanism of Erosion of Ductile Metals", *Proc. 3rd U.S. National Congress of Applied Mechanics,* ASME, New York, 527-532, 1958.

Finnie, I., "Erosion of Surface by Solid Particles", *Wear,* 3, 87-103, 1960.

Finnie, I., "Some Observations on the Erosion of Ductile Metals", *Wear,* 19, 81-90, 1972.

Finnie, I., "Erosion of Metals", *Proc. Conf. Corrosion/Erosion of Coal Conversion System Materials,* 429-443, 1979.

Finnie, I. and McFadden, D. H., "On the Velocity Dependence of the Erosion of Ductile Metals by Solid Particles at Low Angles of Incidence", *Wear,* 48, 181-190, 1978.

Finnie, I., Levy, A. and McFadden, D. H., "Fundamental Mechanisms in the Erosive Wear of Ductile Metals by Solid Particles", in *Erosion: Prevention and Useful Applications,* W. F. Adler ed, ASTM STP 664, 36-58, 1979.

Finnie, I., Wolak, J. and Kabil, Y. "Erosion of Metals by Solid Particles", *J. Mater.,* 2, 682-700, 1967.

Gamble, R. L., "Operation of the Georgetown University Fluidized Bed System", *Fluidised Combustion: Systems and Applications,* Inst. of Energy, London, IB1.1-IB1.10, Nov., 1980.

Geldart, D, "The Size and Frequency of Bubbles in Two- and Three-dimensional Gas-Fluidized Beds", *Powder Tech.,* 4, 41-45, 1970.

Gilmour, J. B., Briggs, D. C., Lui, A. W. and Hindam, H., "Preliminary Results of the Canadian AFBC Materials Tests", Corrosion/85, NACE, March, 1985.

Ginoux, J. J., Geyter, F. M. and Kilkis, B., "Hydrodynamics of a Two-Dimensional Fluidized Bed in the Vicinity of a Cylinder with Horizontal Axis", *Proc. Int. Symp. on Fluidization and its Application,* Toulouse, France, 274-282, Oct., 1973.

Glass, D. H. and Harrison, D., "Flow Patterns Near a Solid Obstacle in a Fluidized Bed", *Chem. Eng. Sci.,* 19, 1001-1002, 1964.

Grace, J. R., "Fluidized-Bed Hydrodynamics", Chapter 8.1 in *Handbook of Multiphase Systems,* G. Hetsroni ed., Hemisphere Publ. Corp., Washington D.C., 1982.

Grace, J. R. and Baeyens J., "Instrumentation and Experimental Techniques", Chapter 13 in *Gas Fluidization Technology,* D. Geldart ed., John Wiley and Sons Ltd., 1985.

Grace, J. R. and Harrison, D., "The Distribution of Bubbles with a Gas-Fluidized Bed", *Inst. Chem. Eng. Symp. Ser.,* 30, 105-113, 1968.

Grace, J. R. and Hosny, N., "Forces on Horizontal Tubes in Gas Fluidized Beds", *Chem. Eng. Research and Design,* 63, 191-198, 1985.

Grace, J. R., Lim, C. J., Brereton, C. M. H. and Chaouki, J., "Circulating Fluidized Bed Reactor Design and Operation", *Sadhana,* 10, 35-48, 1987.

Grace, J. R., Lim, C. J. and Evans, R. L., "Preparatory Report of Pressurized Fluidized Bed Combustion", Submitted to the Government of Canada under Contract 1SU82-00251, March, 1983.

Hager, W. R. and Schrag, S. D., "Particle Circulation Downstream from a Tube Immersed in a Fluidized Bed", *Chem. Eng. Sci.,* 31, 657-659, 1976.

Hager, W. R. and Thompson W. J., "Bubble Behaviour around Immersed Tubes in a Fluidized Bed", *AIChE Symp. Ser.,* Vol 69, No. 128, 68-77, 1973.

Harrison, D. and Grace, J. R., "Fluidized Beds with Internal Baffles", in *Fluidization,* J. F. Davidson & D. Harrison eds., Academic Press, London and New York, 599-626, 1971.

Hearn, E. J., "Simple Stress and Strain", Chapter 1 in *International Series on Materials Science and Technology, Vol. 19: Mechanics of Materials,* 2nd ed., Pergamon Press, 1985.

Hogmark, S., Hammarsten, A. and Soderberg, S., "On the Combined Effect of Corrosion and Erosion", *Proc. Int. Conf. on Erosion by Liquid and Solid Impact,* 37.1-37.8, 1983.

Horio, M. and Nonaba, A., "A Generalized Bubble Diameter Correlation for Gas-Solid Fluidized Bed", *AIChE Journal,* 33, 1865-1872, 1987.

Hosny, N., "Forces on Tubes Immersed in a Fluidized Bed", *Ph.D Dissertation, UBC,* Aug., 1982.

Hosny, N. and Grace, J. R., "Forces on Tubes Immersed within a Fluidized Bed", in *Fluidization IV,* D. Kunii and R. Toei eds., Engineering Foundation, New York, 111-120, 1983.

Hosny, N. and Grace, J. R., "Transient Forces on Tubes within an Array in a Fluidized Bed", *AIChE Journal,* 30, 974-976, 1984.

Hovmand, S. and Davidson, J., F., "Pilot Plant and Laboratory Scale Fluidized Reactors at High Gas Velocities: the Relevance of Slug Flow", Chapter 5 **in** *Fluidization,* J. F. Davidson and D. Harrison eds., Academic Press, London and New York, 193-259, 1971.

Hutchings, I. M., "Mechanisms of the Erosion of Metals by Solid Particles", **in** *Erosion: Prevention and Useful Applications,* W. F. Adler ed, ASTM STP664, 59-76, 1979a.

Hutchings, I. M., "Mechanical and Metallurgy Aspects of the Erosion of Metals", *Proc. Conf. on Corrosion/Erosion of Coal Conversion System Materials,* NACE, Houston Texas, 393-428, 1979b.

Hutchings, I. M., "Recent Advances in the Understanding of Solid Particle Erosion", *Mecanique Materiaux Electrilité,* 365, 185-192, 1980.

Hutchings, I. M., "A Model for the Erosion of Metals by Spherical Particles at Normal Incidence", *Wear,* 70, 269-281, 1981.

Hutchings, I. M., "Wear by Particulates", *Chem. Eng. Sci.,* 42, 869-878, 1987.

Ives, L. K., Young, J. P. and Ruff, A. W., "Particle Erosion Measurements on Metal At Elevated Temperatures", US Dept. of Comm., NITS PB 265 552, 1976.

Jackson, R., "Hydrodynamic Stability of Fluid-Particle Systems", **in** *Fluidization, (2nd ed.),* J. F. Davidson, R. Clift & D. Harrison eds, Academic Press, 47-72, 1985.

Jansson, S, A., "Erosion and Erosion-Corrosion in Fluidized Bed Combustor Systems", *Conf. on Corrosion-Erosion-Wear of Materials in Engineering Fossil Energy Systems,* Berkeley, 548-560, Jan., 1982.

Jansson, S, A., "Tube Wastage Mechanisms in Fluidized-Bed Combustion Systems", *Proc. 8th Int. Conf. on Fluidized Bed Combustion,* Vol. 2, Houston, 1985.

Jin, Y, Tsinghua University, Beijing, China, Personal Communications, 1984 and 1986.

Jin, Y., Yu, Z., Wang, Z. and Cai, P., "A Criterion for Transition from Bubbling to Turbulent Fluidization", **in** *Fluidization V,* K. Østergaard and A. Sørnsen eds., Engineering Foundation, 1986.

Kennedy, T. C. and Donovan, J. E., "Forces on Immersed Tubes in Fluidized Beds", *AIChE Journal,* 27, No.3, 351-357, 1981.

Kobro, H., "A Discussion of the Operation and Performance of a 2.5 MW Fast Fluidized Bed Combustor and a 16 MW Bubbling Bed Combustor", in *Fluidized Combustion: Is It Achieving Its Promise?,* Inst. of Energy, London, Preprints, Vol. 1: 110-120, Oct., 1984.

Krause, H. H., Vaughan, D. A., Sexton, R. W. and Boyd, W. K., "Erosion-Corrosion Effects on Boiler Tube Metals in a Multisolids Fluidized-bed Coal Combustor", *Trans. ASME Journal of Engineering for Power,* 101, 1-8, 1979.

Kunii, D. and Levenspiel, O., *Fluidization Engineering,* John Wiley, New York, 1969.

Leckner, B., Johnsson, F. and Andersson, S., "Material Loss from the Heat Exchange Surfaces of the Chalmers 16 MW Fluidized Bed Boiler", Workshop on Materials Issues in Fluidized Bed Combustion, Nova Scotia, July, 1985a.

Leckner, B., Johnsson, F. and Andersson, S., "Erosion in Fluidized Beds – Influence of Bubbles", Workshop on Materials Issues in Fluidized Bed Combustion, Nova Scotia, July, 1985b.

Levy, A. V., "The Erosion of Metal Alloys and Their Scales", *Conf. Proc.: Corrosion-Erosion-Wear of Mater. in Emerging Fossil Energy Syst.,* Berkeley, 298-376, Jan., 1982.

Levy, A. V., "Erosion Mechanism in Ductile and Brittle Materials", *Proc. 6th Int. Conf. on Erosion by Liquid and Solid Impact,* 39.1-39.7, 1983.

Levy, A. V., "The Erosion-Corrosion of Heat Exchanger Tubes in Fluidized Bed Combustors", *Proc. 9th Int. Conf. on Fluidized Bed Combustion,* Vol. 2, 637-655, Boston, May., 1987.

Liu, Y. and the Teaching and Research Group of Metal Materials, *Wear of Metals (in Chinese),* Dept. Mechanical Eng., Tsinghua Univ. Press, 1984.

Loew, O., Shmutter, B. and Resnick, W., "Particle and Bubble Behaviour and Velocity in a Large-particle Fluidized Bed with Immersed Obstacles", *Powd. Tech.,* 22, 45-57, 1979.

Lund, J. A, Dept. of Metals and Materials Engineering, University of British Columbia, Personal Communication, 1987.

Lyczkowski, R. W., "Erosion Modeling in Fluidized-Bed Combustors", EPRI Workshop on *Wastage of In-Bed Surfaces in Fluidized-Bed Combustors,* Argonne, Illinois, Nov., 1987.

Mann, M. D., Kalmanovitch, D. P. and Hajicek, D. R., "Boiler Tube Corrosion/ Erosion/Deposition Resulting from Fluidized Bed Combustion", Joint ASME/IEEE Power Generation Conf., Miami Beach, Oct., 1987.

Massimilla, L., "Gas Jets in Fluidized Bed", Chapter 4 in *Fluidization, (2nd ed.),* J. F. Davidson, R. Clift & D. Harrison eds, Academic Press, 133-172, 1985.

Merry, J. M. D., "Penetration of Vertical Jets into Fluidized Beds", *AIChE Journal,* 21, 507-510, 1975.

Minchener, A. J., Stringer, J., Brooks, S. et al. "Materials Studies at the IEA Grimethorpe PFBC Experimental Facility", *Proc. 8th Int. Conf. on Fluidized Bed Combustion,* Vol. 2, 760-771, Houston, Oct., 1985.

Monenco Consultants Ltd., "Engineering Evaluation of Fluidized Bed Boiler Demonstration at Canadian Forces Base, Summerside, Prince Edward Island", *Final report to Energy, Mines and Resources of Canada,* March 1987.

Mori, S. and Wen, C. Y., "Estimation of Bubble Diameter in Gaseous Fluidized Beds", *AIChE Journal,* 21, 109-115, 1975.

Natesan, K., Miller, S. A. and Podilski, W. F., "An Assessment of the Performance of Heat Exchange Materials in Fluidized-Bed Combustors", Argonne National Laboratory, ANL-86-42, Feb., 1987.

Park, W. H., Kang, W. K., Capes, C. E. and Osberg, G. L., "The Properties of Bubbles in Fluidized Beds of Conducting Particles as Measured by Electroresistivity Probe", *Chem. Eng. Sci.,* 24, 851-865, 1969.

Parkinson, M. J., Napier, B. A., Jury, A. W. and Kempton, T. J., "Cold Model Studies of PFBC Tube Erosion", *Proc. 8th Int. Conf. on Fluidized Bed Combustion,* Vol. 2, Houston, 1985.

Peeler, J. P. K. and Whitehead, A. B., "Solid Motion at Horizontal Tube Surfaces in a Large Gas-Solid Fluidized Bed", *Chem. Eng. Sci.,* 37, No.1 77-82, 1982.

Preuit, L. C. and Wilson, K. B., "Atmospheric Fluidized Bed Combustion of Municipal Solid Waste: Test Program Results", *Proc. 6th Int. Conf. on Fluidized Bed Combustion,* Vol.3, 872-883, April, 1980.

Rao, P. V. and Buckley, D. H., "Time Effect of Erosion by Solid Particle Impingement on Ductile Materials", *Proc. 6th Int. Conf. on Erosion by Liquid and Solid Impact,* 38.1-38.10, 1983.

Reuter, H., "On the Nature of Bubbles in Gas and Liquid Fluidized Beds", *Chem. Eng. Prog. Symp. Ser.,* 62, (62), 92-99, 1966.

Rickerby, D. G., "Correlation of Erosion with Mechanical Properties in Metals", *Wear,* 84, 393-395, 1983.

Rooney, N. M. and Harrison, D., "Flow Patterns near Horizontal Tubes in a Gas-Fluidized Bed", in *Fluidization Technology,* D. L. Keairns ed., Hemisphere Pub. Corp., Washington, D. C., Vol. 2, 3-6, 1976.

Rowe, P. N., "Experimental Properties of Bubbles", Chapter 4 in *Fluidization,* J. F. Davidson & D. Harrison eds., Academic Press, London and New York, 121-191, 1971.

Rowe, P. N., "Prediction of Bubble Size in a Gas Fluidized Bed", *Chem. Eng. Sci.,* 31, 285-288, 1976.

Rowe, P. N. and Everett D. J., "Fluidised Bed Bubbles Viewed by X-rays", *Trans. Inst. Chem. Engrs.,* 50, 42-48, 1972.

Rowe, P. N. and Partridge, B. A., "An X-ray Study of Bubbles in Fluidized Beds", *Trans. Inst. Chem. Engrs.,* 43, 157-175, 1965.

Rowe, P. N. and Yacono, C., "The Distribution of Bubble Size in Gas Fluidized Beds", *Trans. Inst. Chem. Engrs.,* 53, 59-60, 1975.

Rubin, G., A., Leach, M., F. and Seari, A., "Acoustic Emission Analysis, Audiocontrolled Grinding Circuit Possible Use of Technique", *Research,* Sept., 1985.

Ruff, A. W., "Introductory Remarks on Erosion", *Conf. Proc.: Corrosion/Erosion of Coal Conversion System Materials,* 383-392, 1979.

Ruff, A. W. and Wiederhorn, S. M., "Erosion by Solid Particle Impact", **in** *Treatise on Materials Science and Technology, Vol.16: Erosion,* C. M. Preece ed., Academic Press, 69-126, 1979.

Schmitt, G. F., "Liquid and Solid Particle Impact Erosion", **in** *Wear Control Handbook,* M. B. Peterson and W. O. Winer eds, ASME, 231-282, 1980.

Sitnai, O. and Whitehead, A. B., "Immersed Tube and Other Internals", Chapter 14 **in** *Fluidization, (2nd ed.),* J. F. Davidson, R. Clift & D. Harrison eds, Academic Press, 473-493, 1985.

Smith, A. A., "A State of the Art Resume", *Proc. 5th Conf. on Fluidized Bed Combustion,* Washington, D. C., Vol. 2, 4-12, Dec., 1977.

Smith, D., Anderson, J. S., Atkin, J. A. R. et al, "IEA Grimethorpe 2m x 2m Pressurized Fluidised Bed Combustion Project - Experimental Performance Results and Future Plans", *Proc. 7th Int. Conf. on Fluidized Bed Combustion,* Vol. 1, 439-452, Oct., 1982.

Soo, S. L., "A Note on Erosion by Moving Dust Particles", *Powd. Tech.,* 17, 259-263, 1977.

Staub, F. W. and Canada, G. S., "Effect of Tube Bank and Gas Density on Flow Behavior and Heat Transfer in Fluidized Beds", **in** *Fluidization,* J. F. Davidson and D. L. Keairns eds., Cambridge University Press, 1978.

Stewart, P. S. B and Davidson, J. F., "Slug Flow in Fluidized Beds", *Powd. Tech.,* 1, 61-80, 1967.

Stringer, J., "Corrosion and Corrosion-Erosion of In-Bed Components in Fluidized Bed Combustion", Paper 90, Corrosion/86, NACE, March, 1986.

Stringer, J., "Current Information on Metal Wastage in Fluidized Bed Combustors", *Proc. 9th Int. Conf. on Fluidized Bed Combustion,* Vol. 2, 685-706, Boston, May., 1987.

Stringer, J., Ellis, F. and Stockdale, W., "In-Bed Erosion in Atmospheric Fluidized-Bed Combustors", *Proc. 8th Int. Conf. on Fluidized Bed Combustion,* Vol. 2, 739-749, Houston, Oct., 1985.

Stringer, J. and Minchener, A. J., "Material Issues in the Development of Fluidized Bed Combustion", *Fluidised Combustion: Is it Achieving its Promise?,* Inst. of Energy, London, Vol. 1 Preprints, 255-274, Oct., 1984.

Stringer, J. and Wright, I. G., "Materials Issues in Fluidized Bed Combustion", *J. Materials for Energy Systems,* 8, 319-331, 1986.

Suh. N. P., "Relationship of Solid Particle Erosion to Other Types of Wear", *Conf. Proc. Corrosion/Erosion of Coal Conversion System Materials,* 551-569, 1979.

Sundararajan, G., "An Analysis of the Localization of Deformation and Weight Loss during Single-Particle Normal Impact", *Wear,* 84, 217-235, 1983.

Sundararajan, G. and Shewmon, P. G., "A New Model for the Erosion of Metals at Normal Incidence", *Wear,* 84, 237-258, 1983.

Swift, W. M., Wheeldon, J. M., Anderson, J. S. et al, "IEA Grimethorpe 2m x 2m PFBC Facility: Test series 2, Experimental Results", *Fluidised Combustion: Is it achieving its Promise?",* Inst. of Energy, London, Vol. 1 Preprints, KN/IV/2.1-2.11, Oct., 1984.

Tabor, D., "The Physical Meaning of Indentation and Scratch Hardness", *British J. of App. Physics,* 7, 159-166, 1956.

Tilly, G. P., "Erosion Caused by Impact of Solid Particles", **in** *Treatise on Materials science and Technology, Vol.13: Wear,* S. Douglas ed, Academic Press, 287-320, 1979.

Turner, M. J. and Irving, D., "Forces on Tubes Immersed in a Fluidized Bed", *Proc. 7th Int. Conf. on Fluidized Bed Combustion,* Vol. 2, 831-839, Oct., 1982.

Vaux, W. G. and Newby, R. A., "Wear on Tubes by Jet Impingement in a Fluidized Bed", *Powd. Tech.,* 19, 79-88, 1978.

Wallis, G. B., *One-Dimensional Two-Phase Flow,* McGraw-Hill, New York, 1969.

Webb, H., A., Dept. of Energy, Morgantown Energy Technology Center, Morgantown, USA, Personal Communication, 1986.

Weimer, A. W. and Clough, D. E., "Improved Bubble Velocity Equation for Bubbling Fluidized Beds", *AIChE Journal,* 29, 411-416, 1983.

Werther, J., "Bubbling in Gas Fluidized Beds", *Trans. Inst. Chem. Engrs.,* 52, 149-159, 1974.

Werther, J., "Influence of the Distributor Design on Bubble Characteristics in Large Diameter Gas Fluidized Beds", **in** *Fluidization,* J. F. Davidson and D. L. Keairns eds., Cambridge University Press, London and New York, 7-12, 1978.

Werther, J. and Molerus, O., "The Local Structure of Gas-Fluidized Beds", *Int. J. Multiphase Flow,* 1, 123-138, 1973.

Wood, R. T. and Woodford, D. A., "Tube Erosion in Fluidized Beds (Final Report)", ERDA Report 81-12 11/ET-FUC/79, Dec., 1980.

Woodford, D. A. and Wood, R. T., "Effect of Particle Size and Hardness on Material Erosion in Fluidized Beds", *Proc. 6th Int. Conf. on Erosion by Liquid and Solid Impact,* 56.1-56.10, 1983.

Wright, I. G., "Erosion/Corrosion of Coal Conversion Environment", *Proc. Corrosion/Erosion of Coal Conversion System Materials Conference,* 103-138, 1979.

Wu, R., "Heat Transfer in Circulating Fluidized Beds", *Ph.D Dissertation,* UBC, 1988.

Yates, J. G., "On the Erosion of Metal Tubes in Fluidized Beds", *Chem. Eng. Sci.,* 42, 379-380, 1987.

Zhang, C., "Design for Preventing Erosion of Boiler Tubes in the Bubbling Section of Fluidized Bed Combustors", *Chemical Engineering (in Chinese),* 5, 21-23, 1982.

Zhang, X., "The Progress of Fluidized-Bed Boilers in People's Republic of China", *Proc. 6th Int. Conf. on Fluidized Bed Combustion,* Washington, D. C., 36-40, Aug., 1980.

Zhang, H., Zhou, N., Wang, N. and Chen, S., "Relative Motion of Fluid and Particles", Chapter 5 **in** *Chemical Engineering (in Chinese),* Y. Su, H. Zhang and J. Lin eds., Vol. 1, 187-216, 1980.

Appendix A: Probability of Particle Collision

As discussed in Chapter 5, the vertical space occupied by particles is only 0.084% of the available space for 1.0 mm particles during the dropping experiments. Assume that the horizontal mean path of a rebounding particle, D_h, is one half of the root square mean of the two dimensions of the rectangular specimen surface

$$(d_1 d_2)^{0.5}/2 = (14.5 \times 7)^{0.5}/2 = 5.0\ mm \qquad (A.1)$$

where d_1 and d_2 are the length and width of the target specimen. 5.0 mm covers 5 particle spaces. The probability for a single rebounding particle not to collide with other dropping particles in the one particle space is then $(1 - 0.00084)$. Supposing that the rebounding particles have 10% energy of the dropping particles and half of that energy contribute to the horizontal velocity, the horizontal velocity component for the rebounding particles is $\{(5.0\ m/s)^2 \times 5\%\}^{1/2} = 1.12\ m/s$. Therefore, for 5 particle spaces, the probability of collision is

$$(1 - 0.00084 \times \frac{5.0m/s}{1.12m/s})^5 = 0.9814 \qquad (A.2)$$

The probability for a rebounding particle to collide with other dropping particles during the entire travel is then,

$$(100\% - 98.14\%) < 1.9\% \qquad (A.3)$$

Appendix B: Work Done on the Target by a Single Impact

Work equals force multiplied by the distance dh_x over which the force is applied, i.e.

$$dW = F\,dh_x \tag{B.1}$$

Here h_x is the elastically deformed indentation depth and F is the force on the target exerted by the particle, which is

$$F = A_{cap}P = A_{cap}\bar{\epsilon}E_y \tag{B.2}$$

where A_{cap} is the bottom area of the indented sphere cap (Figure B.1), P is the average pressure on the target and $\bar{\epsilon}$ is the average strain of the target. Assuming that the average strain is proportional to the average deformed depth, $\pi h_x^2(d_p/2 - h_x/3)/A_{cap}$, then we can write

$$F \propto A_{cap}\frac{\pi h_x^2(d_p/2 - h_x/3)}{A_{cap}}E_y \tag{B.3}$$

Considering that $h_x << d_p/2$, the radius of the particle, we have:

$$F \propto \pi d_p h_x^2 E_y/2 \tag{B.4}$$

Then

$$\Delta W \propto \int_0^h F\,dh = \pi d_p h^3 E_y/6 \tag{B.5}$$

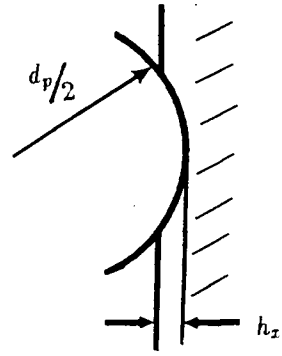

Figure B.1 Indentation formed by elastic deformation

Appendix C: Some Computer Programs Used in This Project

```
C PROGRAM 1 ----- File name: ZC
C
C       This program is used to treat raw data, to compute erosion
C     rate. The program will write out weight loss, volume loss and
C     erosion rate.
C
C  Variables:
C          R   - Title
C          ID  - Numbers
C          DIA - Ring diameter
C          WID - Ring width
C          DEN - Density
C          T   - Time
C          DA  - Raw data
C          L1  - Row dimension
C          L2  - Column dimension
C          WLA - Average weight loss
C          WLS - Weight loss at certein time interval
C          ERA - Erosion rate from WLA
C          ERS - Erosion rate from WLS
C          VL  - Total volume loss
C          VLS - Volume loss over certain period of time

      DIMENSION R(70), T(25), ID(30), DA(30,25)
      DIMENSION DEN(30), DIA(30), WID(30), MID(15)
      DIMENSION WLA(30,25), WLS(30,25)
      DIMENSION ERA(30,25), ERS(30,25)
      DIMENSION VL(30,25), VLS(30,25)



C  Read in data

      READ (5,10) (R(I), I=1,70)
 10   FORMAT(70A1)
      READ (5,20) L1, I0, L3
 20   FORMAT(1X,I2,2X,I1,2X,I2)

      READ (5,30) (T(J),J=1,15)
 30   FORMAT(/27X,15F9.2)
      DO 40 J=1,15
      IF (T(J).LT.-0.5) GO TO 50
 40   CONTINUE

 50   L2=J-1
      DO 70 I=1,L1
      READ (5,60) ID(I), MID(I), DEN(I), WID(I), DIA(I),
     *            (DA(I,J), J=1,L2)
 60   FORMAT(1X,I2,2X,I2,2X,F4.2,2X,F4.2,2X,F5.2,1X,15F9.3)
 70   CONTINUE


C
C  Calculate weight loss
C


      DO 90 I=1,L1
```

```
59          WLA(I,1)=0.
60          WLS(I,1)=0.
61          DO 90 J=2,L2
62          WLA(I,J)=DA(I,J)-DA(I,1)-(DA(1,J)-DA(1,1)+DA(2,J)-DA(2,1))/2.
63          WLS(I,J)=WLA(I,J)-WLA(I,J-1)
64     90   CONTINUE
65
66
67    C
68    C Calculate the total volume loss and the erosion rates
69    C
70
71          DO 100 I=3,L1
72          VL(I,1)=0.
73          VLS(I,1)=0.
74          ERA(I,1)=0.
75          ERS(I,1)=0.
76          DO 100 J=2,L2
77          VL(I,J)=WLA(I,J)/DEN(I)
78          VLS(I,J)=WLS(I,J)/DEN(I)
79          IF (IO.EQ.2) GO TO 95
80          ERA(I,J)=-10**5*VL(I,J)/T(J)/WID(I)/DIA(I)/3.14159265
81          ERS(I,J)=-10**5*VLS(I,J)/(T(J)-T(J-1))/WID(I)/DIA(I)/3.14159265
82          GO TO 100
83     95   ERA(I,J)=-10**5*VL(I,J)/T(J)/(WID(I)*ASIN(DIA(I)/31.75)*31.75)
84          ERS(I,J)=-10**5*VLS(I,J)/(T(J)-T(J-1))/(WID(I)*
85         *          ASIN(DIA(I)/31.75)*31.75)
86    100   CONTINUE
87
88    C Write out weight loss
89    C
90    C Average Weight Loss
91
92          WRITE(6,210) (R(I), I=1,70)
93    210   FORMAT('1'//12X,8A1,20X,15A1///8X,11A1,2X,26A1,3X,10A1/
94         *//22X,'Average Weight Loss (Miligram)')
95          WRITE(6,220) (T(J),J=1,L2)
96    220   FORMAT(///6X,'No.',1X'Time(h) ',F8.2,14F10.2)
97
98          DO 260 I=1,L1
99          WRITE(6,230) ID(I), (DA(I,J),J=1,L2)
100   230   FORMAT(/5X,I3,2X,'Weight',14F10.2)
101         WRITE(6,240) (WLA(I,J),J=2,L2)
102   240   FORMAT(9X,' Loss ',11X,13F10.2)
103   260   CONTINUE
104
105   C Individual Weight Loss
106
107         WRITE(6,211) (R(I), I=1,70)
108   211   FORMAT('1'//12X,8A1,20X,15A1///8X,11A1,2X,26A1,3X,10A1/
109        *//22X,'Individual Weight Loss (miligram)')
110         WRITE(6,221) (T(J),J=1,L2)
111   221   FORMAT(///6X,'No. Time(h) ',F8.2,14F10.2)
112
113         DO 261 I=1,L1
114         WRITE(6,231) ID(I), (DA(I,J),J=1,L2)
115   231   FORMAT(/5X,I3,2X,'Weight',14F10.2)
116         WRITE(6,241) (WLS(I,J),J=2,L2)
```

```
117      241  FORMAT(9X,' Loss ',11X,13F10.2)
118      261  CONTINUE
119
120     C Write out volume loss
121     C
122     C Accumulated volume loss
123
124           WRITE(6,212) (R(I), I=1,70)
125      212  FORMAT('1'//12X,8A1,20X,15A1///8X,11A1,2X,26A1,3X,10A1/
126          *//16X,'Accumulated Volume Loss (mm*mm*mm)')
127           WRITE(6,222) (T(J),J=2,L2)
128      222  FORMAT(///6X,'No.',5X'Time(h) ',15F10.2//)
129
130           DO 252 I=3,L1
131           WRITE(6,232) ID(I), (VL(I,J),J=2,L2)
132      232  FORMAT(2X/5X,I2,'  Volume Loss ',2X,13F10.3)
133      252  CONTINUE
134
135     C Individual volume loss
136
137           WRITE(6,213) (R(I), I=1,70)
138      213  FORMAT('1'//12X,8A1,20X,15A1///8X,11A1,2X,26A1,3X,10A1/
139          *//18X,'Individual Volume Loss (mm*mm)')
140           WRITE(6,223) (T(J),J=2,L2)
141      223  FORMAT(///6X,'No. Time(h) ',F8.2,14F10.2)
142
143           DO 253 I=1,L1
144           WRITE(6,233) ID(I), (VLS(I,J),J=2,L2)
145      233  FORMAT(2X/5X,I2,'  Volume Loss ',2X,13F10.3)
146      253  CONTINUE
147
148     C Write out erosion rate
149     C
150     C Average Erosion Rate
151
152           WRITE(6,215) (R(I), I=1,70)
153      215  FORMAT('1'//12X,8A1,20X,15A1///8X,11A1,2X,26A1,3X,10A1/
154          *//22X,'Average Erosion rate ( u/100h)'
155          */'+',21X,'______________________')
156           WRITE(6,225) (T(J),J=2,L2)
157      225  FORMAT(///8X,'No. Time(h)',F6.2,14F10.2)
158           WRITE(6,235)
159      235  FORMAT(1X)
160
161           DO 265 I=3,L1
162           WRITE(6,245) ID(I), (ERA(I,J),J=2,L2)
163      245  FORMAT(/8X,I2,5X,14F10.2)
164      265  CONTINUE
165
166     C Individual Erosion Rate
167
168           WRITE(6,216) (R(I), I=1,70)
169      216  FORMAT('1'//12X,8A1,20X,15A1///8X,11A1,2X,26A1,3X,10A1/
170          *//22X,'Individual Erosion Rate ( u/100h)'
171          */'+',21X,'________________________')
172           WRITE(6,226) (T(J),J=2,L2)
173      226  FORMAT(///8X,'No. Time(h)',F6.2,14F10.2 )
174           WRITE(6,236)
```

```
  236  FORMAT(1X)

       DO 266 I=3,L1
       WRITE(6,246) ID(I), (ERS(I,J),J=2,L2)
  246  FORMAT(/8X,I2,5X,14F10.2)
  266  CONTINUE


       STOP
       END
```

```
C  PROGRAM 2 ----- File name: UAL
C    This program is used to statistically analyze raw data from
C  the high speed camera films. It reads in individual particle
C  locations at different frame and compute the particle velocity
C  and its direction. Some statistical results are also given,
C  such as: the average particle velocity, average velocities of
C  particles at different relative position with the bubbles,
C  velocity distributions and deviation etc.
C
C
C      Varibles:
C
C         ID  -- Particle ID
C         F1  -- The frame number at which the particle being
C                first tracked
C         F2  -- The frame number at which the particle being
C                last tracked
C         I1  -- Total particle ID number
C         J1  -- Total particles sampled
C         P   -- The sample particle number
C         SDT -- Standard deravation of VMN
C         SD  -- Standard deravation of VGM
C         SDTE-- Standard deravation of VME
C         SDE -- Standard deravation of VGE
C      SPEED  -- Camera shooting speed
C         T   -- Time interval between two frames
C         V   -- Particle velocities
C              VS  - Instantanous particle velocity
C              V   - Single particle velocity
C              VE  - Single particle velocity at impact
C              VV  - 2.3 power of particle velocity at impact
C              VX  - Single particle velocity at X direction (ABS)
C              VXD - Single particle velocity at X direciton
C              VYD - Single particle velocity at Y direciton
C              VY  - Single particle velocity at Y direction
C              VMN - Average particle velocity
C              VME - Average particle velocity at impact
C              VME2- 2.3 power mean part. vel. at impact
C              VMX - Average particle velocity at X direction
C              VMY - Average particle velocity at Y direction
C              VG  - Particle average velocity for one group
C              VG2 - Part. 2.3 power mean vel. for one group
C              VGE - Particle ave. vel. at impact for one group
C              VGE2- Part. 2.3 power mean vel. at impact for one group
C              VGX - Particle ave. vel. for one group at X direction
C              VGY - Particle ave. vel. for one group at Y direction
C        ANG  -- Particle inpingement angle
C        ANG 1-- Angular position on tube surface
C        AME  -- average impingement angle
C        AG   -- average impingement angle for one group
C
C        X,Y -- Coordinates of particle positions
C      XC,YC -- Coordinates of tube center
C      XX,YY -- Coordinates of particle impact positions
C        A,B -- Coefficients of linear equation for projectory line
C         A1 -- Slope of tangent line at impact point
C
C
```

```
C
      DIMENSION ID(300), F1(300), F2(300), P(300)
      DIMENSION V(300), VE(300), VX(300), VY(300), R(120)
      DIMENSION VXD(300), VYD(300), VV(300), VE2(300)
      DIMENSION X(30), Y(30), VS(30)
      DIMENSION VG(7), VG2(7), VGE(7), VGE2(7), VGX(7), VGY(7), AG(7)
      DIMENSION II(7), II1(7), SD(7), SDE(7)
      DIMENSION SG(7), SG2(7), SGE(7), SGE2(7), SGX(7), SGY(7), SGA(7)
      DIMENSION A(300), B(300), A1(300), XX(300), YY(300)
      DIMENSION ANG(300), ANG1(300)
      DIMENSION DIS(20), POINT(21), PER(7)
      INTEGER   F1, F2, P, SPEED, SPEED1


C  Read in general data:

      READ(5,10) (R(I), I=1,60), I1,J1,J2,SPEED,PS,PSR,WIDTH,XC,YC,RC,
     *           (PER(I), I=1,I1)
 10   FORMAT(60A1/1X,4I6/1X,6F9.2/1X,F9.4)

C   Zero:
      SUMT=0.0
      SUMT2=0.0
      SUMTE=0.0
      SUMTE2=0.0
      SUMX=0.0
      SUMY=0.0
      SUMA=0.0
      DO 20 I=1, I1
      II(I)=0
      II1(I)=0
      SG(I)=0.0
      SG2(I)=0.0
      SGE(I)=0.0
      SGE2(I)=0.0
      SGX(I)=0.0
      SGY(I)=0.0
      SGA(I)=0.0
 20   CONTINUE

      J3=J1
      T=1./FLOAT(SPEED)
      DO 100 J=1,J1

C  Read in data of each particle

      IF(J.EQ.J2) PS1=PS
      IF(J.EQ.J2) PSR1=PSR
      IF(J.EQ.J2) SPEED1=SPEED
      IF(J.EQ.J2) XC1=XC
      IF(J.EQ.J2) YC1=YC
      IF(J.EQ.J2) RC1=RC
      IF(J.EQ.J2) READ(5,25) PS, PSR, SPEED, XC, YC, RC
      IF(J.EQ.J2) T=1./FLOAT(SPEED)
 25   FORMAT(1X,2F6.1,I5,3F9.4)

      READ(5,30) P(J), ID(J), F1(J), F2(J)
```

```
 30   FORMAT(1X,4I5)
      IO=F2(J)-F1(J)+1
      READ(5,40) (X(I), Y(I), I=1,IO)
 40   FORMAT(20(1X,F6.1,F5.1))

C  Calculate the velocity and impingement angle of single particle

C   Basic calculations:

      IOM=IO-1
      IOM2=IO-2
      IOM3=IO-3
      SUMS=0.0

C   Curvature correction for Group 4, 5, 6, 7

      IF(ID(J).LT.4) GO TO 46
      ANG(J)=-1.
      ANG1(J)=-1.
      DO 45 I=IOM3, IO
      IF(ID(J).EQ.4.OR.ID(J).EQ.6) Y(I)=RC*ARSIN(ABS((Y(I)-YC)/RC))+YC
      IF(ID(J).EQ.5.OR.ID(J).EQ.7) X(I)=RC*ARSIN(ABS((X(I)-XC)/RC))+XC
 45   CONTINUE

C   Calculate individual velosities

 46   DO 50 I=1,IOM
      VS(I)=SQRT((X(I+1)-X(I))*(X(I+1)-X(I))+
     *           (Y(I+1)-Y(I))*(Y(I+1)-Y(I)))*PSR/T/PS/100.
      SUMS=SUMS+VS(I)
 50   CONTINUE

      V(J)=SUMS/IOM
      VV(J)=ABS(V(J))**2.3
      VE(J)=(VS(IOM)+VS(IOM2))/2.
      VE2(J)=ABS(VE(J))**2.3
      VX(J)=ABS(X(IO)-X(IOM2))/T/200.*PSR/PS
      VY(J)=ABS(Y(IO)-Y(IOM2))/T/200.*PSR/PS
      VXD(J)=(X(IO)-X(IOM2))/T/200.*PSR/PS
      VYD(J)=(Y(IO)-Y(IOM2))/T/200.*PSR/PS

C  Calculate particle impingement angles

      IF(ID(J).GT.3) GO TO 57

C Find  XX, YY

      IF(X(IO).NE.X(IOM2))    GO TO 52
      IF(XX(J).GT.XC+RC+1.1.OR.XX(J).LT.XC-RC-1.1)  WRITE(6,501)
 501  FORMAT(60X,'!!Missed!!')
      IF(XX(J).GT.XC+RC+1.1.OR.XX(J).LT.XC-RC-1.1)  GO TO 56
      XX(J)=X(IO)
      IF(XX(J).GT.XC+RC) XX(J)=XC+RC
      IF(XX(J).LT.XC-RC) XX(J)=XC-RC
      ROOT1=RC*RC-(XX(J)-XC)*(XX(J)-XC)
      YY(J)=YC-SQRT(ROOT1)
      A(J)=1.E+10
      GO TO 54
```

```
175
176      52    A(J)=(Y(IO)-Y(IOM2))/(X(IO)-X(IOM2))
177            B(J)=Y(IO)-A(J)*X(IO)
178            C=B(J)/A(J)+XC
179            AA=1./A(J)/A(J)+1.
180            AB=2.*(C/A(J)+YC)
181            AC=YC*YC+C*C-RC*RC
182            ROOT=AB*AB-4.*AA*AC
183            IF(ROOT.LT.-10.0) GO TO 56
184            IF(ROOT.LT.0.0) ROOT=0.0
185            YY(J)=(AB-SQRT(ROOT))/AA/2.
186      53    XX(J)=(YY(J)-B(J))/A(J)
187
188      C  Find impact angle  and tangent line angle
189
190      54    IF(YY(J).NE.YC) GO TO 55
191            ANG(J)=90.-180./3.14159265*ATAN(ABS(A(J)))
192            ANG1(J)=90.
193            GO TO 57
194
195      55    A1(J)=-(XX(J)-XC)/(YY(J)-YC)
196            ANG(J)=180./3.14159265*ABS(ATAN(A(J))-ATAN(A1(J)))
197            ANG1(J)=180./3.14159265*ABS(ATAN(A1(J)))
198            IF(ANG(J).GT.90.) ANG(J)=180.-ANG(J)
199            GO TO 57
200
201      56    ANG(J)=-1.
202            ANG1(J)-1.
203            J3=J3-1
204
205      C  Calculate the sum of particle velocities and impact angles
206
207      57    SUMT=SUMT+V(J)
208            SUMT2=SUMT2+VV(J)
209            SUMTE=SUMTE+VE(J)
210            SUMTE2=SUMTE2+VE2(2)
211            SUMX=SUMX+VX(J)
212            SUMY=SUMY+VY(J)
213            SUMA=SUMA+ANG(J)
214            DO 60 I=1,I1
215            IF(ID(J).EQ.I) GO TO 70
216      60    CONTINUE
217            GOTO 100
218      70    II(I)=II(I)+1
219            IF (ANG(J).NE.0.0) II1(I)=II1(I)+1
220            SG(I)=SG(I)+V(J)
221            SG2(I)=SG2(I)+VV(J)
222            SGE(I)=SGE(I)+VE(J)
223            SGE2(I)=SGE2(I)+VE2(J)
224            SGX(I)=SGX(I)+VX(J)
225            SGY(I)=SGY(I)+VY(J)
226            SGA(I)=SGA(I)+ANG(J)
227      100   CONTINUE
228
229      C  Write out detail results
230
231            GO TO 400
232            J4=J1-J3
```

```
      WRITE(6,1001) (R(I),I=1,60)
      WRITE(6,1002)
      WRITE(6,1003) (J,ID(J),VXD(J),VYD(J),VE(J),V(J),
     *                          ANG1(J), ANG(J),J=1,50)
      WRITE(6,1001) (R(I),I=1,60)
      WRITE(6,1002)
      IF (J1.LE.100) WRITE(6,1003) (J, ID(J), VXD(J),VYD(J),
     *              VE(J), V(J), ANG1(J), ANG(J),  J=51,J1)
      IF (J1.GT.100) WRITE(6,1003) (J, ID(J), VXD(J),VYD(J),
     *              VE(J), V(J), ANG1(J), ANG(J), J=51,100)
      IF (J1.GT.100) WRITE(6,1001) (R(I),I=1,60)
      IF (J1.GT.100) WRITE(6,1002)
      IF (J1.GT.100) WRITE(6,1003) (J, ID(J), VXD(J),VYD(J),
     *              VE(J), V(J), ANG1(J), ANG(J), J=101,J1)
      WRITE(6,1004) J4, J1, RC
 1001 FORMAT('1'//5X,30A1/40X,30A1)
 1002 FORMAT(/5X,'The individual particle velocities'
     *       //5X,' No    ID    VX       VY       ',
     *        'VE      V    ANGLE1, ANGLE'/)
 1003 FORMAT(5X,I3,4X,I2,6F8.3)
 1004 FORMAT(//10X,I3,'  Missing particles out of ',I3,'   !!!!',
     *        /10X,'        RC=',F5.2//)

C  Calculate the average velocities and inpingement angles

  400 VMN=SUMT/J1
      VMN2=(SUMT2/J1)**(1./2.3)
      VME=SUMTE/J1
      VME2=(SUMTE2/J1)**(1./2.3)
      VMX=SUMX/J1
      VMY=SUMY/J1
      AME=SUMA/J3
      DO 120 I=1,I1
      IF(II(I).NE.0) VG(I)=SG(I)/II(I)
      IF(II(I).NE.0) VG2(I)=(SG2(I)/II(I))**(1./2.1)
      IF(II(I).NE.0) VGE(I)=SGE(I)/II(I)
      IF(II(I).NE.0) VGE2(I)=(SGE2(I)/II(I))**(1./2.1)
      IF(II(I).NE.0) VGX(I)=SGX(I)/II(I)
      IF(II(I).NE.0) VGY(I)=SGY(I)/II(I)
C     WRITE(6,607) I, II1(I), II(I)
C607  FORMAT(/5X,'For group',I1,':  ',I2,' sampled out of',I3)
      IF(II1(I).NE.0) AG(I)=SGA(I)/II1(I)
  120 CONTINUE

C  Statistical results

C   Zero:
      SUMT=0.0
      DO 130 I=1,I1
      SG(I)=0.0
  130 SGE(I)=0.0

      DO 160 J=1, J1
      SUMT=SUMT+(V(J)-VMN)*(V(J)-VMN)
      SUMTE=SUMTE+(VE(J)-VME)*(VE(J)-VME)
      DO 140 I=1,I1
      IF(ID(J).EQ.I) GO TO 150
  140 CONTINUE
```

```
291        150  SG(I)=SG(I)+(V(J)-VG(I))*(V(J)-VG(I))
292             SGE(I)=SGE(I)+(VE(J)-VGE(I))*(VE(J)-VGE(I))
293        160  CONTINUE
294
295             SDT=SQRT(SUMT/FLOAT(J1-1))
296             SDTE=SQRT(SUMTE/FLOAT(J1-1))
297             DO 180 I=1,I1
298             SD(I)=SQRT(SG(I)/(II(I)-1))
299             SDE(I)=SQRT(SGE(I)/(II(I)-1))
300        180  CONTINUE
301
302       C  Calculate particle velocity distributions:
303
304             DO 200 I=1,21
305        200  DIS(I)=0
306             POINT(1)=0.0
307             DO 210 I=1,20
308             POINT(I+1)=I*WIDTH
309        210  DIS(I)=0
310             DO 300 J=1,J1
311             DO 240 I=1,20
312             IF(VE(J).LT.POINT(I+1)) GO TO 260
313        240  CONTINUE
314        260  DIS(I)=DIS(I)+1*PER(I)
315        300  CONTINUE
316
317
318       C  Write out the results
319
320       C   General results:
321
322             WRITE(6,410) (R(I),I=1,60)
323        410  FORMAT('1'/5X,30A1/40X,30A1)
324
325             WRITE(6,411) SPEED, I1, J1, PS, PSR
326       C2    WRITE(6,411) SPEED1, SPEED, I1, J1, PS1, PS, PSR1, PSR
327       C1    WRITE(6,411) SPEED, I1, J1, PS1, PS, PSR
328        411  FORMAT(//6X,'The operating conditions are:'
329            * /'+',5X,'_____________________________'
330       C2   *   //10X,'Film shooting speed:        ',I5,' & ',I5,' frame/s'
331            *   //10X,'Film shooting speed:        ',I5,' frame/s'
332            *    /10X,'Total clasification number:',I5
333            *    /10X,'Total sample size:          ',I5
334            *    /10X,'Plug size on the film:      ',F5.2
335       C12  *    /10X,'Plug size on the film:      ',F5.2,' & ',F5.2
336            *    /10X,'Real plug size:             ',F5.2,' cm')
337       C2   *    /10X,'Real plug size:             ',F5.2,' & ',F5.2,' cm')
338
339             WRITE(6,420) VME, SDTE, VME2, VMX, VMY, AME
340        420  FORMAT(//6X,'The overall results are:'
341            *    /'+',5X,'_______________________'
342            *      //10X,'The impingment mean velocity=',F10.3,' m/s'
343            *       /10X,'The standard deviation      =',F10.3,' m/s'
344            *      //10X,'The 2.3 power mean velocity =',F10.3,' m/s'
345            *    /'+',9X,'                                        _____'
346            *       /10X,'The velocity at X direction =',F10.3,' m/s'
347            *       /10X,'The velocity at Y direction =',F10.3,' m/s'
348            *       /10X,'The impingment angle        =',F10.3,' degree')
```

```
349
350          WRITE(6,425)
351     425  FORMAT(///6X,'*****************************************'
352         *          /6X,'The results of different classifications:'
353         *     /'+',5X,'_____________________________________')
354          DO 435 I=1,I1
355          IF (I.GT.3) GO TO 430
356          WRITE(6,440) I,II(I),VGE(I),SDE(I),VGE2(I),VGX(I),VGY(I),AG(I)
357          GO TO 435
358     430  WRITE(6,445) I,II(I),VGE(I), SD(I),VG2(I), VGX(I),VGY(I),AG(I)
359     435  CONTINUE
360     440  FORMAT(/15X,'Group',I1,':', /20X,I2,' particles sampled'
361         *       /15X,'V (mean impact)       =',F10.3,' m/s'
362         *       /15X,'Stad Deviation        =',F10.3,' m/s'
363         *       /15X,'V (2.3 power mean)    =',F10.3,' m/s'
364         *   /'+',14X,'                                  _____'
365         *       /15X,'V (mean X direction) =',F10.3,' m/s'
366         *       /15X,'V (mean y direction) =',F10.3,' m/s'
367         *       /15X,'A (Angle at impact)  =',F10.3,' degree'/)
368     445  FORMAT(/15X,'Group',I1,':', /20X,I2,' particles sampled'
369         *       /15X,'V (mean velocity)     =',F10.3,' m/s'
370         *       /15X,'Stad Deviation        =',F10.3,' m/s'
371         *       /15X,'V (2.3 power mean)    =',F10.3,' m/s'
372         *   /'+',14X,'                                  _____'
373         *       /15X,'V (mean X direction) =',F10.3,' m/s'
374         *       /15X,'V (mean y direction) =',F10.3,' m/s'
375         *       /15X,'A (Angle at impact)  =',F10.3,' degree'/)
376
377          WRITE(6,460) (R(I),I=1,60)
378     460  FORMAT('1'///5X,30A1,5X,30A1)
379          WRITE(6,480)
380     480  FORMAT(///5X,'The results of particle distribution'
381         *     /'+',5X,'_____________________________________')
382          WRITE(6,490) (POINT(I), POINT(I+1), DIS(I), I=1,20)
383     490  FORMAT(/10X,F8.3,' < Particle velocity < ',F8.3,' --- ',I4)
384
385
386     500  STOP
387          END
388
389
390
```

```
C  PROGRAM 3  ----- File name: GDR
C
C     This file is used to regress directly the equation:
C                Y = A1 *  Y2**A2 * Y3**A3 * ... * Yn**An
C  for the experimental results.
C

      DIMENSION X(7,16), Y(16), A(7), Y1(16), ERR(16)


C
C  Read in results
C
      READ(5,10) M, N, EPS
 10   FORMAT(1X,2I3,F10.6)
      READ(5,20) (A(I),I=1,N)
 20   FORMAT(7F10.6)

      NN=300
      VAR=0.
      E=EXP(1.)
      DO 40 J=1,M
      READ(5,30) (X(I,J),I=2,5), Y(J), (X(I,J),I=6,N)
 30   FORMAT(7F8.2)
      X(1,J)=E
 40   CONTINUE
      WRITE(6,60) (Y(J),(X(I,J),I=2,N), J=1,M)
 60   FORMAT(/5X,7F9.2)

C
C  Carry out calculations
C

      CALL NWDRCT(X,Y,N,M,A,EPS,NTIME,NN,IFLAG)
      IF(IFLAG.EQ.2) GOTO 111
      IF(IFLAG.EQ.0) GOTO 90

C
C  Write out results:
C

      WRITE(6,80)
 80   FORMAT(///10X,'Number of cycles is beyond what is given'//)

 90   A(1)=EXP(A(1))
      DO 100 J=1,M
      Y1(J)=A(1) * X(2,J)**A(2) * X(3,J)**A(3) * X(4,J)**A(4)
     *           * X(5,J)**A(5) * X(6,J)**A(6) * X(7,J)**A(7)
      ERR(J)=(Y(J)-Y1(J))/Y(J)*100.
      VAR=VAR+(Y(J)-Y1(J))*(Y(J)-Y1(J))
 100  CONTINUE
      SY=SQRT(VAR/(M-1))

      WRITE(6,110)
 110  FORMAT('1'//20X,'************ Final results ***********'
     *          //5X,'    E(Exp)   E(Calc)  Error(%)   M         Vp    '
     *                 ,'    Dp       Hp       Fi       Ym    ')
      WRITE(6,115) (Y(J), Y1(J), ERR(J), (X(I,J),I=2,N), J=1,M)
```

```
 115  FORMAT(//5X,9F9.2)

      WRITE(6,120)
 120  FORMAT(///10X,' ************* The coefficient ************'//)
      WRITE(6,130)  (I, A(I),I=1,N)
 130  FORMAT(/10X,'A(',I1,')=',F13.6)
      WRITE(6,140) NTIME, VAR, SY
 140  FORMAT(//10X,'The number of circle is ',I3
     *       //10X,'The true variance is ',F15.6
     *       //10X,'The standard deviation is: ',F12.4)
      GO TO 500

C  Abnormal results

 111  WRITE(6,112)
 112  FORMAT(//10X,' Something is wrong with Gauss method')

 500  STOP
      END


      SUBROUTINE  NWDRCT(X,Y,N,M,A,EPS,NTIME,NN,IFLAG)

C   This subroutine is to use Newton's direct method to
C       get the coefficients of
C             Y=E**A1*X2**A2*X3**A3*........*Xn**An
C       from data set of Y, X1,X2,X3....Xn


      DIMENSION X(N,M),Y(M),A(N),FA(7,8),B(7)

      N1=N+1
      NTIME=0


C   CARRY OUT NEWTOM'S METHOD

 10   CALL FUN(FA,N,M,N1,X,Y,A)

      CALL GAUSS(FA,N,N,N1,B,RES,IERROR)

      IF(IERROR.EQ.2) GO TO 200

C   COMPARE THE RESULTS OF A

      NTIME=NTIME+1

      DO 30 I=1,N
      IF (ABS(B(I)).GT.EPS)   GOTO 40
 30   CONTINUE
      GO TO 100
 40   IF(NTIME.GT.NN) GO TO 80

C   MODIFY VALUES OF ARRAY A

      DO 50 I=1,N
      A(I)=A(I)+B(I)
 50   CONTINUE
```

```
      GO TO 10

 80   IFLAG=1
      RETURN
 100  IFLAG=0
      RETURN
 200  IFLAG=2
      RETURN
      END


      SUBROUTINE FUN(FA,N,M,N1,X,Y,A)

C   THE SUBROUTINE IS USED TO GET THE VALUES OF THE FUNCTION
C       AND THE VALUES OF F'

      DIMENSION X(N,M),Y(M),A(N),FA(N,N1)

      DO 50 I=1,N
      DO 50 J=1,N1
 50   FA(I,J)=0.

      E=EXP(A(1))
      DO 10 I=1,N
      DO 20 L=1,M
      T=E
      DO 30 IL=2,N
 30   T=T*X(IL,L)**A(IL)
      ALOGX=ALOG(X(I,L))
      FA(I,N1)=FA(I,N1)-T*ALOGX*(Y(L)-T)
      DO 40 J=1,N
 40   FA(I,J)=FA(I,J)+(Y(L)-2*T)*ALOGX*T*ALOG(X(J,L))
 20   CONTINUE
 10   CONTINUE
      RETURN
      END



      SUBROUTINE GAUSS(A,N,NDR,NDC,X,RES,IERROR)
      DIMENSION A(NDR,NDC),X(N),B(50,51)
      NM=N-1
      NP=N+1

      DO 20 I=1,N
      DO 10 J=1,NP
      B(I,J)=A(I,J)
 10   CONTINUE
 20   CONTINUE

      DO 80 K=1,NM
      KP=K+1

      BIG=ABS(B(K,K))
      IPIVOT=K
      DO 30 I=KP,N
      AB=ABS(B(I,K))
      IF(AB.LE.BIG) GO TO 30
```

```
      BIG=AB
      IPIVOT=I
30    CONTINUE

      IF(IPIVOT.EQ.K) GO TO 50
      DO 40 J=K,NP
      TEMP=B(IPIVOT,J)
      B(IPIVOT,J)=B(K,J)
      B(K,J)=TEMP
40    CONTINUE
50    IF(B(K,K).EQ.0.) GO TO 130

      DO 70 I=KP,N
      QUOT=B(I,K)/B(K,K)
      B(I,K)=0.
      DO 60 J=KP,NP
      B(I,J)=B(I,J)-QUOT*B(K,J)
60    CONTINUE
70    CONTINUE
80    CONTINUE

      IF(B(N,N).EQ.0.) GO TO 130

      X(N)=B(N,NP)/B(N,N)
      DO 100 II=1,NM
      SUM=0.
      I=N-II
      IP=I+1
      DO 90 J=IP,N
      SUM=SUM+B(I,J)*X(J)
90    CONTINUE
      X(I)=(B(I,NP)-SUM)/B(I,I)
100   CONTINUE


      RSQ=0.
      DO 120 I=1,N
      SUM=0.
      DO 110 J=1,N
      SUM=SUM+A(I,J)*X(J)
110   CONTINUE
      RSQ=RSQ+(ABS(A(I,NP)-SUM))**2
120   CONTINUE
      RES=SQRT(RSQ)
      IERROR=1
      RETURN
130   IERROR=2
      RETURN
      END
```

Appendix D: Raw Data From the Experiments

Appendix D includes three parts:

D.1 Raw Data from the Cold Model Three-Dimensional Column

The erosion rates shown in the following pages are the erosion rates for the time interval between the previous sampling time and the time shown at the top of that column.

Since the computer does not write subscripts and Greek letters, the following symbols are used in **D.1**:

$u(mf)$	for	u_{mf}
$D(t)$	for	D_t
$d(p)$	for	d_p
Fi	for	Φ
$H(p)$	for	H_p
$um/100h$	for	$\mu m/100h$

D.2 Raw Data from the High Temperature Experiments

The symbols are the same as those for the cold model three-dimensional experiments. The temperatures are recorded as "Bed temperature"/"Tube surface temperature".

D.3 Intermediate Results From the Two-Dimensional Fluidization Column

The following symbols are used in **D.3**:

$V(x)$	Horizontal component of the particle impact velocity
$V(y)$	Vertical component of the particle impact velocity
$V(i)$	Particle velocity at impact
$V(mean)$	Average particle velocity over the sampling period
$Angle$	Angular position on the tube where the particle impacts

The ring positions in the three-dimensioal fluidized bed experiments (high and low temperature) are listed below

Ring position*

	Brass	Copper	Al2011	SS304	CS1050	SS316	CS1050	Iron	Pure Al	KWS1	KWS2	KWS3	KWS4
Runs 1, 2, 3, 5, 6, 7, 16, 41, 52 - 59	(All rings were closely located withing 30 mm from the center)												
Runs 4, 8, 9, 10, 11, 12, 13, 14, 15, 17, 18, 20, 29, 36, 38	Center	L13mm	L25mm	R25mm	R13mm								
Runs 19, 21, 22, 23, 25, 26, 30, 31, 34, 35, 40	L30mm	L22mm	L14mm	R21mm	R40mm	R14mm	R30mm	L46mm	L40mm	L10mm	L 6mm	R 6mm	R10mm
Run 32	L46mm	L40mm	L33mm	L14mm	R 2mm	L22mm	L 6mm						
Run 33	R21mm	R29mm	R37mm	L24mm	L10mm	L30mm	L14mm	R 5mm	R11mm				

Runs 24, 27, 28 see Table 7.6

* Positions were measured from the centre of the tube, L = left, R = right. The positions of the center of single rings were given, or the positions of the partitions line between the two rings were provide in case of two rings of same materials were tested together (rings of the same materials were always placed side by side)

Run 1 Silica Sand

u=0.88m/s u-u(mf)=1.32m/s D(t)=32mm d(p)=1.00mm Fi=0.83 H(p)=350kg/mm*mm

Erosion Rate (um/100h)

Time(h)	52.00	145.35	201.38	250.00	Average
Ring #					
1 SS304	0.29	0.31	0.23	0.32	0.29
5 CS1050	0.44	0.43	0.52	0.42	0.45
9 Brass	2.21	3.05	2.95	2.58	2.76
11 Copper	1.61	2.10	1.75	1.75	1.85
13 Al2011	3.20	2.94	3.01	3.72	3.16

Run 2 Silica Sand

u=1.88m/s u-u(mf)=1.32m/s D(t)=32mm d(p)=1.00mm Fi=0.83 H(p)=350kg/mm*mm

Erosion Rate (um/100h)

Time(h)	20.00	40.00	60.00	Average
Ring #				
1 SS304	1.03	1.46	1.06	1.18
5 CS1050	2.02	2.67	2.87	2.52
9 Brass	15.43	16.52	17.48	16.46
11 Copper	6.49	9.11	10.80	8.75
13 Al2011	15.12	14.13	17.78	15.65

Run 3 Silica Sand

u=2.13m/s u-u(mf)=1.57m/s D(t)=32mm d(p)=1.00mm Fi=0.83 H(p)=350kg/mm*mm

Erosion Rate (um/100h)

Time(h)	14.05	Average
Ring #		
1 SS304	2.15	2.15
5 CS1050	2.54	2.54
9 Brass	19.17	19.17
11 Copper	13.90	13.90
13 Al2011	18.01	18.01

Run 4' Silica Sand

u=1.86m/s u-u(mf)=1.30m/s D(t)=32mm d(p)=1.00mm Fi=0.84 H(p)=350kg/mm*mm

Erosion Rate (um/100h)

Time(h)	20.00	40.00	60.00	80.00	100.05	Average
Ring #						
1 SS304	0.90	1.03	1.30	1.12	1.43	1.15
2 SS304	1.31	1.18	1.32	0.90	1.58	1.26
5 CS1050	2.19	1.98	2.12	1.49	2.45	2.05
6 CS1050	2.22	1.89	2.25	1.75	2.31	2.08
9 Brass	12.71	16.94	15.05	15.70	18.16	15.71
10 Brass	15.84	12.27	11.69	12.18	18.78	14.15
11 Copper	8.71	6.73	7.41	5.72	9.51	7.62
12 Copper	7.54	8.92	8.70	7.64	8.59	8.28
13 Al2011	13.58	13.91	13.48	11.78	12.24	13.00
14 Al2011	14.38	13.85	14.07	12.61	14.32	13.85

Run 5 Silica Sand

u=2.03m/s u-u(mf)=1.47m/s D(t)=32mm d(p)=1.00mm Fi=0.84 H(p)=350kg/mm*mm

Erosion Rate (um/100h)

Time(h)	15.00	40.00	Average
Ring #			
1 SS304	1.21	0.87	0.99
5 CS1050	2.65	2.27	2.41
9 Brass	22.68	16.47	18.80
11 Copper	10.87	9.44	9.97
13 Al2011	16.07	13.89	14.70

Run 6 Silica Sand

u=1.89m/s u-u(mf)=1.33m/s D(t)=32mm d(p)=1.00mm Fi=0.84 H(p)=350kg/mm*mm

Erosion Rate (um/100h)

Time(h)	4.12	10.00	15.00	Average
Ring #				
1 SS304	1.46	0.50	2.14	1.31
3 SS304	0.58	1.37	1.66	1.25
5 CS1050	1.71	4.08	1.53	2.58
7 CS1050	1.12	2.62	1.84	1.95
9 Brass	12.32	20.01	17.58	17.09
11 Copper	10.63	13.01	11.58	11.88
13 Al2011	14.07	16.92	21.23	17.57

Run 7 Silica Sand

u=1.89m/s u-u(mf)=1.33m/s D(t)=32mm d(p)=1.00mm Fi=0.84 H(p)=350kg/mm*mm

Erosion Rate (um/100h)

Time(h)	5.00	10.15	15.15	20.00	Average
Ring #					
2 SS304	1.11	1.12	2.18	1.50	1.47
6 CS1050	3.38	1.91	3.09	3.07	2.85
10 Brass	20.62	20.96	20.11	17.00	19.70
12 Copper	13.04	11.13	10.88	11.18	11.56
14 Al2011	25.34	19.27	19.39	19.42	20.85

Run 8 Silica Sand

u=1.84m/s u-u(mf)=1.28m/s D(t)=32mm d(p)=1.00mm Fi=0.84 H(p)=350kg/mm*mm

Erosion Rate (um/100h)

Time(h)	16.00	32.05	48.05	64.12	79.25	Average
Ring #						
1 SS304	1.13	1.61				1.37
2 SS304	1.35	1.12	1.52	1.13	0.95	1.22
5 CS1050	1.45	2.79				2.12
6 CS1050	2.80	2.23	3.37	3.24	1.98	2.73
9 Brass	13.55	17.06				15.32
10 Brass	17.18	14.61	17.55	12.04	11.89	14.68
11 Copper	9.65	8.34				9.00
12 Copper	8.12	7.92	9.23	7.65	9.12	8.40
13 Al2011	14.60	14.45				14.53
14 Al2011	10.90	14.39	13.10	13.99	15.97	13.65

Run 9 Silica Sand

u=1.86m/s u-u(mf)=1.30m/s D(t)=32mm d(p)=1.00mm Fi=0.84 H(p)=350kg/mm*mm

Erosion Rate (um/100h)

Time(h)	16.00	60.00	Average
Ring #			
1 SS304	1.60	0.98	1.15
2 SS304	0.76	1.24	1.11
5 CS1050	2.28	1.52	1.72
6 CS1050	2.70	2.26	2.38
9 Brass	12.82	11.53	11.88
10 Brass	14.38	14.00	14.10
11 Copper	8.17	6.76	7.13
12 Copper	9.19	7.35	7.84
13 Al2011	15.75	13.24	13.91
14 Al2011	11.67	10.74	10.99

Run 10 Silica Sand

u=1.88m/s u-u(mf)=1.31m/s D(t)=32mm
d(p)=1.10mm Fi=0.86 H(p)=350kg/mm*mm

Erosion Rate (um/100h)

Time(h)	18.50	64.33	Average
Ring #			
1 SS304	1.45	1.06	1.17
2 SS304	1.82	1.69	1.73
5 CS1050	2.08	1.97	2.00
6 CS1050	3.48	3.13	3.23
9 Brass	16.17	17.49	17.11
10 Brass	21.20	16.61	17.93
11 Copper	8.69	11.23	10.50
12 Copper	12.56	10.19	10.87
13 Al2011	23.20	15.95	18.04
14 Al2011	17.82	19.43	18.97

Run 10+ Silica Sand

u=1.88m/s u-u(mf)=1.31m/s D(t)=32mm
d(p)=1.04mm Fi=0.86 H(p)=350kg/mm*mm

Erosion Rate (um/100h)

Time(h)	42.25	63.75	Average
Ring #			
1 SS304	0.90	1.30	1.03
2 SS304	1.38	1.39	1.38
5 CS1050	1.74	1.67	1.72
6 CS1050	2.69	2.59	2.66
9 Brass	14.60	10.43	13.19
10 Brass	14.67	16.85	15.41
11 Copper	8.92	9.29	9.05
12 Copper	8.19	7.78	8.05
13 Al2011	15.62	13.51	14.91
14 Al2011	12.89	12.79	12.86

Run 11 Silica Sand

u=1.95m/s u-u(mf)=1.31m/s D(t)=32mm
d(p)=1.30mm Fi=0.86 H(p)=350kg/mm*mm

Erosion Rate (um/100h)

Time(h)	20.00	40.00	61.00	Average
Ring #				
1 SS304	0.91	0.83	0.88	0.88
2 SS304	0.87	1.25	1.17	1.10
5 CS1050	1.90	1.98	1.95	1.94
6 CS1050	2.51	2.16	2.05	2.24
9 Brass	21.05	21.02	18.83	20.28
10 Brass	23.46	18.83	14.01	18.69
11 Copper	12.98	8.21	9.10	10.08
12 Copper	9.64	11.88	6.77	9.39
13 Al2011	20.21	27.01	16.86	21.29
14 Al2011	25.16	15.34	12.93	17.73

Run 11+ Silica Sand

u=1.95m/s u-u(mf)=1.31m/s D(t)=32mm
d(p)=1.30mm Fi=0.86 H(p)=350kg/mm*mm

Erosion Rate (um/100h)

Time(h)	22.00	46.85	110.52	Average
Ring #				
1 SS304	1.32	0.64	0.91	0.93
2 SS304	1.29	1.24	1.42	1.35
5 CS1050	2.14	2.27	1.91	2.04
6 CS1050	3.87	2.44	2.50	2.76
9 Brass	21.07	26.67	15.78	19.28
10 Brass	26.88	20.36	16.39	19.37
11 Copper	14.49	8.59	6.69	8.67
12 Copper	13.77	12.40	9.61	11.07
13 Al2011	20.03	16.14	14.03	15.70
14 Al2011	30.05	23.80	16.75	20.98

Run 12 Silica Sand

u=1.95m/s u-u(mf)=1.31m/s D(t)=32mm
d(p)=1.30mm Fi=0.86 H(p)=350kg/mm*mm

Erosion Rate (um/100h)

Time(h)	20.00	64.00	Average
Ring #			
1 SS304	2.29	1.58	1.81
2 SS304	1.88	1.85	1.86
5 CS1050	3.84	3.45	3.57
6 CS1050	3.40	2.65	2.88
9 Brass	18.92	17.87	18.20
10 Brass	25.93	17.68	20.25
11 Copper	11.47	8.82	9.65
12 Copper	9.77	10.89	10.54
13 Al2011	18.60	18.89	18.80
14 Al2011	19.59	15.39	16.70

Run 13 Silica Sand

u=1.71m/s u-u(mf)=1.31m/s D(t)=32mm
d(p)=0.67mm Fi=0.86 H(p)=350kg/mm*mm

Erosion Rate (um/100h)

Time(h)	22.50	70.33	Average
Ring #			
1 SS304	1.21	0.76	0.91
2 SS304	1.34	0.88	1.02
5 CS1050	2.31	1.45	1.73
6 CS1050	2.14	1.57	1.75
9 Brass	8.78	5.92	6.83
10 Brass	9.83	8.27	8.77
11 Copper	8.67	5.49	6.50
12 Copper	6.47	4.88	5.39
13 Al2011	14.31	9.89	11.30
14 Al2011	9.10	10.13	9.80

Run 14+ Silica Sand

u=1.56m/s u-u(mf)=1.31m/s D(t)=32mm
d(p)=0.30mm Fi=0.86 H(p)=350kg/mm*mm

Erosion Rate (um/100h)

Time(h)	68.62	Average
Ring #		
1 SS304	0.28	0.28
2 SS304	0.30	0.30
5 CS1050	0.46	0.46
6 CS1050	0.53	0.53
9 Brass	2.65	2.65
10 Brass	2.58	2.58
11 Copper	2.27	2.27
12 Copper	2.32	2.32
13 Al2011	3.74	3.74
14 Al2011	3.60	3.60

Run 14 Silica Sand

u=1.56m/s u-u(mf)=1.31m/s D(t)=32mm
d(p)=0.30mm Fi=0.86 H(p)=350kg/mm*mm

Erosion Rate (um/100h)

Time(h)	62.00	Average
Ring #		
1 SS304	0.29	0.29
2 SS304	0.30	0.30
5 CS1050	0.61	0.61
6 CS1050	0.59	0.59
9 Brass	2.99	2.99
10 Brass	3.01	3.01
11 Copper	3.12	3.12
12 Copper	2.67	2.67
13 Al2011	5.64	5.64
14 Al2011	3.95	3.95

Run 15+ Silica Sand

u=2.09m/s u-u(mf)=1.31m/s D(t)=32mm
d(p)=1.51mm Fi=0.86 H(p)=350kg/mm*mm

Erosion Rate (um/100h)

Time(h)	14.57	30.39	47.89	61.22	Average
Ring #					
1 SS304	3.52	2.13	1.73	2.44	2.41
2 SS304	3.95	1.63	1.40	2.19	2.24
5 CS1050	5.39	3.05	2.80	3.37	3.61
6 CS1050	5.73	2.55	2.59	3.07	3.43
9 Brass	40.04	34.18	28.44	20.83	31.03
10 Brass	42.01	33.41	24.38	30.24	32.18
11 Copper	25.67	18.34	12.50	12.06	17.05
13 Al2011	43.73	38.92	21.73	22.76	31.63
14 Al2011	41.66	22.28	25.56	22.80	27.94

Run 15 Silica Sand

u=2.09m/s u-u(mf)=1.31m/s D(t)=32mm
d(p)=1.51mm Fi=0.86 H(p)=350kg/mm*mm

Erosion Rate (um/100h)

Time(h)	15.91	48.91	85.41	Average
Ring #				
1 SS304	5.44	2.28	1.24	2.42
2 SS304	7.10	2.53	1.06	2.75
5 CS1050	8.26	3.30	2.26	3.78
6 CS1050	8.50	4.35	2.30	4.25
9 Brass	72.45	42.52	24.03	40.19
10 Brass	56.80	36.20	23.19	34.48
11 Copper	36.91	17.00	11.61	18.41
13 Al2011	64.56	39.76	16.79	34.56
14 Al2011	63.16	26.64	18.85	30.11

Run 16 Silica Sand

u=1.87m/s u-u(mf)=1.31m/s D(t)=32mm
d(p)=1.00mm Fi=0.86 H(p)=350kg/mm*mm

Erosion Rate (um/100h)

Time(h)	141.45	Average
Ring #		
1 SS304	0.77	0.77
2 SS304	0.90	0.90
5 CS1050	1.54	1.54
6 CS1050	1.83	1.83

Run 17 Silica Sand

u=1.87m/s u-u(mf)=1.31m/s D(t)=25mm
d(p)=1.00mm Fi=0.86 H(p)=350kg/mm*mm

Erosion Rate (um/100h)

Time(h)	16.67	33.75	54.41	Average
Ring #				
1 SS304	0.93	0.97	1.10	1.01
2 SS304	1.18	0.73	1.13	1.02
5 CS1050	2.79	2.08	2.31	2.39
6 CS1050	2.70	2.33	2.44	2.49
9 Brass	7.07	7.07	9.12	7.85
10 Brass	6.93	7.28	8.77	7.74
11 Copper	5.93	5.59	5.76	5.76
12 Copper	4.80	4.97	6.03	5.32
13 Al2011	10.31	7.93	8.39	8.84
14 Al2011	7.90	8.39	7.50	7.90

Run 20 Silica Sand

u=1.87m/s u-u(mf)=1.31m/s D(t)=15mm
d(p)=1.00mm Fi=0.89 H(p)=350kg/mm*mm

Erosion Rate (um/100h)

Time(h)	21.73	45.43	65.50	Average
Ring #				
1 SS304	3.57	2.28	2.27	2.71
2 SS304	3.22	2.70	2.15	2.70
5 CS1050	7.63	5.61	5.54	6.26
6 CS1050	7.35	5.42	5.57	6.11
9 Brass	39.83	38.41	36.84	38.40
10 Brass	42.09	45.91	39.43	42.66
11 Copper	10.83	7.07	6.61	8.18
12 Copper	9.41	6.21	6.99	7.51
13 Al2011	20.67	25.14	22.68	22.90
14 Al2011	24.62	20.51	24.93	23.23

Run 19 Silica Sand

u=0.89m/s u-u(mf)=0.31m/s D(t)=32mm
d(p)=1.00mm Fi=0.89 H(p)=350kg/mm*mm

Erosion Rate (um/100h)

Time(h)	18.50	43.51	64.71	Average
Ring #				
51 Brass	1.28	1.40	2.11	1.60
52 Brass	1.58	1.51	2.05	1.64
53 Copper	1.06	1.03	1.27	1.12
54 Copper	1.12	1.00	1.32	1.14
55 Al2011	1.84	1.68	2.28	1.92
56 Al2011	1.92	1.53	2.11	1.83
31 SS316	0.40	0.18	0.28	0.27
32 SS316	0.48	0.22	0.23	0.30
35 SS304	0.42	0.32	0.06	0.26
36 SS304	0.56	0.16	0.12	0.26
23 Pure Al	2.43	4.67	4.69	4.04
24 Pure Al	3.78	4.34	5.64	4.60
41 CS1020	1.19	0.57	0.57	0.75
42 CS1020	0.86	0.43	0.66	0.63
45 CS1050	0.96	0.28	0.53	0.56
46 CS1050	1.27	0.48	0.68	0.77
15 Pure Fe	0.73	0.43	0.45	0.53
16 Pure Fe	0.75	0.42	0.76	0.62
19 KWS	0.02	-0.03	0.54	0.17
20 KWS	0.02	-0.03	0.29	0.09
21 KWS	0.03	-0.03	0.12	0.04
22 KWS	0.02	-0.03	0.22	0.07

Run 18 Silica Sand

u=1.87m/s u-u(mf)=1.31m/s D(t)=25mm
d(p)=1.00mm Fi=0.86 H(p)=350kg/mm*mm

Erosion Rate (um/100h)

Time(h)	22.83	46.67	Average
Ring #			
1 SS304	1.16	0.80	0.98
2 SS304	0.89	1.24	1.07
5 CS1050	3.12	2.40	2.75
6 CS1050	3.16	2.29	2.72
9 Brass	20.40	12.88	16.56
10 Brass	15.83	12.06	13.91
11 Copper	8.90	5.66	7.24
12 Copper	10.05	6.38	8.17
13 Al2011	19.98	10.02	14.89
14 Al2011	17.25	9.96	13.52

Run 21 Silica Sand

u=1.38m/s u-u(mf)=0.82m/s D(t)=32mm
d(p)=1.00mm Fi=0.89 H(p)=350kg/mm*mm

Erosion Rate (um/100h)

Time(h)	55.17	Average
Ring #		
51 Brass	8.18	8.18
52 Brass	6.81	6.81
53 Copper	3.96	3.96
54 Copper	3.51	3.51
55 Al2011	7.47	7.47
56 Al2011	7.56	7.56
31 SS316	0.89	0.89
32 SS316	1.08	1.08
35 SS304	0.46	0.46
36 SS304	0.56	0.56
23 Pure Al	16.65	16.65
24 Pure Al	23.25	23.25
41 CS1020	3.05	3.05
42 CS1020	2.53	2.53
45 CS1050	1.15	1.15
46 CS1050	1.24	1.24
15 Pure Fe	3.31	3.31
16 Pure Fe	2.58	2.58

Run 22 Silica Sand

u=1.87m/s u-u(mf)=1.31m/s D(t)=32mm
d(p)=1.00mm Fi=0.89 H(p)=350kg/mm*mm

Erosion Rate (um/100h)

Time(h)	43.10	86.97	Average
Ring #			
51 Brass	12.94	11.17	12.05
52 Brass	11.25	9.69	10.47
53 Copper	5.87	6.00	5.94
54 Copper	5.97	6.84	6.41
55 Al2011	12.04	11.14	11.58
56 Al2011	13.34	13.26	13.30
31 SS316	1.14	0.96	1.05
32 SS316	0.95	1.16	1.05
35 SS304	0.99	0.91	0.95
36 SS304	1.12	1.02	1.07
23 Pure Al	21.79	17.95	19.85
24 Pure Al	28.92	29.12	29.02
41 CS1020	2.86	2.47	2.66
42 CS1020	2.78	2.76	2.77
45 CS1050	3.27	2.82	3.05
46 CS1050	3.01	2.61	2.81
15 Pure Fe	3.14	3.01	3.07
16 Pure Fe	2.08	2.17	2.13
19 KWS	2.29	2.10	2.20
20 KWS	2.35	1.22	1.78
21 KWS	2.05	1.55	1.80
22 KWS	1.86	1.36	1.61

Run 23 Silica Sand

u=1.98m/s u-u(mf)=1.42m/s D(t)=32mm
d(p)=1.00mm Fi=0.89 H(p)=350kg/mm*mm

Erosion Rate (um/100h)

Time(h)	21.05	36.10	Average
Ring #			
51 Brass	13.83	11.31	12.78
52 Brass	13.04	14.09	13.48
53 Copper	8.04	6.43	7.37
54 Copper	5.64	7.77	6.53
55 Al2011	12.51	12.66	12.57
56 Al2011	14.61	15.10	14.82
31 SS316	0.89	1.03	0.95
32 SS316	0.95	0.90	0.93
35 SS304	0.67	0.98	0.80
36 SS304	0.80	0.98	0.87
23 Pure Al	19.98	21.92	20.79
24 Pure Al	32.41	35.11	33.54
41 CS1020	2.08	3.32	2.59
42 CS1020	2.65	2.88	2.74
45 CS1050	2.04	2.79	2.35
46 CS1050	2.33	2.95	2.59
15 Pure Fe	2.66	3.27	2.91
16 Pure Fe	2.04	2.22	2.12
19 KWS	1.75	1.68	1.72
20 KWS	1.45	1.74	1.57
21 KWS	1.59	1.75	1.66
22 KWS	1.73	1.74	1.74

Run 24 Silica Sand

u=1.87m/s u-u(mf)=1.31m/s D(t)=32mm
d(p)=1.00mm Fi=0.89 H(p)=350kg/mm*mm

Erosion Rate (um/100h)

Time(h)	44.40	Average
Ring #		
61 Brass	8.01	8.01
62 Brass	8.22	8.22
63 Brass	11.23	11.23
64 Brass	12.49	12.49
65 Brass	11.38	11.38
66 Brass	12.13	12.13
67 Brass	8.37	8.37
68 Brass	7.54	7.54

Run 25 Silica Sand

u=2.52m/s u-u(mf)=1.96m/s D(t)=32mm
d(p)=1.00mm Fi=0.89 H(p)=350kg/mm*mm

Erosion Rate (um/100h)

Time(h)	22.75	Average
Ring #		
51 Brass	22.59	22.59
52 Brass	17.94	17.94
53 Copper	10.83	10.83
54 Copper	10.91	10.91
55 Al2011	21.38	21.38
56 Al2011	23.79	23.79
31 SS316	0.83	0.83
32 SS316	1.27	1.27
35 SS304	1.36	1.36
36 SS304	1.03	1.03
23 Pure Al	33.46	33.46
24 Pure Al	35.56	35.56
41 CS1020	3.07	3.07
42 CS1020	3.90	3.90
45 CS1050	3.06	3.06
46 CS1050	3.50	3.50
15 Pure Fe	3.34	3.34
16 Pure Fe	3.90	3.90
19 KWS	2.19	2.19
20 KWS	1.62	1.62
21 KWS	1.36	1.36
22 KWS	2.08	2.08

Run 26 Silica Sand

u=2.22m/s u-u(mf)=1.66m/s D(t)=32mm
d(p)=1.00mm Fi=0.89 H(p)=350kg/mm*mm

Erosion Rate (um/100h)

Time(h)	23.17	51.48	Average
Ring #			
51 Brass	13.87	14.85	14.41
52 Brass	14.02	13.39	13.67
53 Copper	10.98	8.46	9.59
54 Copper	9.55	9.05	9.28
55 Al2011	18.92	13.82	16.11
56 Al2011	17.40	15.64	16.43
31 SS316	1.99	1.59	1.77
32 SS316	1.77	1.56	1.65
35 SS304	1.85	1.27	1.53
36 SS304	1.94	1.27	1.57
23 Pure Al	33.05	37.81	35.66
24 Pure Al	31.39	33.97	32.81
41 CS1020	4.43	3.85	4.11
42 CS1020	4.99	3.99	4.44
45 CS1050	4.37	3.48	3.88
46 CS1050	4.07	3.43	3.72
15 Pure Fe	3.86	3.08	3.43
16 Pure Fe	4.36	4.08	4.21
19 KWS	2.80	2.01	2.37
20 KWS	2.83	1.68	2.19
21 KWS	2.44	1.49	1.92
22 KWS	2.15	1.08	1.56

Run 27 Silica Sand

u=1.87m/s u-u(mf)=1.31m/s D(t)=32mm
d(p)=1.00mm Fi=0.89 H(p)=350kg/mm*mm

Erosion Rate (um/100h)

Time(h)	44.05	Average
Ring #		
61 Brass	7.40	7.40
62 Brass	9.09	9.09
63 Brass	9.88	9.88
64 Brass	13.43	13.43
65 Brass	11.49	11.49
66 Brass	10.41	10.41
67 Brass	6.82	6.82
68 Brass	7.33	7.33

Run 28 Silica Sand

u=1.87m/s u-u(mf)=1.31m/s D(t)=32mm
d(p)=1.00mm Fi=0.89 H(p)=350kg/mm*mm

Erosion Rate (um/100h)

Time(h)	44.40	Average
Ring #		
61 Brass	22.81	22.81
62 Brass	13.12	13.12
63 Brass	22.77	22.77
64 Brass	22.60	22.60
65 Brass	7.67	7.67
66 Brass	13.41	13.41
67 Brass	23.25	23.25
68 Brass	38.56	38.56

Run 29 Silica Sand

u=1.87m/s u-u(mf)=1.31m/s D(t)=20mm
d(p)=1.00mm Fi=0.89 H(p)=350kg/mm*mm

Erosion Rate (um/100h)

Time(h)	21.75	65.05	Average
Ring #			
1 SS304	1.86	1.60	1.69
2 SS304	1.90	2.02	1.98
5 CS1050	4.52	4.16	4.28
6 CS1050	4.59	4.00	4.20
9 Brass	14.28	13.79	13.95
10 Brass	13.62	14.38	14.13
11 Copper	8.40	7.64	7.89
12 Copper	9.06	8.24	8.51
13 Al2011	16.37	13.08	14.18
14 Al2011	15.22	12.06	13.12

Run 30 Silica Sand

u=2.23m/s u-u(mf)=1.67m/s D(t)=32mm
d(p)=1.00mm Fi=0.89 H(p)=350kg/mm*mm

Erosion Rate (um/100h)

Time(h)	28.31	Average
Ring #		
51 Brass	14.85	14.85
52 Brass	13.39	13.39
53 Copper	8.46	8.46
54 Copper	9.05	9.05
55 Al2011	13.82	13.82
56 Al2011	15.64	15.64
31 SS316	1.59	1.59
32 SS316	1.56	1.56
35 SS304	1.27	1.27
36 SS304	1.27	1.27
23 Pure Al	37.81	37.81
24 Pure Al	33.97	33.97
41 CS1020	3.85	3.85
42 CS1020	3.99	3.99
45 CS1050	3.48	3.48
46 CS1050	3.43	3.43
15 Pure Fe	3.08	3.08
16 Pure Fe	4.08	4.08
19 KWS	2.01	2.01
20 KWS	1.68	1.68
21 KWS	1.49	1.49
22 KWS	1.08	1.08

Run 31 Silica Sand

u=1.88m/s u-u(mf)=1.32m/s D(t)=32mm
d(p)=1.00mm Fi=0.91 H(p)=350kg/mm*mm

Erosion Rate (um/100h)

Time(h)	35.01	Average
Ring #		
51 Brass	11.44	11.44
52 Brass	9.79	9.79
53 Copper	5.49	5.49
54 Copper	5.86	5.86
55 Al2011	10.38	10.38
56 Al2011	9.95	9.95
31 SS316	1.04	1.04
32 SS316	1.25	1.25
35 SS304	1.05	1.05
36 SS304	0.89	0.89
23 Pure Al	28.75	28.75
24 Pure Al	22.29	22.29
41 CS1020	2.49	2.49
42 CS1020	3.12	3.12
45 CS1050	2.59	2.59
46 CS1050	2.67	2.67
15 Pure Fe	2.48	2.48
16 Pure Fe	2.30	2.30
19 KWS	1.66	1.66
20 KWS	1.01	1.01
21 KWS	1.14	1.14
22 KWS	1.05	1.05

Run 32 Silica Sand

u=1.88m/s u-u(mf)=1.32m/s D(t)=32mm
d(p)=1.00mm Fi=0.91 H(p)=350kg/mm*mm

Erosion Rate (um/100h)

Time(h)	141.50	Average
Ring #		
51 Brass	5.44	5.44
52 Brass	5.80	5.80
53 Copper	2.98	2.98
54 Copper	3.27	3.27
55 Al2011	6.56	6.56
56 Al2011	6.28	6.28
31 SS316	0.57	0.57
32 SS316	0.60	0.60
35 SS304	0.45	0.45
36 SS304	0.49	0.49
41 CS1020	1.65	1.65
42 CS1020	1.39	1.39
45 CS1050	1.47	1.47
46 CS1050	1.42	1.42

Run032+ Silica Sand

u=1.88m/s u-u(mf)=1.32m/s D(t)=32mm
d(p)=1.00mm Fi=0.91 H(p)=350kg/mm*mm

Erosion Rate (m/100h)

Time(h)	20.33	61.75	Average
Ring #			
51 Brass	7.31	5.28	5.95
52 Brass	6.44	7.03	6.83
53 Copper	3.83	4.10	4.01
54 Copper	4.40	4.24	4.29
55 Al2011	6.73	6.10	6.31
56 Al2011	7.60	7.14	7.29
31 SS316	0.56	0.66	0.62
32 SS316	0.62	0.53	0.56
35 SS304	0.49	0.53	0.52
36 SS304	0.56	0.61	0.60
41 CS1020	1.48	1.16	1.27
42 CS1020	1.52	1.47	1.49
45 CS1050	1.45	1.44	1.44
46 CS1050	1.32	1.52	1.45

Run 33 Silica Sand

u=1.88m/s u-u(mf)=1.32m/s D(t)=32mm
d(p)=1.00mm Fi=0.91 H(p)=350kg/mm*mm

Erosion Rate (um/100h)

Time(h)	22.41	46.13	Average
Ring #			
51 Brass	9.09	10.96	10.05
52 Brass	8.97	7.85	8.39
53 Copper	6.74	6.94	6.84
54 Copper	6.67	6.85	6.77
55 Al2011	8.86	9.58	9.23
56 Al2011	12.09	10.56	11.30
31 SS316	0.85	0.95	0.90
32 SS316	0.91	1.18	1.05
35 SS304	0.79	0.84	0.82
36 SS304	1.01	0.87	0.94
23 Pure Al	41.01	33.48	37.14
24 Pure Al	26.29	24.01	25.12
41 CS1020	2.43	2.18	2.30
42 CS1020	2.08	2.30	2.19
45 CS1050	2.04	2.08	2.06
46 CS1050	2.45	2.37	2.41
15 Pure Fe	2.92	2.69	2.80
16 Pure Fe	2.14	2.26	2.20
19 KWS	1.69	1.35	1.51
20 KWS	1.04	0.81	0.92
21 KWS	0.94	1.00	0.97
22 KWS	1.08	0.89	0.98

Run 34 Silica Sand

u=1.88m/s u-u(mf)=1.32m/s D(t)=32mm
d(p)=1.00mm Fi=0.91 H(p)=350kg/mm*mm

Erosion Rate (um/100h)

Time(h)	17.17	35.00	Average
Ring #			
51 Brass	7.08	7.91	7.50
52 Brass	8.88	7.94	8.40
71 Brass	7.10	6.76	6.93
72 Brass	5.88	6.87	6.39
53 Copper	5.63	5.87	5.75
54 Copper	6.46	6.63	6.55
73 Copper	5.50	5.59	5.55
55 Al2011	12.52	10.06	11.27
56 Al2011	10.79	8.67	9.71
75 Al2011	11.53	10.71	11.11
76 Al2011	22.18	20.84	21.50
31 SS316	0.99	0.98	0.99
32 SS316	0.95	0.94	0.95
77 SS316	1.71	0.95	1.32
78 SS316	4.16	1.78	2.95
80 SS316	1.39	1.03	1.20
41 CS1020	2.77	2.36	2.56
42 CS1020	2.44	2.46	2.45
44 CS1020	11.94	7.69	9.78
48 CS1050	12.20	7.75	9.93

Run 35 Silicon Carbide

u=2.01m/s u-u(mf)=1.31m/s D(t)=32mm
d(p)=1.06mm Fi=0.86 H(p)=590kg/mm*mm

Erosion Rate (um/100h)

Time(h)	17.50	33.55	56.60	Average
Ring #				
51 Brass	19.63	15.78	12.56	15.66
52 Brass	22.59	11.81	16.52	17.06
53 Copper	21.21	13.49	11.85	15.21
54 Copper	25.65	12.47	14.05	17.19
55 Al2011	25.33	15.06	22.42	21.23
56 Al2011	25.54	17.21	16.27	19.41
31 SS316	10.02	5.13	5.07	6.62
32 SS316	9.66	6.62	7.55	7.94
35 SS304	9.11	4.59	4.55	5.97
36 SS304	9.36	4.96	5.48	6.53
23 Pure Al	29.00	14.65	16.77	19.95
24 Pure Al	31.01	18.92	20.76	23.41
41 CS1020	11.28	6.70	6.38	7.98
42 CS1020	12.00	6.44	8.21	8.88
45 CS1050	12.40	7.11	7.03	8.71
46 CS1050	11.19	6.19	6.26	7.76
15 Pure Fe	11.14	8.05	6.22	8.26
16 Pure Fe	9.43	4.77	6.08	6.75
19 KWS	10.44	7.34	4.92	7.31
20 KWS	8.84	4.72	6.55	6.74
21 KWS	11.67	4.78	3.92	6.56
22 KWS	7.40	5.78	6.68	6.65

Run 36 Silica Sand

u=1.89m/s u-u(mf)=1.33m/s D(t)=15mm
d(p)=1.00mm Fi=0.91 H(p)=350kg/mm*mm

Erosion Rate (um/100h)

Time(h)	16.50	Average
Ring #		
1 SS304	2.47	2.47
2 SS304	2.16	2.16
5 CS1050	5.02	5.02
6 CS1050	4.98	4.98
9 Brass	28.67	28.67
10 Brass	35.65	35.65
11 Copper	3.66	3.66
12 Copper	4.43	4.43
13 Al2011	17.64	17.64
14 Al2011	19.25	19.25

Run 38 Silica Sand

u=1.95m/s u-u(mf)=1.31m/s D(t)=32mm
d(p)=1.30mm Fi=0.86 H(p)=350kg/mm*mm

Erosion Rate (um/100h)

Time(h)	25.25	47.65	Average
Ring #			
1 SS304	1.91	1.05	1.51
2 SS304	1.73	1.08	1.42
5 CS1050	2.55	2.09	2.34
6 CS1050	2.93	2.26	2.62
51 Brass	25.51	17.36	21.68
52 Brass	23.22	15.37	19.53
53 Copper	9.31	7.05	8.25
54 Copper	10.69	8.35	9.59
55 Al2011	15.14	15.55	15.33
56 Al2011	19.45	12.59	16.22

Run 41 Silica Sand

u=1.88m/s u-u(mf)=1.32m/s D(t)=32mm
d(p)=1.00mm Fi=0.91 H(p)=350kg/mm*mm

Erosion Rate (um/100h)

Time(h)	311.00	Average
Ring #		
101 Top	0.27	0.27
102 Bottom	10.49	10.49
103 Front	1.12	1.12
104 Back	1.14	1.14

Run 40 Glass Beads

u=1.79m/s u-u(mf)=1.31m/s D(t)=32mm
d(p)=0.90mm Fi=1.00 H(p)=340kg/mm*mm

Erosion Rate (um/100h)

Time(h)	41.05	Average
Ring #		
51 Brass	2.79	2.79
52 Brass	3.10	3.10
53 Copper	3.42	3.42
54 Copper	3.06	3.06
55 Al2011	6.95	6.95
56 Al2011	5.53	5.53
31 SS316	0.08	0.08
32 SS316	0.12	0.12
35 SS304	0.10	0.10
36 SS304	0.11	0.11
23 Pure Al	29.46	29.46
24 Pure Al	27.68	27.68
41 CS1020	0.37	0.37
42 CS1020	0.42	0.42
45 CS1050	0.34	0.34
46 CS1050	0.34	0.34
15 Pure Fe	0.32	0.32
16 Pure Fe	0.33	0.33
19 KWS	0.17	0.17
20 KWS	0.08	0.08
21 KWS	0.09	0.09
22 KWS	0.07	0.07

Run 52 Silica Sand Room Temperature

u=1.86m/s u-u(mf)=1.31m/s D(t)=32mm d(p)=0.92mm Fi=0.86 H(p)=350kg/mm*mm

Erosion Rate (um/100h)

Time(h)	43.17	Average
Ring #		
71 Brass	3.32	3.32
72 Brass	3.10	3.10
73 Copper	2.63	2.63
74 Copper	2.74	2.74
75 Al2011	5.02	5.02
76 Al2011	5.33	5.33
33 SS316	1.00	1.00
34 SS316	0.96	0.96
37 SS316	0.96	0.96
38 SS304	1.01	1.01
43 SS304D	2.05	2.05
44 CS1020	1.98	1.98
47 CS1050	2.38	2.38
48 CS1050	1.97	1.97
81 SS316	1.05	1.05
82 SS316	1.26	1.26
83 SS316	1.08	1.08
84 SS316	1.10	1.10
85 SS304	0.99	0.99
86 SS304	0.98	0.98
87 SS304	1.07	1.07
88 SS304	0.90	0.90

Run 53 Silica Sand 400/120 C

u=1.86m/s u-u(mf)=1.31m/s D(t)=32mm d(p)=0.92mm Fi=0.86 H(p)=350kg/mm*mm

Erosion Rate (um/100h)

Time(h)	30.00	Average
Ring #		
33 SS316	0.85	0.85
34 SS316	0.99	0.99
37 SS304	0.75	0.75
38 SS304	0.81	0.81
43 CS1020	1.50	1.50
44 CS1020	1.79	1.79
47 CS1050	1.07	1.07
48 CS1050	0.86	0.86

Run 54 Silica Sand 400/130 C

u=1.86m/s u-u(mf)=1.31m/s D(t)=32mm d(p)=0.92mm Fi=0.86 H(p)=350kg/mm*mm

Erosion Rate (um/100h)

Time(h)	27.33	Average
Ring #		
71 Brass	7.19	7.19
72 Brass	8.86	8.86
73 Copper	21.24	21.24
75 Al2011	6.21	6.21
76 Al2011	7.37	7.37
33 SS316	0.79	0.79
34 SS316	0.93	0.93
37 SS304	1.01	1.01
38 SS304	0.93	0.93
44 CS1020	1.27	1.27
47 CS1050	1.48	1.48

Run 55 Silica Sand 750/145 C

u=1.86m/s u-u(mf)=1.31m/s D(t)=32mm d(p)=0.92mm Fi=0.86 H(p)=350kg/mm*mm

Erosion Rate (um/100h)

Time(h)	30.00	Average
Ring #		
72 Brass	11.93	11.93
74 Copper	20.61	20.61
76 Al2011	16.12	16.12
34 SS316	0.74	0.74
37 SS304	0.72	0.72
38 SS304	0.49	0.49
44 CS1020	-4.67	-4.67
47 CS1050	-3.42	-3.42
48 CS1050	-3.75	-3.75
81 SS316	0.86	0.86
82 SS316	0.82	0.82
83 SS316	0.80	0.80
84 SS316	0.68	0.68
85 SS304	0.76	0.76
86 SS304	0.72	0.72
87 SS304	0.88	0.88
88 SS304	0.74	0.74

Run 56 Silica Sand 750/520 C

u=1.86m/s u-u(mf)=1.31m/s D(t)=32mm d(p)=0.92mm Fi=0.86 H(p)=350kg/mm*mm

Erosion Rate (um/100h)

Time(h)	30.27	Average
Ring #		
37 SS304	-1.05	-1.05
38 SS304	-1.17	-1.17
81 SS316	-0.92	-0.92
82 SS316	-0.77	-0.77
83 SS316	-0.98	-0.98
84 SS316	-0.90	-0.90
85 SS304	-0.89	-0.89
86 SS304	-0.53	-0.53
87 SS304	-0.87	-0.87
88 SS304	-0.73	-0.73

Run 57 Silica Sand 780/520 C

u=1.86m/s u-u(mf)=1.31m/s D(t)=32mm d(p)=0.92mm Fi=0.86 H(p)=350kg/mm*mm

Erosion Rate (um/100h)

Time(h)	27.33	Average
Ring #		
82 SS316	-0.21	-0.21
83 SS316	0.15	0.15
84 SS316	-0.38	-0.38
85 SS304	-0.06	-0.06
86 SS304	-0.41	-0.41
87 SS304	-0.10	-0.10

Run 58 Silica Sand 750/520 C

u=1.86m/s u-u(mf)=1.31m/s D(t)=32mm d(p)=0.92mm Fi=0.86 H(p)=350kg/mm*mm

Erosion Rate (um/100h)

Time(h)	73.75	Average
Ring #		
83 SS316	0.02	0.02
84 SS316	-0.26	-0.26
85 SS304	-0.16	-0.16
86 SS304	-0.27	-0.27
87 SS304	-0.28	-0.28
78 SS316	0.08	0.08
80 SS316	0.13	0.13

Run 59 Silica Sand Room Temperature

u=1.86m/s u-u(mf)=1.31m/s D(t)=32mm d(p)=0.92mm Fi=0.86 H(p)=350kg/mm*mm

Erosion Rate (um/100h)

Time(h)	34.90	Average
Ring #		
71 Brass	4.13	4.13
72 Brass	3.14	3.14
73 Copper	3.82	3.82
75 Al2011	7.59	7.59
76 Al2011	15.69	15.69
84 SS316	0.99	0.99
85 SS304	3.45	3.45
86 SS304	2.88	2.88
87 SS304	1.84	1.84
44 CS1020	10.73	10.73
48 CS1050	17.91	17.91

Results for: Single bubble injection

No	ID	VX	VY	VE	Angle	Vmean
1	1	-0.14	0.34	0.40	68.	0.28
2	1	0.0	0.34	0.34	52.	0.25
3	1	0.20	0.27	0.37	12.	0.20
4	1	0.14	0.34	0.38	68.	0.22
5	1	0.07	0.27	0.29	52.	0.23
6	2	-0.07	-0.75	0.76	51.	0.79
7	2	0.14	-0.68	0.71	51.	0.67
8	2	-0.61	-0.75	0.97	54.	0.77
9	2	-0.41	-0.54	0.71	50.	0.73
10	2	0.14	-0.89	0.90	51.	0.77
11	3	0.0	0.48	0.48	31.	0.32
12	3	0.0	0.41	0.41	53.	0.43
13	3	0.0	0.41	0.41	35.	0.38
14	3	-0.20	0.34	0.40	39.	0.47
15	3	-0.27	0.41	0.50	38.	0.57
16	1	-0.41	-0.14	0.43	66.	0.37
17	1	-0.41	0.14	0.45	51.	0.33
18	1	-0.14	0.34	0.37	68.	0.25
19	1	0.14	0.27	0.30	52.	0.27
20	1	0.27	0.20	0.34	51.	0.27
21	2	-0.07	-0.61	0.62	56.	0.58
22	2	-0.07	-0.68	0.69	57.	0.57
23	2	-0.14	-0.54	0.58	51.	0.48
24	2	-0.20	-0.61	0.68	51.	0.51
25	2	0.41	-0.20	0.46	54.	0.42
26	3	0.07	1.02	1.03	53.	0.77
27	3	0.0	0.95	0.95	45.	0.83
28	3	-0.07	0.95	0.96	5.	0.87
29	3	0.0	0.89	0.89	36.	0.84
30	3	0.0	0.89	0.89	57.	0.82
31	3	-0.14	0.75	0.78	18.	0.81
32	3	-0.14	0.61	0.64	26.	0.76
33	1	0.0	0.20	0.20	52.	0.34
34	1	0.0	0.34	0.34	52.	0.35
35	1	0.07	0.20	0.23	78.	0.22
36	1	0.14	0.34	0.42	68.	0.35
37	1	0.0	0.20	0.20	52.	0.19
38	2	0.07	-0.75	0.76	56.	0.64
39	2	0.0	-0.75	0.75	30.	0.59
40	2	0.0	-0.75	0.75	45.	0.59
41	2	0.14	-0.75	0.78	51.	0.67
42	2	0.07	-0.54	0.55	44.	0.55
43	3	-0.27	0.75	0.80	70.	0.75
44	3	-0.20	0.95	0.98	36.	0.62
45	3	-0.27	0.89	0.93	23.	0.76
46	1	0.20	0.20	0.29	51.	0.25
47	1	0.07	0.20	0.23	52.	0.24
48	1	-0.34	0.20	0.41	53.	0.33
49	1	-0.20	0.14	0.25	24.	0.34
50	1	-0.14	0.27	0.30	52.	0.22
51	2	0.27	-0.61	0.67	22.	0.76
52	2	0.61	-0.41	0.74	10.	0.64
53	2	-0.07	-0.75	0.75	80.	0.68
54	2	0.0	-0.89	0.89	51.	0.73
55	2	0.48	-0.75	0.89	2.	0.80

Results for: Single bubble injection

No	ID	VX	VY	VE	Angle	Vmean
56	3	0.0	0.43	0.43	36.	0.45
57	3	0.0	0.50	0.50	45.	0.53
58	3	0.0	0.43	0.43	25.	0.54
59	3	0.0	0.43	0.43	46.	0.60
60	3	0.0	0.57	0.57	35.	0.66
61	3	-0.28	0.50	0.58	60.	0.50
62	3	-0.21	0.43	0.49	9.	0.51
63	1	0.0	0.43	0.43	52.	0.35
64	1	0.21	0.36	0.43	51.	0.34
65	1	0.07	0.28	0.30	7.	0.28
66	1	0.07	0.28	0.30	33.	0.29
67	1	0.0	0.21	0.21	52.	0.27
68	2	0.14	-0.85	0.88	0.	0.93
69	2	0.0	-0.92	0.92	43.	1.11
70	2	0.14	-1.00	1.01	5.	0.95
71	2	0.14	-0.78	0.80	80.	0.86
72	2	0.07	-0.85	0.86	48.	1.05
73	3	0.0	0.92	0.92	44.	0.68
74	3	0.0	0.85	0.85	26.	0.62
75	3	0.0	0.78	0.78	31.	0.58
76	3	0.0	0.78	0.78	46.	0.58
77	3	0.0	0.71	0.71	54.	0.55
78	1	0.0	0.36	0.36	57.	0.33
79	1	0.0	0.43	0.43	58.	0.35
80	1	0.07	0.28	0.30	46.	0.27
81	1	0.0	0.28	0.32	41.	0.33
82	1	0.0	0.36	0.38	30.	0.29
83	2	0.64	-0.71	0.99	50.	1.03
84	2	0.28	-0.71	0.78	68.	0.83
85	2	0.71	-0.78	1.07	50.	0.88
86	2	0.57	-0.71	0.91	50.	0.97
87	2	0.57	-0.50	0.76	50.	0.73
88	3	0.0	0.57	0.57	40.	0.60
89	2	0.0	0.50	0.50	51.	0.49
90	3	0.0	0.43	0.43	40.	0.49
91	3	0.0	0.43	0.43	40.	0.51
92	3	0.28	0.57	0.64	44.	0.59
93	3	0.14	0.50	0.52	11.	0.55
94	1	0.0	0.43	0.43	52.	0.46
95	1	0.07	0.43	0.44	51.	0.46
96	1	0.07	0.36	0.37	42.	0.33
97	1	-0.07	0.57	0.58	65.	0.52
98	1	0.0	0.43	0.43	26.	0.59
99	2	0.07	-0.92	0.93	51.	1.08
100	2	-0.07	-0.78	0.79	48.	0.77
101	2	0.21	-1.64	1.65	83.	0.77
102	2	-0.07	-0.64	0.65	53.	0.71
103	2	-0.21	-0.78	0.84	51.	0.81
104	3	0.0	0.71	0.71	34.	0.66
105	3	0.0	0.78	0.78	44.	0.81
106	3	0.0	0.85	0.85	24.	0.84
107	3	0.0	1.00	1.00	57.	0.88
108	3	0.0	0.92	0.92	41.	0.92
109	3	-0.14	0.85	0.87	64.	0.76
110	3	-0.43	1.00	1.08	47.	0.81

Results for: Bubble coalescence

No	ID	VX	VY	VE	Angle	Vmean
1	1	-0.06	0.38	0.39	51.	0.31
2	1	0.06	0.32	0.33	52.	0.29
3	1	0.19	0.32	0.37	6.	0.27
4	1	0.13	0.26	0.29	50.	0.25
5	1	0.19	0.19	0.29	49.	0.22
6	2	-0.45	0.77	0.89	35.	1.01
7	2	-0.13	0.77	0.79	81.	0.99
8	2	0.58	1.02	1.21	49.	1.44
9	2	-0.70	1.02	1.24	49.	1.34
10	2	0.13	1.28	1.29	50.	1.45
11	3	0.0	1.02	1.02	38.	0.90
12	3	0.0	1.02	1.02	36.	0.94
13	3	0.0	1.09	1.09	28.	1.29
14	3	0.0	1.22	1.22	33.	1.22
15	3	0.0	1.28	1.28	45.	1.18
16	2	-0.13	1.54	1.55	50.	1.27
17	2	-0.13	1.66	1.67	50.	1.53
18	2	0.06	1.54	1.54	55.	1.46
19	2	0.0	1.73	1.73	53.	1.56
20	2	0.0	1.92	1.92	45.	1.74
21	3	0.0	0.96	0.96	34.	0.95
22	3	0.0	0.96	0.96	43.	0.96
23	3	0.0	1.28	1.28	38.	0.85
24	3	0.0	0.64	0.64	40.	0.70
25	3	0.0	0.77	0.77	46.	0.73
26	1	0.19	0.51	0.55	52.	0.41
27	1	0.13	0.45	0.47	55.	0.48
28	1	0.19	0.45	0.49	35.	0.46
29	1	0.06	0.45	0.46	26.	0.39
30	1	0.19	0.64	0.67	70.	0.47
31	1	0.06	0.26	0.27	60.	0.27
32	1	0.0	0.32	0.35	50.	0.24
33	1	-0.06	0.32	0.34	79.	0.34
34	1	-0.06	0.32	0.34	50.	0.29
35	1	0.0	0.26	0.26	50.	0.19
36	2	-0.96	0.77	1.26	15.	1.02
37	2	-0.70	0.51	0.89	49.	0.94
38	2	-0.77	0.96	1.23	8.	1.15
39	3	0.0	0.90	0.90	38.	0.73
40	3	0.0	0.96	0.96	47.	0.82
41	3	0.0	1.15	1.15	29.	1.02
42	3	0.0	0.77	0.77	36.	1.05
43	3	0.0	0.77	0.77	31.	0.95
44	3	0.19	0.83	0.86	77.	0.56
45	3	0.06	0.83	0.86	15.	0.71
46	2	0.32	0.90	0.95	50.	0.96
47	2	-0.83	1.28	1.54	49.	1.56
48	2	-0.26	1.28	1.31	50.	1.39
49	2	0.0	1.34	1.34	50.	1.71
50	2	0.0	1.47	1.47	50.	1.83

Results for: Bubble coalescence

No	ID	VX	VY	VE	Angle	Vmean
51	2	0.0	2.33	2.33	45.	1.79
52	2	0.0	2.20	2.20	46.	1.77
53	2	0.0	1.77	1.77	37.	1.72
54	2	0.0	1.51	1.51	69.	1.65
55	2	0.0	1.38	1.38	73.	1.63
56	2	-0.56	1.81	1.90	36.	1.55
57	2	0.0	2.16	2.16	50.	1.65
58	2	0.0	2.07	2.07	56.	1.58
59	2	0.0	2.20	2.20	53.	1.61
60	3	0.0	0.99	0.99	42.	0.97
61	3	0.0	0.95	0.95	47.	0.86
62	3	0.0	0.69	0.69	42.	0.73
63	3	0.0	0.69	0.69	36.	0.64
64	3	0.0	0.60	0.60	34.	0.58
65	2	0.0	0.95	0.95	46.	1.04
66	2	0.43	0.95	1.12	26.	1.09
67	2	0.0	0.82	0.82	54.	1.03
68	2	0.0	1.12	1.12	23.	1.09
69	2	0.0	1.42	1.42	25.	1.22
70	3	0.0	0.56	0.56	39.	0.57
71	3	0.0	0.65	0.65	25.	0.62
72	3	0.0	0.82	0.82	59.	0.63
73	3	0.0	0.69	0.69	36.	0.56
74	3	0.0	0.65	0.65	33.	0.58
75	2	-0.22	0.60	0.64	52.	0.76
76	2	-0.09	0.73	0.74	35.	0.69
77	2	-0.17	0.82	0.84	24.	0.82
78	2	0.0	0.82	0.82	45.	0.72
79	2	0.0	0.78	0.78	50.	0.79
80	3	-0.22	0.43	0.49	8.	0.53
81	3	-0.17	0.43	0.46	17.	0.51
82	3	-0.22	0.47	0.52	27.	0.49
83	3	0.09	0.34	0.36	89.	0.34
84	3	-0.09	0.43	0.47	64.	0.43
85	2	0.0	1.08	1.08	45.	0.91
86	2	0.0	1.08	1.08	66.	0.97
87	2	0.0	1.16	1.16	46.	1.05
88	2	0.0	0.86	0.86	53.	0.81
89	2	0.0	1.12	1.12	53.	1.16
90	3	0.0	0.56	0.56	64.	0.71
91	3	0.0	0.69	0.69	47.	0.73
92	3	0.0	0.65	0.65	39.	0.62
93	3	0.09	0.60	0.61	22.	0.65
94	3	0.13	0.60	0.62	19.	0.60
95	2	0.0	0.78	0.78	46.	0.75
96	2	0.0	1.12	1.12	50.	0.84
97	2	0.0	1.16	1.16	50.	0.93
98	2	-0.69	0.86	1.11	88.	0.98
99	2	-0.34	0.95	1.01	61.	0.94

Results for: Free bubbling 1.87 m/s

No	ID	VX	VY	VE	Angle	Vmean
1	1	-0.54	1.09	1.22	63.	1.22
2	1	-0.48	1.16	1.26	26.	1.26
3	2	-1.02	0.75	1.27	36.	1.27
4	3	-2.04	1.91	2.80	43.	2.80
5	3	-0.61	2.04	2.13	3.	2.13
6	3	-0.54	1.36	1.47	15.	1.47
7	2	-0.82	1.43	1.65	25.	1.65
8	1	0.20	1.43	1.88	43.	1.88
9	3	-0.61	1.97	2.07	31.	2.07
10	3	-0.61	2.25	2.33	11.	2.33
11	2	-0.68	1.97	2.09	71.	2.09
12	2	0.14	1.77	1.78	32.	1.78
13	2	0.0	1.70	1.70	32.	1.70
14	3	0.34	1.63	1.70	14.	1.70
15	3	0.20	1.70	1.73	1.	1.73
16	3	0.20	1.70	1.73	20.	1.73
17	3	0.0	1.70	1.70	51.	1.70
18	3	0.0	1.70	1.70	52.	1.70
19	2	-0.20	1.36	1.40	81.	1.40
20	3	0.0	1.97	1.97	52.	1.97
21	3	0.34	2.18	2.21	5.	2.21
22	3	0.41	2.31	2.35	15.	2.35
23	1	0.68	0.68	0.96	64.	0.96
24	1	0.89	0.89	1.25	78.	1.25
25	2	0.68	0.95	1.18	31.	1.18
26	2	0.68	0.89	1.12	50.	1.12
27	2	0.54	0.89	1.11	72.	1.11
28	3	0.68	0.82	1.07	5.	1.07
29	3	0.95	0.82	1.28	20.	1.28
30	3	0.27	2.04	2.06	18.	2.06
31	3	0.0	2.18	2.20	52.	2.20
32	2	0.20	2.38	2.39	49.	2.39
33	2	0.20	2.31	2.32	70.	2.32
34	2	0.20	2.11	2.12	38.	2.12
35	1	1.09	-0.27	1.15	19.	1.15
36	1	1.23	-0.14	1.24	68.	1.24
37	3	-1.02	1.50	1.83	21.	1.83
38	3	-0.82	1.97	2.14	14.	2.14
39	2	-0.68	1.50	1.65	16.	1.65
40	2	-0.68	1.09	1.29	30.	1.29
41	3	-0.68	1.50	1.65	66.	1.65
42	1	0.89	1.09	1.40	82.	1.40
43	1	0.54	1.50	1.60	84.	1.60
44	3	-0.61	1.29	1.44	11.	1.44
45	3	-0.41	1.50	1.57	8.	1.57
46	2	-0.68	1.16	1.35	16.	1.35
47	2	-0.68	1.23	1.40	44.	1.40
48	1	-0.75	1.09	1.33	54.	1.33
49	1	-0.61	1.16	1.31	74.	1.31
50	3	0.34	1.36	1.40	22.	1.40

Results for: Free bubbling 1.87 m/s

No	ID	VX	VY	VE	Angle	Vmean
51	3	0.68	1.36	1.52	4.	1.52
52	2	0.48	1.29	1.40	70.	1.40
53	2	0.54	1.63	1.72	72.	1.72
54	2	-1.02	1.36	1.72	35.	1.72
55	2	-0.82	1.23	1.47	26.	1.47
56	1	0.75	-0.20	0.80	9.	0.80
57	1	0.68	-0.54	0.92	39.	0.92
58	1	-1.57	0.20	1.58	70.	1.58
59	1	-1.77	0.61	1.89	77.	1.89
60	1	-1.23	1.09	1.64	74.	1.64
61	1	-1.02	1.36	1.72	53.	1.72
62	3	0.89	1.09	1.40	33.	1.40
63	3	0.34	1.29	1.34	27.	1.34
64	3	0.68	1.36	1.52	35.	1.52
65	2	0.68	1.50	1.65	62.	1.65
66	2	0.48	1.16	1.27	39.	1.27
67	1	0.34	0.89	0.96	69.	0.96
68	1	0.34	1.09	1.14	73.	1.14
69	2	0.82	0.75	1.11	55.	1.11
70	2	0.61	1.16	1.31	42.	1.31
71	3	-0.68	1.36	1.55	63.	1.55
72	3	-0.75	1.50	1.68	10.	1.68
73	3	-0.68	1.16	1.34	1.	1.34
74	2	-0.68	1.50	1.65	17.	1.65
75	2	-0.68	1.23	1.41	38.	1.41
76	3	-0.68	2.25	2.35	37.	2.35
77	3	-0.68	2.38	2.48	1.	2.48
78	3	-0.82	1.97	2.15	11.	2.15
79	2	-1.02	1.97	2.23	46.	2.23
80	1	-0.82	1.84	2.02	62.	2.02
81	3	-1.84	3.06	3.57	20.	3.57
82	3	-1.70	2.93	3.40	6.	3.40
83	2	-1.91	3.13	3.69	11.	3.69
84	2	-1.63	3.00	3.41	34.	3.41
85	2	-1.16	2.72	2.97	31.	2.97
86	2	-1.02	2.38	2.59	41.	2.59
87	3	-1.02	2.52	2.75	46.	2.75
88	3	-1.02	2.52	2.72	6.	2.72
89	3	-1.02	2.72	2.91	21.	2.91
90	2	-0.54	2.66	2.71	37.	2.71
91	2	-0.82	2.79	2.91	50.	2.91
92	3	-0.07	2.11	2.11	14.	2.11
93	3	-0.34	1.97	2.01	18.	2.01
94	3	-0.61	1.84	1.94	29.	1.94

Results for: Free bubbling 1.87 m/s

No	ID	VX	VY	VE	Angle	Vmean
1	3	-0.56	1.51	1.74	65.	1.48
2	2	-0.38	1.51	1.56	55.	1.11
3	1	-0.19	0.56	0.64	53.	0.87
4	3	0.0	1.88	1.88	52.	1.89
5	3	-0.19	1.51	1.53	52.	1.60
6	7	-1.51	1.51	2.13	--	1.49
7	4	0.0	0.57	0.94	--	1.44
8	5	0.77	-0.19	0.81	--	1.46
9	4	0.19	2.29	2.31	--	2.07
10	1	0.56	0.94	1.11	46.	1.54
11	3	0.75	3.39	3.49	52.	2.82
12	2	0.56	1.69	1.80	52.	1.62
13	5	0.19	0.38	0.69	--	0.97
14	3	-1.51	0.94	1.78	80.	2.09
15	6	0.19	-0.38	0.45	--	0.83
16	1	0.56	-0.19	0.64	25.	0.72
17	3	0.75	0.19	0.83	85.	0.87
18	2	-0.56	-0.19	0.64	13.	0.83
19	5	-0.75	-0.19	0.80	--	1.75
20	4	-0.19	0.57	0.65	--	1.02
21	3	-1.69	0.94	1.96	83.	1.57
22	2	-0.75	0.56	0.95	60.	1.29
23	3	-0.19	0.56	0.64	52.	0.67
24	2	-0.75	-0.56	0.95	37.	0.97
25	2	-0.94	-0.94	1.36	31.	1.62
26	3	1.32	2.07	2.46	51.	2.03
27	7	1.17	0.0	1.17	--	1.98
28	2	0.38	0.38	0.53	68.	1.19
29	2	0.56	1.13	1.38	32.	1.26
30	6	0.0	-0.57	0.57	--	1.51
31	3	-0.19	2.07	2.09	52.	1.71
32	1	-0.38	0.19	0.45	6.	0.35
33	5	-0.38	0.19	0.46	--	0.48
34	7	-1.70	0.0	1.70	--	3.22
35	4	0.19	0.38	0.46	--	0.90
36	6	0.19	2.09	2.11	--	2.05
37	1	-1.51	1.51	2.15	25.	2.95
38	2	-1.13	2.82	3.06	32.	3.24
39	3	0.38	1.69	1.74	52.	1.30
40	2	-0.19	0.56	0.61	32.	0.45
41	4	0.0	2.85	2.85	--	3.41
42	6	-0.19	2.10	2.11	--	2.03
43	1	-0.75	0.94	1.26	25.	1.16
44	3	0.0	1.88	1.88	52.	1.67
45	1	0.38	0.38	0.61	25.	0.60
46	2	1.88	2.82	3.40	56.	3.13
47	5	0.19	0.19	0.64	--	0.67
48	2	0.19	0.75	0.80	32.	0.65
49	2	1.51	2.45	2.88	31.	2.58
50	4	0.38	2.49	2.55	--	2.36

Results for: Free bubbling 1.87 m/s

No	ID	VX	VY	VE	Angle	Vmean
51	2	1.51	1.32	2.11	44.	1.50
52	5	1.51	-0.38	1.57	--	2.70
53	6	0.0	1.71	1.75	--	1.58
54	3	0.94	2.07	2.35	52.	2.05
55	5	-1.14	0.0	1.14	--	2.02
56	1	0.94	1.69	1.94	39.	2.39
57	1	0.38	1.13	1.22	31.	1.01
58	3	0.19	3.77	3.78	52.	3.48
59	2	0.0	1.88	1.88	32.	1.75
60	4	0.0	0.19	1.32	--	2.29
61	3	0.0	1.13	1.13	52.	1.00
62	6	0.0	0.94	0.94	--	1.31
63	7	-1.97	0.19	1.99	--	5.92
64	2	0.38	1.13	1.20	32.	1.19
65	6	-0.19	-0.95	0.98	--	1.63
66	2	-0.94	2.07	2.35	32.	2.35
67	2	-0.19	3.77	3.82	32.	3.56
68	7	-0.98	0.94	1.38	--	3.84
69	1	-0.19	0.19	0.38	10.	0.25
70	2	-0.56	2.26	2.35	32.	2.62
71	2	-0.75	4.14	4.22	32.	4.58
72	7	1.14	0.0	1.14	--	1.22
73	6	-0.56	-0.57	2.54	--	2.60
74	3	0.0	0.75	0.75	52.	0.60
75	3	0.0	3.77	3.77	52.	3.31
76	2	0.0	1.13	1.13	32.	1.00
77	2	0.75	1.51	1.68	89.	1.66
78	5	-0.19	-0.19	0.27	--	1.65
79	7	-0.98	-0.38	1.05	--	3.52
80	3	1.69	4.52	4.83	52.	4.51
81	5	0.0	-0.75	1.07	--	2.25
82	2	0.38	2.26	2.31	32.	2.67
83	2	-0.94	3.39	3.52	32.	4.11
84	6	0.56	0.19	2.52	--	2.58
85	5	-0.19	0.0	0.56	--	0.71
86	4	-0.19	0.19	0.99	--	2.12
87	2	1.51	2.82	3.29	51.	3.27
88	4	0.0	-0.98	0.98	--	2.74
89	3	0.0	0.94	0.94	52.	0.77
90	2	-1.51	3.20	3.59	32.	3.34
91	6	0.0	1.70	1.70	--	2.58
92	1	1.13	2.07	2.36	33.	2.64
93	3	-0.38	1.51	1.56	76.	1.18
94	7	0.19	0.0	0.19	--	0.71
95	1	-0.19	0.19	0.38	25.	0.50
96	2	1.13	0.19	1.16	66.	1.45
97	5	-1.71	-0.19	1.73	--	2.72
98	2	0.94	-0.19	0.97	8.	1.06
99	2	-1.69	-0.19	1.73	16.	1.61
100	3	-0.38	2.07	2.12	52.	1.62

Results for: Free bubbling 1.87 m/s

No	ID	VX	VY	VE	Angle	Vmean
101	3	0.19	1.13	1.15	52.	0.75
102	7	-1.14	0.38	1.20	--	2.31
103	4	0.19	-0.76	0.80	--	1.81
104	3	0.75	0.56	0.95	73.	0.92
105	2	1.32	-0.19	1.34	40.	0.97
106	3	-1.13	0.94	1.47	51.	1.60
107	7	0.76	0.56	0.95	--	1.40
108	1	0.56	0.19	0.61	25.	16.23
109	1	-0.38	0.38	0.61	4.	0.66
110	5	0.95	-0.19	0.98	--	0.97
111	1	-1.69	0.94	1.94	25.	1.84
112	2	-0.75	-0.94	1.26	27.	1.33
113	6	0.19	0.94	0.98	--	0.87
114	1	-1.32	-1.32	1.86	45.	1.86

Results for: Free bubbling 1.19 m/s

No	ID	VX	VY	VE	Angle	Vmean
1	4	0.0	0.62	0.75	--	1.12
2	5	0.41	0.20	0.49	--	0.45
3	6	0.41	0.63	0.79	--	1.53
4	2	0.61	0.20	0.66	25.	0.51
5	1	-1.02	-0.41	1.19	13.	1.45
6	1	-0.81	-0.20	0.86	49.	0.80
7	3	0.0	-0.61	0.61	73.	0.48
8	1	-0.81	1.43	1.64	49.	1.49
9	2	-0.61	-0.20	0.70	62.	0.82
10	7	0.41	0.41	0.58	--	0.61
11	6	-1.02	1.03	1.45	--	1.26
12	4	0.0	0.82	0.82	--	0.90
13	7	-0.84	0.0	0.84	--	2.59
14	2	-1.02	1.63	1.92	65.	1.90
15	3	0.0	1.43	1.43	73.	1.51
16	5	1.71	-0.20	1.82	--	2.64
17	3	-0.41	-0.61	0.78	72.	0.89
18	3	-0.20	0.61	0.70	64.	0.59
19	4	0.20	-0.61	0.66	--	1.26
20	5	0.20	-0.20	0.41	--	0.53
21	6	0.0	-0.61	0.61	--	0.69
22	1	-0.41	0.81	0.98	63.	0.94
23	5	-0.61	0.0	0.74	--	2.07
24	7	0.21	-0.41	0.61	--	0.93
25	2	0.20	0.41	0.49	62.	0.39
26	3	0.61	-0.61	0.91	72.	1.00
27	1	-0.61	-0.41	0.74	49.	0.76
28	2	0.20	-1.22	1.25	66.	1.20
29	4	0.0	1.25	1.25	--	1.78
30	6	0.20	0.82	0.87	--	1.46
31	3	0.0	0.61	0.61	73.	0.58
32	2	-0.20	0.61	0.70	74.	0.81
33	7	-0.20	0.20	0.41	--	0.86
34	1	0.20	0.41	0.49	50.	0.51
35	2	0.0	0.20	0.49	54.	0.37
36	5	-0.41	0.0	0.41	--	1.26
37	4	-0.41	1.31	1.38	--	3.06
38	3	0.0	0.61	0.61	73.	0.66
39	2	0.0	0.41	0.41	64.	0.58
40	6	-0.20	0.41	0.46	--	0.92
41	1	-0.81	0.20	1.03	49.	0.68
42	2	-0.41	0.20	0.49	63.	0.53
43	3	-0.61	0.20	0.70	19.	0.57
44	1	0.0	0.41	0.41	50.	0.54
45	2	0.61	-0.20	0.70	63.	0.88
46	3	0.0	1.02	1.02	73.	0.90
47	2	0.61	-0.61	1.05	65.	0.97
48	3	-0.20	0.20	0.29	84.	0.55
49	5	0.41	0.20	0.49	--	0.50
50	6	-0.20	0.62	0.67	--	0.79
51	2	-0.82	-0.41	0.98	8.	0.51
52	6	0.0	-0.62	0.62	--	0.36
53	3	-0.41	-0.81	0.91	73.	1.04
54	3	-0.20	0.41	0.49	65.	0.38
55	7	0.0	-0.20	0.20	--	0.17
56	4	0.20	0.62	0.82	--	0.87
57	2	0.61	-0.61	0.86	63.	1.12
58	5	-0.61	-1.02	1.70	--	1.81
59	4	0.20	0.82	0.87	--	0.83
60	2	0.0	0.20	0.20	64.	0.44

Results for: Tube Bundle 1.87 m/s

No	ID	VX	VY	VE	Angle	Vmean
1	3	0.40	0.20	0.49	53.	0.47
2	1	-0.20	0.40	0.49	40.	0.35
3	2	0.61	0.40	0.74	62.	0.55
4	3	-1.01	1.21	1.59	50.	1.42
5	2	0.40	0.20	0.49	64.	0.57
6	1	0.20	-0.40	0.49	63.	0.35
7	3	0.20	1.01	1.04	75.	1.03
8	2	0.40	0.61	0.77	64.	0.69
9	1	-0.40	0.61	0.74	38.	0.68
10	3	0.40	-0.40	0.65	45.	0.33
11	3	0.0	0.20	0.20	75.	0.17
12	2	0.40	0.61	0.74	56.	0.75
13	3	-0.20	1.21	1.25	81.	0.96
14	1	-0.20	0.20	0.40	22.	0.35
15	2	0.40	1.01	1.09	68.	1.18
16	1	-0.40	0.20	0.49	38.	0.39
17	1	0.40	0.20	0.49	18.	0.48
18	2	0.0	0.20	0.49	65.	0.27
19	3	-0.40	0.61	0.74	56.	0.82
20	2	-0.40	0.20	0.49	66.	0.46
21	2	0.20	0.40	0.49	76.	0.48
22	3	0.0	0.30	0.30	75.	8.20
23	1	0.40	0.61	0.74	56.	0.55
24	2	-0.40	0.40	0.57	81.	1.61
25	3	-0.61	0.61	0.86	45.	0.95
26	2	1.01	1.62	1.92	64.	1.53
27	1	0.61	0.20	0.69	38.	0.77
28	3	0.0	0.40	0.40	75.	0.22
29	2	0.81	1.01	1.30	64.	0.98
30	1	0.20	0.61	0.65	45.	0.59
31	3	-0.20	1.01	1.04	79.	0.96
32	3	-0.20	1.01	1.04	79.	0.87
33	2	-0.40	0.20	0.49	81.	0.39
34	3	-0.40	0.81	0.98	63.	0.83
35	2	-0.20	0.40	0.49	63.	0.81
36	2	-0.40	0.20	0.49	66.	0.82
37	1	-0.20	0.40	0.49	47.	0.55
38	2	-0.20	0.40	0.61	60.	0.61
39	1	0.40	0.40	0.81	4.	0.75
40	2	0.61	0.40	0.74	64.	0.56
41	2	0.61	2.02	2.12	73.	2.17
42	1	-1.21	1.82	2.19	56.	2.38
43	2	-0.20	0.81	0.89	76.	0.74
44	1	0.0	1.62	1.62	39.	1.83
45	3	-0.40	0.40	0.65	74.	0.61
46	3	0.0	0.40	0.40	79.	0.43
47	3	-0.20	0.61	0.65	72.	0.49
48	1	-0.20	0.40	0.49	63.	0.38
49	3	0.20	-0.20	0.29	22.	0.32
50	2	0.20	1.01	1.06	79.	0.95

Results for: Tube bundle 1.87 m/s

No	ID	VX	VY	VE	Angle	Vmean
51	2	0.61	0.81	1.42	64.	0.78
52	3	0.40	-0.20	0.49	54.	0.34
53	1	0.61	-3.44	3.67	8.	1.42
54	3	0.0	-0.20	0.20	76.	0.37
55	2	-0.40	0.81	0.98	63.	0.85
56	3	0.0	-0.20	0.20	75.	0.35
57	1	0.20	-0.20	0.40	38.	0.45
58	3	0.0	1.42	1.42	75.	1.21
59	1	0.61	0.61	0.86	45.	0.62
60	3	0.0	0.61	0.61	72.	0.43
61	3	-0.20	0.20	0.40	45.	0.25
62	2	0.40	-0.61	0.74	56.	0.80
63	3	0.0	0.0	-0.00	75.	-0.06
64	2	-0.61	0.40	0.74	88.	0.64
65	2	0.20	-0.40	0.49	62.	0.48
66	3	-0.20	0.81	0.89	76.	0.67
67	3	-0.40	1.01	1.09	75.	1.13
68	2	-0.20	-0.61	0.69	72.	0.63
69	1	0.61	0.81	1.02	53.	0.99
70	3	0.20	0.20	0.40	45.	0.42
71	3	-1.21	1.62	2.04	74.	1.83